Volume 5 Issue 2 (2019) · ISSN 2424-7723

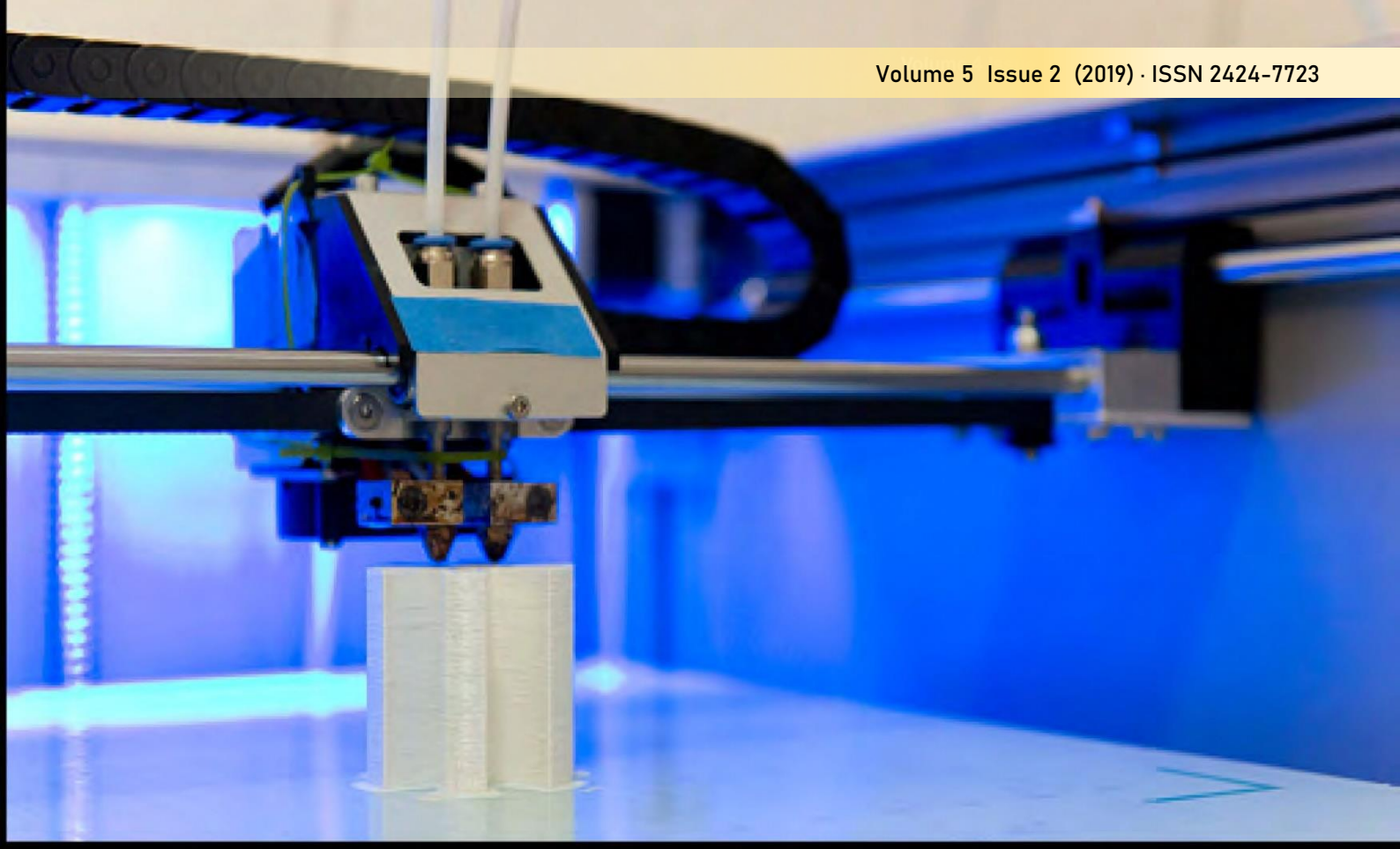

# INTERNATIONAL JOURNAL OF BIOPRINTING

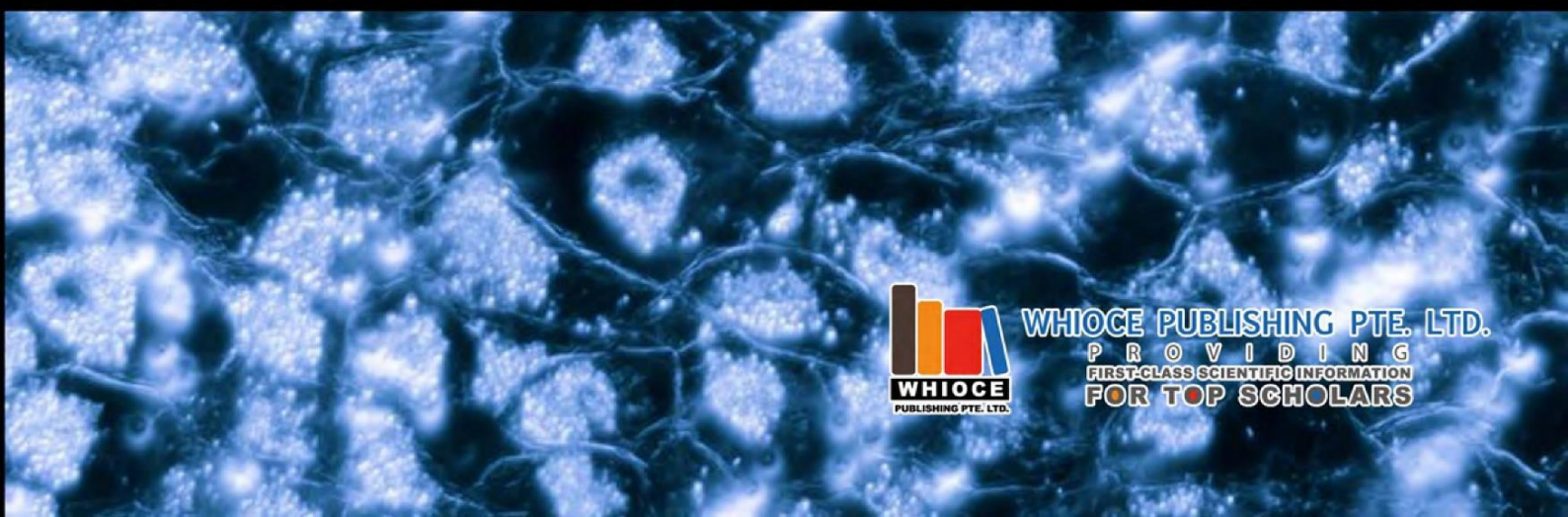

WHIOCE PUBLISHING PTE. LTD.
PROVIDING
FIRST-CLASS SCIENTIFIC INFORMATION
FOR TOP SCHOLARS

Volume 5 Issue 2• 2019
ISSN 2424-7723 (print) ISSN 2424-8002 (online)

# INTERNATIONAL JOURNAL OF BIOPRINTING

**Editor-in-Chief**

**Chee Kai Chua**

*Singapore University of Technology and Design, Singapore*

WHIOCE PUBLISHING PTE. LTD.

Volume 5 | Issue 2 | 2019 | Page 1 – 116 |

**International Journal of Bioprinting**

https://ijb.whioce.com/index.php/int-j-bioprinting

# CONTENTS

EDITORIAL

# Call for special issues

**Editor-in-Chief: Chee Kai Chua**

Head of Pillar, Engineering Product Development, Cheng Tsang Man Chair Professor, Singapore University of Technology and Design, 8 Somapah Rd, Singapore - 487372

http://dx/doi.org/10.18063/ijb.v5i2.228

The idea of bioprinting was conceived more than a decade ago by a small circle of thought leaders in tissue engineering and three-dimensional (3D) printing. The concept gained a slow recognition initially but rapidly spread with the advent of new 3D printing materials and processes. The exponential growth of scientific publications in the past years is remarkable. This uptrend coincides with an increased number of submissions to the journal. It is a positive signal that we should keep our fingers crossed on the evaluation of the International Journal of Bioprinting for acceptance into scientific citation index around the fourth quarter of this year.

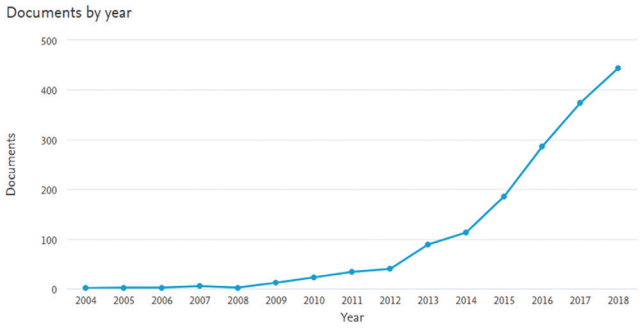


Data source: Scopus

In this July issue, 10 articles are covered. The topics range from the development of new bioinks[1-5] to new bioprinters such as microfluidics-based printers[6,7] and high precision inkjet printer[8], as well as *in vitro* 3D tissue models for tissue engineering[9,10].

Meanwhile, we have planned to enhance the global coverage of bioprinting research specifically in the USA and Asia. This will increase the total number of publications in 2019 by more than 50%, totaling between 30 and 40 articles. Hereby, I sincerely thank Professor Leu and Professor Fuh for their precious time and kind support in editing the following special issues respectively:

1. Special Issue: Bioprinting in the USA (Guest Editor: Professor Ming Leu, Guest Editorial Assistant: Dr. Krishna Kolan)
2. Special Issue: Bioprinting in Asia (Guest Editor: Professor Jerry Fuh, Guest Editorial Assistant: Dr. Sanjairaj Vijayavenkataraman).

On a separate note, I have moved to Singapore University of Technology and Design to pursue my personal goals. However, this will not affect my commitment and responsibilities to the journal. Instead, I see only more and more opportunities brought by this new endeavor. Please do write to my new email address (cheekai_chua@sutd.edu.sg) for matters related to the journal.

## References

1. Mishbak HH, Cooper G, Bartolo PJ, 2019, Development and Characterization of a Photocurable Alginate Bioink for Three Dimensional Bioprinting. *Int J Bioprint*, 5(2):189. DOI 10.18063/ijb.v5i2.189.
2. Arab W, Kahin K, Khan Z, Hauser CA, 2019, Exploring Nanofibrous Self-assembling Peptide Hydrogels Using Mouse Myoblast Cells for 3D Bioprinting and Tissue Engineering Applications. Int J Bioprint, 5(2):198. DOI 10.18063/ijb.v5i2.198.
3. Chen YW, Fang HY, Shie MY, Shen YF, 2019, The Mussel-inspired Assisted Apatite Mineralized on Polyjet Material for Artificial Bone Scaffold. *Int J Bioprint*, 5(2):197. DOI 10.18063/ijb.v5i2.197.
4. Shuai CJ, Yang WJ, Yang YW, Gao CD, He CX, Pan H, 2019, A Continuous Net-like Eutectic Structure Enhances the Corrosion Resistance of Mg alloys. *Int J Bioprint*, 5(2):207. DOI 10.18063/ijb.v5i2.207.
5. Ghalayini S, Susapto HH, Hall S, Kahin K, Hauser CA, 2019, Assessing the Preparation and Printability of Self-assembling Peptide Nanoparticles. *Int J Bioprint*, 5(2):239. DOI 10.18063/ijb.v5i2.239.
6. Zhang Y, 2019, 3D-Printing for Microfluidics or the other way

Call for special issues © 2019 Chua C K, *et al*. This is an Open Access article distributed under the terms of the Creative Commons Attribution-NonCommercial 4.0 International License (http://creativecommons.org/licenses/by-nc/4.0/), permitting all non-commercial use, distribution, and reproduction in any medium, provided the original work is properly cited.

Around? *Int J Bioprint*, 5(2):192. DOI 10.18063/IJB.V5I2.192.

7. Feng F, He JK, Li JX, Mao M, Li DC, 2019, Multi-component Bioprinting of Heterogeneous Hydrogel Constructs Based on Microfluidic Printheads. *Int J Bioprint*, 5(2):202. DOI 10.18063/ijb.v5i2.202.
8. Takagi D, Lin W, Matsumoto T, Yaginuma H, Hemmi N, Hatada S, Seo M, 2019, High-precision Three-Dimensional Inkjet Technology for Live Cell Bioprinting. *Int J Bioprint*, 5(2):208. DOI 10.18063/ijb.v5i2.208.
9. Lenoir L, Segonds F, Nguyen PKA, Pablo B, 2019, A Methodology to Develop a Vascular Geometry for *in vitro* Cell Culture Using Additive Manufacturing. *Int J Bioprint*, 5(2):238. DOI 10.18063/ijb.v5i2.238.
10. Fang A, Hao Z, Wang L, Li DC, He JK, Gao L. Mao X, Paz R, 2019, *In Vitro* Model of the Glial Scar. *Int J Bioprint*, 5(2):235. DOI 10.18063/ijb.v5i2.235.

PERSPECTIVE ARTICLE

# Application of additive manufacturing technology in orthopedic medical implant - Spinal surgery as an example

**Rong Feng Zhang[1], Peng Yun Wang[2]*, Ming Yang[3], Xuebo Dong[1], Xue Liu[1], Yiguang Sang[4], An Tong[5]***

[1]Department of Orthopaedics, Shandong Hospital of People's Liberation Army, 89th Hy, Weifang, Shandong Province, Republic of China
[2]Department of Spine Surgery, Central Hospital, Zibo, Zhangdian, Shandong Province, China
[3]Traditional Chinese Medicine Hospital, Dongying, Hekou, Shandong Province, China
[4]Qilu Hospital, Shandong University, Shandong, China
[5]Department of Orthopedics, People's Hospital of Yan'an, Qilipu Street, Yan'an, Baota, Shaanxi Province, China

**Abstract:** Additive manufacturing has been used in complex spinal surgical planning since the 1990s and is now increasingly utilized to produce surgical guides, templates, and more recently customized implants. Surgeons report beneficial impacts using additively manufactured biomodels as pre-operative planning aids as it generally provides a better representation of the patient's anatomy than on-screen viewing of computed tomography (CT) or magnetic resonance imaging (MRI). Furthermore, it has proven to be very beneficial in surgical training and in explaining complex deformity and surgical plans to patients/parents. This paper reviews the historical perspective, current use, and future directions in using additive manufacturing in complex spinal surgery cases. This review reflects the authors' opinion of where the field is moving in light of the current literature. Despite the reported benefits of additive manufacturing for surgical planning in recent years, it remains a high niche market. This review raises the question as to why the use of this technology has not progressed more rapidly despite the reported advantages – decreased operating time, decreased radiation exposure to patients intraoperatively, improved overall surgical outcomes, pre-operative implant selection, as well as being an excellent communication aid for all medical and surgical team members. Increasingly, the greatest benefits of additive manufacturing technology in spinal surgery are custom-designed drill guides, templates for pedicle screw placement, and customized patient-specific implants. In view of these applications, additive manufacturing technology could potentially revolutionize health care in the near future.

**Keywords:** Additive manufacturing; biomodeling; rapid prototyping; spine deformity; complex spine surgery

*Correspondence to: Peng Yun Wang, Department of Spine Surgery, Central Hospital, Zhangdian, Zibo, Shandong Province, China; wangpengyun1@sina.com; An Tong, Department of Orthopedics, People's Hospital of Yan'an, Qilipu street, Yan'an, Baota, Shaanxi Province, China; Tongangk@163.com

**Received:** October 31, 2018; **Accepted:** April 4, 2019; **Published Online:** July 1, 2019

**Citation:** Zhang RF, Wang PY, Yang M, *et al*., 2019, Application of additive manufacturing technology in orthopedic medical implant – Spinal surgery as an example. Int J Bioprint, 5(2): 168. http://dx.doi.org/10.18063/ijb.v5i2.168

## 1. Introduction

Spine surgeons engage in complex and innovative surgical procedures to stabilize and improve idiopathic, congenital, degenerative, and injury-related spinal deformities. Even though surgical treatment strategies and implants have evolved and improved considerably in recent decades, surgical correction of complex deformities remains very challenging. To evaluate the severity of spinal deformities and plan any required surgical procedures, physicians have

Application of additive manufacturing technology in orthopedic medical implant - Spinal surgery as an example © 2019 Zhang , *et al*. This is an Open Access article distributed under the terms of the Creative Commons Attribution-NonCommercial 4.0 International License (http://creativecommons.org/licenses/by-nc/4.0/), permitting all non-commercial use, distribution, and reproduction in any medium, provided the original work is properly cited.

traditionally relied on imaging modalities including X-rays, fluoroscopy, CT and MRI. Unfortunately, two-dimensional projections of radiographic images or three-dimensional (3D) scan data will always be limited in their ability to accurately display the complete image of 3D anatomic deformities, detracting from their value during the pre-operative planning process. As presented in the other papers in this article, the use of 3D modeling and rapid prototyping (RP) or additive manufacturing has been increasingly used in complex surgical pre-operative planning, as these techniques can accurately reproduce the anatomic details of highly complex deformities that could be missed or misinterpreted with standard imaging modalities.

The purpose of this article is to explore the existing uses of additive manufacturing in complex spinal surgery and to discuss the future potentials of this technology. The common techniques and requirements for additive manufacturing are addressed elsewhere[1]. Literature search was conducted using PubMed for articles containing the terms "additive manufacturing", "RP", "biomodelling", or "biomodeling", and in combination with "spine/spinal" and "surgery/surgical planning". General reviews or discussions of this technology where spinal usage is only briefly mentioned were not included.

## 2. Method

From the 16 articles that were found, one was excluded from further review as it is not available in English. Publication years ranged between 1999 and 2015, with nearly half of the papers published in the past 5 years, consistent with the rapidly increasing interest in this technology. Three key areas of focus are evident: Complex spinal deformity cases in which models have been printed for surgical planning purposes; the design of patient-specific drill guides; and the very recent advent of printing custom titanium implants.

Interestingly, there is a clear change in focus of the publications from 2009 to 2011 when simple printing for surgical planning was replaced by the printing of surgical tools and finally the implants themselves. Although publications on the use of additive manufacturing for surgical planning have declined in numbers recently, the current usage rates remain unclear. Has the spinal surgical community adopted this as a routine technology, or abandoned it in the past 10 years altogether? To better understand this shift, we conducted a survey of spinal surgeons attending the 2015 Annual Scientific Meeting of the Spine Society of Australia and presented the results here.

## 3. Historical Usage and Current Trends

The use of additively manufactured models in complex spine deformity surgical planning was first reported in 1999 by a group of researchers from Australia. D'Urso *et al*.[2] reported the previous use of the technology in craniomaxillofacial surgery and undertook a preliminary prospective study of five complex cases to determine its usefulness in spine deformity surgery. Members of this group continue to be at the forefront in this area, having published a number of other key papers in the field[3-5]. These papers include a total of 51 cases where spine biomodels have been utilized, with the remaining four papers in this field are from Japan and China, which describe 53 additional cases[6-9]. All the authors from these published articles agreed that a 3D reconstructed model is required to obtain comprehensive information about the complex spinal deformities that would have been unavailable if conventional imaging modalities were exclusively used. They found that although CT 3D reconstruction could be displayed and viewed from any direction and angle on the computer, these method lack of tactile view which frequently view the biomodel separately and results in some alteration being made to the surgical case, be it an implant, approach, or fixation related[6-9].

## 4. Complex Spinal Deformity Surgical Planning

Literature findings concluded that the use of additively manufactured biomodels offered numerous benefits resulting in better surgical outcomes for the patients for example, Mizutani *et al*.[7] fifteen cases were evaluated and reported that 3D modeling was beneficial as a pre-operative planning tool in rheumatoid cervical spine surgery. This was attributed to a better assessment of the trajectory and entry points of cervical pedicle screws, as well as allowing for the ability to determine the entire plate-rod contours for occipitocervical junctions, avoiding post-operative dysphagia. Although having a 3D biomodel have advantages such as a detailed representation of anatomy and as a tool for planning surgical procedures, the authors concluded that coupling the 3D model with computer-assisted navigation systems likely provided better surgical results. Izatt *et al*.[5] aim to quantify the surgeon's perception on the usefulness of biomodels compared with standard imaging modalities as a pre-operative planning tool and as an intraoperative anatomic reference in 26 spinal tumor and deformity cases. This study entailed a survey completed by the surgeons after each surgical case and found that anatomic details were better or exclusively visible on the biomodel (65% and 11%, respectively) compared with the CT or MRI 3D reconstructions. Therefore, different decisions were made as a direct result of the biomodel regarding the materials used (52%) and implantation sites (74%), thereby reducing the likelihood of surgical revision being required. Importantly, this paper also recorded an estimated 17% decrease in operating time for all 26 patients, with

an 8% reduction in surgery time for tumor patients (mean 46 min per case) and 22% reduction in the deformity cases (mean 68 min per case) which directly reduced the cost of surgery in addition to the other reported benefits. Reasons given for the reduction in surgical time were included: easier, accurate and more efficient implant and screw positioning; less frequent reference to other imaging resources and reduced number of instrumentations due to better anatomic visualization; and detailed pre-operative planning. A recent systematic review paper by Martelli *et al*.[10] based on 52 papers reported that time was saved due to additive manufacturing. Likewise, Mao *et al*.[8] also confirmed that 3D biomodels were helpful in improving pre-operative planning and surgical treatment of complex severe spinal deformities compared with either CT or MRI 3D spinal reconstructions. This paper suggested that the biomodels were a superior visual aid when confirming the position of an anatomic landmark, helped the surgeon plan the surgery, facilitated the choice of internal fixation instrumentation, and improved the accuracy, and therefore, the safety of pedicle screw insertion all of which would influence the direct costs of the surgical cases and the risk of revision surgery being required in the future.

Another important factor discussed by both Mao *et al*.[8] and Izatt *et al*.[5] was the use of additively manufactured biomodels as a communication tool with both colleagues and patients/parents. Patients (or if they were <18 years old, their parents/guardians) were contacted after the surgery, and all stated that the biomodels improved their anatomic understanding of the condition; the procedure and the risks associated with it, and, therefore, improved their ability to give fully informed consent. Similarly, biomodels enabled better communication and teaching within the surgical team both preoperatively and intraoperatively. Of course, there were also limitations presented in using this technology mainly related to the extra time, labor, and the associated costs of biomodel manufacture. Nevertheless, it was argued that these issues were offset by the cost savings from shorter surgical times, the reduced complication rates, and the likelihood of surgical revision being required in the future[3,5,7].

Presented below are two case studies performed by the authors of this article where additively manufactured biomodels were used for pre-operative planning.

### 4.1. Patient A

A 12 year old male, diagnosed with neurofibromatosis type 1 with complex occipitocervical spinal deformities and a large neuroma in close proximity to the upper cervical spine. The patient was demonstrating steadily worsening neurological signs in all limbs and had experienced a number of episodes of intermittent quadriparesis indicative of progressive brainstem/spinal cord compression, requiring surgical decompression and stabilization. Preoperatively, the patient had posterior-anterior (PA) and lateral (LAT) cervical and full spine radiographs (Figure 1), brain and full spine MRI (Figure 2), and 3D CT scans (Figure 3). The CT scan was used to create a 3D anatomic biomodel (Figure 4).

After viewing the available imaging data, the initial surgical plan was to perform a posterior instrumented fusion from occiput to T4 with screw fixation into the occiput and thoracic spine only. Due to the small size and deformity of the cervical vertebrae, it was considered that the upper cervical vertebrae were too small to be able to insert any fixation points for the planned posterior construct. After receiving the biomodel, it became evident that the C2 laminae were of sufficient size for small translaminar screws to be used on each side. The surgical instrumentation was changed to include these translaminar screws in addition to the fixation points already planned at the occiput and T3-4 levels.

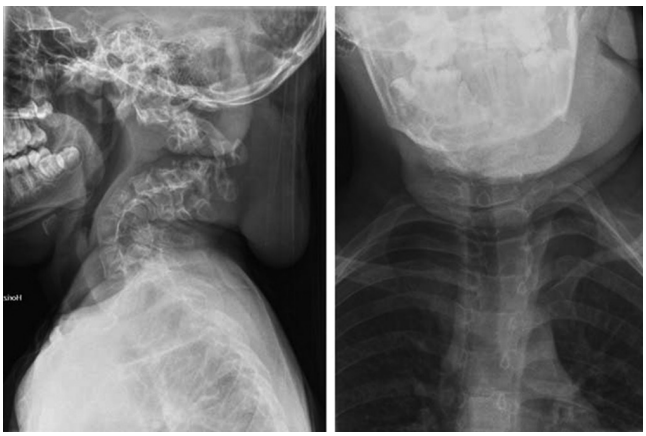

**Figure 1.** Pre-operative lateral and posterior-anterior radiographs of the cervical and upper thoracic spine of 12-year-old male (neurofibromatosis type 1, plexiform neuroma posterior to cervical spine), which did not provide clear anatomic detail of significant upper cervical deformity.

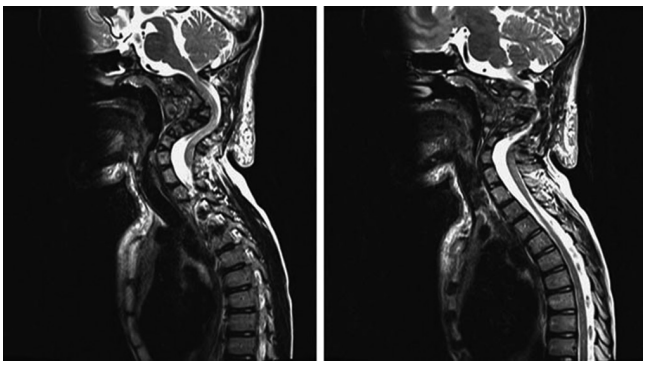

**Figure 2.** Sagittal slices of pre-operative magnetic resonance imaging showing the reduced size of the spinal canal in the upper cervical spine with insufficient posterior element bony detail (patient A).

The biomodel greatly assisted with the explanation to the child's parents regarding the surgery planned and the associated risks involved, thereby, helped to obtain informed consent.

The surgeons reported that the addition of fixation to the upper cervical spine had made the instrumented construct more robust and had improved the deformity correction achieved by the procedure in addition to the decompression and stabilization components. With the additional fixation points, the surgeon reported that the risk of requiring a revision procedure in the future was also less likely. Although the pedicle screw placement in the thoracic spine was not optimum, they have held well to date, the patient's neurological signs have improved and thereafter remained stable, with no loosening or loss of correction now 10 months postoperative. Supine LAT and PA radiographs 1 month after surgery and the most recent LAT view at 10 months post-operative are shown in Figure 5.

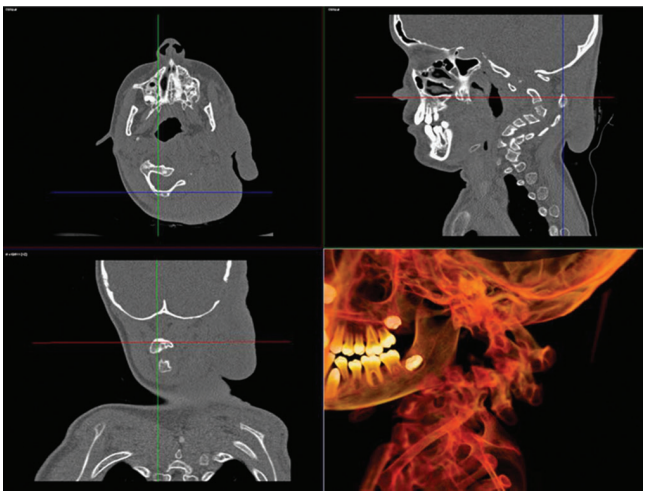

**Figure 3.** Multiplanar views of pre-operative computerized tomographic (CT) scan at the C2 level and three-dimensional CT reconstruction (lower right), which suggested insufficient vertebral bone in the posterior elements of the upper cervical spine for posterior fixation (patient A).

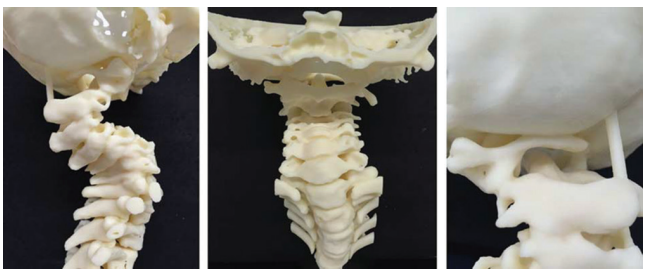

**Figure 4.** Three-dimensional printed biomodel (sagittal, anterior, and upper cervical close-up views) demonstrates that the anatomy of the C2 laminae was of sufficient size to accept fixation posteriorly in addition to the previously planned fixation points in the base of the skull and upper thoracic spine (patient A).

## 4.2. Patient B

A 9 year old female, diagnosed with myelomeningocele spina bifida (neurological deficit below T10) with severe collapsing T10-S1 due to the total absence of posterior elements. The resulting kyphotic deformity was causing seating difficulties and the maintenance of the integrity of the skin over the kyphotic deformity was becoming challenging, with skin breakdown becoming more frequent. It was considered that kyphectomy and posterior instrumented fusion would improve the quality and length of life. Preoperatively, the patient had PA and LAT sitting spine radiographs (Figure 6), thoracolumbar spine CT with 3D reconstruction (Figure 7), and a biomodel was ordered (Figure 8).

The surgical plan was to ideally perform a kyphectomy between two and five levels followed by deformity correction and stabilization with a posterior instrumented fusion from the upper thoracic spine to the pelvis; however, the thoracolumbar anatomy, especially the thoracolumbar junction anatomy, remained unclear. Having no posterior spinal elements to fix

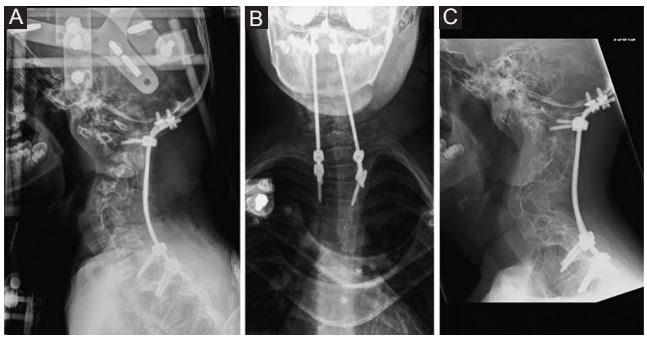


**Figure 5.** Post-operative lateral (**A**) and posterior-anterior radiographs (**B**) of the cervical and upper thoracic spine with halo brace *in situ* illustrating the instrumented correction and stabilization achieved surgically for patient a. Follow-up radiographs, 10-month postoperative (**C**).

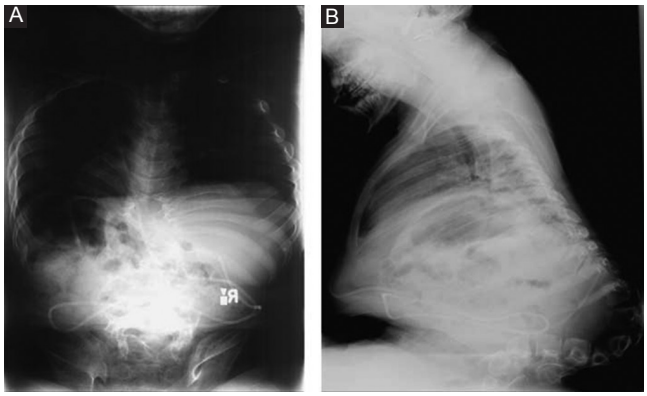


**Figure 6.** Pre-operative sitting posterior-anterior (**A**) and lateral (**B**) radiographs of the entire spine of a 9-year-old female (myelomeningocele spina bifida) with collapsing kyphosis (patient B).

instrumentation into, alternative fixation points were required. After receiving the biomodel, the anatomy of the lower thoracic and lumbar spine was clear and the decision was made with some confidence to proceed with the kyphectomy of L1-L3 followed by an instrumented fusion from T3-pelvis (Figures 9 and 10). The biomodel also greatly assisted with the explanation to the child's parents regarding the planned surgery and the associated risks involved, thereby, helped to obtain informed consent. The patient recovered well, and the parents reported that caring for their child was much easier, as was her comfort when seated in her wheelchair. There was an added benefit of being able to sleep supine for the 1st time in many years. There were no longer any issues with skin integrity or pressure areas over her spine. The fixation has remained stable with no complications.

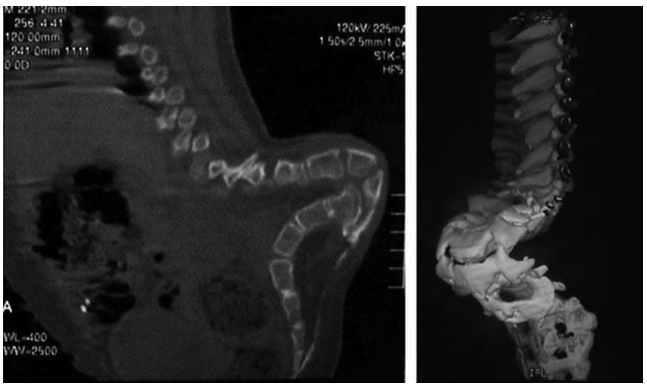

**Figure 7.** Sagittal views from pre-operative computerized tomographic (CT) scan and three-dimensional CT reconstruction (far right) of the thoracic and lumbar spine showing more anatomic detail than radiographs of the deformity, but insufficient detail to decide how many levels to remove and the precise fixation points for the instrumentation (patient B).

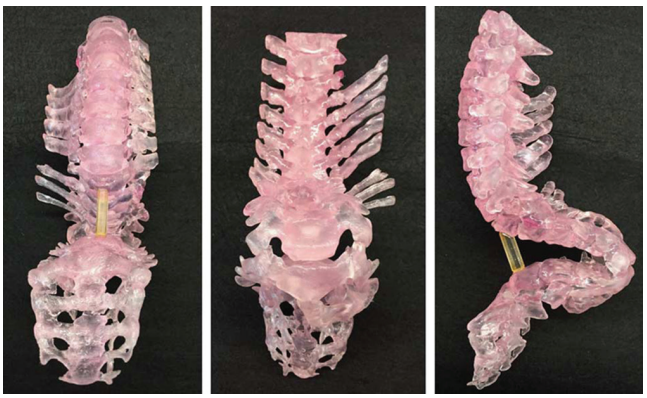

**Figure 8.** Three-dimensional printed biomodel (anterior, posterior, and lateral views) demonstrates the anatomy of the thoracic and lumbosacral spine providing the necessary detail for the kyphectomy and subsequent successful deformity correction and instrumented fusion procedure patient.

## 5. Surgical Tools and Guides

Since 2009, designing and printing guides for pedicle screw placement has emerged as a new area of additive manufacturing for spinal surgical planning, particularly in the cervical spine[11,12]. The anatomy in this region is quite compact and even more so in pediatric cases, with delicate neural tissue in close proximity making precise screw insertion of great importance.

The earlier papers from Lu *et al*.[11,12] utilized additively manufactured drill guides for two kinds of screw placement in the cervical spine. These plastic guides were placed directly in contact with the patient's exposed bony anatomy in the operating room and used to insert screws along predefined trajectories. The author reported that this technique is highly accurate. Additionally, reduces both the surgery time and radiation exposure. These

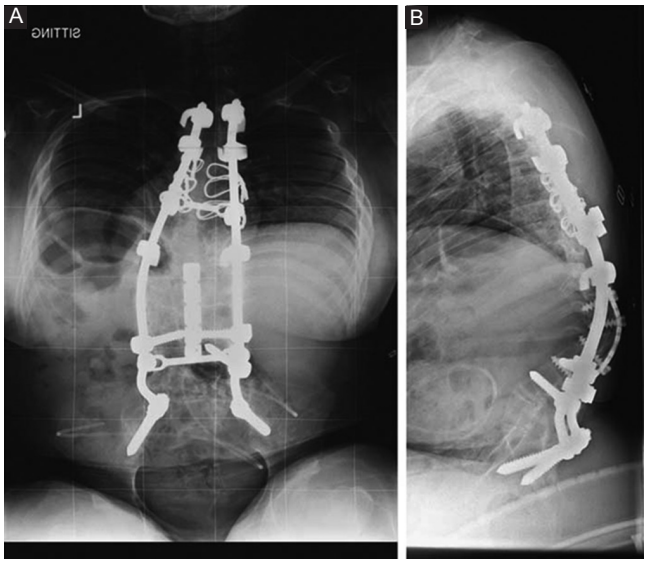

**Figure 9.** Post-operative anterior-posterior (**A**) and lateral (**B**) radiographs illustrating the instrumented correction and stabilization achieved surgically for patient B.

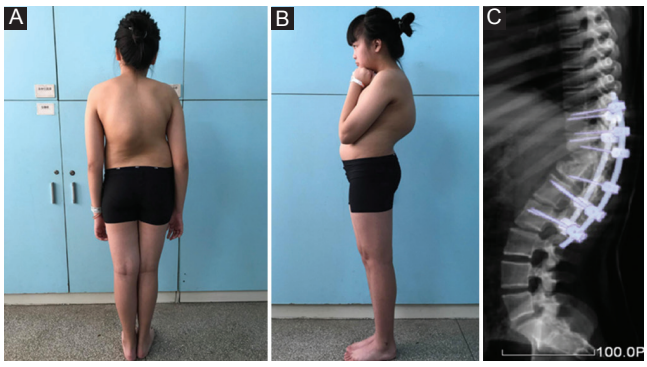

**Figure 10.** Pre-operative (**A** and **B**) and post-operative (**C**) photographs showing cosmetic aspects of the deformity before and after surgical correction assisted by the use of the three-dimensional printed biomodel (patient B).

papers were then followed by a series of cadaveric studies describing the effectiveness of additively manufactured plastic pedicle screw template[13,14]. In summary, the researchers found that by using the screw template the intended insertion location and angle correlate.

As a result, titanium was proposed as an alternative to plastic models for surgical guides; however, it was also found to have disadvantages such as cost and availability. In the study by Takemoto *et al*.,[15] additive manufactured titanium thoracic pedicle screw templates were assessed specifically looking at the landmarks used as contact points for the template, to ensure reproducibility and stability. This study showed a very high success rate for their templates, with failure defined as perforation of the pedicle wall by the screw, 98.4% of pedicle screws were placed successfully for scoliosis patients and 100% for ligament ossification patients. The issue of cost was also addressed in this study stating that the production cost of 10 templates in a singular patient amounted to $1000 for titanium versus $200 for the plastic polyamide.

The authors pointed out that even though the non-metallic materials have approval from the US Pharmacopeia for use in the human body for 24 h when in contact with drills and surgical tools; the plastic would likely produce debris, which would accumulate in the wound. The long-term effect of this residual material is unknown, and in close proximity to the spinal cord, its safety is clearly questionable. The titanium templates also have the advantage of higher strength and rigidity, being metallic. This ensures greater accuracy and reliability, reduces the chance of warping and flexing, and eliminates the potential of the drill or screw cutting through the material and/or producing debris as is the case for plastic guides.

## 6. Additively Manufactured Custom Implants

Recent advances and the increased availability of metal-based additive manufacturing technologies such as direct or selective laser sintering (LS) and electron beam melting have allowed for the development of customized spinal implants into current surgical practice.

Off the shelf, vertebral body and intervertebral disc implants are already commonly used, but the ability to 3D print both generic and custom metal implants has a number of potential advantages. For instance, intervertebral discs that can be printed to conform to the patient's specific vertebral end plate geometry have performed well in cadaveric studies, achieving higher compressive failure loads, and better stiffness characteristics than flat implants produced in the same manner[16]. On the other hand, a high-temperature LS allows fabrication layering of complex structure such as high-performance biomaterial polymer, i.e., polyether ether ketone was applied by Berretta *et al*. in the manufacturing of cranial implant[17]. Both the mechanical performance, density variation, and dimensional accuracy of the implants were found comparable to the design model and show the highest compressive strength resistance.

Evidently, an additively manufactured porous titanium structures have great potential for use as bone substitute biomaterials. Titanium alloys have been used for decades as a bioactive material[18], encouraging bony ingrowth onto exposed surfaces. For instance, titanium-tantalum (Ti-Ta) alloy can be fabricated using selective laser melting[19]. Ti-Ta alloys are promising materials for biomedical applications and surgical implants because it has high biocompatibility, corrosion resistance, and good mechanical properties. Besides, electron beam melting allows porous implants made from titanium alloys to be created with control over the shape and pore structure. This technology has the potential to develop both patient-specific custom implants, as well as generic bone substitute implants. Yang *et al*.[20] examined a self-stabilizing artificial vertebral body created this way in an *in vivo* sheep model of the cervical spine. This study found that these porous metal implants facilitated bony ingrowth and resulted in very stable fixation in a load-bearing application – something that is not currently possible with other additively manufactured scaffold structures.

Worldwide, a number of companies are already making additively manufactured customized surgical tools and templates to aid in spinal procedures, as well as custom spinal implants designed specifically for particular patients. Besides the customized spinal implants, the similar technologies were applied to other recent orthopedic regenerative medicine treatment[21]. A mandible that is coated with hydroxyapatite has been additively manufactured[22]. Furthermore, Mertens *et al*. constructed a titanium-made midfacial support and a graft fixture through additive manufacturing for patient with midface defect[23]. Customized cranial implants were designed and additively manufactured by Jardini *et al*. in the surgical reconstruction of a large cranial defect[24].

## 7. Surgeon Survey

Spinal surgeons attending the Annual Scientific Meeting of the Spine Society of Australia 2015 held in Canberra, Australia, were asked to complete a short survey on their knowledge and use of RP technology (additive manufacturing) in their surgical practices and experience. 35 surgeons completed the survey, of which 81% (27) were experienced, senior consultants. Although 80% of respondents had heard of using additive manufacturing for surgical planning, only 10 had ever used it. Of these 10, eight reported using it 0–2 times per year and two reported using it 3–5 times per year. Most users (7/10) reported that it improved the surgical outcome, with the

others saying that it made no difference to the surgical outcome. However, additionally, the comment was made that while they felt that the biomodel did enhance surgical planning and the ability to perform the surgical intervention, the outcome to the patient was the same as if they had not used it.

For those who were not using the technology, most reported that this was due to availability issues (44%). However, only 54% said that they would use it should it ever become available in their hospital. Other minority reasons given for not using biomodels were cost (4%, $n$ = 1) and other reasons (12%, $n$ = 3), predominantly being that they do not or have not had a suitable case for which to use it to date.

These results, together with discussions with the surgeons while they were completing the survey, highlighted a number of important considerations: That of the suitability of cases for this type of procedure in a particular surgeon's practice, as well as the usefulness of biomodels for purposes other than developing the actual surgical plan. The surgeons who currently used additive manufacturing for surgical planning all worked with patients who had complex progressive deformities, whereas those who did not use biomodels treated less complex and mainly adult degenerative cases, for which the added expense and time delay to print the model was thought to likely not be of sufficient benefit to their surgical planning and/or surgical procedure.

According to surgeons, the usage of additively manufactured models are often extended, which is beyond the surgical planning phase. Hence, patient or their guardian needs to be aware of the this situation when signing the informed consent form. Having a physical model available of a complex spinal deformity made the explanation of the current condition as well as the intended surgical procedure to patients and family much simpler and easier to understand. The description of both the severity and the reasons for the current symptoms caused by the spinal deformity could be explained more clearly as well as exactly what the surgery would entail and the possible complications and consequences that may occur with or without the intended surgical procedure. This sentiment has also been reported in literature discussed above[4]. Furthermore, using the additively manufactured models with surgical trainees form an important teaching tool during the surgical planning phase, during the surgical procedure, and as retrospective case studies.

### 7.1. Future Perspectives

As reflected in this review, the use of additive manufacturing as a pre-operative planning tool in spinal surgery is still relatively uncommon, even though the technology has continued to develop over the past three decades. This review raises the question as to why the use of this technology has not progressed more rapidly despite the reported advantages – decreased operating time, decreased radiation exposure to patients intraoperatively, improved overall surgical outcomes, pre-operative implant selection, as well as being an excellent communication aid for all medical and surgical team members. Regardless of the reported clinical success, the lack of usage of 3D RP or printing has been attributed to the availability and cost of the technology, as well as the time delay between the scan of the patient is performed and the biomodel being produced (several days) and then delivered to the requesting surgeon. The other main reason given for not using physical 3D biomodels was that the particular surgeon did not treat the type of spinal deformity patients that would benefit from this technology, who are managed by a small contingent of highly specialized complex deformity surgeons.

The future success of this technology is dependent on how useful surgeons find the biomodels to be for pre-operative planning and consent and/or for intraoperative anatomic reference compared with standard visualization modalities such as CT scans. Do additively manufactured biomodels have the potential to become part of the standard of care, or will it always be used only for the most complex deformity cases by specialist spinal surgeons and how will the success of the technology be measured? Answering these questions will be vital for additive manufacturing to become an essential part of spinal deformity surgery as the technology continues to improve, becomes more affordable and faster to produce. It seems clear that even if biomodels are only used on a limited basis during the surgical procedure for the most complex cases of spinal deformities, there is certainly value in the exercise of virtual planning or 3D computer modeling, a processing step that is generated before final additive manufacturing occurs. The generation of the 3D computer model allows for the on-screen manipulation of the patient's-specific anatomy generated from their CT scan for the purpose of visualization of the deformity for pre-operative planning and rehearsal of the intended surgery. Therefore, whether or not the final stage of printing goes ahead; utilization of the technology of 3D computer modeling will most likely become a routine part of spinal surgery for the benefit of clinicians and patients alike.

It is worth noting that based on the number of publications found in literature, China has the appearance of leading the medical field in the use of RP technology. Why are some countries such as China more readily accepting RP technology and why are they at the forefront in using it compared with the western world? Perhaps, it is related to the fact that in western countries, private biomedical companies are driving this technology and its use rather than research institutions, which often does not translate into peer-reviewed publications.

In contrast, for the design of surgical tools, templates, and personalized patient implants, additive manufacturing technology has found a new niche which is demonstrating a rapid advance and may be the most promising application in the medical field. We believe that the future of customized patient-specific implants will be the greatest benefit of additive manufacturing technology, potentially revolutionizing health care, and benefitting the largest number of patients. This is especially true as the trend continues toward less invasive and more precise surgical treatment strategies, and as clinicians increasingly relies on advanced technologies for planning and delivering customized and patient-specific medical care.

Further discussion on the techniques, technology, and limitations of additive manufacturing in health care can be found in other articles in this issue.

## References


1. Green N, Glatt V, Tetsworth K, *et al*., 2016, A Practical Guide to Image Processing in the Creation of 3D Models for Orthopaedics. *Tech Orthop*, 31(3):153-63. DOI 10.1097/BTO.0000000000000181.
2. D'Urso P, Askin G, Earwaker J, 1999, Spinal Biomodeling. *Spine (Phila Pa 1976)*, 24:1247-51. DOI 10.1097/00007632-199906150-00013.
3. D'Urso PS, Williamson OD, Thompson RG, 2005, Biomodeling as an Aid to Spinal Instrumentation. *Spine (Phila Pa 1976)*, 30(12):2841-5. DOI 10.1097/01.brs.0000190886.56895.3d.
4. D'Urso PS, 2006, Biomodelling. In: Gibson I, editor. *Advanced Manufacturing Technology for Medical Applications: Reverse Engineering, Software Conversion and Rapid Prototyping*. Chichester, United Kingdom: John Wiley and Sons Ltd., p31-57. DOI 10.1002/0470033983.ch3.
5. Izatt MT, Thorpe PLP, Thompson RG, *et al*., 2007, The use of Physical Biomodelling in Complex Spinal Surgery. *Eur Spine J*, 16(9):1507-18. DOI 10.1007/s00586-006-0289-3.
6. Yamazaki M, Akazawa T, Okawa A, *et al*., 2007, Usefulness of Three-dimensional Full-scale Modeling of Surgery for a Giant Cell Tumor of the Cervical Spine. *Spinal Cord*, 45:250-53. DOI 10.1038/sj.sc.3101959.
7. Mizutani J, Matsubara T, Fukuoka M, *et al*., 2008, Application of Full-scale Three-dimensional Models in Patients with Rheumatoid Cervical Spine. *Eur Spine J*, 17(5):644-9. DOI 10.1007/s00586-008-0611-3.
8. Mao K, Wang Y, Xiao S, *et al*., 2010, Clinical Application of Computer-designed Polystyrene Models in Complex Severe Spinal Deformities: A Pilot Study. *Eur Spine J*, 19(5):797-802. DOI 10.1007/s00586-010-1359-0.
9. Yang JC, Ma XY, Lin J, *et al*., 2011, Personalised Modified Osteotomy using Computer-aided Design-rapid Prototyping to Correct Thoracic Deform-ities. *Int Orthop*, 35(12):1827-32. DOI 10.1007/s00264-010-1155-9.
10. Martelli N, Serrano C, van den Brink H, *et al*., 2016, Advantages and Disadvantages of 3-dimensional Printing in Surgery: A Systematic Review. *Surgery*, 159(6):1485-500. DOI 10.1016/j.surg.2015.12.017.
11. Lu S, Xu YQ, Lu WW, *et al*., 2009, A Novel Patient-specific Navigational Template for Cervical Pedicle Screw Placement. *Spine (Phila Pa 1976)*, 34(26):E959-66. DOI 10.1097/BRS.0b013e3181c09985.
12. Lu S, Xu YQ, Zhang YZ, *et al*., 2009, A Novel Computer-assisted Drill Guide Template for Placement of C2 Laminar Screws. *Eur Spine J*, 18(9):1379-85. DOI 10.1007/s00586-009-1051-4.
13. Fu M, Lin L, Kong X, *et al*., 2013, Construction and Accuracy Assessment of Patient-specific Biocompatible Drill Template for Cervical Anterior Transpedicular Screw (ATPS) Insertion: An *in vitro* Study. *PLoS One*, 8(1):e53580. DOI 0.1371/journal.pone.0053580.
14. Hu Y, Yuan Z, Spiker WR, *et al*., 2013, Deviation Analysis of C2 Translaminar Screw Placement Assisted by a Novel Rapid Prototyping Drill Template: A Cadaveric Study. *Eur Spine J*, 22(12):2770-6. DOI 10.1007/s00586-013-2993-0.
15. Takemoto M, Fujibayashi S, Ota E, *et al*., 2016, Additive-Manufactured Patient-specific Titanium Templates for Thoracic Pedicle Screw Place-ment: Novel Design with Reduced Contact Area. *Eur Spine J*, 25:1698-705. DOI 10.1007/s00586-015-3908-z.
16. de Beer N, Scheffer C, 2012, Reducing Subsidence Risk by using Rapid Manufactured Patient-specific Intervertebral Disc Implants. *Spine J*, 12(11):1060-6. DOI 10.1016/j.spinee.2012.10.003.
17. Berretta S, Evans KE, Ghita OR, 2018, Additive Manufacture of PEEK Cranial Implants: Manufacturing Considerations Versus Accuracy and Mechanical Performance. *Mater Des*, 139(1):141-52. DOI 10.1016/j.matdes.2017.10.078.
18. Cook HP, 1969, Titanium in Mandibular Replacement. *Br J Oral Surg*, 7:108-11. DOI 10.1016/S0007-117X(69)80005-3.
19. Sing S, Yenog WY, Wiria FE, 2018, Selective Laser Melting of Titanium Alloy with 50 wt% Tantalum: Effect of Laser Process Parameters on Part Quality. *Int J Refract Met Hard Mater*, 77:120-7. DOI 10.1016/j.ijrmhm.2018.08.006.
20. Yang J, Cai H, Lv J, *et al*., 2014, *in vivo* Study of a Self-Stabilizing Artificial Vertebral Body Fabricated by Electron Beam Melting. *Spine (Phila Pa 1976)*, 39(8):E486-92. DOI 10.1097/BRS.0000000000000211.

21. Wang X, Xu S, Zhou S, *et al*., 2016, Topological Design and Additive Manufacturing of Porous Metals for Bone Scaffolds and Orthopaedic Implants: A Review. *Biomaterials*, 83:127-41. DOI 10.1016/j.biomaterials.2016.01.012.
22. Xillo, 2011, The World's First 3D Printed Total Jaw Reconstruction. Available from: http://www.xilloc.com/patients/stories/total-mandibular-implant.
23. Mertens C, Lowenheim H, Hoffmann J, 2013, Image Data Based Reconstruction of the Midface Using a Patient-specific Implant in Combination with a Ascularized Osteomyocutaneous Scapular Flap. *J Cranio Maxillofac Surg*, 41:219-25. DOI 10.1016/j.jcms.2012.09.003.
24. Jardini AL, Larosa MA, Zavaglia CAC, *et al*., 2014, Customised Titanium Implant Fabricated in Additive Manufacturing for Craniomaxillofacial Surgery. *Virtual Phys Prototyp*, 9:115-25. DOI 10.1080/17452759.2014.900857.

RESEARCH ARTICLE

# Development and characterization of a photocurable alginate bioink for three-dimensional bioprinting

**H. H. Mishbak[1,2], Glen Cooper[2], P. J. Bartolo[2]***

[1]Department of Biomedical Engineering, School of Engineering, University of Thi-Qar. Thi-Qar, Iraq
[2]Manufacturing Group, School of Mechanical, Aerospace and Civil Engineering, The University of Manchester, Manchester, UK

**Abstract:** Alginate is a biocompatible material suitable for biomedical applications, which can be processed under mild conditions on irradiation. This paper investigates the preparation and the rheological behavior of different pre-polymerized and polymerized alginate methacrylate systems for three-dimensional photopolymerization bioprinting. The effect of the functionalization time on the mechanical, morphological, swelling, and degradation characteristics of cross-linked alginate hydrogel is also discussed. Alginate was chemically-modified with methacrylate groups and different reaction times considered. Photocurable alginate systems were prepared by dissolving functionalized alginate with 0.5- 1.5% w/v photoinitiator solutions and cross-linked by ultraviolet light (8 mW/cm$^2$ for 8 minutes).

**Keywords:** 3D bioprinting; Alginate hydrogel; Functionalization; Photopolymerization; Rheology

*Correspondence to: P. J. Bartolo, School of Mechanical, Aerospace and Civil Engineering, Manchester Biomanufacturing Centre, Manchester Institute of Biotechnology, University of Manchester, Manchester, UK; paulojorge.dasilvabartolo@manchester.ac.uk

**Received:** March 4, 2019; **Accepted:** March 25, 2019; **Published Online:** July 1, 2019

**Citation:** Mishbak HH, Cooper G, Bartolo PJ, 2019, Development and characterization of a photocurable alginate bioink for three dimensional bioprinting. Int J Bioprint, 5(2): 189. http://dx.doi.org/10.18063/ijb.v5i2.189

## 1. Introduction

Three different approaches are being explored for tissue engineering applications[1,2]. The first approach, cell therapy, is based on harvesting cells, sorting, expanding, and implanted them. This is a simple process but presents limited outcomes as it is difficult to keep the cells in the desired region for clinically relevant periods of time[3]. The second approach, scaffold-based approach, is based on the use of three-dimensional support structures that provide the necessary environment for cell attachment, differentiation, and proliferation[4]. In this approach, scaffolds can be directly implanted after fabrication or seeded with cells and pre-cultured in a bioreactor before implantation[5]. Finally, the third approach (bioprinting) uses bioinks (hydrogels and cells) to create cell-laden constructs. This is a highly relevant approach allowing *in situ* printing[6,7]. Technologies such as inkjet bioprinting, extrusion-based, and photopolymerization-based process are being explored. Among them, photopolymerization is a very versatile method allowing a rapid crosslinking under biocompatible reaction conditions without the use of solvents[1,6]. In addition, photocurable hydrogels are particularly relevant for biomedical applications due to the advantage of being able to encapsulate cells and the mild processing conditions that allow their *in situ* crosslinking within a patient during a surgical procedure.

Suitable hydrogels for bioprinting must be biocompatible, biodegradable, present appropriate mechanical properties, which depend on the type of tissue, good printability,[8] and shear thinning properties to facilitate the printing process[9]. In the case of photopolymerization bioprinting systems, the amount and type of photoinitiator are also critical as determines the crosslinking density, cytotoxicity, mechanical properties, and biocompatibility[10]. The increase of crosslinking density is usually associated with an increase of printability and mechanical properties and a decrease of biocompatibility due to the reduction of free space to accommodate cell proliferation[11].

Development and characterization of a photocurable alginate bioink for three-dimensional bioprinting © 2019 Mishbak, *et al*. This is an Open Access article distributed under the terms of the Creative Commons Attribution-NonCommercial 4.0 International License (http://creativecommons.org/licenses/by-nc/4.0/), permitting all non-commercial use, distribution, and reproduction in any medium, provided the original work is properly cited.

Alginate is a suitable material for bioprinting[12]. It is a natural water-soluble linear polysaccharide derived from alginic acid, extracted from several species of brown algae, such as *Laminaria hyperborea*, *Ascophyllum nodosum,* and *Macrocystis pyrifera*[13-15]. Its structure contains 1,4-linked β-D-mannuronic (M) and α-L-guluronic (G) acid residues (Figure 1), arranged in a non-regular and block-wise fashion along the chain[16-18]. Alginate shows good biocompatibility, low cytotoxicity, and high-water content (high swelling ratio), mimicking the structure of the natural extracellular matrix[19-23]. These properties make alginate a suitable material for wound dressings, drug delivery systems, and soft tissue engineering applications[24].

This paper investigates the preparation of alginate-based systems for ultraviolet (UV) bioprinting applications. The material is characterized both before and after the curing process, and the effect of functionalization time on the rheological, mechanical, morphological, swelling, and degradation properties was investigated. The effect of photoinitiator concentration in terms of rheological and mechanical properties is also assessed and discussed. The biological characteristics are not reported in this manuscript, but preliminary results with human chondrocytes show that the materials considered here do not present any cytotoxicity and allow cell attachment and proliferation[26].

## 2. Materials and Methods

### 2.1 Synthesis of Methacrylate Alginate

Photocurable alginates were prepared through a functionalization mechanism with methacrylate anhydride (MA)[27]. Briefly, sodium alginate powder 1%, 2%, and 3% (w/v) (Sigma-Aldrich, UK) was dissolved in Dulbecco's phosphate-buffered saline (Sigma-Aldrich, UK) and then mixed with MA (Sigma-Aldrich, UK) at 15 mL MA/g of alginate under vigorous stirring. The pH of the solution was kept around 7.4–8.0 during the reaction time by adding 5M of NaOH. Maintaining a higher pH during the reaction is crucial since higher pH enhances the reaction among the amine and hydroxyl groups, which lead to a higher degree of modification[28]. Two different reaction times (8 and 24 h) were used to assess the effect of the reaction time on the degree of functionalization.

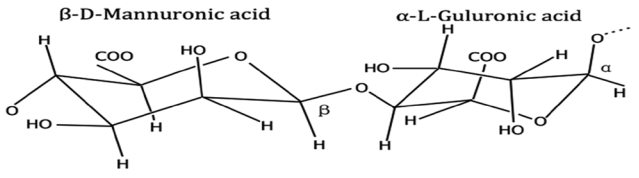


**Figure 1.** Alginate showing a linkage between the mannuronic and guluronic acid[25].

After the chemical modification reaction, the polymeric solution was precipitated and totally mixed in 100 mL of ethanol (100% ethanol) and dried in an oven overnight at 50°C. The precipitate polymer was dissolved in distilled water (di$H_2O$), loaded in the dialysis tubes membranes (SnakeSkin Dialysis Tubing from Thermo Fisher Scientific, UK), sealing both sides and dialyzed the solution against NaCl for 7 days with periodic water changes every day. The solution was freeze at −80°C and the polymer recovered by lyophilization.

### 2.2 Characterization of Pre-polymerized Methacrylate Alginate

#### *2.2.1 Nuclear magnetic resonance (NMR)*

The chemical structure of functionalized alginate was assessed through $^1$HNMR spectroscopy, using the B400 Bruker Avance III 400 MHz (Billerica, Massachusetts, USA). Polymeric materials were dissolved in deuterium oxide (Sigma-Aldrich, UK), transferred to NMR tubes and the spectra acquired with 128 scans.

#### *2.2.2 Rheological characterization*

The rheological tests were performed to characterize the viscoelastic behavior of both pre-polymerized and polymerized alginate. The rheological assessment of pre-polymerized alginate systems was carried out using the DHR2 TA Instrument (USA). Samples were placed between two parallel plates and two different tests (rotational and oscillation) were considered. Rotational tests were performed to evaluate the viscosity and material strength. In these tests it is assumed that the material flows by applying stress, being the response measured alongside time (temperature was not considered in this work). Controlled stress was applied, and the resulting movement measured. Oscillation tests were considered to evaluate the viscoelastic behavior of the material and dynamic moduli. The viscoelastic behavior was characterized by measuring the energy stored (storage modulus, G′) in the material during shearing and the energy subsequently lost (loss modulus, G″). Shear strain was controlled by varying the oscillation amplitude.

To assess the rheological changes during the photopolymerization process, the rheological tests were carried out using the Bohlin Gemini system (Malvern Instruments) equipped with the OmniCure® S1000 light source irradiating in the range of 254–450 nm wavelength, and oscillation tests were considered. The light intensity was 10 mW/cm$^2$.

The rheological behavior of the materials is described by the following equation:

$$\tau = \eta \dot{\gamma}^n \quad (1)$$

Where $\tau$ is the $\dot{\gamma}$ shear stress (Pa), is the shear rate ($s^{-1}$), $\eta$ the consistency index or equivalent viscosity (Pa. s), and n is the power law index (dimensionless) that varies as follows:

n<1: Shear-thinning system;
n=1: Newtonian system;
n>1: Shear-thickening system.

## 2.3 Hydrogel Formation

Photocrosslinked alginate methacrylate hydrogels were prepared by dissolving 2% w/v alginate methacrylate with different photoinitiator concentration solutions (0.5-1.5% w/v) of VA-086 photoinitiator solutions (2,2'-Azobis[2-methyl-N-(2-hydroxyethyl) propionamide azo initiator (Wako Pure Chemical Industries, USA). Cross-linked disks were produced by pipetting the alginate solution in an acrylic mold with 8 mm diameter and 4 mm height. Photopolymerization was conducted using a 365 nm UV light (Model Dymax 2000-EC, Dymax Europe GmbH, Wiesbaden, Germany) irradiating at 8 mW/cm$^2$ during 8 min.

The photopolymerization process of alginate methacrylate is a radicular polymerization process started by the absorption of UV light by the photoinitiators followed by the generation of free radicals and a cross-linking chain reaction[29]. The mechanism is briefly presented in Figure 2.

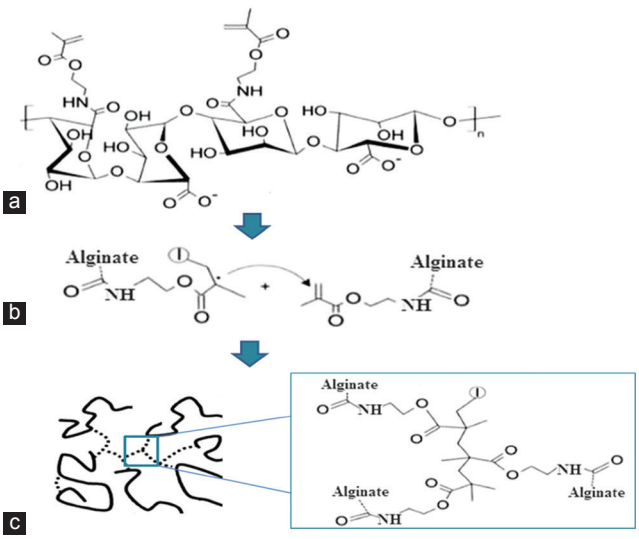


**Figure 2.** Schematic representation of the photopolymerization process of alginate methacrylate. (a) After exposing the polymer solution to ultraviolet radiation, the photoinitiators generated free radicals that react with the vinyl methylene starting the crosslinking reaction; (b) the reaction propagates with macroradicals reacting with unreacted carbon-carbon double bonds. (c) At the end through a bimolecular termination mechanism, a three-dimensional network of the cross-linked hydrogel is formed[30].

## 2.4 Characterization of Photocrosslinked Hydrogels

### *2.4.1 Morphological characterization*

The morphology of the internal structure of the hydrogels was investigated through scanning electron microscopy (SEM), using the Hitachi S3000N VPSEM system. Alginate samples were produced using cylindrical molds (8 mm diameter and 4 mm high). After hydrogel formation, samples were extensively washed in di$H_2O$, frozen at −80°C and lyophilized. Samples were fixed on stubs using double-sided adhesive tape and sputter coated with platinum sputter-coating.

### *2.4.2 Mechanical characterization*

Compression tests were performed at a constant strain rate using the Instron 3344 machine equipped with a 10-N load cell (Instron, Buckinghamshire, UK). Cross-linked alginate hydrogel disks were prepared as described in section (2.2) and maintained in di$H_2O$ at 37ºC following the protocol described by Jeon *et al*.[27]. After 24 h of incubation, swollen alginate methacrylate hydrogel disks were measured using calipers to determine both the diameter and thickness and unconfined compression tests were performed on the hydrogel disks at room temperature, 0.5 mm/min of speed at a rate of 20% strain. Compressive modulus was determined from the slope of stress versus strain plots and limited to the first 10% of strain as recommended for cartilage applications[31].

### *2.4.3. Swelling and degradation characterization*

Alginate methacrylate hydrogel disks were frozen at −80°C, then, lyophilized and the dry weights (Wi) were measured. Afterward, the dried hydrogel samples were immersed in di$H_2O$ and the same number of samples were also immersed in Dulbecco's Modified Eagle's Medium (DMEM) – high glucose (Sigma-UK) diluted with 10% fetal bovine serum (Thermofisher, UK) at pH 7 and incubated at 37°C to reach an equilibrium swelling state. The di$H_2O$ and DMEM were replaced every 1–2 days. Over the course of 3 weeks, samples were removed from the DMEM/di$H_2O$ and the swollen hydrogel sample weights (Ws) measured. The swelling ratio (water content Q) was calculated according to the following equation:

$$Q = \frac{Ws}{Wi} \quad (2)$$

Where Wi is the dry weight and Ws is the weight of the swollen hydrogel sample. After this, the swollen hydrogels were lyophilized and weighed again. The percentage of mass loss was calculated as follows:

$$(W_i - W_d)/W_i \times 100 \quad (3)$$

Where $W_d$ is the weight after lyophilization ($n$ = 3 for each time point).

## 3. Results and Discussion

### 3.1 Alginate Functionalization

The alginate modification with MA was performed under standard conditions, allowing the introduction of photo-reactive methacrylate groups into the polymer backbone, as confirmed by $^1$HNMR analysis (Figures 3-5). Results indicate the presence of new characteristic peaks of methacrylate (MA) at 5.63 ppm and 6.09 ppm attributed to the methylene group in the vinyl bond, and a peak at 1.82 ppm assigned to the methyl group, which are not present in the non-modified polymer, showing that the polymers were successfully functionalized.

Two different functionalization reaction times (8 and 24 h) were also considered and the degree of modification determined by dividing the relative integrations of methylene to carbohydrate protons[32,33]. Results, presented in Table 1, show that the degree of modification increases by increasing the reaction time, reaching a maximum value of 33% at 24 h.

### 3.2 Rheological Behavior of Pre-polymerized Alginate Methacrylate Systems

Figures 6-9 showed the stress versus shear rate behavior of solutions containing 1, 2, and 3% (w/v) of alginate methacrylate reacted for 8 and 24 h. Key rheological parameters are presented in Tables 2 and 3. A non-linear behavior is observed for all samples. Samples containing 2% w/v obtained after 24 h of reaction show a clear Bingham behavior[34]. Results also show a decrease of the equivalent viscosity by increasing the alginate concentration for samples obtained after 24 h of reaction, while no trend was observed for samples obtained after 8 h of reaction. The flow behavior is also closer to a Newtonian fluid for samples containing high concentrations of alginate. Based on these results, the system containing 2% w/v of alginate

**Table 1.** Effect of reaction time on the modification degree of alginate methacrylate

| Composition (% w/v) | Reaction time (hours) | Degree of modification (%) |
|---|---|---|
| 2% | 8 | 21 |
| 2% | 24 | 33 |

**Table 2.** Rheological constants for solutions containing 15 mL of methacrylate and different alginate concentrations, 24 h

| Composition (%w/v) | Equivalent viscosity (Pa. s) | Power law constant |
|---|---|---|
| 1 | 4.36 | 0.23 |
| 2 | 0.54 | 0.68 |
| 3 | 0.16 | 0.72 |

**Table 3.** Rheological constants for solutions containing 15 mL of methacrylate and different alginate concentrations, 8 h

| Composition (%w/v) | Equivalent viscosity (Pa. s) | Power law constant |
|---|---|---|
| 1 | 0.09 | 0.81 |
| 2 | 0.48 | 0.48 |
| 3 | 0.08 | 0.74 |

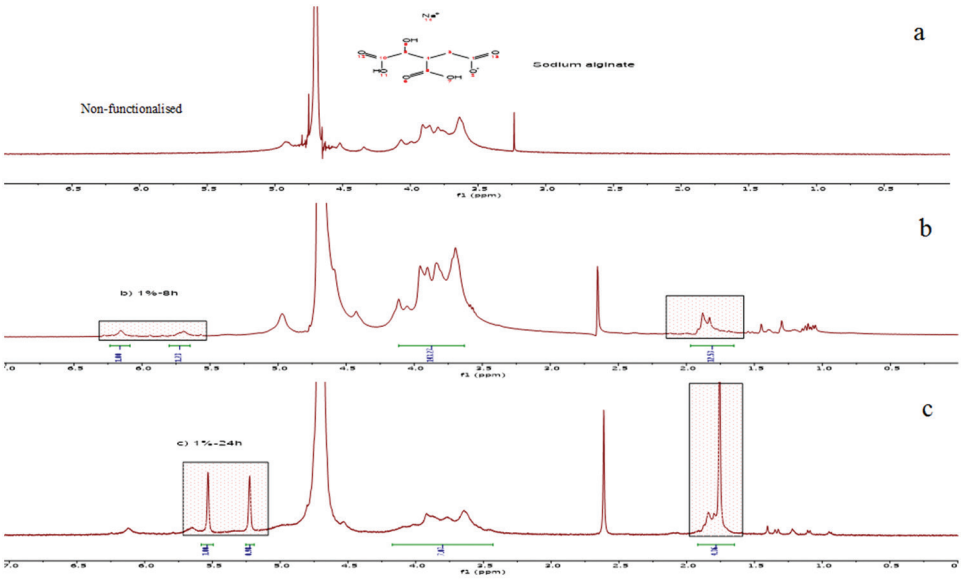


**Figure 3.** (a) Non-functionalized alginate (1% w/v), (b) functionalized alginate (1% w/v) after 8 h of reaction, (c) functionalized alginate (1% w/v) after 24 h of reaction. The functionalization is confirmed by the presence of new peaks in the spectra at 5.63 ppm and 6.09 ppm attributed to the methylene group and a peak at 1.82 ppm that corresponds to the methyl group.

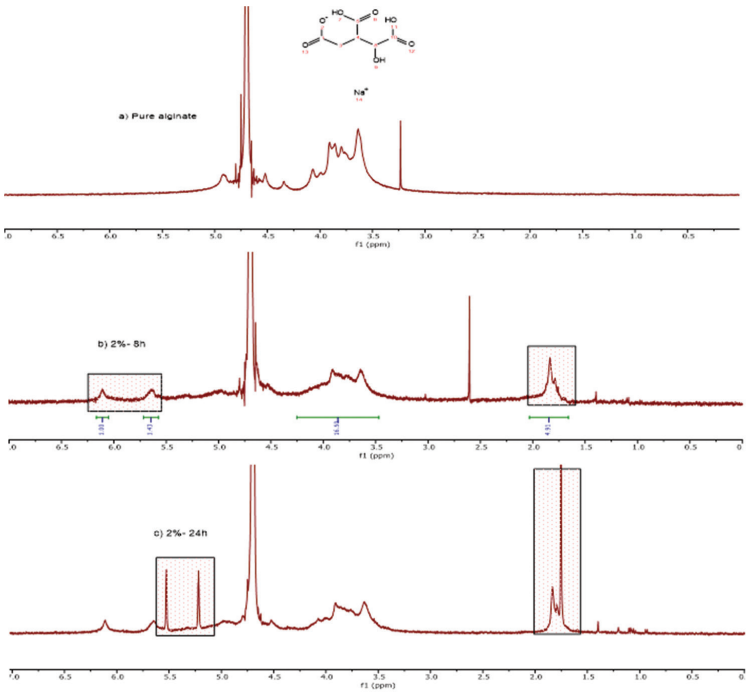


**Figure 4.** (a) Non-functionalized alginate (2% w/v), (b) functionalized alginate (2% w/v) after 8 h of reaction, (c) functionalized alginate (2% w/v) after 24 h of reaction. The functionalization is confirmed by the presence of new peaks in the spectra at 5.63 ppm and 6.09 ppm attributed to the methylene group and a peak at 1.82 ppm that corresponds to the methyl group.

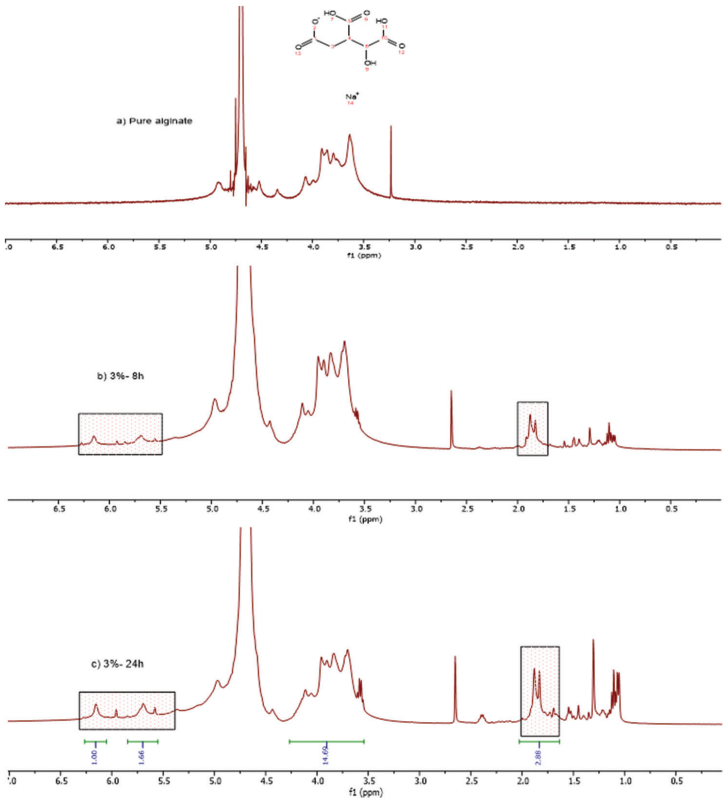


**Figure 5.** (a) Non-functionalized alginate (3% w/v), (b) functionalized alginate (2% w/v) after 8 h of reaction, (c) functionalized alginate (2% w/v) after 24 h of reaction. The functionalization is confirmed by the presence of new peaks in the spectra at 5.63 ppm and 6.09 ppm attributed to the methylene group and a peak at 1.82 ppm that corresponds to the methyl group.

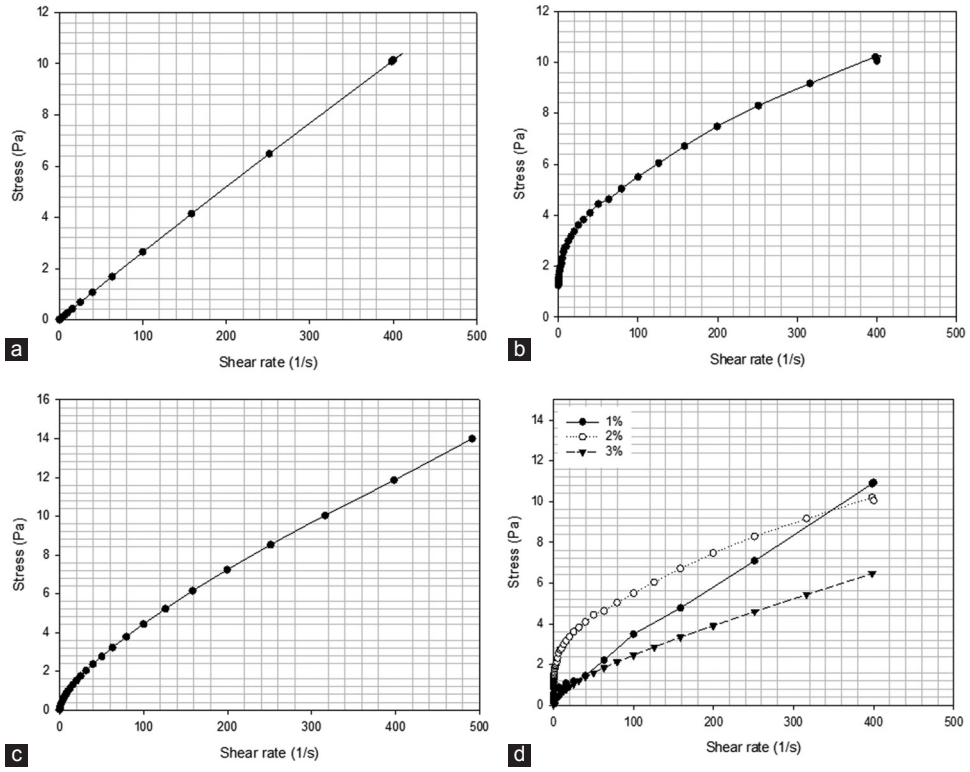


**Figure 6.** Stress versus shear rate profiles for alginate methacrylate solutions containing different alginate methacrylate concentrations, reacted for 8 h. (a) 1% w/v of alginate, (b) 2% w/v of alginate, (c) 3% w/v of alginate, (d) comparison of all compositions.

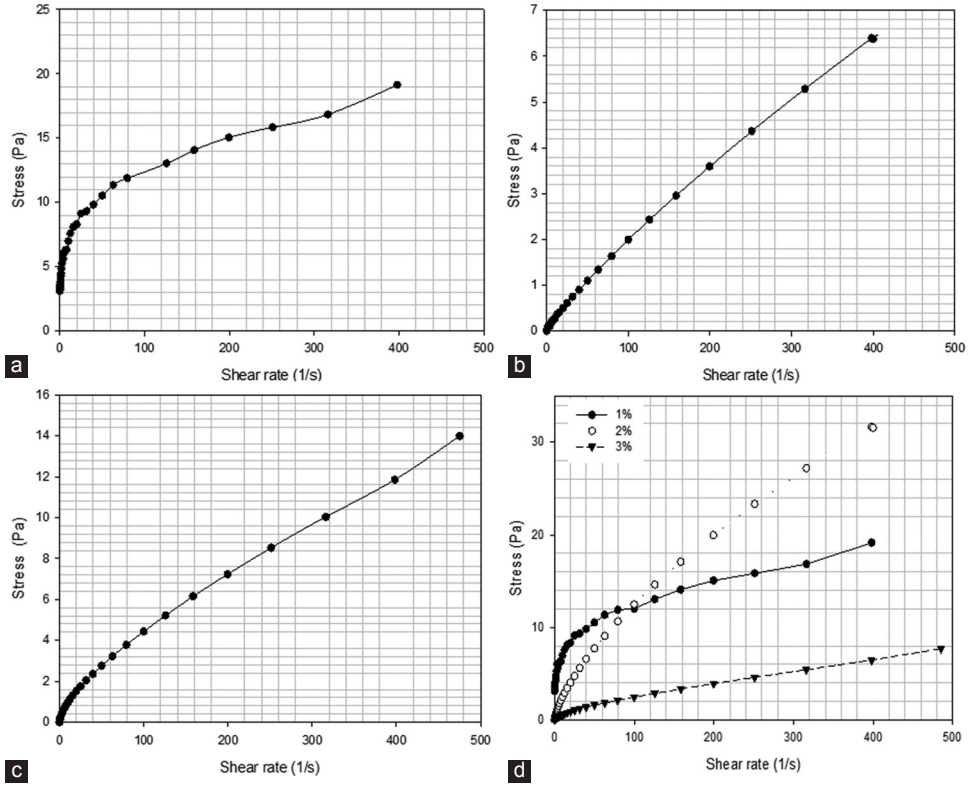


**Figure 7.** Stress versus shear rate for solutions containing different alginate methacrylate concentrations reacted for 24 h. (a) 1% w/v of alginate, (b) 2% w/v of alginate, (c) 3% w/v of alginate, (d) comparison of all compositions.

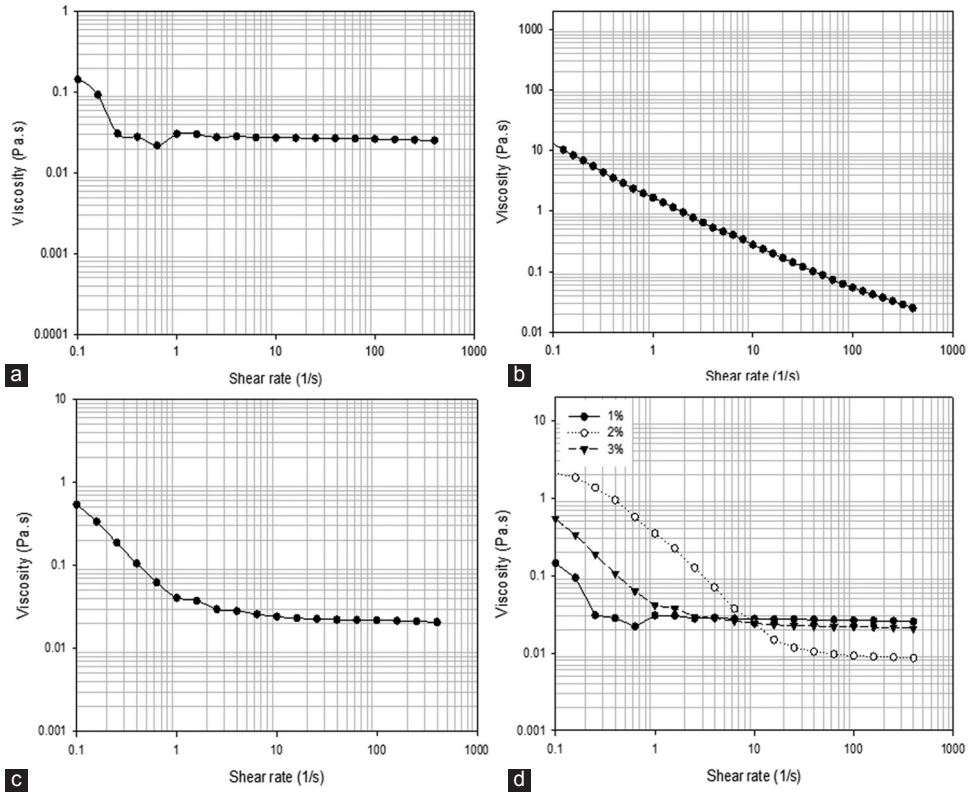


**Figure 8.** Viscosity versus shear rate for solutions containing different alginate methacrylate concentrations reacted for 8 h. (a) 1% w/v, (b) 2% w/v, (c) 3% w/v, (d) comparison of all compositions.

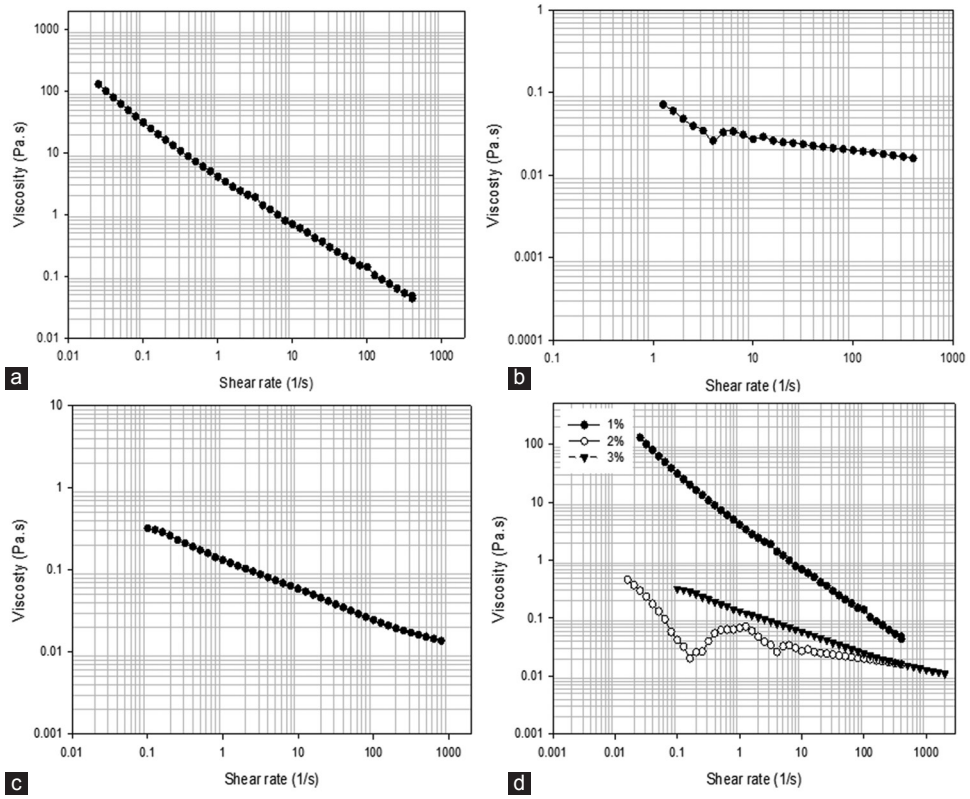


**Figure 9.** Viscosity versus shear rate for solutions containing different alginate methacrylate concentrations reacted for 24 h. (a) 1% w/v, (b) 2% w/v, (c) 3% w/v, (d) comparison of all compositions.

was selected as presents less variation of viscosity with the reaction time and a clear shear-thinning behavior being also less dependent with the reaction time compared to the other systems.

Figures 10 and 11 show the variation of storage modulus (G′), loss modulus (G″), complex modulus, and tan δ as a function of frequency and strain for systems containing 2% w/v alginate methacrylate concentrations

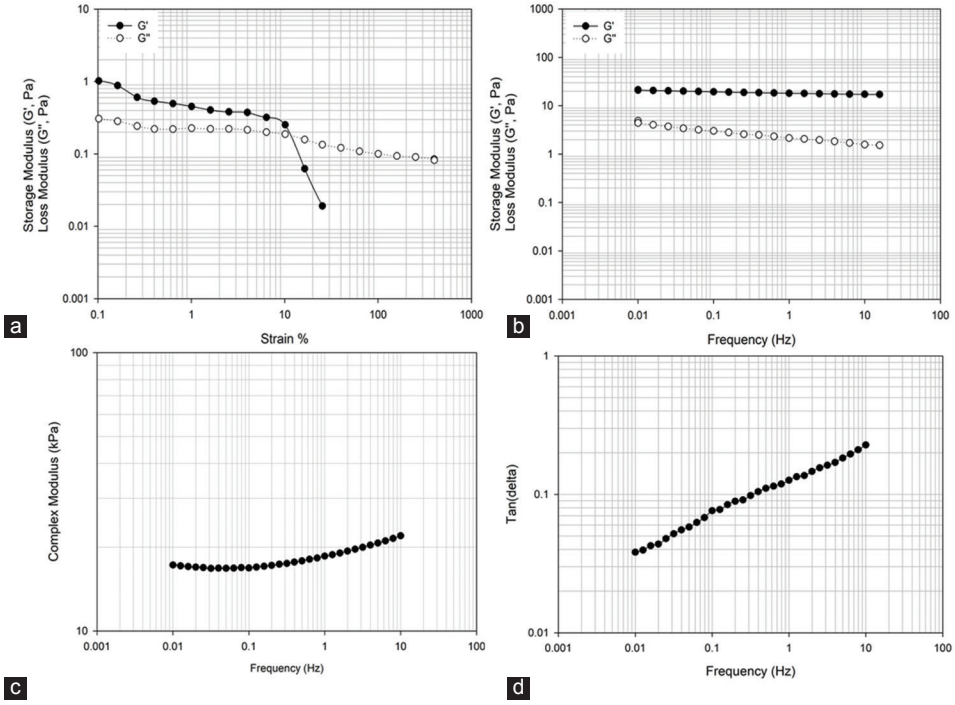


**Figure 10.** 2% wt. alginate solution reacted for 8 h. (a) storage and loss modulus versus strain (b) storage and loss modulus versus frequency, (c) complex modulus versus frequency, (d) tan δ versus frequency.

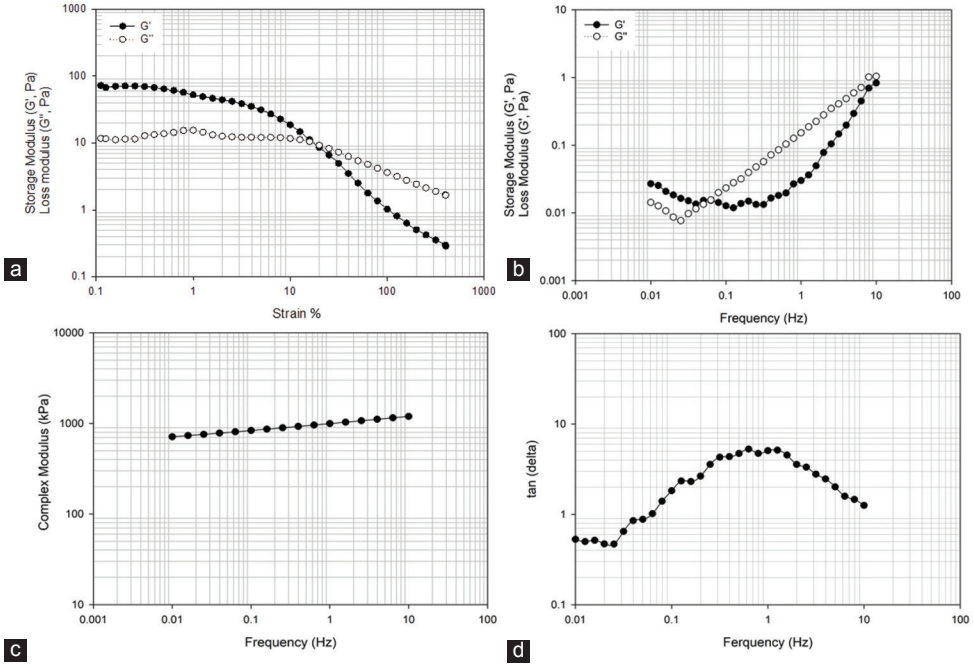


**Figure 11.** 2% wt. alginate solution reacted for 24 h. (a) storage and loss modulus versus strain, (b) storage and loss modulus versus frequency, (c) complex modulus versus frequency, (d) tan δ versus frequency.

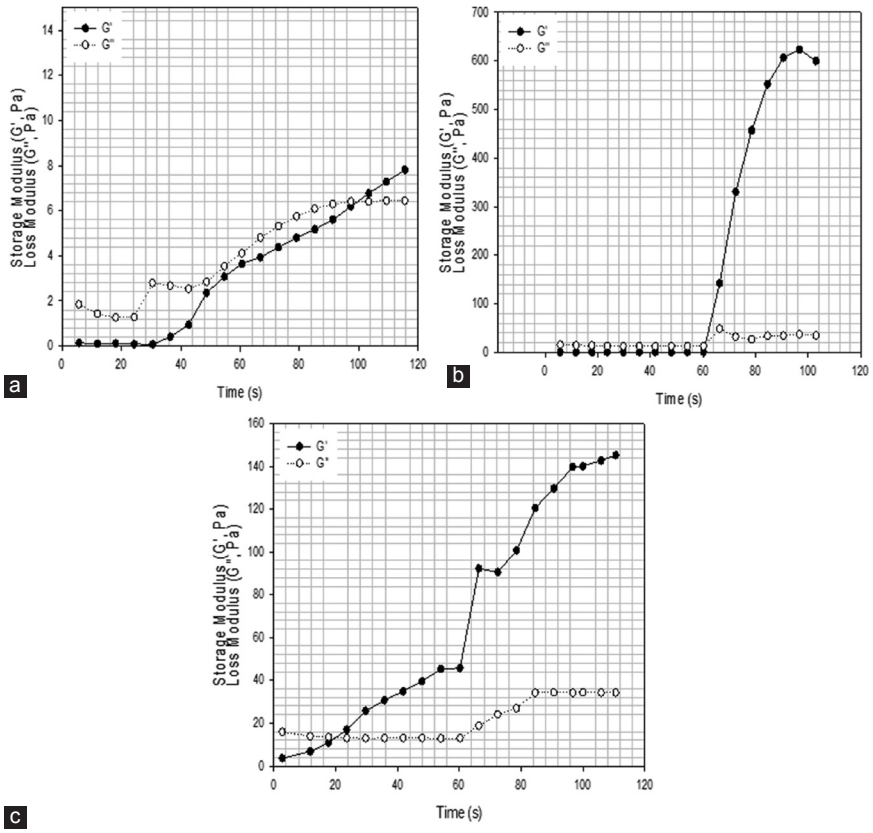


**Figure 12.** 2% wt. methacrylate alginate with different concentration of VA-086 photoinitiators functionalized for 8 h (a) 0.5% w/v of VA-086, (b) 1% w/v of VA-086, (c) 1.5% w/v of VA-086, d) 0.05%.

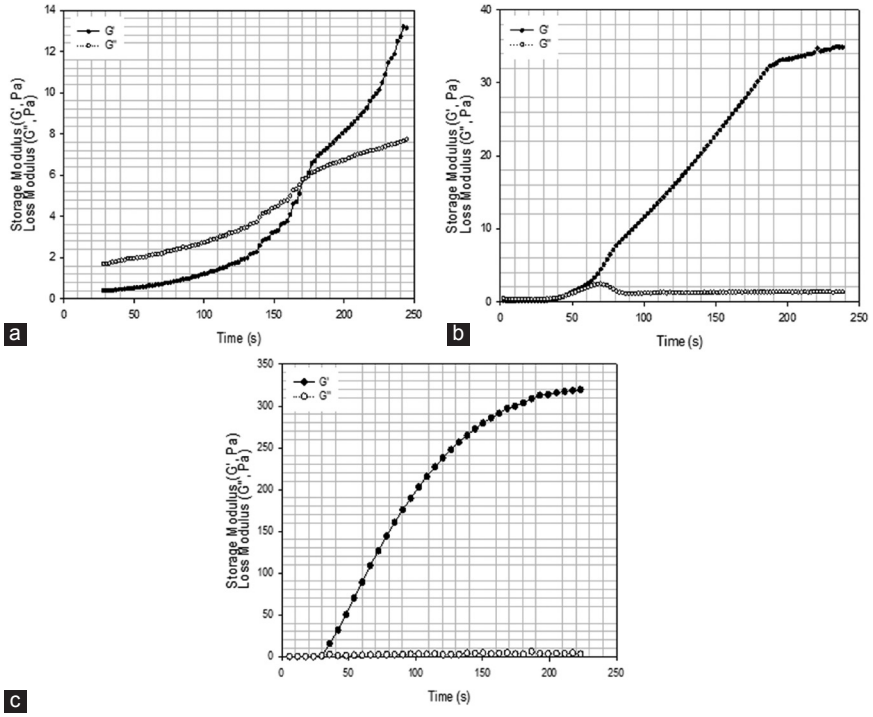


**Figure 13.** 2% wt. methacrylate alginate with different concentration of VA-086 photoinitiators functionalized for 8 h (a) 0.5% w/v of VA-086, (b) 1% w/v of VA-086, (c) 1.5% w/v of VA-086, (d) 0.05%.

and different reaction times. The results show that both the storage and loss modulus are higher in samples obtained after high functionalization times. In both cases, the complex modulus increases with frequency, while the variation of G′ and G″ with strain shows a shift point after which G″ becomes higher than G′. This shift occurs at high frequencies for alginate samples obtained with high functionalization times.

### 3.3 Rheological Changes during the Photopolymerization Process

Based on the characterization of the pre-polymerized samples, only systems containing 2% w/v of alginate were considered for photopolymerization studies. The curing kinetics was assessed by monitoring the variation of G′ and G″ at room temperature through a controlled frequency of (1Hz). Photorheology was used to characterize the curing process (photopolymerization) of functionalized alginate polymers obtained after 8 and 24 h of reaction time, mixed with 0.5-1.5% w/v, and of VA-086 photoinitiator solutions.

As observed from Figures 12 and 13 by increasing the curing time G′ increases becoming significantly higher than G″. It is also possible to observe that by increasing the photoinitiator concentration the gelation time, which corresponds to the time point where the G′ curve crosses the G″ curve, decreases. Notably observed that by increasing the amount of photoinitiators concentration G′ seems to tend to a plateau which corresponds to a verification stage of the curing process[35,36]. The possible explanation for this observation is that, for the layer thickness considered in this study (~100 μm), the photoinitiator concentration is approaching a critical value. By increasing the photoinitiator concentration above the critical values, the polymerization occurs very fast at the polymer surface, reducing the light penetration and, consequently, the overall polymerization reduces.

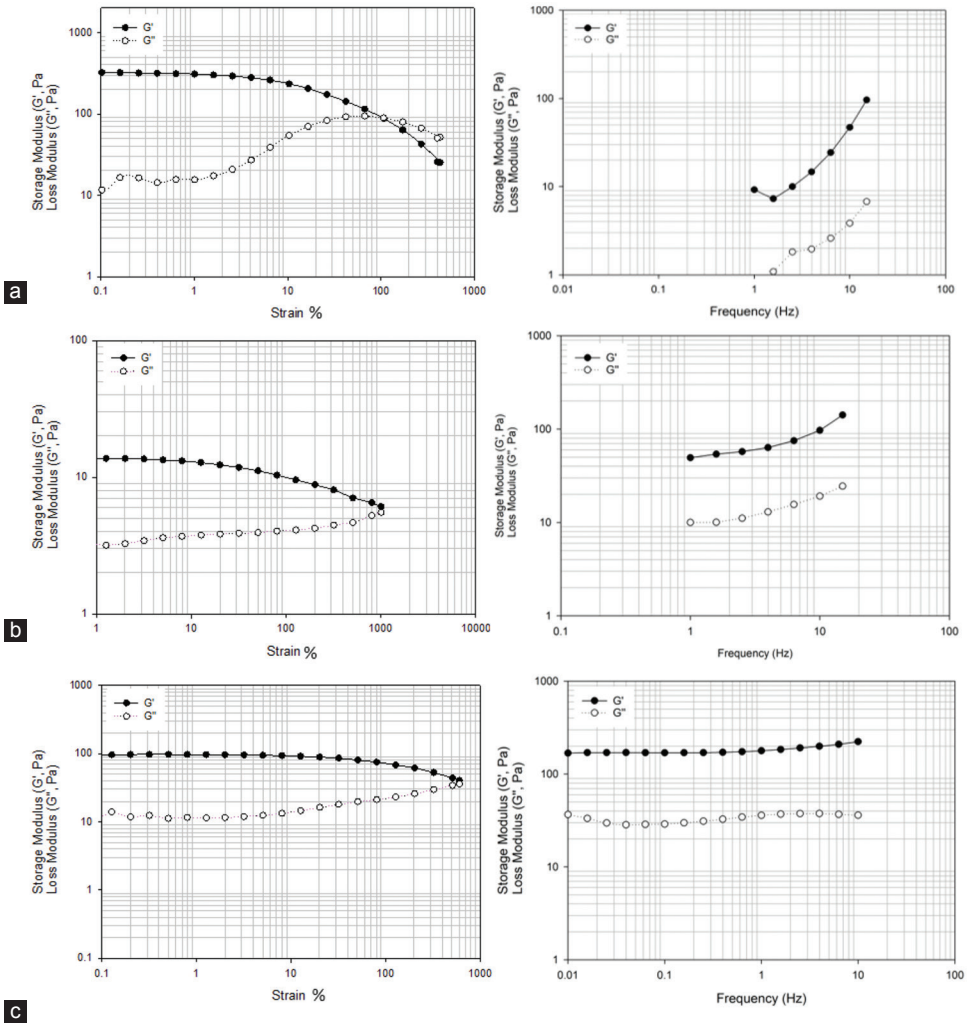


**Figure 14.** 2% wt. methacrylate alginate hydrogel with different concentration of VA-086 functionalized for 8 h. (a) 0.5 w/v % of VA-086, (b) 1 w/v % of VA-086, (c) 1.5 w/v % of VA-086.

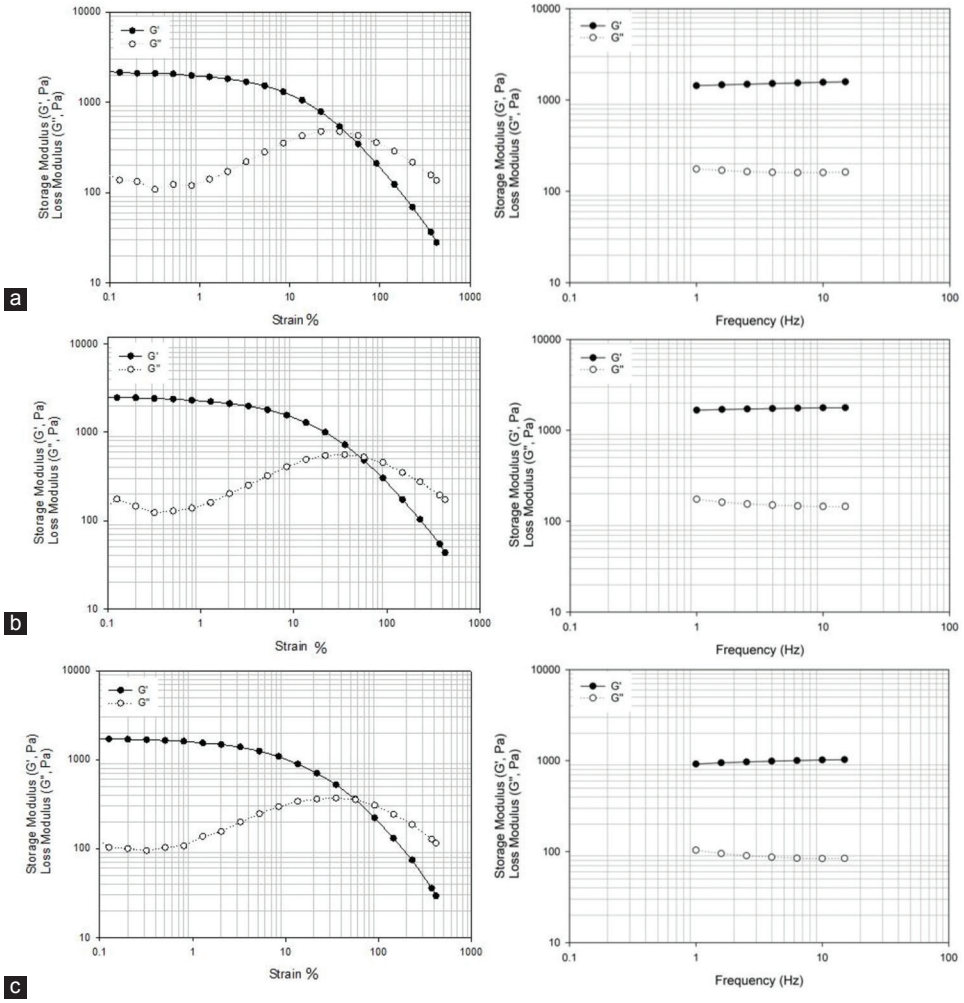


**Figure 15.** 2% wt. methacrylate alginate with different concentration of VA-086 functionalized for 24 h. (a) 0.5 w/v % of VA-086, (b) 1 w/v % of VA-086, (c) 1.5 w/v % of VA-086.

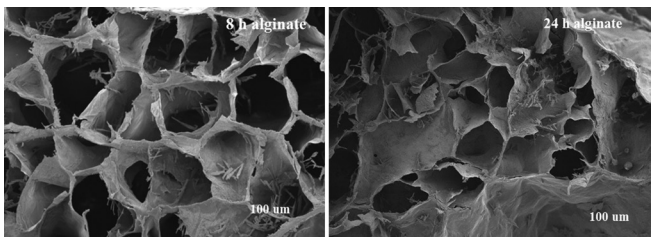


**Figure 16.** Scanning electron microscopy images of cross-linked methacrylate alginate hydrogel structures obtained from alginate-methacrylate at different reaction times: 8 and 24 h.

## 3.4 Viscoelastic Properties of Formed Hydrogels

Hydrogel disks (4 mm of height and 8 mm of diameter) were produced using an acrylic machined mold. Samples of 2 % w/v of alginate methacrylate obtained after both 8 and 24 h of reaction time containing different concentrations of photoinitiator (0.5, 1, and 1.5% w/v) were polymerized during 8 min under a light intensity of 8 mW/cm$^2$. Produced disks were then assessed and both G′ and G″ measured at room temperature through a controlled frequency of 1Hz as presented in Figures 14 and 15. In the case of alginate methacrylate samples obtained after 8 h of reaction time, its possible to observe that there is no significant change of both G′ and G″ (the storage modulus is always higher than the elastic modulus) with the increase in the photoinitiator concentration. In the case of alginate methacrylate samples obtained after 24 h of reaction time, results show that by increasing the photoinitiator concentration G′ and G″ increases. In this case, it is also possible to observe that the difference between G′ and G″ increases with the increase of photoinitiator concentration, which is associated with the high cross-linked density.

The viscoelastic nature of the cross-linked disks is also observed from the G′ and G″ versus strain graphs. In this case, it is possible to observe for all samples that, till a critical strain value, the storage modulus is

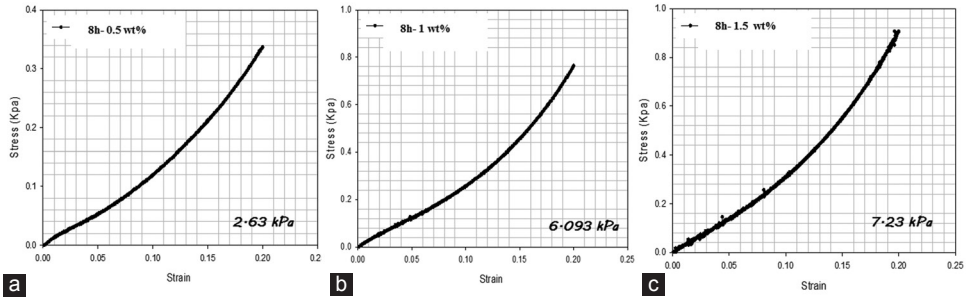


**Figure 17.** Compression tests for alginate methacrylate samples (8 h) with different photoinitiator concentrations (a) 0.5% w/v VA-086, (b) 1% w/v VA-086, (c) 1.5% w/v VA-086.

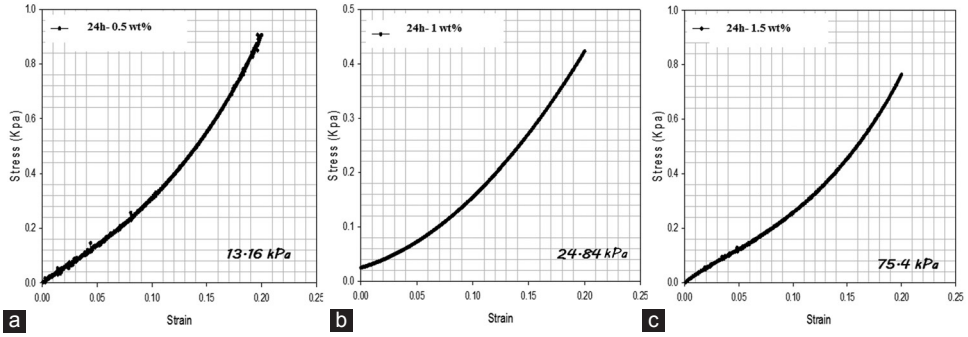


**Figure 18.** Compression tests for alginate methacrylate samples (24 h) with different photoinitiator concentrations (a) 0.5% w/v VA-086, (b) 1% w/v VA-086, (c) 1.5% w/v VA-086.

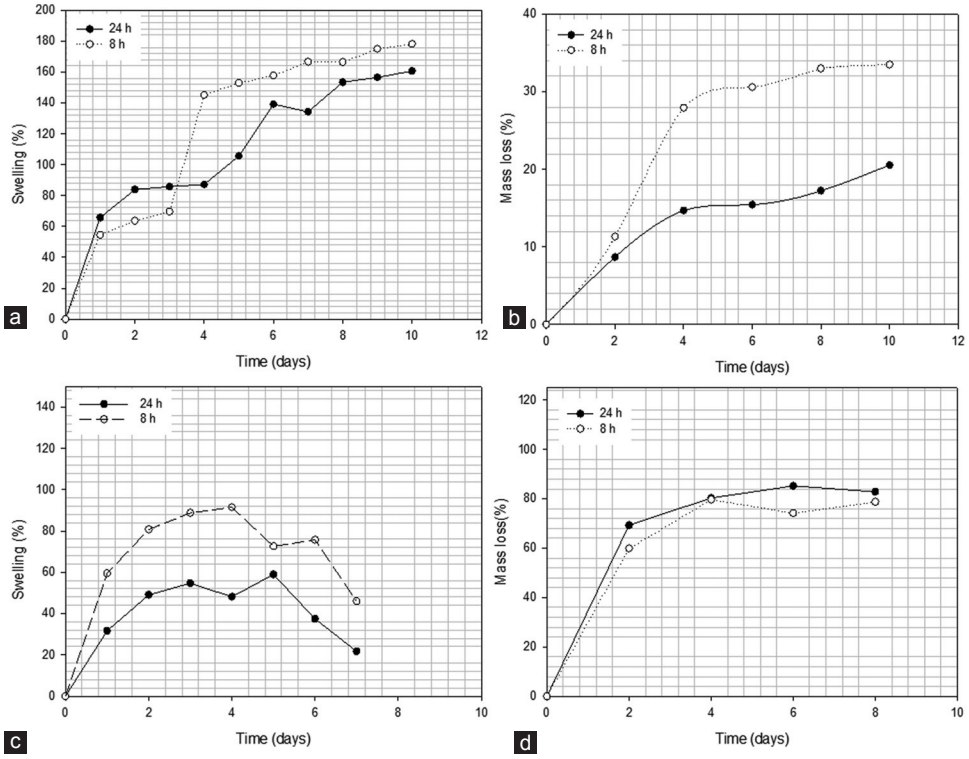


**Figure 19.** Swelling and degradation rate for 2% wt. functionalized alginate (24 and 8 h) reaction time in (a) distilled water (di$H_2O$), (b) degradation rate in di$H_2O$, (c) Dulbecco's Modified Eagle's Medium (DMEM), (d) degradation rate in DMEM.

higher than the loss modulus. After the strain critical value, the loss modulus becomes more significant due to the break of the cross-linked network. In the case of alginate methacrylate samples obtained after 24 h of reaction time, G′-24h modulus is always higher than G′-8h of alginate methacrylate samples obtained after 8 h of reaction time. This is due to the high-crosslinking density of the alginate methacrylate samples obtained after 24 h of reaction time.

### 3.5 Internal Morphology of Alginate Hydrogels

The internal structure of cross-linked alginate methacrylate is presented in Figure 16. SEM images were obtained for samples containing 2% w/v of alginate prepared during 8 and 24 h of reaction time and 1 w% of a photoinitiator. Results show that the reaction time influences the hydrogel morphology, with high reaction times being associated with structures presenting both small pore size and number of pores. In addition, results seem to indicate that long reaction times generate structures with more closed pores.

### 3.6 Mechanical Characterization

The mechanical performance of cross-linked alginate structures is presented in Figures 17 and 18. As observed, high compression moduli was obtained for cross-linked disks produced with high functionalization times (13.16 kPa for 24 h of reaction time and 2.63 kPa for 8 h of reaction time) and 0.5% w/v photoinitiator concentration. These results can be explained by the high crosslinking density that characterizes the structures obtained from alginate samples functionalized during long reaction times and the corresponding internal morphology characterized by small size and a low number of pores. It is also possible to observe that the mechanical properties increase by increasing the photoinitiator concentration. For samples containing 1.5% w/v of photoinitiator, compression moduli was obtained (75.4 kPa for 24 h of reaction time and 7.23 kPa for 8 h of reaction time).

### 3.7 Swelling and Degradation Kinetics

The swelling and degradation behavior of cross-linked alginate hydrogel disks are presented in Figure 19 (a,b,c and d). Results show that samples absorb both DMEM and di$H_2O$ until reaching a state of equilibrium. This state is accomplished when the osmotic pressure from the swelling and the elasticity of the hydrogel network is equal. It is also possible to observe that cross-linked samples prepared with alginate methacrylate obtained after 24 h of functionalization present low swelling ratio, which shows that the degree of crosslinking controls the swelling properties of the hydrogel. In all samples, the equilibrium status was reached on day 3. Cross-linked alginate structures based on functionalized alginate prepared during 24 h of reaction time swelled up to 155%, while alginate structures based on functionalized alginate prepared during 8 h of reaction time swelled up to 190%. Moreover, it is also possible to observe that the level of functionalization of the pre-polymerized alginate not only determines the internal morphology of the cross-linked structures but also the degradation process as shown in Figure 19b and d.

## 4. Conclusion

This paper describes the synthesis and characterization of alginate systems for UV-based bioprinting applications. The alginate was successfully functionalized in the presence of methacrylate to introduce the necessary number of unsaturation allowing its crosslinking on photopolymerization. Two different functionalization reaction times were considered and photocurable systems containing different photoinitiator concentrations prepared. From the results, it is possible to conclude that high functionalization reaction times originates cross-linked structures with less porosity, smaller pores and a larger number of closed pores, less swelling, higher degradation properties, and higher mechanical stiffness. By increasing photoinitiator concentration, it was possible to observe an increase of mechanical properties and gelation time. Moreover, for high values of photoinitiator concentration, the reaction tends to reach verification.

## Acknowledgment

Mr. H.H. Mishbak wishes to acknowledge the support of the Government of Iraq for supporting his PhD through a grant provided by the Higher Committee for Development Education Iraq. We would like to thank our colleagues from School of Materials, and the School of Mechanical, Aerospace, and Civil Engineering, The University of Manchester who provided insight and expertise with the mechanical compression test and rheological test that greatly assisted the research.

## References

1. Pereira R, Bártolo PJF, 2015, 3D Bioprinting of Photocrosslinkable Hydrogel Constructs. *Appl Polym Sci,* 132(48):132A4. DOI 10.1002/app.42458.
2. Zhou D, Yoshihiro I, 2014, Visible Light-curable Polymers for Biomedical Applications. *Sci China Chem*, 57(4):510-21. DOI 10.1007/s11426-014-5069-z.
3. Pereira RF, Sousa A, Barrias CC, *et al*., 2018, A Single-component Hydrogel Bioink for Bioprinting of Bioengineered 3D Constructs for Dermal Tissue *Engineering*. *Mater Horiz,* 5(6):1100-11. DOI 10.1039/c8mh00525g.

4. Vyas C, Pereira R, Huang B, *et al*., 2017, *Engineering* the Vasculature with Additive Manufacturing. *Curr Opin Biomed Eng*, 2:1-13.
5. Wang W, Caetano G, Ambler W S, *et al*., 2016, Enhancing the Hydrophilicity and Cell Attachment of 3D Printed PCL/Graphene Scaffolds for Bone Tissue *Engineering*. *Materials (Basel, Switzerland)*, 9(12):992. DOI 10.3390/ma9120992.
6. Fand PR, Bártolo PJ, 2015, 3D Photo-fabrication for Tissue *Engineering* and Drug Delivery. *Engineering*, 1(1):90-112.
7. Dand NG, Bryant SJ, 2008, Cell Encapsulation in Biodegradable Hydrogels for Tissue *Engineering* Applications. *Tissue Eng Part B Rev,* 14(2):149-65. DOI 10.1089/ten.teb.2007.0332.
8. You F, Fand EB, Chen X, 2017, Application of Extrusion-based Hydrogel Bioprinting for Cartilage Tissue *Engineering*. *Int J Mol Sci,* 18(7):1597.
9. Highley CB, Rodell CB, Burdick JA, 2015, Direct 3D Printing of Shear-thinning Hydrogels into Self-healing Hydrogels. *Adv Mater,* 27(34):5075-9. DOI 10.1002/adma.201501234.
10. Pawar AA, Saada G, Cooperstein I, *et al*., 2016, High-performance 3D Printing of Hydrogels by Water-dispersible Photoinitiator Nanoparticles. *Appl Sci Eng,* 2(4):e1501381. DOI 10.1126/sciadv.1501381.
11. Banerjee A, Arha M, Choudhary S, *et al*., 2009, The Influence of Hydrogel Modulus on the Proliferation and Differentiation of Encapsulated Neural Stem Cells. *Biomaterials,* 30(27):4695-9. DOI 10.1016/j.biomaterials.2009.05.050.
12. Song SJ, Choi J, Park YD, *et al*., 2011, Sodium Alginate Hydrogel-based Bioprinting using a Novel Multinozzle Bioprinting System. *Artif Organs*, 35(11):1132-6. DOI 10.1111/j.1525-1594.2011.01377.x.
13. Pereira R, Tojeira A, Vaz DC, *et al*., 2011, Preparation and Characterization of Films Based on Alginate and *Aloe vera. Int J Polym Anal Charact*, 16(7):449-64.
14. Pereira R, Carvalho A, Vaz DC, *et al*., 2013, Development of Novel Alginate Based Hydrogel Films for Wound Healing Applications. *Int J Biol Macromol*, 52:221-30.
15. Pawar SN, Edgar KJ, 2012, Alginate Derivatization: A Review of Chemistry, Properties and Applications. *Biomaterials,* 33(11):3279-305. DOI 10.1016/j.biomaterials.2012.01.007.
16. Hermansson E, Schuster E, Lindgren L, *et al*., 2016, Impact of Solvent Quality on the Network Strength and Structure of Alginate Gels. *Carbohydr Polym,* 144:289-96. DOI 10.1016/j.carbpol.2016.02.069.
17. Hand D, Barikani M, 2012, Synthesis and Characterization of Calcium Alginate Nanoparticles, Sodium Homopolymannuronate Salt and its Calcium Nanoparticles. *Sci Iran,* 19(6):2023-8. DOI 10.1016/j.scient.2012.10.005.
18. Ouwerx C, Velings N, Mestdagh MM, *et al*., 1998, Physico-chemical Properties and Rheology of Alginate Gel Beads Formed with Various Divalent Cations. *Polym Gels Netw,* 6(5):393-408. DOI 10.1016/s0966-7822(98)00035-5.
19. Stagnaro P, Schizzi I, Utzeri R, *et al*., 2018, Alginate-polymethacrylate Hybrid Hydrogels for Potential Osteochondral Tissue Regeneration. *Carbohydr Polym,* 185:56-62. DOI 10.1016/j.carbpol.2018.01.012.
20. Yang X, Lu Z, Wu H, *et al*., 2018, Collagen-alginate as Bioink for Three-dimensional (3D) Cell Printing Based Cartilage Tissue *Engineering*. *Mater Sci Eng C,* 83:195-201. DOI 10.1016/j.msec.2017.09.002.
21. Müller M, Öztürk E, Arlov Ø, *et al*., 2017, Alginate Sulfate Nanocellulose Bioinks for Cartilage Bioprinting Applications. *Ann Biomed Eng,* 45(1):210-23. DOI 10.1007/s10439-016-1704-5.
22. Axpe E, Oyen ML, 2016, Applications of Alginate-based Bioinks in 3D Bioprinting. *Int J Mol Sci,* 17(12):e1976. DOI 10.3390/ijms17121976.
23. Szekalska M, Puciłowska A, Szymańska E, *et al*., 2016, Alginate: Current use and Future Perspectives in Pharmaceutical and Biomedical Applications. *Int J Polym Sci,* 2016:17. DOI 10.1155/2016/7697031.
24. Augst AD, Kong HJ, Mooney DJ, 2006, Alginate Hydrogels as Biomaterials. *Macromol Biosci,* 6(8):623-33.
25. Spadari CDC, Lopes LB, Ishida K, 2017, Potential use of Alginate-based Carriers as Antifungal Delivery System. *Front Microbiol*, 8:97. DOI 10.3389/fmicb.2017.00097.
26. Mishbak CVH, Cooper G, Bartolo P, 2019, Development and Characterisation of a Photocurable Gelatin/Alginate Bioink for 3D Bioprinting, Prof Dimiter Dimitrov D HH. In: von Leipzig K, editor. *Department of Industrial Engineering Stellenbosch University. International Conference on Competitive Manufacturing (COMA 19)*. DOI 10.18063/ijb.v5i2.189.
27. Jeon O, Bouhadir KH, Mansour JM, *et al*., 2009, Photocrosslinked Alginate Hydrogels with Tunable Biodegradation Rates and Mechanical Properties. *Biomaterials,* 30(14):2724-34. DOI 10.1016/j.biomaterials.2009.01.034.
28. Benton JA, DeForest CA, Vivekanandan V, *et al*., 2009, Photocrosslinking of Gelatin Macromers to Synthesize Porous Hydrogels that Promote Valvular Interstitial Cell Function. *Tissue Eng Part A,* 15(11):3221-30. DOI 10.1089/ten.tea.2008.0545.
29. Sudhakar CK, Upadhyay N, Jain A, *et al*., 2015, Hydrogels Promising Candidates for Tissue *Engineering*. In: Thomas S, Grohens Y, Ninan N, editors. *Nanotechnology Applications*

*for Tissue Engineering.* Ch. 5. William Andrew Publishing, Oxford, p77-94. DOI 10.1016/b978-0-323-32889-0.00005-4.

30. Bonino CA, Samorezov JE, Jeon O, *et al*., 2011, Real-time in Siturheology of Alginate Hydrogel Photocrosslinking. *Soft Matter,* 7(24):11510-7. DOI 10.1039/c1sm06109g.
31. Smeriglio P, Lai JH, Yang F, *et al*., 2015, 3D Hydrogel Scaffolds for Articular Chondrocyte Culture and Cartilage Generation. *J Vis Exp*, 104:53085. DOI 10.3791/53085.
32. Çiğdem KM, Doğan Ö, Faika DS, 2013, Comparison of Chemical Fractionation Method and 1H-NMR Spectroscopy in Measuring the Monomer Block Distribution of Algal Alginates. *J Polym Eng,* 33(3):239-46. DOI 10.1515/polyeng-2012-0066.
33. Smeds KA, Pfister-Serres A, Miki D, *et al*., 2001, Photocrosslinkable Polysaccharides for in situ Hydrogel Formation. *J Biomed Mater Res,* 55(2):254-5. DOI 10.1002/1097-4636(200105)55:2<254::aid-jbm1012>3.0.co;2-5.
34. Lam C, Jefferis SA, 2014, Interpretation of Viscometer Test Results for Polymer Support Fluids. *Tunneling Undergr Constr,* 2014:439-49. DOI 10.1061/9780784413449.043.
35. Bartolo P, Lenz EJC, 2006, Computer Simulation of Stereolithographic Curing Reactions: Phenomenological Versus Mechanistic Approaches. *CIRP Ann,* 55(1):221-5. DOI 10.1016/s0007-8506(07)60403-x.
36. Matias JM, Bartolo PJ, Pontes AV, 2009, Modeling and Simulation of Photofabrication Processes using Unsaturated Polyester Resins. *Appl Polym Sci,* 114(6):3673-85. DOI 10.1002/app.30405.

RESEARCH ARTICLE

# High-precision three-dimensional inkjet technology for live cell bioprinting

**Daisuke Takagi*, Waka Lin, Takahiko Matsumoto, Hidekazu Yaginuma, Natsuko Hemmi, Shigeo Hatada, Manabu Seo**

Ricoh Company Ltd., Healthcare Business Group, Biomedical Business Center, Kawasaki-city, 210-0821, Japan

**Abstract:** In recent years, bioprinting has emerged as a promising technology for the construction of three-dimensional (3D) tissues to be used in regenerative medicine or *in vitro* screening applications. In the present study, we present the development of an inkjet-based bioprinting system to arrange multiple cells and materials precisely into structurally organized constructs. A novel inkjet printhead has been specially designed for live cell ejection. Droplet formation is powered by piezoelectric membrane vibrations coupled with mixing movements to prevent cell sedimentation at the nozzle. Stable drop-on-demand dispensing and cell viability were validated over an adequately long time to allow the fabrication of 3D tissues. Reliable control of cell number and spatial positioning was demonstrated using two separate suspensions with different cell types printed sequentially. Finally, a process for constructing stratified Mille-Feuille-like 3D structures is proposed by alternately superimposing cell suspensions and hydrogel layers with a controlled vertical resolution. The results show that inkjet technology is effective for both two-dimensional patterning and 3D multilayering and has the potential to facilitate the achievement of live cell bioprinting with an unprecedented level of precision.

**Keywords:** Drop-on-demand; three-dimensional tissue engineering; drug discovery; regenerative medicine; hydrogel

*Correspondence to: Daisuke Takagi, Ricoh Company Ltd., Healthcare Business Group, Biomedical Business Center, Kawasaki-city, 210-0821, Japan; daisuke.Takagi@jp.ricoh.com

**Received:** May 14, 2019; **Accepted:** May 27, 2019; **Published Online:** July 1, 2019

**Citation:** Takagi D, Lin W, Matsumoto T, *et al*., 2019, High-precision three-dimensional inkjet technology for live cell bioprinting. Int J Bioprint, 5(2): 208. http://dx.doi.org/10.18063/ ijb.v5i2.208

## 1. Introduction

The field of tissue engineering has developed considerably in recent years, along with the increasing interest in regenerative medicine globally. Advances in stem cell research, particularly the discovery of induced pluripotent stem cells[1], have provided a means to culture and manipulate cells from organs, which were once considered impossible to regenerate. *In vitro* production of functional tissue analogs has become a reality, and tissue engineering has numerous potential applications in therapeutic areas including tissue repair and organ replacement, in addition to developing applications for drug discovery, disease modeling, and alternatives for animal testing. Today, one of the major challenges remains how to reproduce three-dimensional (3D) structures of tissues with matching complexity and functionality. The development of novel technologies for biofabrication, particularly bioprinting, has attracted a lot of attention considering their potential to arrange cells and materials into structurally organized constructs[2].

Current bioprinting technologies are based on three major approaches, including inkjet, extrusion, and laser printing methods[3,4]. Extrusion-based strategies are the most extensively developed due to their capacity to develop 3D constructs and networks in a relatively straightforward manner using high viscosity materials that can integrate extracellular matrix (ECM) such as collagen. However, the approach is not suitable since it does not facilitate precise control over the deposition of a small number of cells. Although laser facilitates printing with a very high resolution, its productivity remains limited due to the complexity and cost of the system, in

High-precision three-dimensional inkjet technology for live cell bioprinting © 2019 Takagi, *et al*. This is an Open Access article distributed under the terms of the Creative Commons Attribution-NonCommercial 4.0 International License (http://creativecommons.org/licenses/by-nc/4.0/), permitting all non-commercial use, distribution, and reproduction in any medium, provided the original work is properly cited.

addition to the requirement for the preparation of ribbons of cells and hydrogels. Conversely, inkjet printing, and more generally, droplet-based bioprinting[5], have great promise as a simple and efficient method for the precise patterning of multiple cell types and bioink components including active biomacromolecules[6], especially since a drop-on-demand control of small volumes down to a few hundred picoliters can be expected. However, inkjet technology has several limitations that impair its further adoption in 3D construction. Although some of the earliest reports of successful bioprinting in the mid-2000s were inkjet based[7-9], few concrete results of fully functional inkjet-produced tissues have been reported to date.

The first notable limitation of inkjet bioprinting is that ejecting large cell-sized particles from common printheads is a challenge. Successful ejection has been reported[10-13], and acoustic ejection achieved in live cell printing[13]; however, cell sedimentation inside the printhead chamber and clogging of the nozzle is expected to rapidly compromise any reliable control of droplet formation over the length of time required to produce a 3D tissue. Second, the range of materials that can be used as substrates to carry the cells is limited to ejectable low-viscosity liquids so that shaping fine 3D structures with suitable mechanical properties is particularly challenging. Various strategies have been reported including coprinting hydrogel precursors with the appropriate cross-linking agent, which facilitates rapid gelation on contact[14-16] or deposition of one liquid into a bath of the other one[17]. However, so far, the results have been generally limited to two-dimensional (2D) cell patterning or roughly shaped 3D cell-laden structures with no spatial positioning at the cellular level.

To address the above challenges, we report here the development of an inkjet bioprinter equipped with a newly designed printhead specially optimized for live cell ejection. For this purpose, we have adapted a bending-type piezoelectric actuator coupled to a simple open head chamber without any narrow flow channel. Such a piezoelectric device has been applied in some previous publications from other groups for continuous cell spraying, but very few studies have reported its application to drop-on-demand cell deposition[18]. The present study integrates the droplet formation and mixing mechanism in our prototype printhead. Stability of cell dispensing and viability is validated over an adequately extended period to facilitate the fabrication of a substantial tissue construct. We then demonstrate the feasibility of building a multi-ink printing system to construct stratified Mille-Feuille-like structures with controlled thickness by alternating cell suspension and hydrogel layers. Therefore, exploiting the full potential of inkjet technology promises to facilitate high-precision multi-ink 3D bioprinting.

## 2. Materials and Methods

### 2.1. Cell Cultures

All cells were cultured in a 5% $CO_2$ incubator at 37.0°C and passaged manually every 2 to 3 days to maintain a subconfluent state. NIH/3T3 mouse fibroblast cell line (clone 5611, JCRB Cell Bank) and normal human dermal fibroblasts (NHDF, CC-2509, Lonza Inc.) were cultured in Dulbecco's Modified Eagle's Medium (Thermo Fisher Scientific Inc.) supplemented with 10% fetal bovine serum (Biowest) and 1% penicillin-streptomycin (26253-84, NACALAI TESQUE, INC). Human umbilical blood vein endothelial cells (HUVEC, CC-2519, Lonza Inc.) were cultured in endothelial cell growth medium (EGM, Lonza Inc.) with supplements as recommended by the manufacturer. For bioink preparation, the cells were washed twice with Dulbecco's phosphate-buffered saline without calcium and magnesium (DPBS, Thermo Fisher Scientific Inc.), detached with 0.05% Trypsin-EDTA (25300054, Thermo Fisher Scientific Inc.), and centrifuged at 400 g for 5 min at 4°C. The cell pellets were re-suspended in fresh DPBS at room temperature and used within 30 min after suspension.

### 2.2. Inkjet Print Head Development

The cell-printing head in Figure 1A presents an original architecture comprising a chamber holding the cell suspension, a disk membrane (which is fixed at the circumference of the bottom of the chamber), a nozzle with an aperture at the center of the membrane, and an annular piezoelectric actuator fixed outside below the membrane

We were able to perform subsequent experiments with more advanced processes for the spatial positioning of cell-containing droplets by achieving a reliable ejection of living cell.

### 2.3. Evaluation of Inkjetting Condition

To determine the optimal printing conditions, optical monitoring devices were assembled as follows. Observation of drop formation was carried out with an experimental apparatus with a high-speed camera (HPV-2, Shimadzu Corporation) and a stroboscopic flash lamp (PE60-SG, Panasonic) aligned on a horizontal axis under the printhead nozzle. The chamber was filled with NIH/3T3 suspension with DPBS solution. By applying a signal to the piezoelectric actuator of the cell-printing head, a droplet is ejected from the cell-printing head. The frequency of the applied signal was fixed to the fundamental frequency of the membrane.

### 2.4. Evaluation of Mixing Condition

Observation of cell suspension mixing was carried out with an experimental apparatus with a ring-type illumination

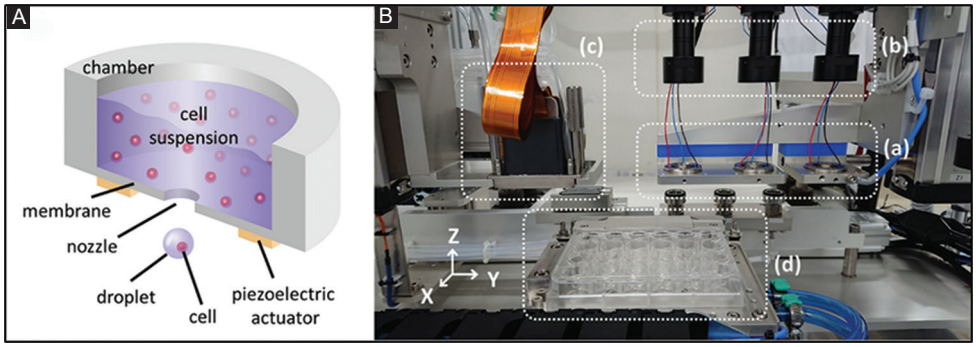


**Figure 1.** Overview of the inkjet bioprinting system. (**A**) Schematic cross-sectional three-dimensional (3D) view of the cell-printing head. (**B**) Photograph of the 3D bioprinting system setup composed of (a) three cell-printing heads controlled in the X and Z directions, (b) cameras for real-time observation of the mixing state in the inkjet head chambers, (c) two industrial inkjet heads for hydrogel printing controlled in the same directions as (a), and (d) a plate/slide holding stage controlled in the Y direction.

source, a macro zoom lens (TS-93005, SUGITOH), and a CCD image sensor (DFK23U618, Imaging Source) placed above the print head chamber. The chamber was filled with 3T3 suspension with DPBS solution, and the signal with several frequency components was applied to the piezoelectric actuator for observation.

## 2.5. Evaluation of Cell Ejection Stability

To evaluate ejection stability, NIH/3T3 cell suspensions were fluorescently labeled with Cell Tracker Green (Thermo Fisher Scientific Inc.) and diluted in DPBS at determined densities before being loaded into the inkjet printhead chamber. Ejecting mode signals and mixing mode signals as defined above were applied alternately at intervals of 500 ms, which allowed the deposition of droplets at a frequency of 2 Hz. The droplets were deposited onto glass slides fixed to an automated moving stage so that the number of cells in each droplet could be counted after printing under a fluorescence microscope (Axio observer D1, Carl Zweiss).

## 2.6. Cell Viability Assay After Ejection

NIH/3T3 or HUVEC cell suspensions were prepared at concentrations of $1 \times 10^6$ cells/ml in DPBS. 30 µL of the cell suspension was loaded into the inkjet head chamber. The cells were ejected for about 30 min with a droplet ejection frequency of 100 Hz into a microcentrifuge tube containing 1 ml of the appropriate culture medium and then counted and dispensed into a 96-well culture plate at a density of $3 \times 10^3$ cells per well. Cell ejection experiments were conducted in triplicate. As control samples, the initial cell suspensions before ejection were manually dispensed into a 96-well culture plate using a 100 µL micropipette. The plates were placed in a 5% $CO_2$ incubator at 37.0°C until measurement. Apoptotic and necrotic cells were quantified in each well using the Apoptotic/Necrotic cell detection kit (Promokine, PromoCell GmbH) according to the instructions of the manufacturer. The stained cultures were observed under a fluorescence microscope (Axio observer D1, Carl Zeiss), and images were taken so that between 200 and 500 cells could be analyzed for each sample. Early apoptotic cells were identified on the basis of green fluorescent staining (FITC-Annexin V) of their plasma membranes and necrotic cells based on red fluorescent staining (EthD-III) of their nuclei. Double positive cells exhibiting both green and red fluorescent staining were considered late apoptotic cells. The total number of cells was determined by counting all the nuclei stained in blue by Hoechst 33342.

## 2.7. Cell Proliferation Assay

The cell suspensions were ejected into a microcentrifuge tube for the cell viability assay and dispensed into a 96-well culture plate at a density of $3 \times 10^3$ cells per well. The WST-1 colorimetric assay (Premix WST-1Cell Proliferation Assay System, Takara Bio Inc.) was used to evaluate the proportion of actively metabolizing live cells in each well. Measurements were performed in triplicate using three wells at each time point. 10 µL of the WST-1 reaction solution was added to each well containing the cells and 100 µL culture medium. The plates were returned to the 5% $CO_2$ incubator for 1 h and incubated at 37.0°C. Absorbance at 420 nm was measured using a plate reader (Cytation 5, BioTek Instruments, Inc.). The measured data were normalized relative to the measurements obtained 4 h post-ejection.

## 2.8. Embryonic Stem Cell Clonogenic Assay and Immunostaining

Mouse embryonic stem cells (mES cells, Merck) were maintained in gelatin-coated dishes with feeder cells (Merck) as recommended by the manufacturer. The cells were detached using Accutase (Merck), centrifuged at 100 g for 5 min at 4°C, and suspended in DPBS through a 20 µm filter to make bioinks. After ejection, the cells

were seeded at a density of $2.5 \times 10^4$ cell/well in 24-well plates and cultured for 3 days. The average numbers of colony-forming units were counted after staining with red alkaline phosphatase substrate kit (VECTOR laboratories). For immunostaining, the cells were fixed with 4% paraformaldehyde and incubated overnight at 4°C with primary antibodies, Nanog (abcam) 1:200, SSEA-1 (abcam) 1:100, 2 h at room temperature with secondary antibodies, and 5 min with 1:10,000 Hoechst 33342 (Thermo Fisher Scientific).

### 2.9. 3D Bioprinting System Setup

A bioprinting system has been designed as shown in Figure 1B for constructing 3D tissues with multiple cell types. The present system is equipped with newly developed cell-printing inkjet heads and commercial industrial inkjet heads for ejecting biomaterials. A maximum of three cell-printing inkjet heads can be mounted in parallel so that three types of cells can be printed sequentially to develop tissues with heterogeneous patterns. The position of the nozzle is controlled horizontally on the X-axis and vertically on the Z-axis to allow the deposition of cells not only for surface patterning but also in three dimensions. In addition, two industrial multi-nozzle inkjet heads (MH2420 Print Head, Ricoh) allow the successive printing of two different liquids such as a hydrogel precursor and an appropriate cross-linking reagent, enabling the formation of fast-gelling layers over a large area. The industrial heads can also be controlled independently on the X- and Z-axis. The stage is controlled on the Y-axis and can hold glass slides at the back and culture plates at the front.

### 2.10. 2D Drop-on-demand Patterning Evaluation

To evaluate the control of droplet deposition using two cell-printing heads in a sequential manner, two separate suspensions of NIH/3T3 cells were prepared at a concentration of $3 \times 10^6$ cells/ml in DPBS. To distinguish between the suspensions, the cells were fluorescently labeled with CellTracker Green or Orange (Thermo Fisher Scientific Inc.) according to the instructions of the manufacturer. Cell-containing droplets were deposited with a sinusoidal waveform and an ejection frequency of 50 Hz onto a glass slide. Phase-contrast and fluorescent microscopy images were taken using a laser scanning confocal microscope (FV10i, Olympus Corporation).

### 2.11. 3D Multilayering Evaluation

For 3D constructs, the general process for developing multilayered structures with alternating cell and hydrogel deposition is described in Figure 2 in section 3. Four separate bioinks were prepared as follows: 0.5 wt% sodium alginate as scaffold bioink 1; 100 mM calcium chloride ($CaCl_2$) as scaffold bioink 2; $5 \times 10^7$ cells/ml NHDF cells stained with Cell Tracker Green and suspended in DPBS and 0.5 wt% sodium alginate as cell-laden bioink 1; and $5 \times 10^7$ cells/ml NHDF cells stained with Cell Tracker Orange and suspended in DPBS and 0.5 wt% sodium alginate as cell-laden bioink 2. Printing was performed on a glass slide as follows: (a) A layer of sodium alginate was deposited by ejecting scaffold bioink 1 using the first industrial head at 10 Hz, immediately followed by (b) a layer of $CaCl_2$ using the second industrial head for rapid gelling of a thin alginate hydrogel scaffold layer; (c) cell-laden bioink 1 was deposited with a cell-printing printhead at 10 Hz to draw a 10 mm line along the X-axis; (d) a hydrogel scaffold layer was superimposed onto the cell layer using the same procedure in (a) and (b); and (e) the cell-laden bioink 2 was deposited with a cell-printing printhead at 10 Hz to draw a 10 mm line along the Y-axis. The steps from (a) to (e) were repeated until a 10-layer construct was achieved. To observe the superposition of layers, cross-sectional Z-stack images of the multilayered constructs were acquired using a confocal laser scanning microscope (TCS SP8 STED CW, Leica Microsystems) at the intersection of the green and orange cell lines after fixation in ethanol.

## 3. Results

### 3.1. Inkjet Printhead Design

Ejecting living cell suspensions using inkjet technology generally presents several challenges. Figure 3A illustrates a simplified representation of a common piezoelectric inkjet printhead and summarizes the three most notable issues when using such a device. First, the typical cell size is 100 times larger than typical pigments in printing ink solutions so that nozzle and channel clogging occurs as cells rapidly sink to the bottom. Cell sedimentation also makes it a challenge to obtain a stable number of cells per droplet since the density inside the chamber is not maintained at a homogeneous state. Second, air bubbles are trapped in the cell suspension due to high surface tension, which negatively affects the reliability of droplet ejection. Third, a cell suspension with a large volume is required to fill up the entire chamber and enable the piezoelectric actuator induce liquid pressure for droplet ejection.

Therefore, here, we have developed a novel printhead optimized for live cell-printing (cell-printing head) that could replace conventional printheads. As shown in Figure 3B, the cell-printing head is composed of an open chamber where the cells are directly loaded, a disc-shaped membrane fixed at the circumference of the bottom of the chamber, a nozzle with an aperture at the center of the

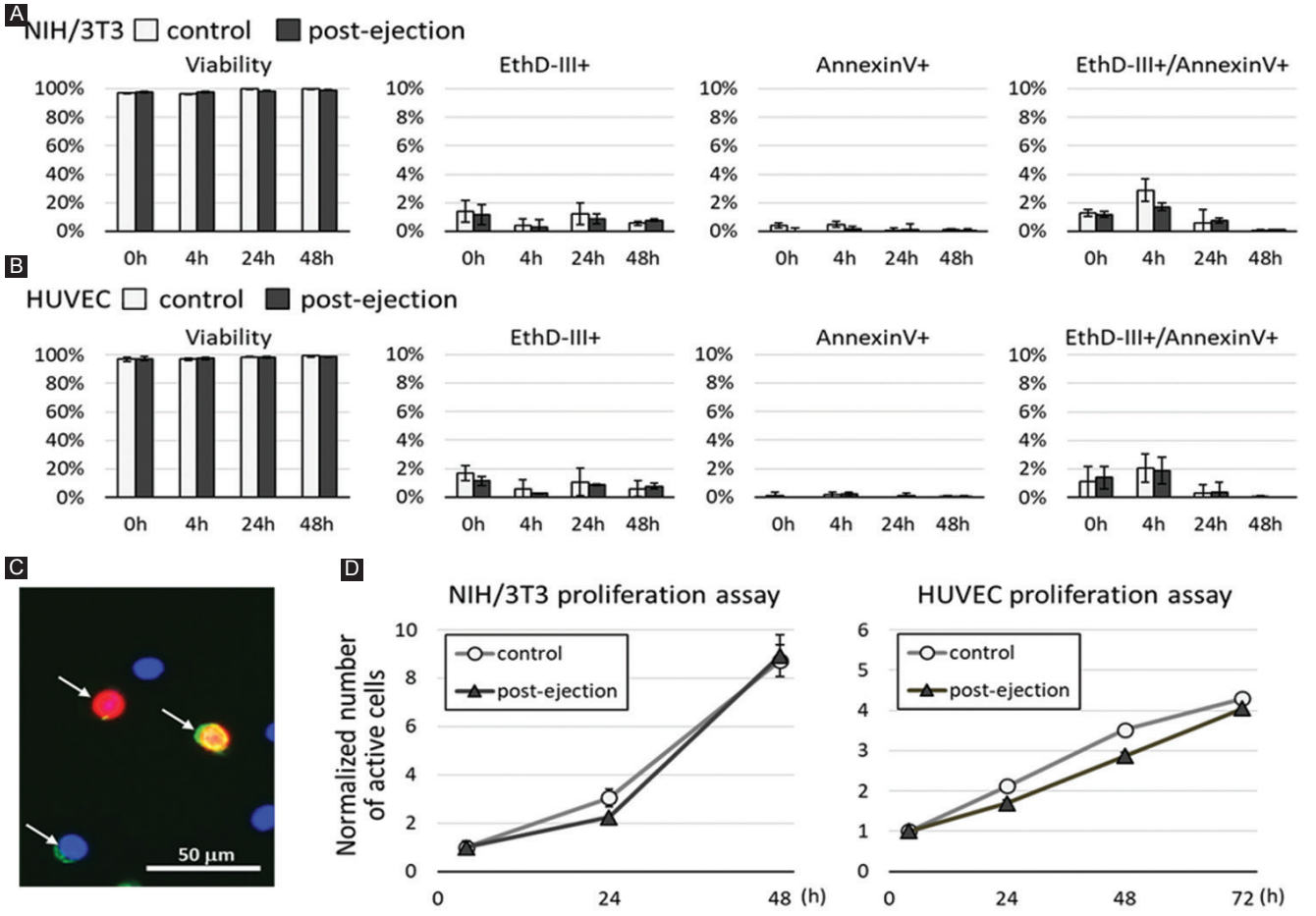


**Figure 2.** Analysis of cell survival after ejection from the new inkjet head. (**A**) Percentages of unstained viable cells, EthD-III positive (necrotic) cells, FITC-Annexin V positive (apoptotic) cells, and double positive (late apoptotic) cells in NIH/3T3 cell cultures from 0 to 48 h post-ejection compared with control cultures seeded by manual pipetting. Error bars show the standard deviations of triplicate cultures with 200-500 cells analyzed per sample. (**B**) Same as (**A**) for human umbilical blood vein endothelial cell (HUVEC) cultures. (**C**) Representative fluorescence microscopy image of NIH/3T3 cells stained using the Apoptotic/Necrotic cell detection kit. White arrows indicate the three different types of stained cells: Red cells for EthD-III, green cells for FITC-Annexin V, and double positive yellow cells. All cell nuclei are stained blue with Hoechst 33342. Scale bar: 50 µm. (**D**) Quantification of active live cells in NIH/3T3 and HUVEC in WST-1 proliferation assay. The data were normalized and reported as a ratio relative to the measurement at 4 h.

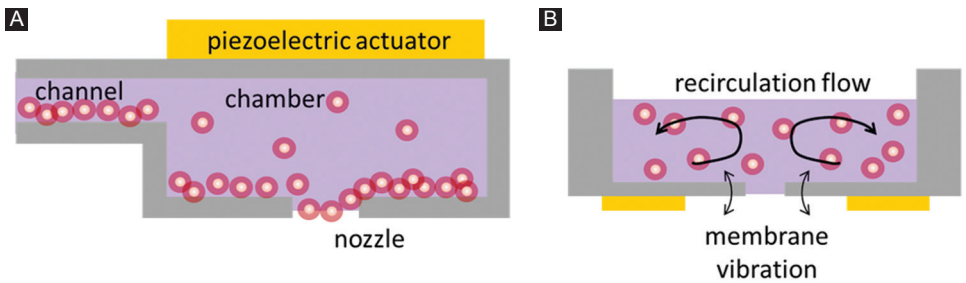


**Figure 3.** Schematic diagram of a cross-sectional view of inkjet heads. (**A**) Common printhead showing nozzle clogging with the sedimentation of cells. (**B**) Cell-printing head, with a recirculation flow generated by membrane vibration to prevent nozzle clogging.

membrane, and an annular piezoelectric actuator fixed on the outer side of the membrane. The advantages of the cell-printing head are that first, as illustrated in Figure 3B, membrane movements driven by the piezoelectric actuator can establish a recirculating flow inside the chamber to prevent cell sedimentation. Second, air bubbles trapped during droplet ejection can be easily evacuated from the open side. Third, the cell-printing head can be loaded

with volumes as low as a few dozen microliters without compromising droplet formation.

### 3.2. Evaluation of Inkjetting Condition

To determine the optimal printing conditions, optical monitoring devices were assembled as follows. Observation of drop formation was carried out, as illustrated in Figure 4A. By applying a signal as shown in Figure 4B to the piezoelectric actuator of the cell-printing head, a droplet is ejected from the cell-printing head. Frequency of the applied signal was fixed to the fundamental frequency of the membrane.

Results of drop formation with voltage amplitudes between 4.4 and 5.8 V are shown in Figure 4C. One drop formation is achieved when the voltage V ranges from 4.8 to 5.4 V. When the voltage is lower than 4.8 V, the pressure required for drop formation cannot be achieved. Conversely, when the voltage is higher than 5.4 V, minute droplets (mist and satellite) are formed.

A droplet forming process in the cell printhead will be described with reference to the schematic view as shown in Figure 4E and F. When the membrane is displaced from the original state to the liquid chamber side and suddenly pushes the liquid; pressure is generated at the interface between the membrane and liquid. Since the pressure is easily released into the atmosphere through the nozzle rather than through the upper aperture of the chamber or pushes back the membrane, the meniscus protrudes out of the nozzle (Figure 4E). Thereafter, the membrane attempts to revert to the original position. However, if the liquid in the nozzle portion at the time receives an adequate velocity, the liquid droplet is considered to be formed, as shown in Figure 4F.

### 3.3. Evaluation of Mixing Condition

Observation of cell suspension mixing was carried out as illustrated in Figure 5A, and the signal is shown in Figure 5B with several frequencies applied to the piezoelectric actuator for the observation.

The circle in each figure indicates the membrane. The nozzle is located in the center of the membrane, and ring-shaped mirror images of the illuminations are seen in each figure. In Figure 5C, uniform mixing mode is observed by applying the signal at a frequency near the fundamental frequency of the membrane (20 kHz). Conversely, the periodic pattern is observed by applying a

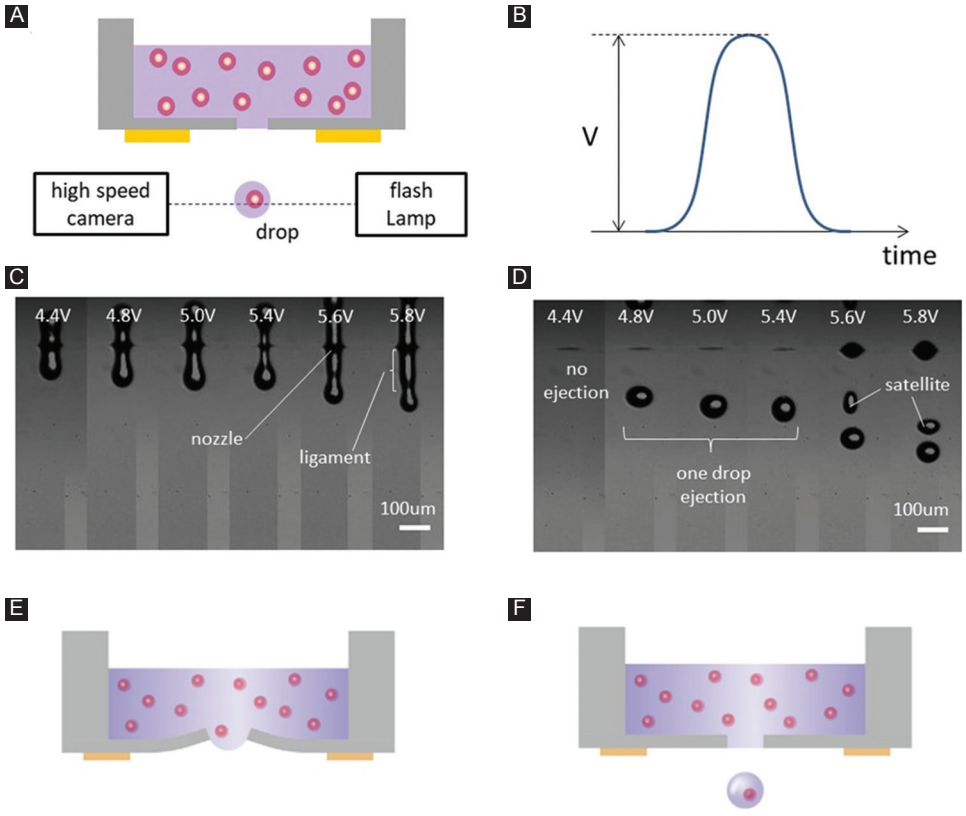


**Figure 4.** Observation of droplet formation from the cell printhead. (**A**) Observing mechanism of droplet formation using a high-speed camera and a flash lamp. (**B**) Addition of sine curve signals to piezoelectric actuator. (**C**) Observation of droplet after 200 µs, addition of 4.4, 4.8, 5.0, 5.4, 5.6, and 5.8 V and compare each droplet formation. (**D**) Observation of droplet after 316 µs, one drop ejection with 4.8, 5.0, and 5.4 V. (**E**) Schematic diagram of droplet formation in 200 µs. (**F**) Schematic diagram of droplet forming in 316 µs.

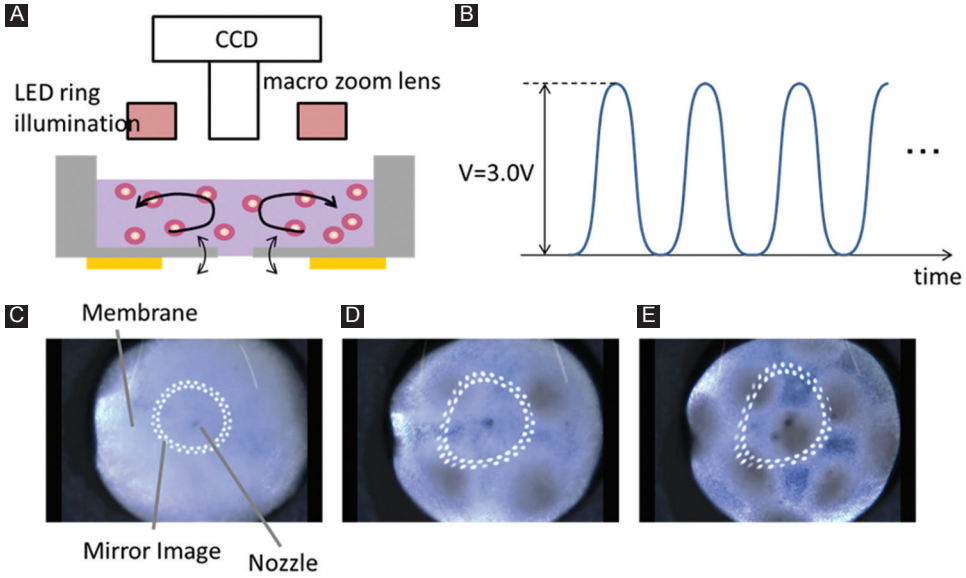


**Figure 5.** Observation of mixing cell suspension in the chamber. (**A**) Mixing status is checked by CCD, a micro zoom lens, and ring illumination. (**B**) For mixing cell suspension, a sinusoidal signal was applied with a fixed amplitude of 3.0 V. (**C**) Mixing status with the fundamental frequency of the membrane, 20 kHz. (**D**) and (**E**) Mixing mode with higher-order vibration mode, 72.0 and 74.0 kHz.

higher frequency such as 72.0 kHz. 74.0 kHz is applied in Figure 5D and E. The phenomena are expected to induce higher-order vibration modes. At such a higher-order vibration mode, the antinodes and nodes of vibration are generated, and cells gathering into the node position were observed, as shown in Figure 5D and E. Therefore, the preferred signal frequency for mixing cells is not one of a higher-order vibration mode of the membrane but one near the fundamental mode.

Appropriate single cell droplet formation was achieved when a single peak sinusoidal signal was applied to the piezoelectric actuator with a voltage amplitude between 4.8 and 5.4 V (ejecting mode), whereas uniform mixing was achieved when the signal had a frequency close to the fundamental frequency of the vibrating membrane at a fixed amplitude of 3 V (mixing mode).

### 3.4. Evaluation of Ejection Stability

Developing bioprinted tissue at any substantial volume or amount, as required in applications such as organ regeneration or drug screening, would require a reliable deposition of cell-containing droplets over a considerable period. Therefore, maintaining a stable number of cells per droplet for an adequately long time is critical in inkjet bioprinting. Optimization of the signals applied to the piezoelectric actuator to enable the use of the cell-printing head is described in section 2.2. Briefly, a single peak sinusoidal signal with a voltage amplitude between 4.8 and 5.4 V (ejecting mode) allows a single cell-containing droplet to be ejected by the movement of the membrane at the nozzle. Drop-on-demand ejection, therefore, can be achieved by controlling the signal applied to the printhead. Between each ejection, a weak sinusoidal vibration is applied to the membrane to maintain the cells in suspension (mixing mode). Alternating the ejecting mode and mixing mode signals at fixed time intervals allows the deposition of droplets at a constant frequency. The results for the evaluation of ejection stability are shown in Figure 6A. Droplets were ejected at a frequency of 2 Hz using cell suspensions at three different cell densities and were ejected without mixing mode as a reference. The number of cells per droplet was stable for over 15 min at any of the tested cell densities with mixing mode. Conversely, unstable ejecting was observed with the reference sample. At 0 min, the same cell number was observed with mixing and without mixing; however, average cell number increased with the lapse of time. The observations indicate that mixing mode could be ejected with stable cell number. The graph in Figure 6B illustrates the average cell number and the standard deviation with mixing mode samples calculated over the entire length of the 15 min ejection experiment. The average number of cells per droplet had a linear relationship with the initial density of cell suspension, which suggests that the number of cells per droplet can be adjusted by selecting the appropriate cell density when preparing the bioink cell suspension. Here, using a bioink with a cell density of $3 \times 10^6$ cells/ml would allow the deposition of around 1.5 cells per droplet on average. This indicates that high accuracy control of cell number in each droplet is achieved using the cell-printing head.

In addition, the histograms in Figure 7 show that the number of cells per droplet at 0 and 15 min is consistent with a Poisson distribution profile at any of the tested cell

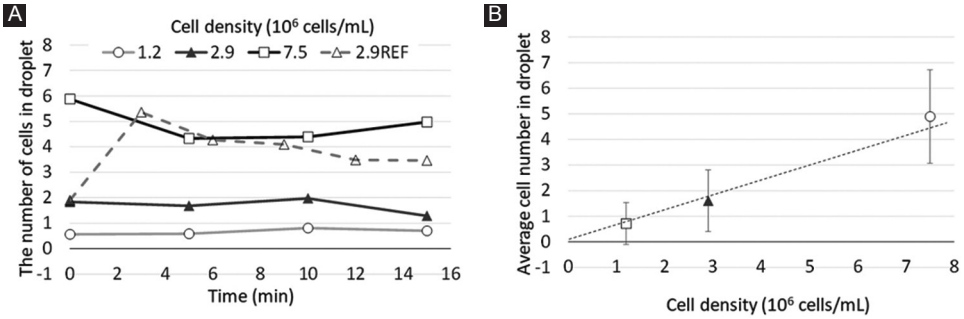


**Figure 6.** Evaluation of ejection stability. Droplets of cell suspensions were ejected at a frequency of 2 Hz onto a glass slide. Then, the cell number in each droplet was counted under a fluorescence microscope. (**A**) Average cell count per droplet for the three initial cell densities: 1.2E + 06, 2.9E + 06, and 7.5E + 06 cells/mL. As a reference, 2.9E + 06 cells/ml were ejected without mixing mode. (**B**) Average cell number in droplet are plotted with each cell density. Error bar is 1 sigma.

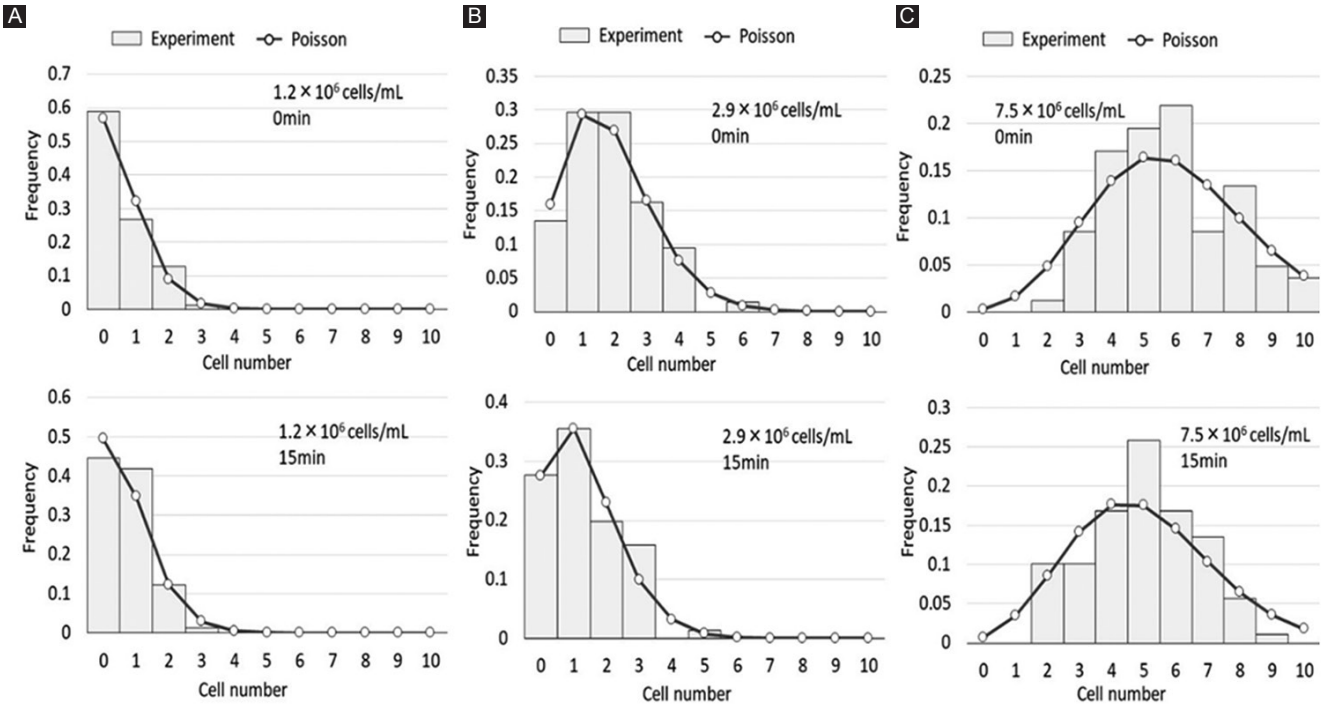


**Figure 7.** Histogram plot of cell number in each droplet. (**A**) Result with 1.2E + 06 cells/ml in 0 and 15 min. Dot is value with the Poisson distribution. The blue bar is experimental value. (**B**) Result with 2.9E + 06 cells/mL. (**C**) Result with 7.5E + 06 cells/mL.

densities. The observation indicates that the cells inside the head chamber were maintained in suspension with a random distribution for a long time, which confirms that the mixing mode of the cell-printing head achieved its function.

### 3.5. Cell Viability and Proliferation after Ejection

Cell viability was evaluated at 0, 4, 24, and 48 h after ejection into the culture medium. Printing was carried out with the voltage previously applied but with the droplet ejection frequency increased to 100 Hz to enable the collecting of a higher number of cells. The cells were ejected into the culture medium for 30 min and then aliquoted into a 96-well plate and placed in a 5% $CO_2$ incubator at 37.0°C. The cultures were then fluorescently stained with FITC-Annexin V to identify early apoptotic cells in green and with Ethidium Homodimer III (EthD-III) to identify necrotic cells in red. The percentages of each cell type relative to the total number of cells analyzed post-ejection were compared with those of control cultures seeded by manual pipetting.

As shown in Figure 2, very high viability of between 97% and 99% was demonstrated for NIH/3T3 and HUVEC after printing. No significant difference was observed compared with the control cultures, either for apoptotic cells or for necrotic cells. The WST-1 proliferation assay revealed

that despite a slight decrease at 24 h in NIH/3T3 cells and between 24 and 48 h for HUVEC, the post-ejection samples recovered normally and achieved a proliferation rate similar to that of the manually seeded controls after 48-72 h. To further assess functional recovery in a more sensitive type of cells, a similar experiment was performed using mES cells, as shown in Figure 8. No significant effect was observed on the clonogenic ability and the expression of stem cell markers in mES cells cultured for 3 days after ejection. Overall, the results demonstrate that using our newly developed inkjet printhead does not significantly affect cell viability and functionality, at least for the cell types used in the present study.

### 3.6. Precise Drop-on-demand Live Cell Patterning

A novel inkjet bioprinting system has been developed as described in Figure 1B of section 2 to demonstrate the feasibility of multi-ink live cell deposition. Our bioprinter is equipped with three of the novel cell-printing heads described previously, which allow handling of up to three independent cell suspensions simultaneously.

Drop-on-demand control of cell deposition was evaluated by ejecting a predefined number of droplets of cell suspensions onto a glass slide. Figure 9A shows the results using two different suspensions of fibroblast cells at a density of $3 \times 10^6$ cells/ml, one labeled with fluorescent cell tracker green and the other with cell tracker orange, with a distance of 500 µm between the dots. The previous results for ejection stability showed that when using a suspension with an initial density of $3 \times 10^6$ cells/mL, about 1.5 cell count per droplet can be expected on average. Here, two droplets were deposited per dot, which allowed the observation of an average of three cell counts per dot.

In addition, the ability to control cell number with variable droplets was assessed, as shown in Figure 9B. The average number of cells per deposition exhibited a linear relationship with the number of ejected droplets, which suggests that the number of cells per deposition can be adjusted by selecting the appropriate number of droplets. This indicates that high accuracy control of cell number in each deposition is also achieved with the cell-printing head.

### 3.7. Biofabrication Process for the Development of 3D Mille-Feuille-like Constructs

A multilayering process for constructing 3D tissues was developed, as described in Figure 10. In addition to being equipped with cell-printing heads, our inkjet bioprinting prototype has two industrial multi-nozzle heads, which allow rapid deposition of two liquid materials such as precursors of hydrogel scaffolds into thin layers.

By alternating hydrogel scaffold layers made of sodium alginate deposition, followed immediately by $CaCl_2$ ion cross-linking, and fluorescently labeled cell suspension layers, Mille-Feuille-like bicolor constructs could be produced, as reported in Figure 11A. Cross-section images along the vertical Z-axis acquired under confocal laser scanning microscopy revealed that the finely stratified multilayer structure was well preserved. As reported in the example of Figure 11B, it was also demonstrated that the distance between each cell layer could be controlled by increasing the number of steps during the deposition of hydrogel scaffold layers.

## 4. Discussion

The newly developed inkjet printhead introduced in the present study has been particularly optimized for live cell bioprinting. The unique features of the cell-printing head allow the controlled ejection of single droplets on demand while maintaining the cells in suspension inside the printhead chamber. The analysis of the number of cells per droplet revealed that a stable ejection could be maintained for dozens of minutes of continuous printing, which is a significant improvement over conventional piezoelectric printheads. Notably, achieving a consistent cell count per droplet and, more preferably, approaching a state where a single cell is contained in each droplet

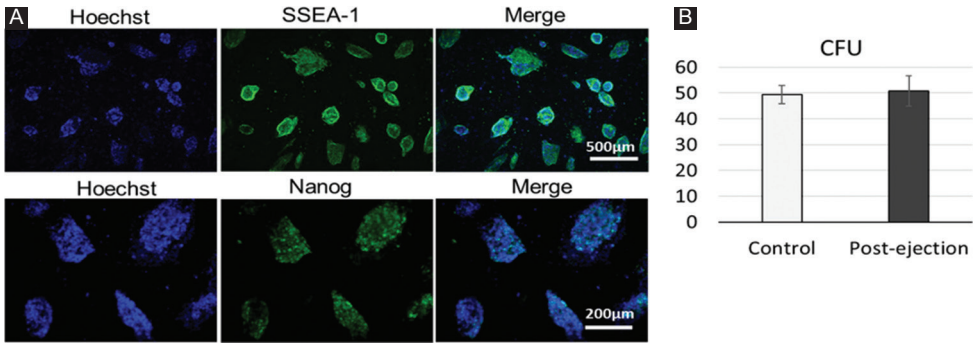


**Figure 8.** Analysis of mouse embryonic stem (mES) cell clonogenic cell survival. (**A**) Immunostaining of mES colonies with stem cell markers. (**B**) Average number of colony-forming unit counted at day 3 of culture after seeding by manual pipetting (control) or by inkjet (post-ejection). Error bars show the standard deviations of four microscopic images.

would be a major step toward the modeling of highly detailed 3D structures at the resolution of a single cell. The results showed that the new cell-printing head could eject cells with a cell per droplet consistent with the Poisson distribution profile, which indicated that the cell suspension was maintained in a well-homogenized state by the mixing system.

However, to achieve an even narrower distribution and further increase the precision of deposition, it would be necessary to bring the state of random distribution closer to a state of uniform distribution for the cells in suspension inside the printhead chamber. This would require a strong repulsive force that acts between the cells, so that they are not brought close to each other, for example, by introducing a polymer with a charge polarity that could provide an electrostatic repulsive force between the cells. We are also investigating the potential of employing additional optical cell count systems to further control the number of cells per droplet.

Regarding the suitability of using the new printheads with living cells, analysis of cell viability and proliferation revealed that the ejected cells were not significantly affected, even following the application of sensitive cells such as undifferentiated stem cells. In contrast to a previous report evaluating cell injury during laser bioprinting[19], no marked increase in necrotic nor in apoptotic cells was observed from 0 to 48 h. The results are potentially because the level of stress induced by our current process is lower than that in laser printing. The cells recovered and proliferated normally after inkjet printing and were expected to maintain the integrity of their functions, including the clonogenicity of stem cells.

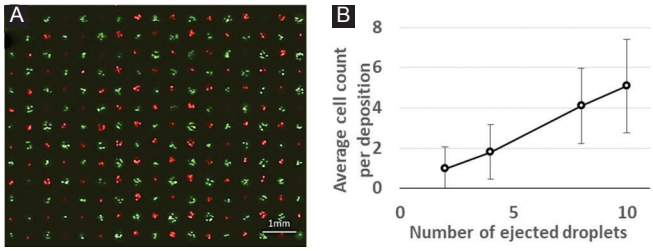


**Figure 9.** Drop-on-demand two-dimensional patterning evaluation (**A**) Fluorescence microscope image of green- and red-labeled NIH/3T3 cells deposited alternately at 500 μm intervals with two cell-containing droplets ejected at each position. (**B**) Ability to control the number of cells based on the number of ejected droplets. Cell ink was formulated to contain one cell in two droplets. Error bars show the standard deviations.

Our printheads bear several features are considerably different from common industrial inkjet heads and could minimize cell damage. The open chamber structure and the mixing system allow use over extended periods without compromising gaseous exchange, whereas rapidly evacuating bubbles before their accumulation increases the risk of damage following rupture[20]. The simplicity of the printhead chamber architecture and the use of membrane vibration for droplet generation avert any excessive increase in liquid pressure and shear stress before ejection. Further investigations are required to assess the physical mechanisms that negatively influence cell viability and function the most.

It is also worth noting, from a practical point of view, particularly considering potential biomedical applications that the printhead chamber was intentionally kept simple to ensure that low volumes of cell suspensions could be loaded easily. Simplifying the procedures for loading and exchanging cell suspensions could further reduce the risks of environmental stress and contamination. This could also be a major advantage when using rare cells that are difficult to expand since our system does not require filling ink cartridges or wasting cell suspensions for maintenance.

Achieving a reliable ejection of living cells allowed us to subsequently experiment with more advanced processes for the spatial positioning of cell-containing droplets. We have demonstrated that an on-demand patterning of cells over a flat surface is feasible with precise control of cell number at each deposition. Most notably, the potential to draw intricate patterns with arrays

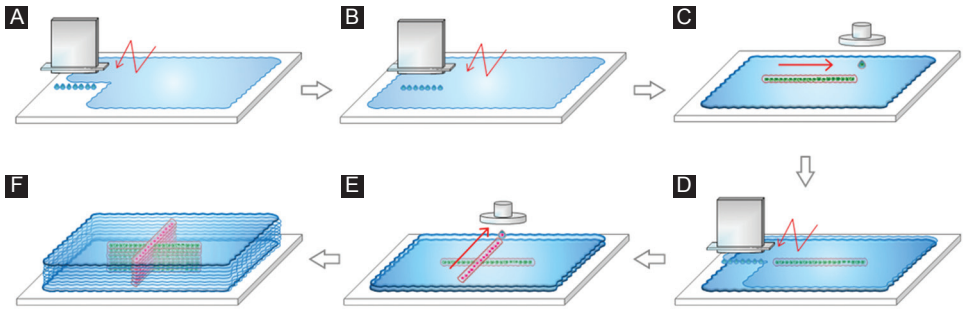


**Figure 10.** Schematic of three-dimensional inkjet cell-printing process. (**A**) Printing of a scaffold hydrogel precursor before gelation. (**B**) Printing of gelation factor. (**C**) Printing of the first cell ink. (**D**) A hydrogel scaffold layer is superimposed onto the cell layer by the same procedure in (**A**) and (**B**). (**E**) Printing of the second cell ink. (**F**) The steps from (**A**) to (**E**) are repeated until a multilayer construct is achieved.

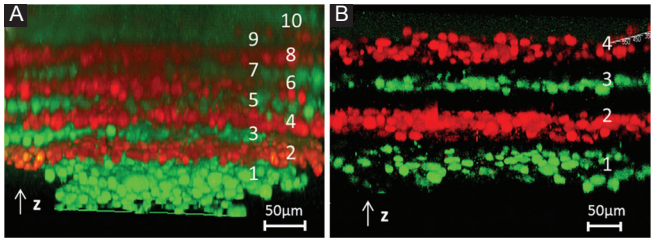


**Figure 11.** Confocal fluorescence microscope Z-stack images of multilayered Mille-Feuille-like three-dimensional cellular constructs. (**A**) Ten-layer constructs made by the alternate printing of green and red fluorescently labeled fibroblasts with alginate hydrogel scaffold layers deposited in between. (**B**) Four-layer constructs with distances between each cell layer increased by the deposition of thicker hydrogel layers.

of multiple cell types and density gradients is a promising feature of inkjet bioprinting that would be unmatched by other methods. Bicolor arrays have been successfully printed in the present study to test the principle, and even more complex pattern designs could be achieved should the need arise. Our unique combination of cell-printing printheads and industrial printheads also allowed us to develop multilayered structures by association with hydrogel biomaterials, with a controlled thickness down to only a dozen micrometers between each layer. Various strategies for layer-by-layer cell deposition have been attempted previously[21,22]; however, to the best of our knowledge, this is the first report of such finely stratified cellular constructs developed entirely based on an inkjet system. One ultimate goal would be to achieve true drop-on-demand printing at single-cell resolution, which would signal the potential for novel approaches for the reconstruction and exploration of the complexity of tissue microenvironments in synergy with the recent rapid advances in single cell analysis.

Despite considerable progress, our technology still faces several limitations that are yet to be resolved. The first issue is that the X-Y surface printing resolution decreases when attempting to draw continuous lines or to increase the density of cellular deposition. Our lines are generally around 100 µm wide, which can be considered quite thick compared with the high resolution we have achieved on the vertical Z direction. This is essentially due to physical properties such as surface tension of the printed materials that can result in the cells moving away from the droplet impact point before their immobilization. Therefore, further optimization and validation are required by taking into account variable cell size, cell density, and materials used as bioink. Finally, the development of bioink materials is also crucial for improving tissue construction in 3D. To obtain fully functional tissues, hydrogel materials that hold the cells together should not only provide physical support but also be biocompatible and able to promote appropriate cellular growth and maturation[23]. In this regard, our method requires fast-gelling materials with rheological properties that are compatible with a stable ejection from the inkjet printhead while ensuring precise deposition and rapid immobilization of cells into layers. We are currently using alginate hydrogel as the material of choice since both its precursor and its cross-linking agent (calcium chloride) can be inkjet-printed and provide adequate mechanical strength by forming a solid scaffold layer on contact. However, alginate is not often appropriate for long-term culture since it lacks the cell-adhesive properties required for the cells to interact and function properly[17]. Investigations on more suitable materials are underway to provide cellular environments closer to native ECM, including the use of modified alginate, or blending with other cell-adhesive and biodegradable polymers such as fibrin and gelatin[24].

## 5. Conclusions

The present study demonstrates that inkjet bioprinting has the potential to become one of the most powerful technologies for precise tissue construction. Our experience in industrial printing allowed us to address each challenge with systematic engineering solutions. First, an innovative printhead specifically designed to eject living cell suspensions has been developed, and the printing conditions have been optimized for reliable dispensing and cell survival. In addition, a multi-ink bioprinting system has been built to demonstrate that cells and materials can be effectively arranged in both 2D high-precision patterns and 3D multilayered constructs in a unique manner. Mechanical refinements and biomaterial development are still required to improve patterning resolution and 3D tissue formation. However, inkjet bioprinting could evolve into a versatile system for the production of structurally organized multicomponent constructs tailored to meet the requirements of various applications such as regenerative medicine, *in vitro* testing, or disease modeling.

## Acknowledgment

We thank Naoki Satoh, Yuzuru Kuramochi, and Satoshi Nakazawa for their technical assistance and the Ricoh Material Analysis Technology Research Department for help in taking confocal images.

## Authors' Contributions

M.S. and D.T. supervised the project and designed the original inkjet device and printing system. W.L., T.M., H.Y., and S.H. designed the experiments. T.M., H.Y., and N.H. conducted the experiments. W.L. and T.M. analyzed the data. D.T. wrote the manuscript. All authors reviewed the manuscript.

## Conflicts of Interest

The authors are employees of the sponsor of this study. However, this did not influence the objectivity of the study. The authors declare that they do not have any competing interests.

## References


1. Takahashi K, Tanabe K, Ohnuki M, *et al*., 2007, Induction of Pluripotent Stem Cells from Adult Human Fibroblasts by Defined Factors. *Cell,* 131(5):861-72. DOI 10.1016/j.cell.2007.11.019.
2. Groll J, Boland T, Blunk T, *et al*., 2016, Biofabrication: Reappraising the Definition in an Evolving Field. *Biofabrication,* 8(1):13001-6. DOI 10.1088/1758-5090/8/1/013001.
3. Murphy SV, Atala A, 2014, 3D Bioprinting of Tissues and Organs. *Nat Biotechnol*, 32(8):773-85. DOI 10.1038/nbt.2958.
4. Arslan-Yildiz A, El Assal R, Chen P, *et al*., 2016, Towards Artificial Tissue Models: Past, Present, and Future of 3D Bioprinting. *Biofabrication,* 8(1):14103. DOI 10.1088/1758-5090/8/1/014103.
5. Gudupati H, Dey M, Ozbolat I, 2016, A Comprehensive Review on Droplet-based Bioprinting: Past, Present and Future. *Biomaterials,* 102:20-42. DOI 10.1016/j.biomaterials.2016.06.012.
6. Derby B, 2008, Bioprinting: Inkjet Printing Proteins and Hybrid Cell-containing Materials and Structures. *J Mater Chem*, 18(47):5717-21. DOI 10.1039/b807560c.
7. Xu T, Jin J, Gregory C, *et al*., 2005, Inkjet Printing of Viable Mammalian Cells. *Biomaterials,* 26(1):93-9. DOI 10.1016/j.biomaterials.2004.04.011.
8. Nakamura M, Kobayashi A, Takagi F, *et al*., 2005, Biocompatible Inkjet Printing Technique for Designed Seeding of Individual Living Cells. *Tissue Eng*, 11(11-12):1658-66. DOI 10.1089/ten.2005.11.1658.
9. Saunders RE, Gough JE, Derby B, 2008, Delivery of Human Fibroblast Cells by Piezoelectric Drop-on-demand Inkjet Printing. *Biomaterials,* 29(2):193-203. DOI 10.1016/j.biomaterials.2007.09.032.
10. Gross A, Schöndube J, Niekrawitz S, *et al*., 2013, Single-cell Printer: Automated, on Demand, and Label Free. *J Lab Autom*, 18(6):504-18. DOI 10.1177/2211068213497204.
11. Cheng E, Yu H, Ahmadi A, *et al*., 2016, Investigation of the Hydrodynamic Response of Cells in Drop on Demand Piezoelectric Inkjet Nozzles. *Biofabrication,* 8(1):15008. DOI 10.1088/1758-5090/8/1/015008.
12. Herran CL, Huang Y, Chai W, 2012, Performance Evaluation of Bipolar and Tripolar Excitations During Nozzle-jetting-based Alginate Microsphere Fabrication. *J Micromech Microeng,* 22(8):85025. DOI 10.1088/0960-1317/22/8/085025.
13. Kim YK, Park JA, Yoon WH, *et al*., 2016, Drop-on-demand Inkjet-based Cell Printing with 30-μm Nozzle Diameter for Cell-level Accuracy. *Biomicrofluidics,* 10(6):064110. DOI 10.1063/1.4968845.
14. Arai K, Iwanaga S, Toda H, *et al*., 2011, Three-dimensional Inkjet Biofabrication Based on Designed Images. *Biofabrication,* 3(3):34113. DOI 10.1088/1758-5082/3/3/034113.
15. Cui X, Boland T, 2009, Human Microvasculature Fabrication using Thermal Inkjet Printing Technology. *Biomaterials,* 30(31):6221-7. DOI 10.1016/j.biomaterials.2009.07.056.
16. Faulkner-Jones A, Fyfe C, Cornelissen DJ, *et al*., 2015, Bioprinting of Human Pluripotent Stem Cells and their Directed Differentiation into Hepatocyte-like Cells for the Generation of Mini-livers in 3D. *Biofabrication,* 7(4):44102. DOI 10.1088/1758-5090/7/4/044102.
17. Nakamura M, Iwanaga S, Henmi C, *et al*., 2010, Biomatrices and Biomaterials for Future Developments of Bioprinting and Biofabrication. *Biofabrication,* 2(1):14110. DOI 10.1088/1758-5082/2/1/014110.
18. Perçin G, Khuri-Yakub BT, 2003, Piezoelectric Droplet Ejector for Ink-jet Printing of Fluids and Solid Particles. *Rev Sci Instrum*, 74(2):1120-7. DOI 10.1063/1.1532839.
19. Zhang Z, Chai W, Xiong R, *et al*., 2017, Printing-induced Cell Injury Evaluation During Laser Printing of 3T3 Mouse Fibroblasts. *Biofabrication,* 9(2):25038. DOI 10.1088/1758-5090/aa6ed9.
20. Hu W, Berdugo C, Chalmers JJ, 2011, The Potential of Hydrodynamic Damage to Animal Cells of Industrial Relevance: Current Understanding. *Cytotechnology,* 63(5):445-60. DOI 10.1007/s10616-011-9368-3.
21. Moon S, Hasan SK, Song YS, *et al*., 2010, Layer by Layer Three-dimensional Tissue Epitaxy by Cell-laden Hydrogel Droplets. *Tissue Eng Part C Methods,* 16(1):157-66. DOI 10.1089/ten.tec.2009.0179.
22. Koch L, Deiwick A, Schlie S, *et al*., 2012, Skin Tissue Generation by Laser Cell Printing. *Biotechnol Bioeng,* 109(7):1855-63.
23. Malda J, Visser J, Melchels FP, *et al*., 2013, 25th Anniversary Article: Engineering Hydrogels for Biofabrication. *Adv Mater,* 25(36):5011-28. DOI 10.1002/adma.201302042.
24. Jungst T, Smolan W, Schacht K, *et al*., 2016, Strategies and Molecular Design Criteria for 3D Printable Hydrogels. *Chem Rev,* 116(3):1496-539. DOI 10.1021/acs.chemrev.5b00303.

RESEARCH ARTICLE

# Multicomponent bioprinting of heterogeneous hydrogel constructs based on microfluidic printheads

**Fan Feng[1,2], Jiankang He[1,2]*, Jiaxin Li[1,2], Mao Mao[1,2], Dichen Li[1,2]**

[1]State Key Laboratory for Manufacturing Systems Engineering, Xi'an Jiaotong University, Xi'an 710049, China
[2]Rapid Manufacturing Research Center of Shaanxi Province, Xi'an Jiaotong University, Xi'an, 710049, China

**Abstract:** Multimaterial bioprinting provides a promising strategy to recapitulate complex heterogeneous architectures of native tissues in artificial tissue analogs in a controlled manner. However, most of the existing multimaterial bioprinting techniques relying on multiple printing nozzles and complicate control program make it difficult to flexibly change the material composition during the printing process. Here, we developed a multicomponent bioprinting strategy to produce heterogeneous constructs using a microfluidic printhead with multiple inlets and one outlet. The composition of the printed filaments can be flexibly changed by adjusting volumetric flow rate ratio. Heterogeneous hydrogel constructs were successfully printed to have predefined spatial gradients of inks or microparticles. A rotary microfluidic printhead was used to maintain the heterogeneous morphology of the printed filaments as the printing path direction changed. Multicellular concentric ring constructs with two kinds of cell types distribution in the printed filaments were fabricated by utilizing coaxial microfluidic printhead and rotary collecting substrate, which significantly improves the printing efficiency for multicomponent concentric structures. The presented approach is simple and promising to potentially print multicomponent heterogeneous constructs for the fabrication of artificial multicellular tissues.

**Keywords:** multicomponent printing; microfluidic printhead; bioprinting; heterogeneous constructs

*Correspondence to: Jiankang He, State key Laboratory for Manufacturing Systems Engineering, Xi'an Jiaotong University, Xi'an 710049, China; jiankanghe@mail.xjtu.edu.cn

**Received:** April 26, 2019; **Accepted:** June 4 2019; **Published Online:** July 1 2019

**Citation:** Feng F, He J, Li J, *et al*., 2019, Multicomponent bioprinting of heterogeneous hydrogel constructs based on microfluidic printheads. Int J Bioprint, 5(2): 202. http://dx.doi.org/10.18063/ijb.v5i2.202

## 1. Introduction

Recent achievements in bioprinting have showed significant promise in fabricating artificial tissues to meet the increasing demands for tissue engineering and drug screening[1,2]. The most prevailing bioprinting techniques are based on jetting and extrusion, which have less damage to cells during printing and widely adopted to produce structures mimicking native tissues[3-6]. However, native tissues are extremely complicated in both architectures and cell compositions. Extrusion-based printing with a single printhead cannot meet the increasing demands for complex tissues with multiple cell types. To address this challenge, multimaterial printing strategies are developed by incorporating multiple separated printheads to print several kinds of inks[7-14]. During printing, different inks can be deposited at predefined positions through switching the printheads. However, as types of inks increase, the number of printheads in a printing system increases correspondingly, which brings complexity of design and printing control. The printing efficiency and accuracy might be negatively affected due to the switching of different printhead. In addition, it is almost impossible to continuously change the concentrations of various inks during the printing process.

Microfluidics showed great advantages in manipulating multiple types of material flows by flexibly designing internal microchannel networks, which provide a promising way to achieve multimaterial bioprinting in a relatively simple manner[15-22]. Amir *et al*. designed a stereolithography-based bioprinting platform which

Multicomponent bioprinting of heterogeneous hydrogel constructs based on microfluidic printheads © 2019 Feng, *et al*. This is an Open Access article distributed under the terms of the Creative Commons Attribution-NonCommercial 4.0 International License (http://creativecommons.org/licenses/by-nc/4.0/), permitting all non-commercial use, distribution, and reproduction in any medium, provided the original work is properly cited.

used a microfluidic device to fabricate multicomponent hydrogel constructs. It enabled different bioinks flow into the microfluidic device and cross-link by ultraviolet[23]. Ghorbanian *et al*. developed a microfluidic direct writer who is capable of alternatively delivering two different alginate gel solutions during the fabrication three-dimensional (3D) hydrogel constructs[24]. Hardin *et al*. developed a microfluidic printhead for the printing of multiple viscoelastic inks such as polydimethylsiloxane (PDMS) and investigated the interface of two inks during printing[25]. However, the effect of laminar flow within the printhead and proportion of flow rate are neglected, which can change the morphology of the printed heterogeneous filaments and further influence printing controllability.

Here, we developed a multicomponent bioprinting system based on microfluidic printhead with three inlets and one outlet, which enables simultaneous multicomponent extrusion and printing of heterogeneous constructs through only one printhead. During the printing process, different inks were connected to different inlets of the printhead and simultaneously or alternatively extruded through the same outlet. We mainly studied spatially controlled distribution of different inks when altering the proportion of volumetric flow rate of different inlets in printing process. In this way, heterogeneous filaments and constructs can be printed along which diverse materials could be spatiotemporally coded. In addition, a rotating motor was added into printing system for printing heterogeneous filament along different printing directions and a coaxial printhead was developed to improve the cross-linking. It could be a possible way to create macro-microscopic integrative multicomponent constructs mimicking native tissues with multiple cells.

## 2. Materials and Methods

### 2.1 Materials

Polydimethylsiloxane (PDMS, Sylgard 184) was obtained from Dow Corning (Midland, MI, USA). Alginate with medium viscosity was purchased from Sigma Aldrich (St. Louis, MO, USA). Calcium chloride powder was bought from Aladdin (Shanghai, China). Agarose powder with low melting temperature (87–89°C) was bought from Biowest (Spain). Green fluorescent particles with a particle size of 10 μm and red fluorescent particles with particle size of 10 μm and 3.2 μm were purchased from Base Line (Tianjin, China). Red/green/blue/yellow pigment was purchased from M and G (China). Alginate solutions with different concentration of 1%, 2%, and 3% (w/v) were prepared by dissolving alginate powder into distilled water or culture medium. About 2% (w/v) agarose solution with 2% (w/v) calcium chloride was prepared by dissolving agarose and calcium chloride powders into distilled water at 100°C. After boiling, agarose solution was poured in a Petri dish and cooled down to form a flat agarose hydrogel with a thickness of 3 mm as the collecting substrate. For cell printing, GFP expressing human umbilical vein endothelial cells (GFP-HUVEC; ATCC, Manassas, VA, USA) and red fluorescent protein embryonic rat cardiomyocytes (H9C2, ATCC, Manassas, VA, USA) were added into 3% alginate solution with a density of $5 \times 10^5$ cells $mL^{-1}$.

### 2.2 Design and Fabrication of Microfluidic Printhead for Multicomponent Printing

The microfluidic printhead was designed to have three inlets and an outlet as shown in Figure 1A. The width ($w_1$) and height ($h_1$) of the inlet channels are 200 μm. The width ($w_2$) and the height ($h_2$) of the outlet channel are 300 μm and 200 μm, respectively. The length of different channels is $l_1$=5 mm and $l_2$=3 mm, respectively. To fabricate the microfluidic printhead, two PDMS components with semi-channels were created by casting PDMS in the designed molds printed by stereolithography technique. During the cast process, the PDMS components were vacuum treated to remove any bubbles and cured at 65ºC for a minimum of 2 h. Then, they were bonded together after oxygen plasma treatment. Finally, the capillary nozzle was inserted into the cylindrical channel (Figure S1, supporting information). The diameter ($d_1$) and the length ($l_3$) of the nozzle is 200 μm and 12 mm. Figure 1B schematically illustrates components of the microfluidic printhead and the fabricated microfluidic printhead is shown in Figure 1C.

### 2.3 Multicomponent Printing Platform Based on Microfluidic Printhead

The microfluidic printhead was connected with a rotating motor and then mounted on the z moving stage (Xiamen Heidelstar Co., China). Different alginate inks were separately loaded into 1 mL syringes, respectively, and the flow rate was controlled by a syringe pump (TJ-2A, Longer Pump, Baoding, China). Each syringe was connected to different inlets of the printhead through PTEE soft tubes. Agarose hydrogel with calcium ions was placed on the x-y moving stage (Xiamen Heidelstar Co., China) as the collecting substrate (Figure 1D and E). The distance between the nozzle tip and the collecting substrate was fixed at 100 μm. During printing, different inks were pushed into the separate inlets and then extruded out of the printhead through the same nozzle. The proportion of different inks in printed filaments was adjusted by controlling the volumetric flow ratio when the total volume flow rate of all inlets was fixed. A 3D structure with different materials can be printed by precisely stacking the filaments in a layer-by-layer manner.

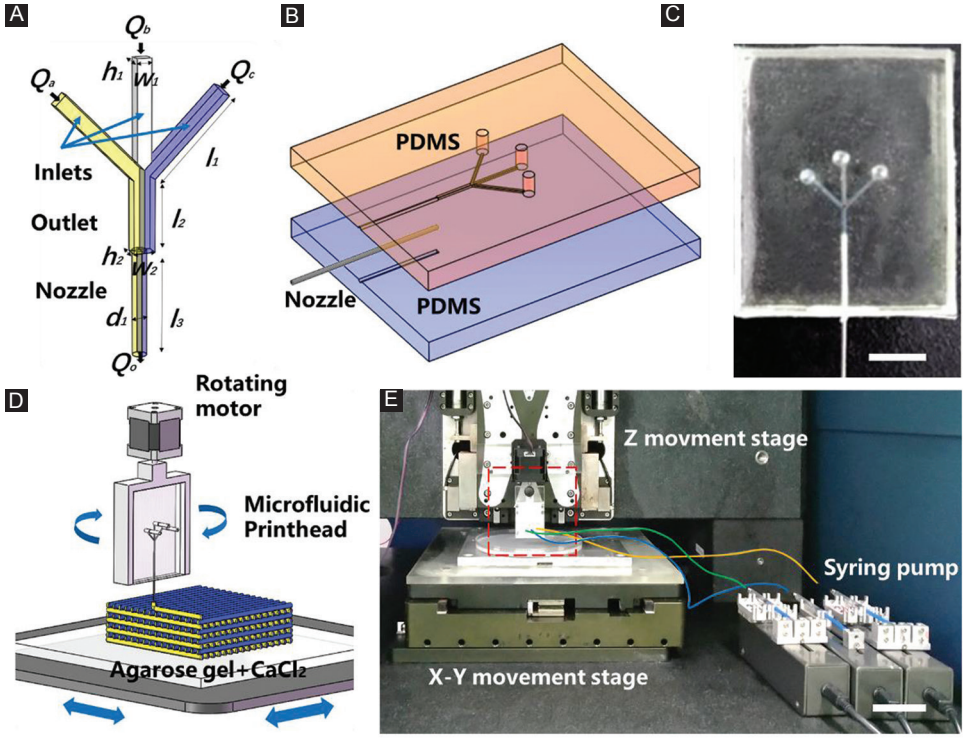


**Figure 1.** Design of microfluidic printhead for multicomponent bioprinting. (**A**) Schematic illustration of microfluidic printheads with multiple inlets and an outlet. (**B**) The assembly of the printhead. (**C**) Photograph of the fabricated microfluidic printhead. Scale bar=5 mm. (**D** and **E**) Schematic and photograph of multicomponent bioprinting platform with microfluidic printhead. Scale bar=5 cm.

## 2.4 Printing of Heterogeneous Filaments

The effect of volumetric flow ratio of different inks on the composition of heterogeneous filament was studied. To code compositions in single printed filament, 3% alginate solutions mixed with green and yellow pigments were used and the flow rate of each inlet was independently controlled by a multichannel syringe pump system. The volumetric flow ratio of two kinds of inks ($Q_1$:$Q_2$) was gradually changed from 3:7 to 7:3 when the total flow rate was 600 μL/h and the speed of moving stage was fixed at 5 mm/s. The line width of different compositions within a single filament was measured, respectively, and the ratio of them was compared with the proportion of flow rate ($Q_1$:$Q_2$). The filaments with three kinds of inks can also be printed by injecting alginate solution with green fluorescent beads through the middle inlet and alginate solution with red fluorescent beads through the left and right inlets. The flow rate of the middle inlet was changed from 200 μL/h to 120 μL/h when the total flow rate of the three inlets was kept at 600 μL/h.

## 2.5 Printing of Multilayer Heterogeneous Constructs

To demonstrate the ability of microfluidic printhead to print heterogeneous constructs, a heterogeneous grid was printed by altering the proportion of flow rate of different 3% alginate solutions mixed with black and white pigment, respectively. The proportion of flow rate was changes from $Q_{black}$: $Q_{white}$=0:1 to $Q_{black}$: $Q_{white}$=1:0. In a similar way, 3% alginate solutions mixed with yellow and blue pigment were chosen to fabricate heterogeneous parallel and multilayered grid constructs. When printing the heterogeneous parallel construct, the proportion of flow rates was altered every 10 lines ($Q_{blue}$:$Q_{yellow}$=2:1, 1:1, 1:2, and 0:1). During the printing of multilayer heterogeneous construct, the proportion of flow rate was changed every two layers ($Q_{blue}$:$Q_{yellow}$=0:1, 1:3, 1:1, 3:1, and 1:0).

To quantitatively analyze and simulate the distribution of different cells in one construct, a coded compositional gradient structure was printed. Green and red fluorescent particles (10 μm) were added into 3% alginate solution and printed by the microfluidic printhead. During printing, the proportion of their flow rate was changed every four layers ($Q_{total}$=600 μL/h, $Q_{red}$: $Q_{green}$=0:1, 1:2, 1:1, 2:1, and 1:0). The fluorescent profiles of the printed constructs were reconstructed using a confocal laser scanning microscope (OLS4000, Olympus, USA). The number of fluorescent particles in specific layers with different flow rate proportion was quantified by ImageJ software.

## 2.6 Design of Coaxial Microfluidic Printhead for 3D Multicellular Constructs

To realize the instant cross-linking of the printed filaments for the fabrication of 3D constructs, a coaxial

microfluidic printhead was developed. Two kinds of 3% alginate solutions were loaded into two syringes and injected into the printhead at the same flow rate of 300 μL/h. The collecting substrate was fixed on a rotating motor, which was mounted on the x-y moving stage. During the printing process, the collecting substrate was rotating and the heterogeneous filaments were deposited to form a layer of concentric ring structure. Multilayer structures can be obtained by repeating this process in a layer-by-layer manner and simultaneously moving up the nozzle to a certain distance after the completion of each layer printing. The diameter of the ring was determined by eccentric distance between axes of the nozzle and the rotating motor. A multicellular concentric ring was printed using two kinds of inks mixed with HUVECs and H9C2s, respectively.

## 3. Results and Discussion

### 3.1 Printing of Heterogeneous Filaments

Unlike laminar flow of two solutions in microfluidic channel, the printing of heterogeneous filaments with microfluidic printhead will subsequently experience deposition and cross-linking processes as shown in Figure 2A. To investigate the effect of these processes on the filament morphology and composition, two kinds of 3% alginate solutions mixed with different color were injected into the microfluidic printhead and extruded from the same outlet. Figure 2B, C, D, E, F illustrates the printed heterogeneous filaments as the flow rate ratio of the two solutions was gradually changed. When the total volumetric flow rate was 600 μL/h, the width of printed filaments was 250±8.89 μm. Since the viscosity of the two solutions was similar, the variation of flow rate ratio had little effect on the filament size. There was a clear boundary of two colored inks in the printed filament. The proportion of two colored materials was approximately equal to that of the flow rate (Figure 2G). This verified that the deposition and cross-linking processes will not affect the printing of heterogeneous filaments. Figure 2H, I, J shows fluorescent images of the filaments printed by injecting different ink from three inlets. As the flow rate of the solution in the middle inlet increased, the number of green fluorescent microbeads in the printed filament increased correspondingly (Figure 2K). Such capability can potentially find various biomedical applications such as accurate patterning of multiple cell types in a single hydrogel filament.

We further investigated the influence of solution viscosity on the morphology of heterogeneous filaments

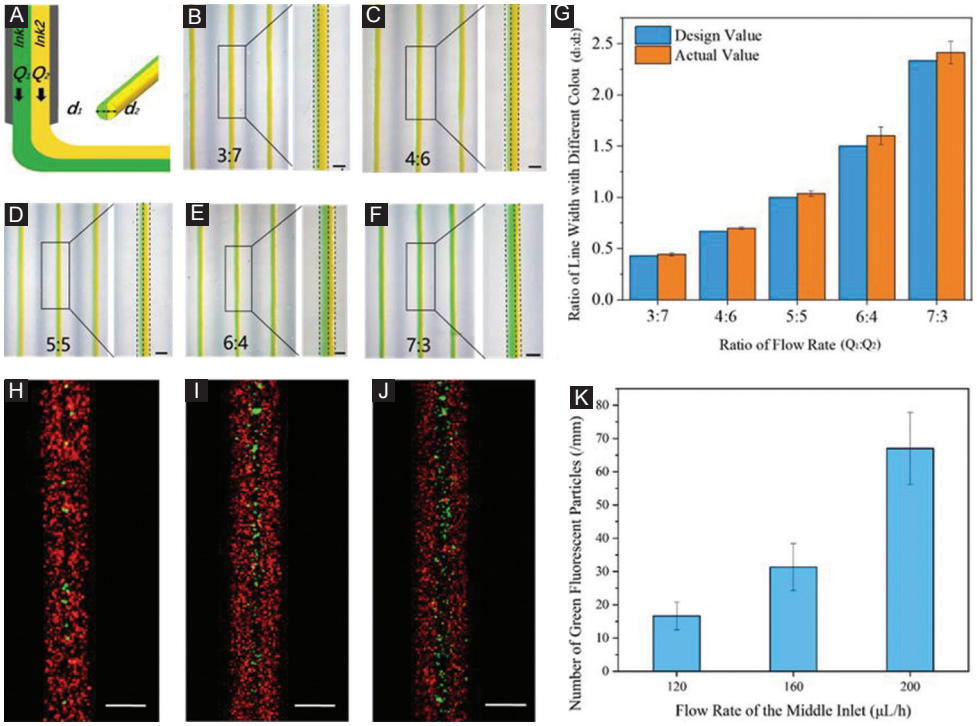


**Figure 2.** Printing of heterogeneous filaments by changing flow rate ration of different solutions in the microfluidic printhead. (**A**) Schematic for the deposition of heterogeneous filaments from the microfluidic printhead. (**B**, **C, D, E**, **F**) Microscopic images of heterogeneous filaments printed by changing the flow rate ratio of two solutions. Scale bar=200 μm. (**G**) Quantification of the composition distribution of two inks in the printed filaments. (**H, I, J**) Fluorescent images of the heterogeneous filaments printed through the three inlets with different flow rate of middle inlet. Scale bar=200 μm. (**K**) Quantification of the number of green fluorescent particles at different flow rate of the middle inlet.

by injecting 3% alginate solution (high viscosity) and 1% alginate solution (low viscosity) into the microfluidic printhead simultaneously (Figure 3). It was found that the ink viscosity significantly affected the flow pattern in the microfluidic channel and further changed the spatial distribution of different bioinks in the printed filament. When two kinds of solutions were initially injected into the printhead at the same flow rate, only a small proportion of low-viscous ink flowed into the outlet channel and gradually diffused into the high-viscous side along the flow direction forming a slanted interface (Figure 3C). When the two inks were extruded out from the nozzle, low-viscous ink was found to fully cover the surface of high-viscous inks (Figure 3D). Parallel heterogeneous filaments were not clearly formed even when the flow rate of low-viscous solution gradually increased (Figure S2A, B, C, D). This implied that the presented multicomponent bioprinting is applicable to the inks with similar viscosity. The previous studies indicated that when the fluids have various viscosities, multiphase flow (liquid-liquid two phase) occurs[26-31]. Since most of the bioinks are miscible fluid and surface tension, diffusivity at the interface is an important factor to regulate the flow pattern[32].

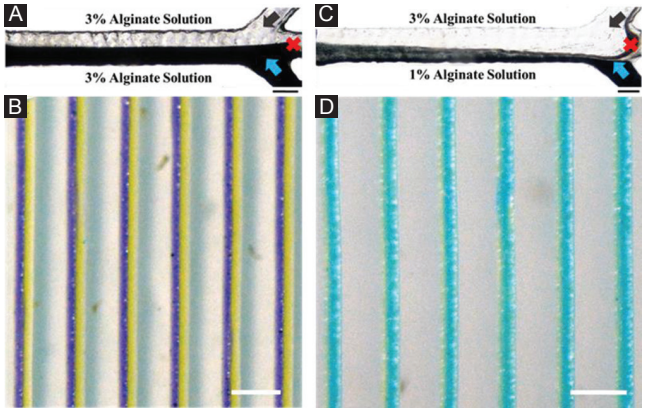


**Figure 3.** Flow pattern and printed filaments of alginate solution with different viscosities. (**A**) Injecting 3% alginate solution (high viscosity) simultaneously and (**B**) printed heterogeneous filaments. (**C**) Injecting 3% alginate solution and 1% alginate solution and (**D**) printed filaments. Scale bars are 200 μm and 1 mm.

### 3.2 Printing of Constructs With Graded Component Composition

Figure 4A demonstrated a 2D filament pattern with gradually changed ink proportion by continuously varying the flow rate ratio of two color-coded inks from 2:1 to 0:1 during printing. A grid pattern with five layers was printed with continuous changed composition as shown in Figure 4B. For each layer, the color of the printed filaments gradually changed from black to white through dynamically adjusting the flow rate of each inlet. Figure 4C schematically illustrates the printing of a multilayered construct with serials of color coding. By sequentially printing two kinds of colored inks with five different flow rate ratios, a vertically gradient structure with 10 layers was finally printed and color of the specific layer was gradually changed from yellow to green and finally to blue as shown in Figure 4D, E, F, G, H.

The microfluidic printhead can also be potentially used to fabricate gradient multicellular 3D constructs. As a proof of concept, fluorescent microparticles with a similar size to living cells were used to demonstrate the feasibility. As schematically shown in Figure 5A, the concentration of green fluorescent particles gradually decreased while that of red fluorescent particles increased from the bottom layer to the top layer by dynamically changing the flow rate ratio of two kinds of inks from 1:0 to 0:1 during printing. Figure 5B illustrates the actual spatial distribution of green and red fluorescent particles within the printed grid hydrogel structure, which are accordant with the predefined situation. Figure 5C, D, E, F, G shows the representative distribution of fluorescent particles within different heights ranging from 65 μm to 585 μm with spacing of 130 μm, which related to the layers consisted of different ink proportion. To quantitatively evaluate the spatial distribution of fluorescent particles, the number of green and red fluorescent particles within these specific heights was counted as shown in Figure 5H. It indicates that the ratio of green and red particles was approximately equal to the ratio of flow rate of two kinds of inks within the printhead, which can finally achieve the spatial gradient distribution of the particles as designed. The unique advantage of this method is that it can generate multicellular constructs with spatiotemporal cell positioning in a controllable manner. These kinds of heterogeneous constructs have the potential to meet the demand of biological scaffold involving different kinds of matrix. Together these results demonstrated the unique ability to continuously print heterogeneous construct in both horizontal and altitude direction without interrupt, which could be an efficient and promising method to create constructs with different properties and functions.

Although the switching process among different printheads is avoided using microfluidic printhead, the transition time to change the proportion of the inks exists during the printing process, which means when changing the flow rates through the syringes, the proportion of inks in the printhead cannot be switched simultaneously. It was found that both flow rate and the concentration influence the transition time (Figure S3 and S4). For inks of alginate solution with concentration ranging from 1% to 3%, all of their transition time decreased with the increase of the flow rate. However, there existed a great drop for the 3% alginate solution, whose transition time was about 430 s at the flow rate of 100 μL/h and about 50 s at the flow rate of 1000 μL/h. For the 1% alginate solution, the transition

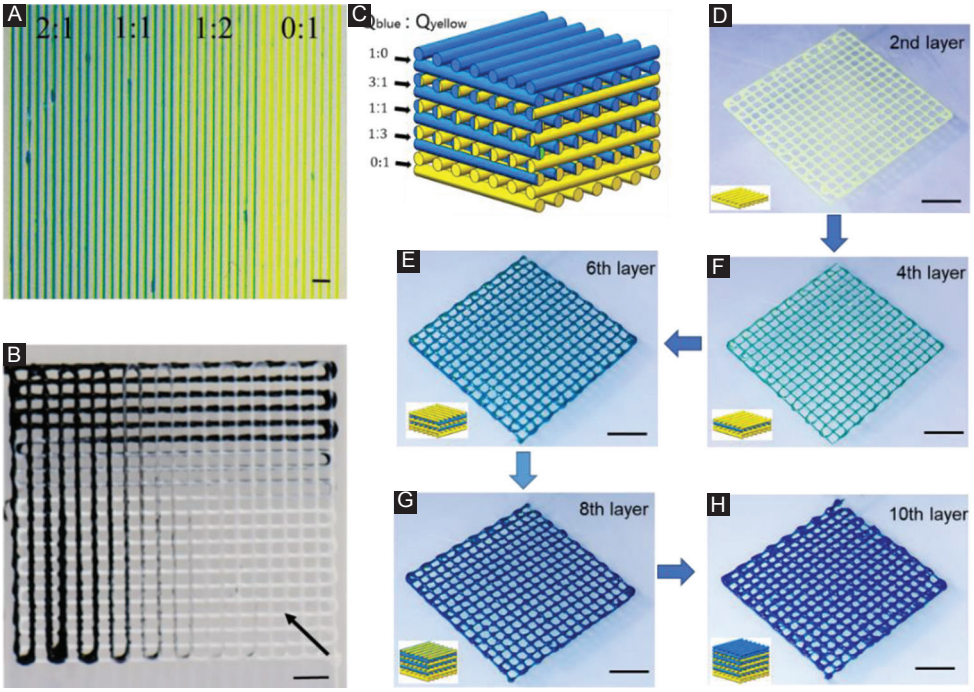


**Figure 4.** Color-coded heterogeneous constructs. (**A** and **B**) Dynamically altering the proportion of different inks during printing. (**C**) Schematic of color-coded gel structure (10 layers) printed under different proportion of flow rate ($Q_{total}$=600 µL/h, $Q_{blue}$: $Q_{yellow}$=0:1, 1:3, 1:1, 3:1, and 1:0) changed per two layers. (**D, E, F, G, H**) Photograph showing a gradient of colors from yellow to blue during printing. Scale bar=2 mm.

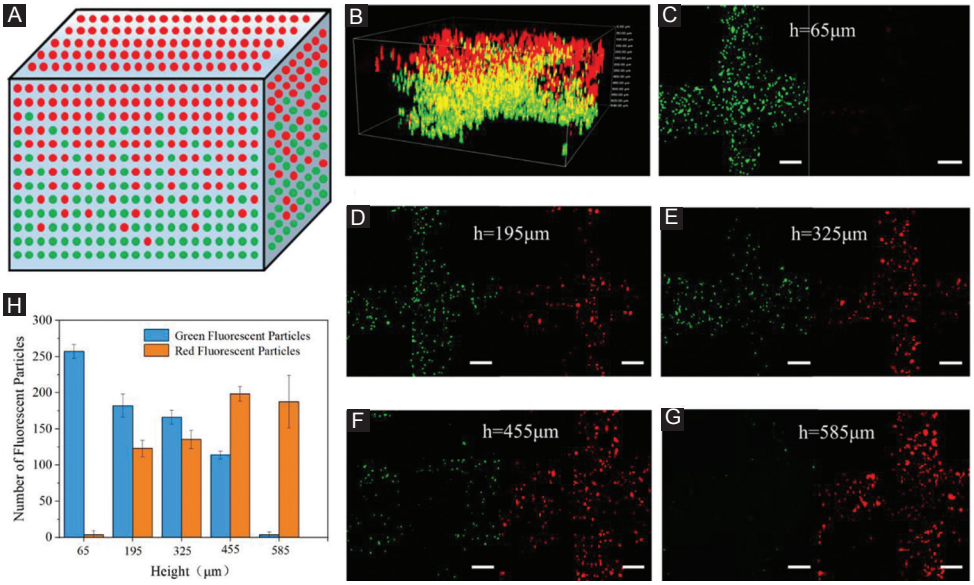


**Figure 5.** Heterogeneous constructs containing red and green fluorescent microparticles. (**A**) Schematic of distribution of green/red fluorescent particles in printed constructs. (**B**) The 3D fluorescence profile of local part of the printed constructs. (**C, D, E, F, G**) The representative distribution of green/red fluorescence particles at the different heights of the printed construct. Scale bar=100 µm. (**H**) Quantification of green/red fluorescence particles at different heights in hydrogel structure.

time was below 50 s at the flow rate of 100 µL/h and 1000 µL/h. The effect of concentration on the transition time might be due to the different viscosity of the alginate solution, which will produce different resistance for ink transition. Thus, the optimum flow rate (600 µL/h) was chose and proportion of flow rate was changed in advance before the designed position. For achieving real-time transition among different inks, integrating small pneumatic valves into microfluidic printhead might be a possible way in the future work.

### 3.3 Rotating Microfluidic Printhead

As shown in Figure 6A, multicomponent filaments with half-green and half-yellow color can be obtained along the printing direction using microfluidic printhead. However, when the printing direction was changed with 90° to print the next layer of the grid structure, the filaments changed from the left-right multicolor into the top-bottom multicolor. To address this issue, a rotating motor was introduced to this printing system, which enabled the printhead to rotate with the designed angles during the printing process for creating heterogeneous filaments along different directions. Figure 6B shows a grid structure consisting of the filaments with left-right multicolor along the different directions, which is achieved by rotating printhead with 90° as designed during the printing process. Furthermore, a triangular pattern with heterogeneous filaments along three directions and a grid structure coded with three compositions within the filaments was printed through rotating printhead (Figure 6C and D). It could provide a way to create a heterogeneous constructs for bioengineering research, such as controlling of cell distribution and study of the interaction among different types of cells.

### 3.4 Printing of Multicellular Constructs Using Coaxial Microfluidic Printheads

To cross-link the printed hydrogel filament during the printing process, a coaxial microfluidic printhead was designed and added into the printing system, as shown in Figure 7A and B. The inner and outer channels were used to deliver the hydrogel ink solution and cross-linking solution independently. The gelation of the inks took place at the tip of the inner nozzle, where these two kinds of solution met. Here, alginate hydrogel solution was printed, which underwent instantaneous gelation when exposed to calcium ions solution. Figure 7C shows the 25-layer heterogeneous hydrogel constructs successfully printed by coaxial printhead.

To improve efficiency of printing multicomponent concentric ring, a rotary substrate was introduced here (Figure 7D). During the printing process, the printhead

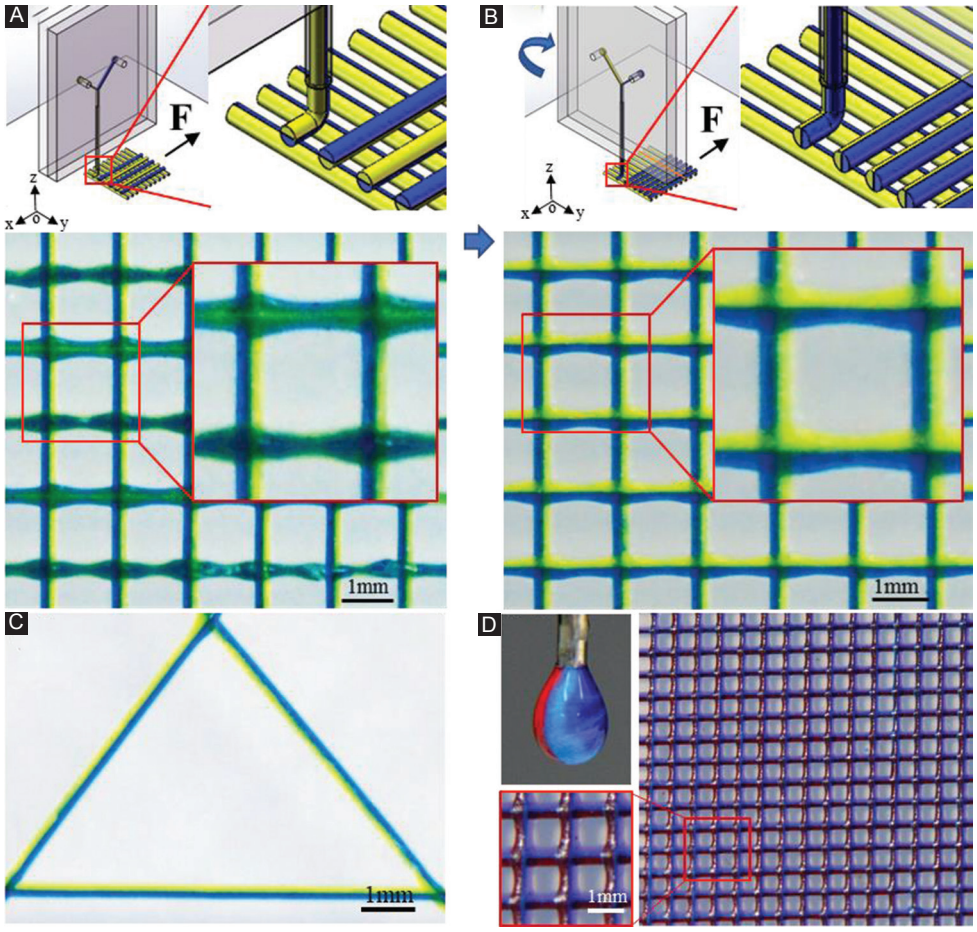


**Figure 6.** Printing of multicomponent grid structure using rotating microfluidic printhead. (**A**) Schematic and photograph illustrating printed grid structure without the rotating printhead. (**B**) Schematic and photograph illustrating printed grid structure with the rotating printhead. (**C**) Printed triangular pattern with the rotating printhead. (**D**) Grid structure consists of heterogeneous filaments (red, blue, and purple).

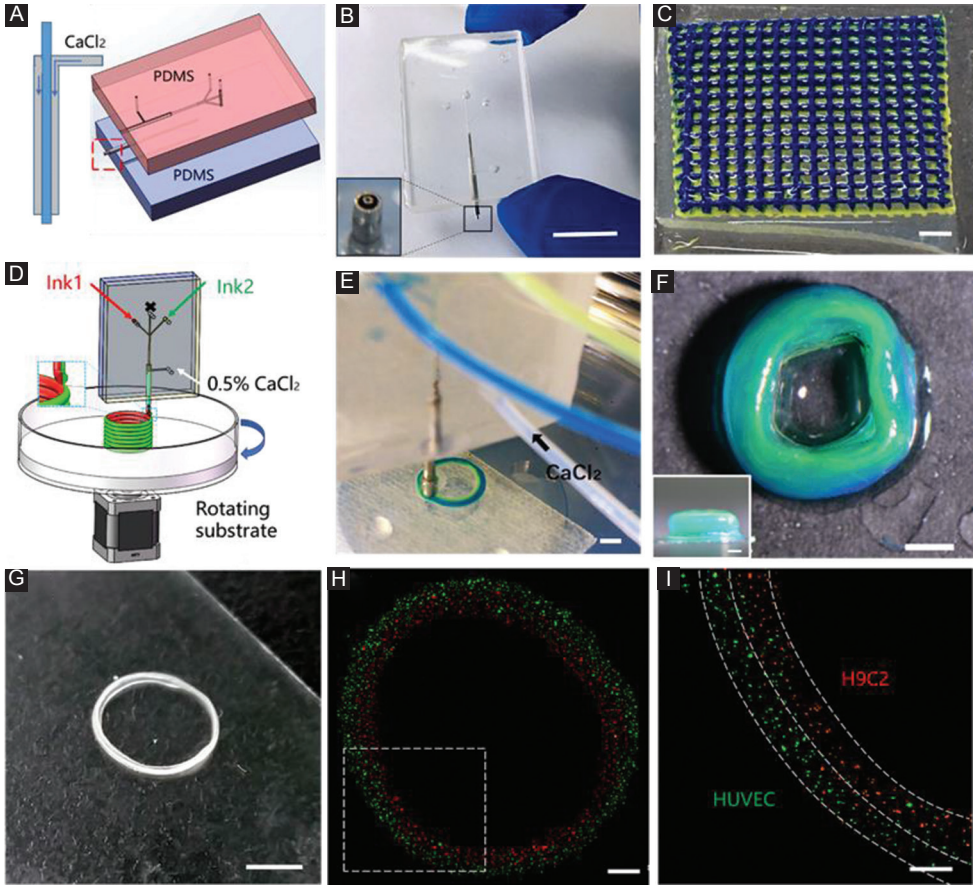


**Figure 7.** Printing heterogeneous constructs through coaxial microfluidic printheads. (**A**) Schematic of the coaxial microfluidic printhead. (**B**) Photograph of the coaxial microfluidic printhead. Scale bar=1 cm. (**C**) Heterogeneous grid structure (25 layers) printed through using the coaxial microfluidic printhead. Scale bar=2 mm. (**D**) Schematic of rotating substrate for creating concentric ring "on-the-fly." (**E** and **F**) Fabrication of a heterogeneous concentric ring. Scale bars are 2 mm and 1 mm, respectively. (**G**) Fabrication of multicellular (H9C2 and HUVEC) concentric rings through coaxial microfluidic printhead. Scale bar=4 mm. (**H** and **I**) Fluorescence microscopy image (top view) of multicellular rings. Scale bars are 1 mm and 500 μm, respectively.

did not move while the collecting substrate rotated along printhead as the center. Figure 7E and F shows a heterogeneous concentric ring with the yellow-coded and green-coded alginate hydrogel at the inner and outer side, respectively. As a proof of concept, a multicellular concentric ring was fabricated "on-the-fly" with the diameter of about 8 mm (Figure 7G). Most of the red H9C2s distributed at the inner side, while green HUVECs mainly distributed at the outer side (Figure 7H and I). This printing method shows the promise to fabricate artificial vessels with multilayer in an "on-the-fly" way, especially those with large diameters such as the inferior vena cava whose internal diameter is approximately from 1.7 cm to 2 cm.

## 4. Conclusion

Here, we demonstrated a multicomponent bioprinting technique based on microfluidic printheads for printing heterogeneous constructs. The microfluidic printhead enables printing of heterogeneous filaments and constructs spatially incorporated with different materials such as particles and cells. Moreover, the constructs consisting of continuous compositional gradient can be fabricated by dynamically altering the flow rates during printing, which is difficult for the multicomponent system with separated printheads to achieve. It was found that the rotating printhead enabled printing the filaments of heterogeneous morphology along different printing directions. The coding of diverse materials on the printed filaments could offer a new way to create functional constructs. Coaxial microfluidic printheads could significantly improve the cross-linking condition. Further exploration of printing multimaterial/cellular concentric rings through the rotating collecting substrate will allow fabrication of artificial vessels efficiently. The proposed method is able to print heterogeneous construct with different components as designed flexibly, which shows promise for a various applications including tissue engineering and soft robots.

## Acknowledgments

This work was supported by the National Natural Science Foundation of China (51675412), Shaanxi Key Research and Development Program (2017ZDXM-GY-058), the Youth Innovation Team of Shaanxi Universities and the Fundamental Research Funds for the Central Universities.

## References

1. Seidi A, Ramalingam M, Elloumi-Hannachi I, *et al.*, 2011, Gradient Biomaterials for Soft-to-hard Interface Tissue Engineering. *Acta Biomater*, 7(4):1441-51. DOI 10.1016/j.actbio.2011.01.011.
2. Khademhosseini A, Langer R, Borenstein J, *et al.*, 2006, Microscale Technologies for Tissue Engineering and Biology. *Proc Natl Acad Sci U S A*, 103(8):2480-7.
3. Sakai S, Ueda K, Gantumur E, *et al.*, 2018, Drop-on-drop Multimaterial 3D Bioprinting Realized by Peroxidase-mediated Cross-linking. *Macromol Rapid Commun*, 39(3):1700534. DOI 10.1002/marc.201700534.
4. Colosi C, Costantini M, Barbetta A, *et al.*, 2016, Microfluidic Bioprinting of Heterogeneous 3D Tissue Constructs. *Adv Mater*, 28(4):677-84. DOI 10.1002/adma.201503310.
5. Rutz AL, Hyland KE, Jakus AE, *et al.*, 2015, A Multimaterial Bioink Method for 3D Printing Tunable, Cell-compatible Hydrogels. *Adv Mater*, 27(9):1607-14. DOI 10.1002/adma.201405076
6. Kang HW, Sang JL, Ko IK, *et al.*, 2016, A 3D Bioprinting System to Produce Human-scale Tissue Constructs with Structural Integrity. *Nat Biotechnol*, 34(3):312-9. DOI 10.1038/nbt.3413.
7. Khalil S, Nam J, Sun W, 2005, Multi-nozzle Deposition for Construction of 3D Biopolymer Tissue Scaffolds. *Rapid Prototyp J*, 11(1):9-17. DOI 10.1108/13552540510573347.
8. Shim JH, Lee JS, Kim JY, *et al.*, 2012, Bioprinting of a Mechanically Enhanced Three-dimensional Dual Cell-laden Construct for Osteochondral Tissue Engineering using a Multi-head Tissue/Organ Building System. *J Micromech Microeng*, 22(8):85014-24. DOI 10.1088/0960-1317/22/8/085014.
9. Edward K, Gi Seok J, Young CY, *et al.*, 2011, Digitally Tunable Physicochemical Coding of Material Composition and Topography in Continuous Microfibres. *Nat Mater*, 10(11):877.
10. Pati F, Jang J, Ha DH, *et al.*, 2014, Printing Three-dimensional Tissue Analogues with Decellularized Extracellular Matrix Bioink. *Nat Commun*, 5:3935. DOI 10.1038/ncomms4935.
11. Kolesky DB, Truby RL, Sydney GA, *et al.*, 2014, 3D Bioprinting of Vascularized, Heterogeneous Cell-laden Tissue Constructs. *Adv Mater*, 26(19):2966-6. DOI 10.1002/adma.201305506.
12. Valentine AD, Busbee TA, Boley JW, *et al.*, 2017, Hybrid 3D Printing of Soft Electronics. *Adv Mater*, 29(40):1703817. DOI 10.1002/adma.201703817.
13. Lind JU, Busbee TA, Valentine AD, *et al.*, 2017, Instrumented Cardiac Microphysiological Devices via Multimaterial Three-dimensional Printing. *Nat Mater*, 16(3):303-8. DOI 10.1038/nmat4782.
14. Sutanto E, Shigeta K, Kim YK, *et al.*, 2012, A Multimaterial Electrohydrodynamic Jet (E-jet) Printing System. *J Micromech Microeng*, 22(4):45008-18. DOI 10.1088/0960-1317/22/4/045008.
15. Cheng Y, Zheng F, Lu J, *et al.*, 2014, Bioinspired Multicompartmental Microfibers from Microfluidics. *Adv Mater*, 26(30):5184-90. DOI 10.1002/adma.201400798.
16. Jun Y, Kang E, Chae S, *et al.*, 2014, Microfluidic Spinning of Micro-and Nano-scale Fibers for Tissue Engineering. *Lab Chip*, 14(13):2145-60. DOI 10.1039/c3lc51414e.
17. Kang E, Jeong GS, Choi YY, *et al.*, 2011, Digitally Tunable Physicochemical Coding of Material Composition and Topography in Continuous Microfibres. *Nat Mater*, 10(11):877. DOI 10.1038/nmat3108.
18. Ouyang L, Highley CB, Sun W, *et al.*, 2017, A Generalizable Strategy for the 3D Bioprinting of Hydrogels from Nonviscous Photo-crosslinkable Inks. *Adv Mater*, 29(8):1604983. DOI 10.1002/adma.201604983.
19. Shi X, Ostrovidov S, Zhao Y, *et al.*, 2015, Microfluidic Spinning of Cell-responsive Grooved Microfibers. *Adv Funct Mater*, 25(15):2250-9. DOI 10.1002/adfm.201404531.
20. Yu Y, Shang L, Gao W, *et al.*, 2017, Microfluidic Lithography of Bioinspired Helical Micromotors. *Angew Chem Int Ed*, 56(40):12127-31. DOI 10.1002/anie.201705667.
21. Yu Y, Wei W, Wang Y, *et al.*, 2016, Simple Spinning of Heterogeneous Hollow Microfibers on Chip. *Adv Mater*, 28(31):6649. DOI 10.1002/adma.201601504.
22. Zhu Y, Wang L, Yin F, *et al.*, 2017, A Hollow Fiber System for Simple Generation of Human Brain Organoids. *Integr Biol*, 9(9):774-81. DOI 10.1039/c7ib00080d.
23. Miri AK, Nieto D, Iglesias L, *et al.*, 2018, Microfluidics-enabled Multimaterial Maskless Stereolithographic Bioprinting. *Adv Mater*, 30(27):e1800242. DOI 10.1002/adma.201800242.
24. Ghorbanian S, Qasaimeh MA, Akbari M, *et al.*, 2014, Microfluidic Direct Writer with Integrated Declogging Mechanism for Fabricating Cell-laden Hydrogel Constructs. *Biomed Microdevices*, 16(3):387-95. DOI 10.1007/s10544-

014-9842-8.

25. Hardin JO, Ober TJ, Valentine AD, *et al.*, 2015, 3D Printing: Microfluidic Printheads for Multimaterial 3D Printing of Viscoelastic Inks. *Adv Mater*, 27(21):3279-84. DOI 10.1002/adma.201570145.
26. Zhao Y, Chen G, Quan Y, 2010, Liquid–liquid Two-phase Mass Transfer in the T-junction Microchannels. *AIChE J*, 53(12):3042-53. DOI 10.1002/aic.11333.
27. Kakavandi FH, Rahimi M, Jafari O, *et al.*, 2016, Liquid–liquid Two-phase Mass Transfer in T-type Micromixers with Different Junctions and Cylindrical Pits. *Chem Eng Process Process Intensification*, 107:58-67. DOI 10.1016/j.cep.2016.06.011.
28. Pandey S, Gupta A, Chakrabarti DP, *et al.*, 2006, Liquid–liquid Two Phase Flow Through a Horizontal T-junction. *Chem Eng Res Des*, 84(10):895-904. DOI 10.1205/cherd05061.
29. Kamholz AE, Weigl BH, Finlayson BA, *et al.*, 1999, Quantitative Analysis of Molecular Interaction in a Microfluidic Channel: The T-sensor. *Anal Chem*, 71(23):5340-7. DOI 10.1021/ac990504j.
30. Ameya J, 2011, Numerical Simulation of Immiscible Liquid-liquid Flow in Microchannels using Lattice Boltzmann Method. *Sci China Chem*, 54(1):244-56. DOI 10.1007/s11426-010-4164-z.
31. Chakraborty D, Bose N, Sasmal S, *et al.*, 2012, Effect of Dispersion on the Diffusion Zone in Two-phase Laminar Flows in Microchannels. *Anal Chim Acta*, 710(2):88-93. DOI 10.1016/j.aca.2011.10.040.
32. Govindarajan R, Sahu KC, 2014, Instabilities in Viscosity-stratified Flow. *Annu Rev Fluid Mech*, 46(1):331-53. DOI 10.1146/annurev-fluid-010313-141351.

RESEARCH ARTICLE

# A continuous net-like eutectic structure enhances the corrosion resistance of Mg alloys

**Cijun Shuai[1,2,3], Wenjing Yang[1,2], Youwen Yang[2], Chengde Gao[1], Chongxian He[2]*, Hao Pan[4]***

[1]State Key Laboratory of High Performance Complex Manufacturing, College of Mechanical and Electrical Engineering, Central South University, Changsha 410083, People's Republic of China
[2]Jiangxi University of Science and Technology, Ganzhou 341000, People's Republic of China
[3]Shenzhen Institute of Information Technology, Shenzhen 518172, People's Republic of China
[4]Department of Periodontics and Oral Mucosal Section, Xiangya Stomatological Hospital, Central South University, Changsha 410078, People's Republic of China

**Abstract:** Mg alloys degrade rather rapidly in a physiological environment, although they have good biocompatibility and favorable mechanical properties. In this study, Ti was introduced into AZ61 alloy fabricated by selective laser melting, aiming to improve the corrosion resistance. Results indicated that Ti promoted the formation of Al-enriched eutectic α phase and reduced the formation of β-$Mg_{17}Al_{12}$ phase. With Ti content reaching to 0.5 wt.%, the Al-enriched eutectic α phase constructed a continuous net-like structure along the grain boundaries, which could act as a barrier to prevent the Mg matrix from corrosion progression. On the other hand, the Al-enriched eutectic α phase was less cathodic than β-$Mg_{17}Al_{12}$ phase in AZ61, thus alleviating the corrosion progress due to the decreased potential difference. As a consequence, the degradation rate dramatically decreased from 0.74 to 0.24 $mg \cdot cm^{-2} \cdot d^{-1}$. Meanwhile, the compressive strength and microhardness were increased by 59.4% and 15.6%, respectively. Moreover, the Ti-contained AZ61 alloy exhibited improved cytocompatibility. It was suggested that Ti-contained AZ61 alloy was a promising material for bone implants application.

**Keywords:** eutectic α phase; net-like structure; selective laser melting; mg alloys; corrosion resistance

*Correspondence to: Dr. Chongxian He, Jiangxi University of Science and Technology, Ganzhou 341000, People's Republic of China; Tel: +86-731-84805412; Fax: +86-731-88879044; hechongxian@csu.edu.cn. Hao Pan, Department of Periodontics and Oral Mucosal Section, Xiangya Stomatological Hospital, Central South University, Changsha 410078, People's Republic of China; panhao@csu.edu.cn

**Received:** May 5, 2019; **Accepted:** June 4, 2019; **Published Online:** July 1, 2019

**Citation:** Shuai C J, Yang W J, Yang Y W, *et al.*, 2019, A continuous net-like eutectic structure enhances the corrosion resistance of Mg alloys. Int J Bioprint, 5(2): 207. http://dx.doi.org/10.18063/ijb.v5i2.207

## 1. Introduction

Mg alloys are potential bone implants in the orthopedic field due to their good biocompatibility, natural biodegradability, and similar density and Young's modulus to nature bone[1-5]. Compared with other Mg alloys, Mg-Al series alloys exhibit more favorable mechanical strength with the help of Al solid solution strengthening and precipitation strengthening, thus attracting intensive researches in recent years[6-8]. Witte *et al.*[9] investigated the degradation behavior and the bone response of Mg-Al series alloys, including AZ31 and AZ91. They reported that a small amount of Al released during the degradation could be tolerable. Wen *et al.*[10] investigated the corrosion behavior of Mg-Al series alloys and claimed that their corrosion resistances were closely related to Al content. Nevertheless, Mg-Al series alloys degrade rather rapidly in physical environments, because the high potential differences between *α*-Mg grains and *β* phase cause severe galvanic corrosion[9,10]. The rapid degradation results in a fast loss of mechanical strength, as well as a large amount of hydrogen accumulation and local alkalization, which significantly limits their clinical applications.

A workable strategy to improve the corrosion resistance is to change the component of the second

A continuous net-like eutectic structure enhances the corrosion resistance of Mg alloys © 2019 Shuai, *et al.* This is an Open Access article distributed under the terms of the Creative Commons Attribution-NonCommercial 4.0 International License (http://creativecommons.org/licenses/by-nc/4.0/), permitting all non-commercial use, distribution, and reproduction in any medium, provided the original work is properly cited.

phase toward reducing their electrochemical nobility. For example, Baek *et al.*[11] investigated the effect of Y on the corrosion behavior of Mg-Al-Ca alloy. It was found that the Y-containing phase was less cathodic and drastically weakened the galvanic corrosion tendency. Liu *et al.*[12] reported that rare earth element enhanced the corrosion resistance of AM60, because the deposited phases containing rare earth were less cathodic than $\beta$-$Mg_{17}Al_{12}$ phase. Another strategy to increase the corrosion resistance is to ameliorate the distribution of the second phase in Mg matrix. Wu *et al.*[13] confirmed that adding proper Al into Mg-Ca alloy formed a continuous second phase, which provided barrier effect, resulting in better corrosion resistance. Shuai *et al.*[14] also reported that Nd-introduced continuous second phase enhanced the corrosion resistance of Mg matrix, with the degradation rate decreased from 5.25 to 1.56 mm/y.

In this study, Ti was introduced into AZ61 to ameliorate the characterizations of precipitates, with an aim to improve the corrosion resistance. In Al-Ti-Mg system, Ti will combine with Al to form precipitates and increase the diffusivity of Al in Mg solute, resulting in the increase of Al content near the eutectic point during the solidification process[15]. Thus, it was expected that Ti could promote the formation of less cathode eutectic $\alpha$ phase, which can reduce the electrode potential differences of the matrix. On the other hand, the precipitation of eutectic $\alpha$ phase will consume Al atoms, which is conducive to reducing the formation of $\beta$-$Mg_{17}Al_{12}$ phase, thus further alleviating the galvanic corrosion in the matrix. The microstructures, mechanical properties, and corrosion behaviors of Ti contained AZ61 alloys fabricated with selective laser melting (SLM) were systematically investigated. Moreover, the biocompatibility was also studied through *in vitro* cell culture experiments.

## 2. Experimental Methods

### 2.1 Specimens Preparation

The gas-atomized AZ61 powder (Weihao Magnesium powder Ltd., China) had a particle size distribution of $d_{10}$=29.04 μm, $d_{50}$=52.68 μm, and $d_{90}$=84.71 μm. The Ti powder (Naiou Nano Science and Technology Ltd., China) had a particle size varying from 20 to 50 nm. The AZ61-*x*Ti (*x*=0, 0.25, 0.5, 0.75, and 1.0 wt.%) mixed powders were prepared using a ball mill with a rotation speed of 200 rpm for 8 h under Ar atmosphere. The morphologies of mixed powders were observed using a scanning electron microscope (SEM, Phenom proX, Phenom-World BV, Netherlands) coupled with an energy dispersive spectroscopy (EDS), with results presented in Figure 1. The element mapping results corresponding to AZ61-0.5Ti mixed powders indicated Ti nanoparticles homogeneously dispersed over the AZ61 particle surface.

Cubic samples (10 × 10 × 10 $mm^3$) were fabricated using a SLM system equipped with an YLR-500-WC fiber laser (IPG Photonics Inc.). The process parameters were determined at a laser power of 120 W, a scanning speed of 10 mm/s, a layer thicknesses of 150 μm, a scanning spacing of 80 μm, and a spot size of 80 μm. All the experiments were performed under a high-purity Ar atmosphere. A zigzag pattern was applied to scan the powder layer.

### 2.2 Microstructural Characterizations

The specimens were grounded, polished, and ultrasonically cleaned with ethanol. Then, the microstructures were investigated using SEM. Moreover, the crystalline structure was observed using an optical microscope (Leica DM200, Leica Microsystems, Germany) after etching with a nitric acid alcohol solution (4%). Furthermore, the phase compositions were identified using X-ray diffraction (XRD, D8 Advance diffractometer, Bruker Inc., German) at a scanning rate of 8 $min^{-1}$.

### 2.3 Mechanical Characterizations

The SLM fabricated samples were cut into 8 mm in length and 4 mm in diameter for compressive tests. The compressive tests were carried out using a universal mechanical testing machine (Instron, USA) with a compression speed of 0.5 mm/min. Microhardness was measured on a microhardness tester with a load of 0.98 N and a holding time of 15 s. The microhardness measurements were taken 5 times for each specimen, and the distance between each adjacent indentation was 500 μm.

### 2.4 Electrochemical Experiments

Electrochemical experiments were performed three a three-electrode system in which the sample was used as the working electrode, a platinum foil as a counter electrode, and a saturated calomel electrode as a reference electrode. All the electrodes were connected to an electrochemical workstation (Interface 1000, Gamry Instrument, USA) and immersed in simulated body fluid (SBF) at 25±0.5°C. The SBF was prepared according to reference[16]. The open circuit potential was first monitored for 2400 s. Then, the potentiodynamic polarization testing was conducted with a scanning rate of 0.333 mV/s.

### 2.5 Immersion Experiments

Immersion experiments were carried out to study the corrosion behavior. Specimens were immersed in SBF at 37°C, with a volume to exposure area ratio of 20 mL $cm^{-2}$. The hydrogen release rate and the pH values during immersion were monitored. Meanwhile, the ion concentrations of the soaked media were measured

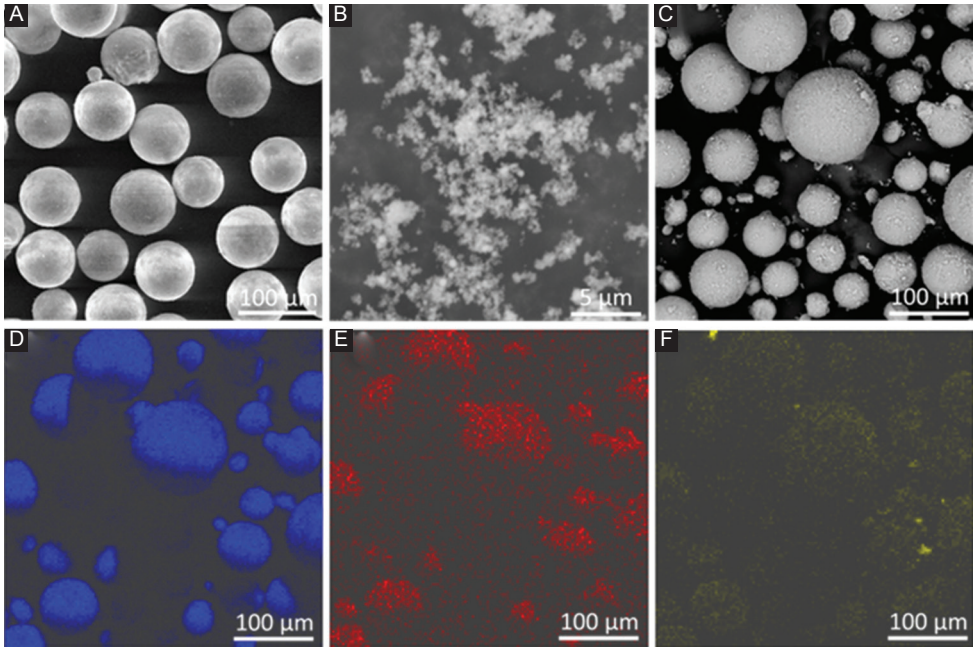


**Figure 1.** Morphologies of original powders: (**A**) AZ61, (**B**) Ti and (**C**) AZ61-0.5Ti mixed powder; (**D**)-(**F**) were the element distributions of Mg, Al, and Ti of AZ61-0.5Ti mixed powder.

using an inductively coupled plasma atomic emission spectroscopy (ICP-OES, PerkinElmer, Optima 5300DV, USA). The corrosion morphologies after immersion for 2 and 7 days were characterized using SEM. Besides, mass loss was obtained after removing the corrosion products in chromic acid solution (200 g/L $CrO_3$, 10 g/L $AgNO_3$). Then, corrosion rates ($C_R$) were obtained using the following equation, $C_R$=3.65 $\Delta W/\rho$, where $\Delta W$ was the mass loss rate (mg $cm^{-2}$/d) and $\rho$ was the density (g $cm^{-3}$).

## 2.6 Cell Culture

Human osteosarcoma cells (MG63, American Type Culture Collection, USA) were employed for the cell tests. DMEM (Gibco, Grand Island, USA) supplemented with 10% fetal bovine serum (Gibco, Grand Island, USA), 100 U/mL penicillin and 100 mg/mL streptomycin (BI, Kibbutz Beit Haemek, Israel) were used as culture medium. The extracts of AZ61-Ti were prepared by immersing the samples in DMEM for 72 h. The ratio of exposed areas to solution volume was 1 $cm^2$/mL. The obtained 100% extracts were then diluted to 50% and 10% concentrations. The pH value and ion concentration of the extracts were also evaluated.

Cell counting kit-8 (CCK-8) assays were adopted to evaluate cell viabilities. Cells were seeded in 96-well plates at a density of $5\times10^4$/mL and cultured for 24 h. Then, the cell culture media were replaced by extracts (100%, 50%, and 10%). Pure DMEM was used as control. After incubating for 1, 3, and 5 days, 10 μL of CCK-8 (5 mg/ml, Sigma-Aldrich, USA) solution was added to each well for 2 h at 37°C. After that, the spectrophotometric absorbance was recorded at a wavelength of 570 nm referenced to 630 nm on a paradigm detection platform (Beckman Coulter, USA).

For LIVE/DEAD cell assay, cells were seeded in 48-well plates with extracts. At each period, the cells were gently rinsed with phosphate-buffered solution (PBS) and stained using Calcein-AM (2 μM) and ethidium homodimer-1 (4 μM). Afterward, the cells were gently washed with PBS and observed under fluorescence microscopy (Olympus, BX60, Japan).

## 2.7 Statistical Analysis

All the experiments in this work were repeated for 3 times. The experimental data were expressed as the average ± standard deviation. One-way analysis of variance was used to analyze the statistical analyses followed by Tukey posthoc analysis. Statistical significance was considered when $P$<0.05.

# 3. Results

## 3.1 Microstructure

SEM and EDS were combined to study the microstructure of the AZ61-Ti, as displayed in Figure 2. In AZ61, some $\beta$ phases (bright particles) homogeneously distributed in Mg matrix (dark regions), as shown in Figure 2A. A close observation revealed that there was some divorced eutectic $\alpha$ phase formed along grain boundaries and interfaces. Combining with the elemental surface analysis,

the eutectic $\alpha$ phase was enriched in Al. With addition of 0.25 wt% Ti, more Al-enriched eutectic $\alpha$ phase and less $\beta$ phase were observed. In AZ61-0.5Ti, the Al-enriched eutectic $\alpha$ phase continuously distributed and constructed a net-like structure, which was also proved by the EDS mapping results. Moreover, only a few $\beta$ phase particles were observed. With Ti further increasing to 0.75 and 1.0 wt%, the $\beta$ phase particles were coarsened and increased, which were enriched in Al and Ti, as revealed by EDS analysis.

The quantitative elemental compositions were obtained, as shown in Figure 2B, in which point 1, point 4, and point 7 represented position in the vicinity of the Al-enriched eutectic $\alpha$ phase, point 2, point 5, and point 8 represented the position in the $\beta$ phase, and point 3, point 6, and point 9 represented the position in the $\alpha$-Mg grains, respectively. It could be seen that the Al contents dissolved in $\alpha$-Mg grains were 2.92±0.74 wt.%. With Ti increasing to 0.5 wt% and 1.0 wt%, the Al contents were dissolved in $\alpha$-Mg grains gradually decreased to 1.93 ± 0.51 and 1.13 ± 0.46 at.%, respectively. Similarly, the Al content in $\beta$ phase was also decreased with increasing Ti content, which was 20.46 at.% for AZ61, 10.29 at.% for AZ61-0.5Ti, and 9.08 at.% for AZ61-1.0Ti. However, the Al content in Al-enriched eutectic $\alpha$ phases showed a different trend. Al-enriched eutectic $\alpha$ phases in AZ61-0.5Ti exhibited the lowest Al content of 5.89 at.%, which was lower than that in AZ61 (6.42 at.%) and AZ61-1.0Ti (6.28 at.%). Their results indicated that the diffusivity of Al was increased with increasing Ti. Besides, Zn was detected in all of the AZ61-Ti alloys. Moreover, a small amount of Ti was detected in the $\beta$ phase of AZ61-1.0Ti.

The area fraction of Al-enriched $\alpha$ phase and $\beta$ phase was measured by the Image-Pro Plus 6.0 software, with results displayed in Table 1. The area fraction of Al-enriched eutectic $\alpha$ phase in AZ61 was 17.3%. With Ti gradually increased to 0.5 wt%, the area fraction of eutectic $\alpha$ phase gradually increased to 42.0%, which indicated that the Al atoms in Mg solute were consumed to constitute more Al-enriched eutectic $\alpha$ phase. With Ti further increased to 1.0 wt%, the area fraction of eutectic $\alpha$ phase was reduced to 27.8%. It was believed that excess Ti reacted with Al to form $\beta$ phase, thus reducing the Al content in eutectic.

The optical microstructure and the calculated grain sizes of the AZ61-Ti are presented in Figures 3A-F. The grain sizes for the AZ61, AZ61-0.25Ti, AZ61-0.5Ti, AZ61-0.75Ti, and AZ61-1.0Ti were 16.4 ± 2.3, 12.7 ± 2.1, 10.4 ± 1.6, 9.5 ± 1.1, and 9.1 ± 0.8 µm, respectively, indicating that Ti significantly refined the grain sizes. The XRD patterns indicated that $\alpha$-Mg was a major phase. Moreover, the $\beta$ phase of AZ61, AZ61-0.25Ti, and

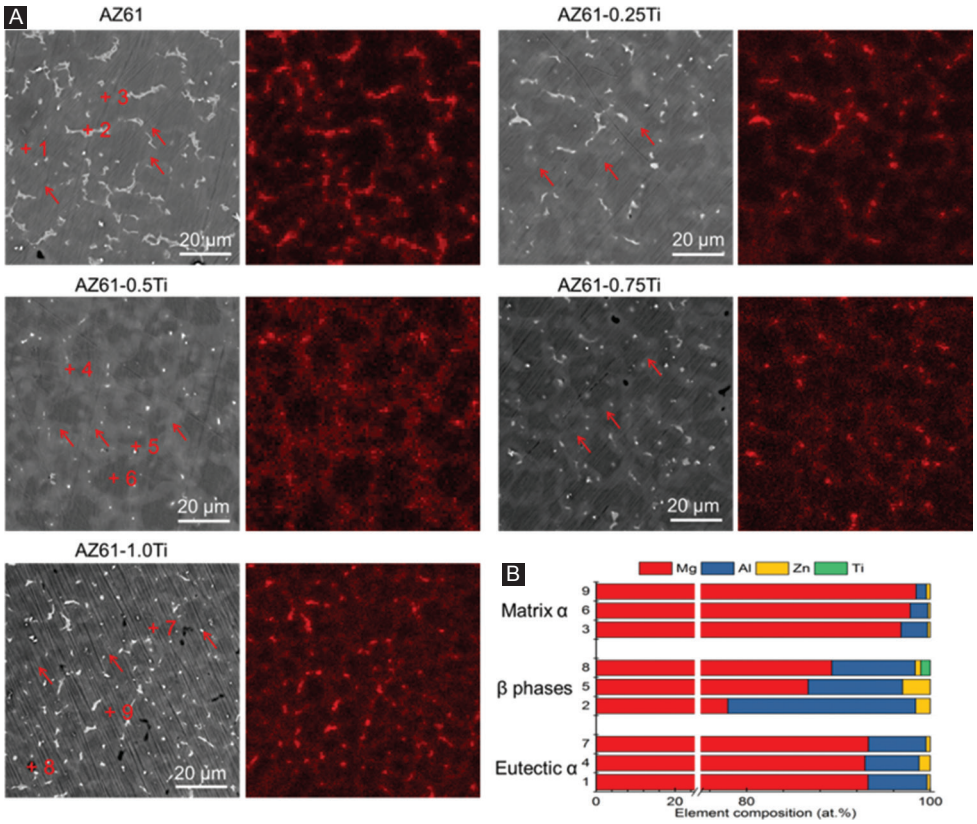


**Figure 2.** (**A**) Microstructure of AZ61-Ti observed under scanning electron microscope and the corresponding elemental distribution of Al; red arrow indicates the eutectic α phase. (**B**) Energy dispersive spectroscopy results corresponding to particles in Figure 2A.

**Table 1.** The calculated area fraction of eutectic α-Mg phase, β-phase, and matrix.

| Samples | Eutectic α | β phases | Matrix |
|---|---|---|---|
| AZ61 | 17.3% | 7.0% | 75.7% |
| AZ61-0.25Ti | 25.8% | 2.1% | 72.1% |
| AZ61-0.5Ti | 42.0% | 0.7% | 57.3% |
| AZ61-0.75Ti | 36.1% | 1.6% | 50.3% |
| AZ61-1.0Ti | 27.8% | 2.6% | 69.6% |

AZ61-0.5Ti was $Mg_{17}Al_{12}$ (Figure 3G). The diffraction intensities corresponding to $Mg_{17}Al_{12}$ phase decreased with increasing Ti content. Moreover, the peaks of $Mg_{17}Al_{12}$ were not detected in AZ61-1.0Ti. Meanwhile, $TiAl_3$ phase could be identified in AZ61-0.75Ti and AZ61-1.0Ti and its diffraction intensities increased with Ti content increasing.

### 3.2 Degradation Behavior

The open circuit potential of AZ61-Ti is given in Figure 4A. During the electrochemical test, the open circuit potential gradually increased and eventually stabilized. From the thermodynamic point of view, a higher open circuit potential indicated a more stable surface. It was believed that the increased open circuit potential was due to a protective $Mg(OH)_2$ layer formed with the dissolution of Mg matrix[17]. More importantly, AZ61-0.5Ti exhibited the highest open circuit potential.

The potentiodynamic polarization curves of the AZ61-Ti are given in Figure 4B. Moreover, the corrosion potential ($E_{corr}$) and cathodic polarization corrosion current density ($i_{corr}$) derived from the potentiodynamic polarization curves are given in Figure 4C and D. The $E_{corr}$, which represented the corrosion tendency, could be ranked as AZ61-0.5Ti >AZ61-0.75Ti >AZ61-0.25Ti >AZ61-1.0Ti >AZ61. Moreoverm the AZ61-0.5Ti exhibited the lowest current density of 9.2±1.4 μA·cm$^{-2}$. It was well known that $i_{corr}$ mainly reflected the intensity of the chemical reaction during the electrochemical corrosion[18,19]. Thus, AZ61-0.5Ti with highest $E_{corr}$ and smallest $i_{corr}$ exhibited the optimal corrosion resistance.

Immersion tests were conducted to further study the corrosion behavior, with results shown in Figure 5. The hydrogen evolution curves are depicted in Figure 5A and the pH value variations are depicted in Figure 5B. Clearly, the degradation behaviors differed with Ti content. AZ61 exhibited the relatively fast hydrogen release and pH increase. When Ti was incorporated, the released hydrogen decreased and the increase rate of pH slowed down. The AZ61-0.5Ti exhibited the least hydrogen evolution volume and the lowest pH compared with other investigated alloys. However, the hydrogen volumes and pH were rapidly increased in AZ61-0.75Ti and AZ61-1.0Ti, implying that the excessive Ti decreased the corrosion resistance.

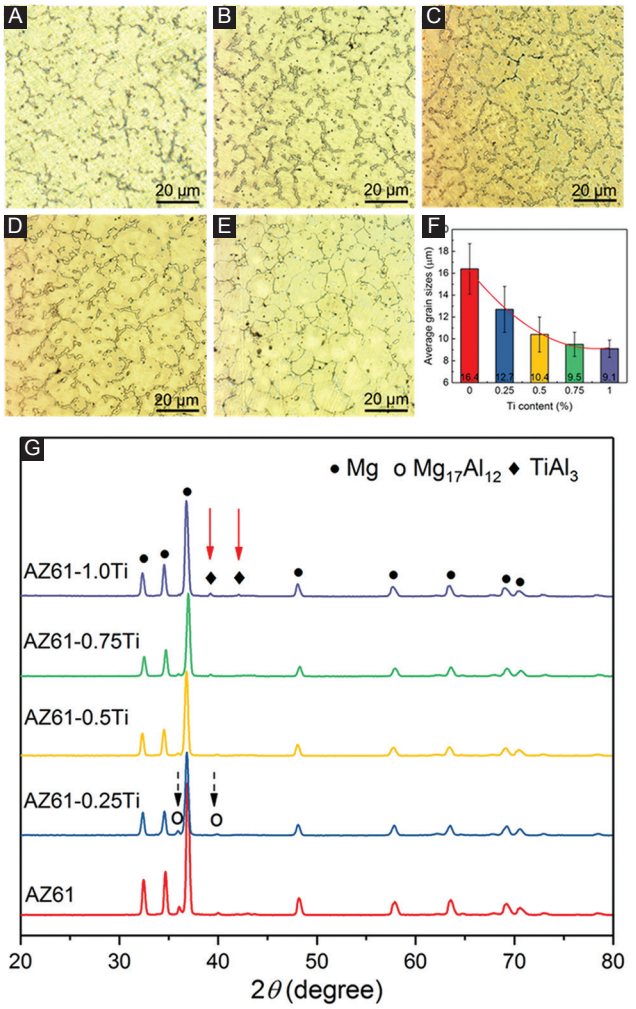


**Figure 3.** Optical microstructure of (**A**) AZ61, (**B**) AZ61-0.25Ti, (**C**) AZ61-0.5Ti, (**D**)AZ61-0.75Ti, and (**E**) AZ61-1.0Ti. (**F**) The measured average grain sizes. (**G**) X-ray diffraction patterns of AZ61-Ti. $Mg_{17}Al_{12}$ and $TiAl_3$ phases were marked by black dash arrow and red solid arrow, respectively.

The variation of Mg ion-releasing behavior during immersion was similar to that of the hydrogen evolution volume and pH variation (Figure 5C). $Mg^{2+}$ concentrations tended to increase with immersion time increasing, indicating the dissolution of specimens. AZ61-0.5Ti released the least amount of $Mg^{2+}$, indicating it has the slowest degradation rate. The $C_R$ calculated by mass loss exhibited a similar trend to that of the Mg ion-releasing (Figure 5D). All the immersion tests demonstrated that AZ61-0.5Ti had the best corrosion resistance.

The typical corrosion morphologies and composition analyses of the corrosion product are displayed in Figure 6. A corrosion product layer was formed on the specimen with some particles deposition. A lot of micro-

cracks appeared on the surface were due to the shrinkage of the corrosion product layer during dehydration. It was obvious that AZ61 suffered the most severe corrosion, which was consistent with its fastest degradation rate (Figure 6A). As a comparison, AZ61-0.5Ti suffered homogeneous corrosion, as depicted in Figure 6C. Some particles were deposited on this layer, which was enriched in Mg, Ca, P, C, and O (area 2), with a higher content of Ca and P than that on area 1 (Figure 6F). Nevertheless, AZ61-0.75Ti and AZ61-1.0Ti both suffered severely localized corrosion. With increasing immersion period to 7 days, the AZ61-0.5Ti was also compact, except for some micro-cracks and particles on the surface. Large cracks and flaking of corrosion product could be observed on AZ61 and AZ61-1.0Ti. The flaking of corrosion products resulted from the thickening of the corrosion layer and dehydration process[20].

### 3.3 Cytotoxicity

The pH and ion concentration of the extracts during the 72 h incubation is summarized in Figures 7A and B. There were no significant differences in the pH of the 100% extracts (all closing to 9). The pH only slightly reduced in 50% extracts due to the buffer effect of the culture medium. When further diluted to 10%, the pH values were decreased to 7.89 (Figure 7A). The $Mg^{2+}$ releasing during the incubation reflected the degradation rate of AZ61-Ti in the culture medium. AZ61-0.5Ti showed the lowest $Mg^{2+}$ concentration, indicating its optimal corrosion resistance. The $Zn^{2+}$ concentrations in the extracts were in the single-digit μg/mL range (Figure 7B). In addition, $Al^{3+}$ concentrations in all the extracts were not detected, due to the small solubility products of aluminum hydroxide ($1.3\times10^{-33}$)[21].

The cell viability of the MG63 incubated in AZ61-Ti extracts is depicted in Figure 7c. After 3 days' culture, all the undiluted extracts (100%) resulted in a significantly reduced cell viability compared to the negative control. However, the toxic effects could be mitigated by dilution. The cell viability was about 90% for AZ61-0.5Ti in 50% extracts, suggesting the AZ61-0.5Ti alloy had good cell compatibility. The cell viability level was further improved with 10% extract dilution. The cell viability was improved with extract dilution which may be in consonance with the clinical condition in which the material becomes diluted with the surrounding tissue fluid[22]. According to ISO 10993-5, all the samples showed acceptable cell viabilities, which were higher than 80%[23-25].

LIVE/DEAD staining assay was further used to evaluate the biocompatibility (Figure 8). Obviously, all

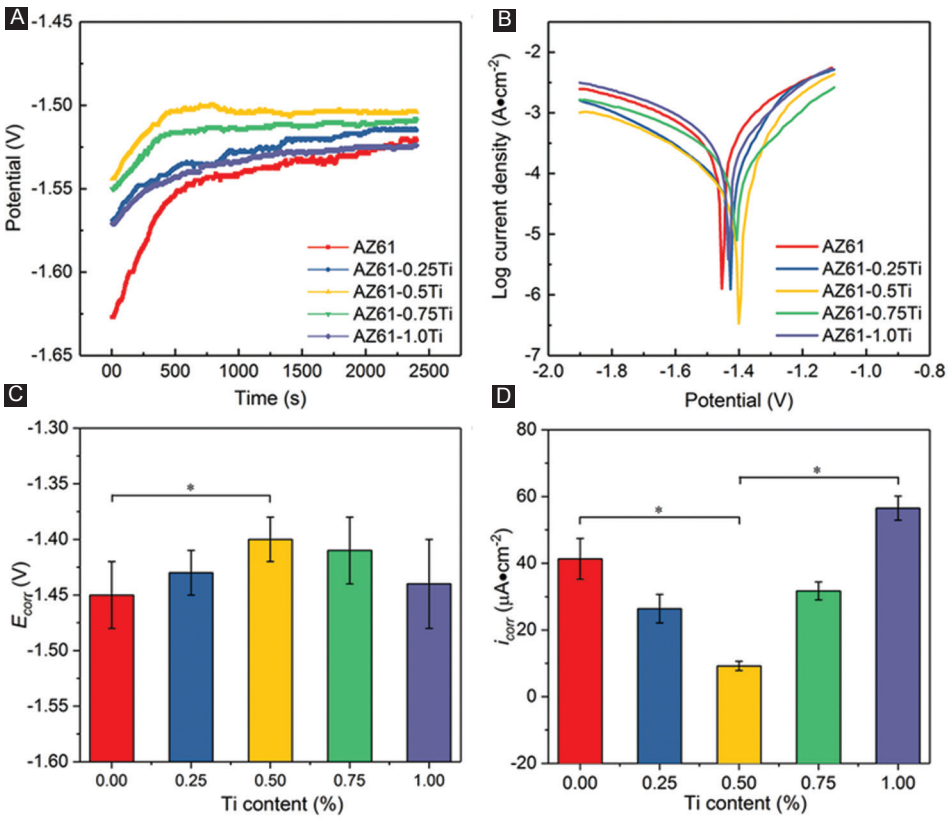


**Figure 4.** Electrochemical testing results of AZ61-Ti: (**A**) open circuit potential curves, (**B**) potentiodynamic polarization curves, (**C**) $E_{corr}$ and (**D**) $i_{corr}$ derived from the potentiodynamic polarization curves by Tafel extrapolation.

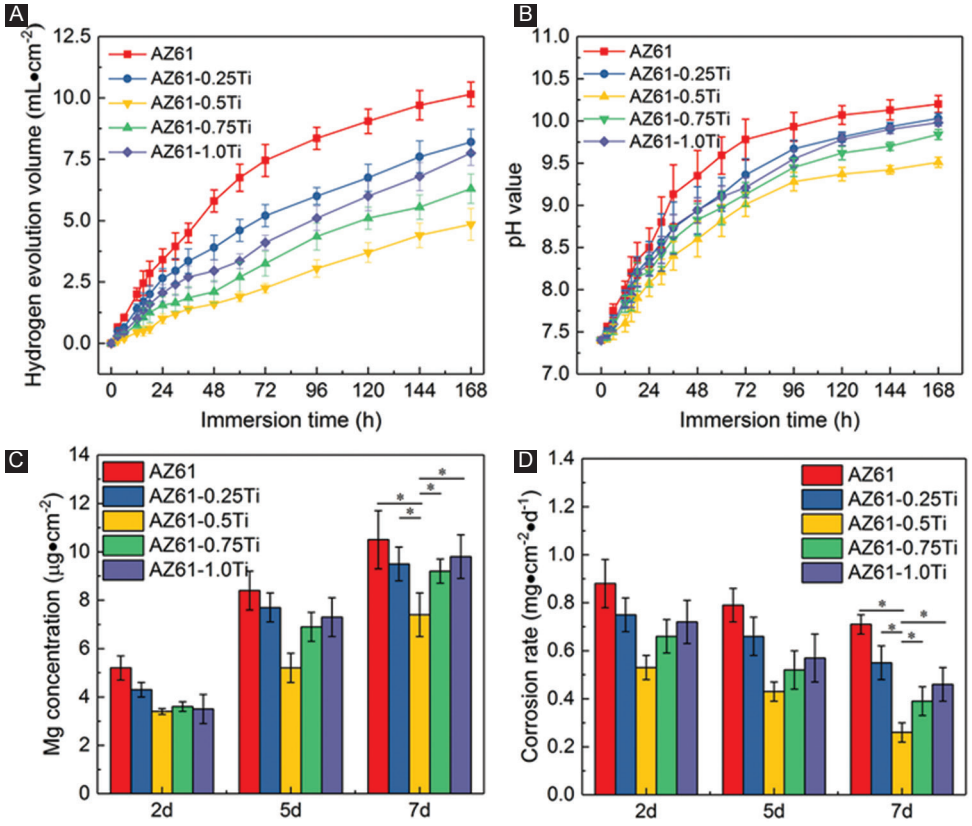


**Figure 5.** Immersion degradation behaviors of AZ61-Ti: (**A**) Hydrogen evolution volumes, (**B**) pH during immersion, (**C**) ion-releasing behavior during immersion, and (**D**) corrosion rate calculated from the mass loss.

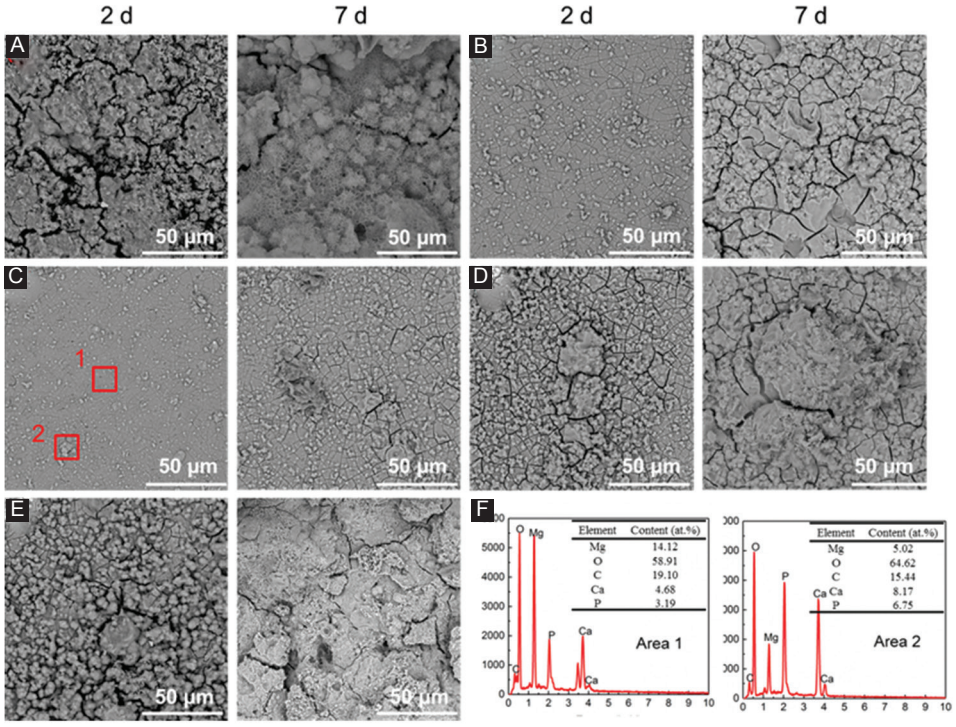


**Figure 6.** Corrosion surfaces of (**A**) AZ61, (**B**) AZ61-0.25Ti, (**C**) AZ61-0.5Ti, (**D**) AZ61-0.75Ti, and (**E**) AZ61-1.0Ti observed under scanning electron microscope after immersion for 2 and 7 days; (**F**) energy dispersive spectroscopy results of specific areas in AZ61-0.5Ti.

the AZ61-Ti extracts exhibited improved cell viability compared with AZ61 as the cell density (number of cells) was enhanced. Specifically, AZ61-0.5Ti exhibited the best cell viability. There were few apoptotic cells (red fluorescence in the nuclei) in each group for all culture periods. Moreover, cells exhibited similar shape after culturing for 24 h and 72 h. Clearly, AZ61-0.5Ti exhibited improved biocompatibility as compared with AZ61. It was believed that the enhanced corrosion resistance should be responsible for the improved biocompatibility[26]. For AZ61-0.5Ti, the enhanced corrosion resistance resulted in a reduced degradation rate, thus decreasing the corrosion products, which might alleviate the cytotoxicity[27].

### 3.4 Mechanical Properties

The compressive strength and microhardness of AZ61-Ti are displayed in Figure 9. AZ61 exhibited a relatively low compressive strength of 110.4 ± 15.2 MPa. With Ti gradually increasing to 0.5 wt%, the compressive strength was gradually improved to 175.6±21.3 MPa. However, with Ti content further increasing to 0.75 wt% and 1.0 wt%, the compressive strength was decreased to 145.3 ± 30.9 MPa and 123.9 ± 34.7 MPa, respectively. AZ61 had a relatively low microhardness of 84.8 ± 3.7 HV. With the increase of Ti, the microhardness gradually increased to 90.1 ± 4.0 HV for AZ61-0.25Ti, 95.2 ± 3.4 HV for AZ61-0.5Ti, 96.3 ± 3.1 HV for AZ61-0.75Ti, and 97.8 ± 4.3 HV for AZ61-1.0Ti, respectively (Figure 9B).

## 4. Discussion

### 4.1 Microstructure and Mechanical Properties

In the present study, the incorporation of moderate Ti induced the formation of continuous net-like eutectic $\alpha$ phase. It was believed that Ti, which had low solid solubility in Mg, would be first rejected into the interdendritic liquid phase during the solidification of the molten pool[28]. From the perspective of thermodynamics, Ti in the interdendritic liquid would catch the Al atoms in Mg solute to form the second phase due to the high affinity between Ti and Al[15]. Thus, the diffusivity of Al would be enhanced during the solidification, resulting in an increased Al content near the eutectic location. With the liquid phase cooling to the eutectic temperature and the Al content close to eutectic composition, the eutectic reaction would occur to form the eutectic phases.

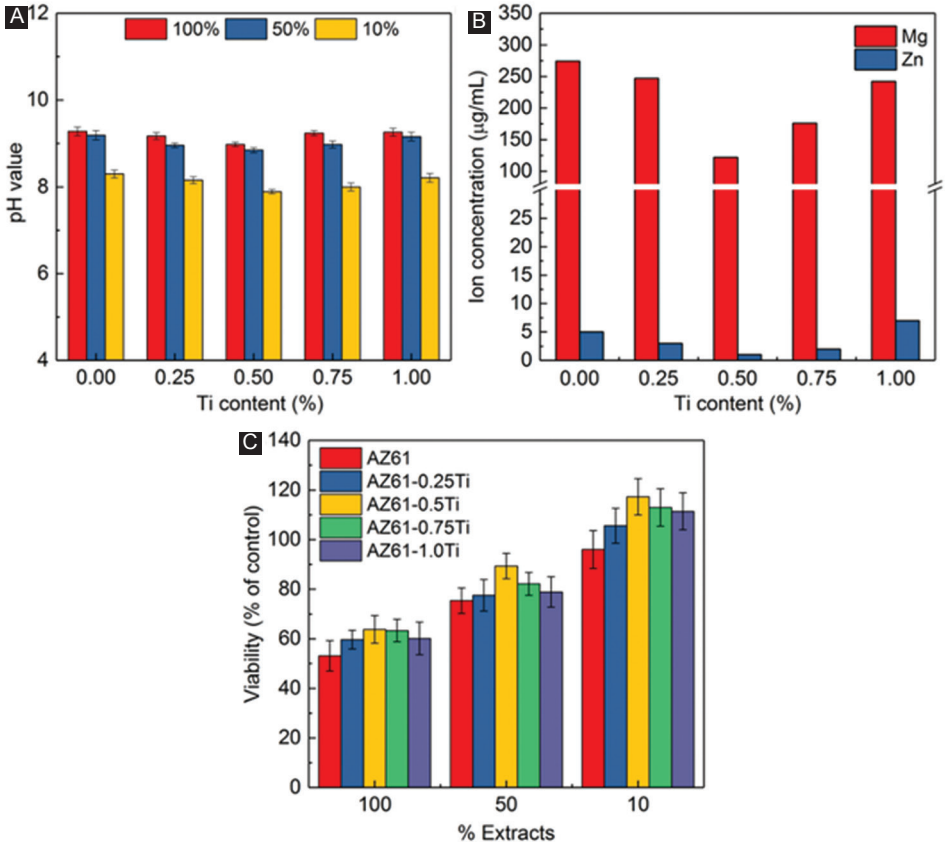


**Figure 7.** (**A**) pH of the extracts; (**B**) Mg and Zn concentration in the extracts; (**C**) relative viability of MG63 cells culture in AZ61-Ti extracts.

On the other hand, the rapid solidification occurred in SLM also played a key role in the formation of continuous net-like eutectic $\alpha$ phase. According to the Mg-Al binary equilibrium phase diagram[29], the maximum solid solubility of Al in $\alpha$-Mg is about 12.7 wt% at the eutectic temperature of 437°C and its solid solubility at room temperature is about 2 wt%. In the present study, SLM, which involved a fast cooling rate, was applied to fabricate AZ61-Ti alloy. Moreover, such a rapid solidification was believed to promote the occurrence of eutectic reaction at lower eutectic temperature and critical hypoeutectic Al content (as compared with equilibrium). The eutectic reaction precipitated the eutectic $\alpha$ phase and eutectic $\beta$ particles, which would attach to the primary $\alpha$-Mg grains and distribute in grain boundaries, respectively. Moreover, the fast cooling rate was conducive for the homogeneous precipitation of the eutectic $\alpha$ phase and eutectic $\beta$ particles. Therefore, the eutectic $\alpha$ phase distributed continuously and formed a net-like structure along the grain boundaries.

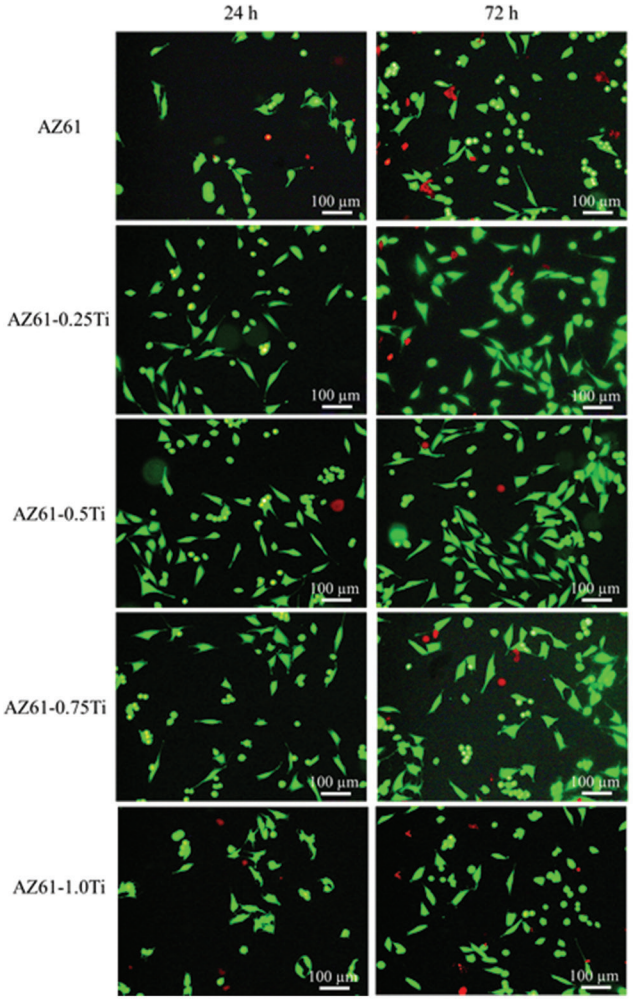


**Figure 8.** LIVE/DEAD staining of MG63 cells seeded in AZ61-Ti 100% extracts for 24 h and 72 h.

Impacts of Ti on the grain sizes were also observed in this study. In Ti containing Mg-Al alloys, Ti element served as a surface active element, which could significantly reduce the alloy solid-liquid interfacial tension and decrease the nucleation energy during the solidification process[30]. According to the nucleation formula, $r^*=-2\sigma_{LS}/\Delta G_m$;[31] where r* was the critical nucleation radius, $\sigma_{LS}$ was the solid-liquid interfacial tension, and $\Delta G_m$ was the Gibbs free energy of solidification. Ti reduced the solid-liquid interfacial tension, thereby reducing the critical nucleation radius. As a result, the ultimately nuclear volume of the primary $\alpha$-Mg was improved, thus forming refined grain size. Furthermore, in AZ61-0.75Ti and AZ61-1.0Ti, excessive Ti combined with Al to form the $TiAl_3$ phase. Although the $TiAl_3$ phase was not regarded as the core of crystal formation, it would be pushed to the front of solid-liquid interfaces and prevented the grain growth. Therefore, the grain sizes decreased continuously with increasing Ti content.

## 4.2 Corrosion Behaviors

It is known that an ideal bone implant should progressively degrade at a suitable rate (approximately

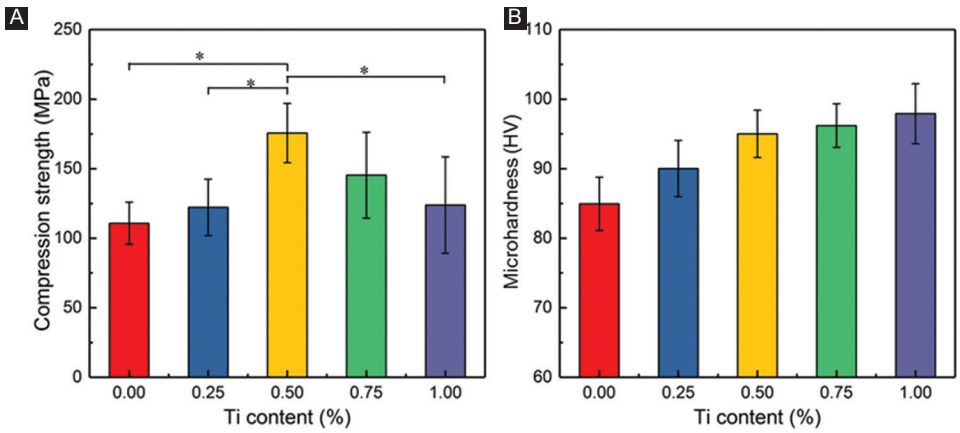


**Figure 9.** Mechanical performances of AZ61-Ti: (**A**) Compression strength and (**B**) microhardness.

0.2~0.5 mm/year) to match the bone healing process. In the present work, the degradation rate of AZ61 alloy was dramatically decreased from 0.74 (1.56 mm/year) to 0.24 $mg \cdot cm^{-2}/d^{-1}$ (0.51 mm/year[1]) after adding 0.5 wt% Ti. The improved corrosion resistance could be explained from two aspects as follows. On the one hand, Ti promoted the formation of divorced eutectic $\alpha$ phase and reduced the formation of divorced $\beta$-$Mg_{17}Al_{12}$ phase. Significantly, the potential difference between the eutectic $\alpha$ phase and $\alpha$-Mg grains was slighter than that between $\beta$-$Mg_{17}Al_{12}$ phases and $\alpha$-Mg grains, due to the lower potential of eutectic $\alpha$ phase[32] and a reduced potential difference would decrease the susceptibility to galvanic corrosion of AZ61-0.5Ti.

On the other hand, the continuous net-like eutectic $\alpha$ phase also did a favor for the enhanced corrosion resistance. During degradation, the $\alpha$-Mg grains dissolved preferentially, leaving the eutectic $\alpha$ phase on the surface[33]. Al-enriched eutectic $\alpha$ phase was relatively inert in the physiological environment. Thus, the exposed eutectic $\alpha$ phase would act as a barrier and retard the corrosion to a certain extent. For AZ61 and AZ61-0.25Ti, the discontinuous eutectic $\alpha$ phase did not form an effective barrier to corrosion attack, as shown in Figure 2. Resultantly, the AZ61-0.5Ti exhibited higher corrosion resistance compared with AZ61 and AZ61-0.25Ti.

It should be noted that with Ti further increasing to 1 wt%, the $TiAl_3$ phase precipitated in grain boundary (Figure 2), which exhibited higher potential difference with $\alpha$-Mg grains than that between the eutectic $\alpha$ phase and $\alpha$-Mg grains. Hence, the $TiAl_3$ phase was considered as the cathode and form galvanic cells with $\alpha$-Mg grains, resulting in dramatically galvanic corrosion. Thus, the galvanic corrosion was considerably enhanced, which decreased corrosion resistance of AZ61-1.0Ti.

### 4.3 Mechanical Properties

Mechanical properties were closely related to microstructure. In the present study, AZ61-Ti exhibited equiaxed grains with eutectic $\alpha$ and $\beta$ phases on the interdendritic regions (Figure 2). The formation of the Al-enriched eutectic $\alpha$ phase was a solid solution of Al in $\alpha$-Mg phase, which caused a negative deformation of the lattice structure and increased the dislocations resistance that occurred in grains[34,35]. Moreover, the addition of Ti significantly refined the grains, increased the grain boundaries, and suppressed the formation of $\beta$ phase. Resultantly, the crack tendency and the fracture propagation were reduced. Thus, the compressive strength of AZ61-Ti was improved. However, as Ti was more than 0.5 wt%, the coarse $TiAl_3$ particles precipitated and aggregated at the grain boundaries, which broke the connection between the adjacent grains. As external force was applied to specimen, stress concentration, and porous around the $TiAl_3$ particles would form, which made the alloys easily to crack in the grain boundary, resulting in reduced compressive strength[36]. The microhardness of AZ61-Ti was increased with the increase of Ti content, which could be attributed to the fine grain strengthening. Besides, the eutectic $\alpha$ and $\beta$ phases had higher microhardness than $\alpha$-Mg matrix, which could also contribute to the increase of microhardness.

## 5. Conclusions

In this study, Ti-introduced AZ61 alloy was fabricated with SLM to enhance the corrosion resistance. Results indicated that Ti promoted the formation of eutectic $\alpha$-Mg phase and reduced the formation of $\beta$-$Mg_{17}Al_{12}$ phase. When the Ti content reached to 0.5 wt%, the eutectic α-Mg phase formed a continuous net-like structure providing resistance for α-Mg matrix. Polarization test, hydrogen evolution, pH value, $Mg^{2+}$ concentration, and mass loss suggested that AZ61-0.5Ti exhibited the optimal corrosion resistance. The typical corrosion morphologies demonstrated that the AZ61-0.5Ti suffered uniform corrosion. Besides, AZ61-0.5Ti showed improved compressive strength and microhardness compared to AZ61 due to solid solution strengthening and fine-grain strengthening. In addition, the Ti contained Mg alloys exhibited good cytocompatibility.

## Acknowledgment

This study was supported by the following funds: (1) The natural science foundation of China (81871494, 81871498, 51705540); (2) Hunan provincial natural science foundation of China (2018JJ3671, 2019JJ50588); (3) Guangdong province higher vocational colleges and schools pearl river scholar funded scheme (2018); (4) The open sharing fund for the large-scale instruments and equipments of central South university; (5) The project of hunan provincial science and technology plan (2017RS3008); Shenzhen science and technology plan project (JCYJ20170817112445033); (6) National postdoctoral program for innovative talents (BX201700291); (7) The China postdoctoral science foundation (2018M632983); (8) The fundamental research funds for the central universities of central South University (2019zzts005).

## References

1. Staiger M, Pietak A, Huadmai J, *et al.*, 2006, Magnesium and its Alloys as Orthopedic Biomaterials: A Review. *Biomaterials*, 27:1728-34. DOI 10.1016/j.biomaterials.2005.10.003.
2. Zhao D, Witte F, Lu F, *et al.*, 2017, Current Status on Clinical Applications of Magnesium-based Orthopaedic Implants: A Review from Clinical Translational

Perspective. *Biomaterials*, 112:287-302. DOI 10.1016/j.biomaterials.2016.10.017.

3. Gao C, Feng P, Peng S, *et al.*, 2017, Carbon Nanotube, Graphene and Boron Nitride Nanotube Reinforced Bioactive Ceramics for Bone Repair. *Acta Biomater*, 61:1-20. DOI 10.1016/j.actbio.2017.05.020.
4. Abidin NIZ, Da Forno A, Bestetti M, *et al.*, 2015, Evaluation of Coatings for Mg Alloys for Biomedical Applications. *Adv Eng Mater*, 17(1):58-67. DOI 10.1002/adem.201300516.
5. Shuai C, Li S, Peng S, *et al.*, 2019, Biodegradable Metallic Bone Implants. *Mater Chem Front*, 3:544-62.
6. Chai Y, Jiang B, Song J, *et al.*, 2018, Role of Al content on the Microstructure, Texture and Mechanical Properties of Mg-3.5 Ca Based Alloys. *Mater Sci Eng A*, 730:303-16.
7. Zheng YF, Gu XN, Witte F, 2014, Biodegradable Metals. *Mater Sci Eng R*, 77:1-34.
8. Cheng W, Bai Y, Wang L, *et al.*, 2018, Strengthening Effect of Extruded Mg-8Sn-2Zn-2Al Alloy: Influence of Micro and Nano-Size Mg-Sn Precipitates. *Materials,* 10(7):822. DOI 10.3390/ma10070822.
9. Witte F, Kaese V, Haferkamp H, *et al.*, 2005, *In vivo* Corrosion of Four Magnesium Alloys and the Associated Bone Response. *Biomaterials*, 26(17):3557-63. DOI 10.1016/j.biomaterials.2004.09.049.
10. Wen Z, Wu C, Dai C, *et al.*, 2009, Corrosion Behaviors of Mg and its Alloys with Different Al contents in a Modified Simulated Body Fluid. *J Alloys Compd*, 488(1):392-9. DOI 10.1016/j.jallcom.2009.08.147.
11. Baek SM, Kang JS, Shin HJ, *et al.*, 2017, Role of Alloyed Y in Improving the Corrosion Resistance of Extruded Mg–Al–Ca-based Alloy. *Corros Sci*, 118:227-32. DOI 10.1016/j.corsci.2017.01.022.
12. Liu W, Cao F, Chang L, *et al.*, 2009, Effect of Rare Earth Element Ce and La on Corrosion Behavior of AM60 Magnesium Alloy. *Corros Sci*, 51:1334-43. DOI 10.1016/j.corsci.2009.03.018.
13. Wu PP, Xu FJ, Deng KK, *et al.*, 2017, Effect of Extrusion on Corrosion Properties of Mg-2Ca-χAl (χ = 0, 2, 3, 5) Alloys. *Corros Sci*, 127:280-90. DOI 10.1016/j.corsci.2017.08.014.
14. Shuai C, Yang Y, Peng S, *et al.*, 2017, Nd-induced Honeycomb Structure of Intermetallic Phase Enhances the Corrosion Resistance of Mg Alloys for Bone Implants. *J Mater Sci Mater Med,* 28(9):130. DOI 10.1007/s10856-017-5945-0.
15. Ai X, Quan G, 2012, Effect of Ti on the Mechanical Properties and Corrosion of Cast AZ91 Magnesium Alloy. *Open Mater Sci J*, 6:6-13.
16. Feng P, Wu P, Gao C, *et al.,* 2018, A Multimaterial Scaffold with Tunable Properties: Toward Bone Tissue Repair. *Adv Sci*, 5(6):1700817. DOI 10.1002/advs.201700817.
17. Li Z, Gu X, Lou S, *et al.*, 2008, The Development of Binary Mg–Ca Alloys for Use as Biodegradable Materials within Bone. *Biomaterials*, 29:1329-44. DOI 10.1016/j.biomaterials.2007.12.021.
18. Shuai C, Wang B, Yang Y, *et al.*, 2019, 3D Honeycomb Nanostructure-encapsulated Magnesium Alloys with Superior Corrosion Resistance and Mechanical Properties. *Compos B*, 162:611-20. DOI 10.1016/j.compositesb.2019.01.031.
19. Lothe J, Pound GM, 1962, Reconsiderations of Nucleation Theory. *J Chem Phys*, 36:2080-5.
20. Bian D, Deng J, Li N, *et al.,* 2018, *In Vitro* and *In Vivo* Studies on Biomedical Magnesium Low-alloying with Elements Gadolinium and Zinc for Orthopedic Implant Applications. *ACS Appl Mater Interfaces*, 10:4394-408. DOI 10.1021/acsami.7b15498.
21. Mochizuki A, Yahata C, Takai H, 2016, Cytocompatibility of Magnesium and AZ31 Alloy with Three Types of Cell Lines using a Direct *In Vitro* Method. *J Mater Sci Mater Med*, 27:145. DOI 10.1007/s10856-016-5762-x.
22. Shuai C, Guo W, Wu P, *et al.*, 2018, A Graphene Oxide-Ag co-dispersing Nanosystem: Dual Synergistic Effects on Antibacterial Activities and Mechanical Properties of Polymer Scaffolds. *Chem Eng J*, 347:322-33. DOI 10.1016/j.cej.2018.04.092.
23. International Organization for Standardization, 2009, ISO 10993-5:2009(E). Biological Evaluation of Medical Devices-Part 5: Tests for *In Vitro* Cytotoxicity. Geneva: International Organization for Standardization.
24. Shuai C, Li Y, Wang G, *et al.*, 2019, Surface Modification of Nanodiamond: Toward the Dispersion of Reinforced Phase in Poly-l-lactic Acid Scaffolds. *Int J Biol Macromol*, 126:1116-24. DOI 10.1016/j.ijbiomac.2019.01.004.
25. Shuai C, Xu Y, Feng P, *et al.*, 2019, Antibacterial Polymer Scaffold Based on Mesoporous Bioactive Glass Loaded with *In Situ* Grown Silver. *Chem Eng J*, 374:304-15. DOI 10.1016/j.cej.2019.03.273.
26. Shuai C, Cheng Y, Yang Y, *et al.*, 2019, Laser Additive Manufacturing of Zn-2Al Part for Bone Repair: Formability, Microstructure and Properties. *J Alloys Compd*, 798:606-15. DOI 10.1016/j.jallcom.2019.05.278.
27. Feng P, He J, Peng S, *et al.,* 2019, Characterizations and Interfacial Reinforcement Mechanisms of Multicomponent Biopolymer Based Scaffold. *Mater Sci Eng C*, 100:809-25.
28. Monas A, Shchyglo O, Kim SJ, *et al.*, 2015, Divorced Eutectic Solidification of Mg-Al Alloys. *JOM*, 67:1805-11.

DOI 10.1007/s11837-015-1418-4.

29. Liang G, Schulz R, 2003, Synthesis of Mg-Ti Alloy by Mechanical Alloying. *J Mater Sci*, 38:1179-84.
30. Xie D, Zhao J, Qi Y, *et al.*, 2013, Decreasing Pores in a Laser Cladding Layer with Pulsed Current. *Chin Opt Lett*, 11:111401. DOI 10.3788/col201311.111401.
31. Choi HY, Kim WJ, 2017, The Improvement of Corrosion Resistance of AZ91 Magnesium Alloy through Development of Dense and Tight Network Structure of Al-rich α Phase by Addition of a Trace amount of Ti. *J Alloys Compd*, 696:736-45. DOI 10.1016/j.jallcom.2016.11.215.
32. Mathieu S, Rapin C, Steinmetz J, *et al.*, 2003, A Corrosion Study of the Main Constituent Phases of AZ91 Magnesium Alloys. *Corros Sci*, 45:2741-55. DOI 10.1016/s0010-938x(03)00109-4.
33. Prabhu DB, Dhamotharan S, Sathishkumar G, *et al.*, 2018, Stress Corrosion Cracking of Biodegradable Mg-4Zn Alloy in Simulated Body Fluid at Different Strain Rates–a Fractographic Investigation. *Mater Sci Eng A*, 730:223-31. DOI 10.1016/j.msea.2018.06.002.
34. Wang F, Hu T, Zhang Y, *et al.*, 2017, Effects of Al and Zn Contents on the Microstructure and Mechanical Properties of Mg-Al-Zn-Ca Magnesium Alloys. *Mater Sci Eng A*, 704:57-65. DOI 10.1016/j.msea.2017.07.060.
35. Fu K, Wang J, Qiu M, *et al.*, 2018, Effects of Cold Rolling on Microstructural Evolution and Mechanical Properties of Mg–14Li–1Zn Alloy. *Adv Eng Mater*, 21:1801344. DOI 10.1002/adem.201801344.
36. Shuai C, Zan J, Qi F, *et al.*, 2019, nMgO-incorporated PLLA Bone Scaffolds: Enhanced Crystallinity and Neutralized Acidic Products. *Mater Des,* 174:107801. DOI 10.1016/j.matdes.2019.107801.

PERSPECTIVE ARTICLE

# Three-dimensional-printing for microfluidics or the other way around?

**Yi Zhang***

Singapore 3D-Printing Center, HP-NTU Digital Manufacturing Corporate Lab, School of Mechanical and Aerospace Engineering, Nanyang Technological University, Singapore

**Abstract:** As microfluidic devices are designed to tackle more intricate tasks, the architecture of microfluidic devices becomes more complex, and more sophisticated fabrication techniques are in demand. Therefore, it is sensible to fabricate microfluidic devices by three-dimensional (3D)-printing, which is well-recognized for its unique ability to monolithically fabricate complex structures using a near-net-shape additive manufacturing process. Many 3D-printed microfluidic platforms have been demonstrated but can 3D-printed microfluidics meet the demanding requirements in today's context, and has microfluidics truly benefited from 3D-printing? In contrast to 3D-printed microfluidics, some go the other way around and exploit microfluidics for 3D-printing. Many innovative printing strategies have been made possible with microfluidics-enabled 3D-printing, although the limitations are also largely evident. In this perspective article, we take a look at the current development in 3D-printed microfluidics and microfluidics-enabled 3D printing with a strong focus on the limitations of the two technologies. More importantly, we attempt to identify the innovations required to overcome these limitations and to develop new high-value applications that would make a scientific and social impact in the future.

**Keywords:** 3D-printing; Bioprinting; Microfluidics

*Correspondence to: Yi Zhang, Singapore 3D-Printing Center, HP-NTU Digital Manufacturing Corporate Lab, School of Mechanical and Aerospace Engineering, Nanyang Technological University, Singapore; yi_zhang@ntu.edu.sg

**Received:** March 15, 2019; **Accepted:** May 30, 2019; **Published Online:** July 3, 2019

**Citation:** Zhang Y, 2019, 3D-Printing for microfluidics or the other way around? Int J Bioprint, 5(2): 192. http://dx.doi.org/10.18063/ijb.v5i2.192

## 1. Introduction

Microfluidics is already a mature technology that is widely adopted in the bioanalytical investigation, clinical diagnostics, and chemical sensing and synthesis. Microfluidic technology has many compelling advantages over its bulk flow counterpart, such as low reagent and sample consumption, favorable thermodynamics and chemical reaction kinetics, laminar flow profile, precise handling of single bioparticles, and high degree of parallelization and multiplexing[1-4]. Many advanced analytical systems, such as next-generation sequencers and molecular diagnostic platforms, incorporate certain microfluidic components these days.

Conventional fabrication of microfluidic devices heavily relies on micromachining techniques. The earlier fabrication methods are derived from techniques used in microelectronic and mechanical systems (MEMS). Various microfluidic components are created by etching microstructures into silicon. The well-established MEMS technology is readily applied to the fabrication of microfluidic chips, giving microfluidics a Kickstart. Innovations in silicon-based microfluidic networks, actuators, pumps, mixers, and valves emerge at a rapid rate, giving rise to many novels and unique microfluidic applications such as cell sorting and trapping, biochemical sensing, genetic analysis, and drug delivery[5-9]. In spite of their great potential to revolutionize biomedical research, these silicon-based microfluidic devices experience difficulty when trying to find their way into biological laboratories, and one of the main obstacles is the complicated fabrication workflow. Although engineers may think that the fabrication of

Three-dimensional-printing for microfluidics or the other way around? © 2019 Zhang. This is an Open Access article distributed under the terms of the Creative Commons Attribution-NonCommercial 4.0 International License (http://creativecommons.org/licenses/by-nc/4.0/), permitting all non-commercial use, distribution, and reproduction in any medium, provided the original work is properly cited.

silicon-based microfluidic devices is simpler compared to MEMS devices, it is still a daunting task for biomedical researchers to take on. This issue is not resolved until the polydimethylsiloxane (PDMS)-based soft lithography, which is a simple molding-based fabrication technique, is developed[10]. Although traditional micromachining process is still involved in PDMS-based fabrication, it is limited to the making of molds. With the ready-made mold, the chip fabrication workflow is reduced to pouring PDMS, punching access ports and bonding PMDS to glass. Compared to the silicon-based microfluidic devices, PMDS-based devices find a bigger audience among biomedical researchers. The PDMS-based device is made more popular by the invention of PDMS-based multilayer pneumatic valves and pumps[11], which enables system-level integration of multifaced devices for intricate tasks such as single-cell analysis[3,12].

The PDMS-based microfluidics has its pros and cons. On the one hand, PDMS is able to precisely replicate the lithographically defined patterns with nanometer resolution. In addition, PDMS is biocompatible and well-suited for cell studies[13-15]. It also has favorable optical properties such as great transparency and low autofluorescence, which is compatible with various optical sensing modalities. The low cost of PDMS and the reusability of the mold make PDMS-based microfluidic devices reasonably affordable. On the other hand, PDMS is water vapor permeable. Samples in PDMS chips are susceptible to evaporation and bubbles in the event of a heating or prolonged incubation. PDMS is also prone to protein fouling, which would affect the accuracy of biosensing. Furthermore, the fabrication of a PDMS-based microfluidic device still heavily relies on manual assembly.

Nowadays, as microfluidic devices are designed to tackle more intricate tasks, the architecture of microfluidic devices becomes more complex, and more sophisticated fabrication techniques are in demand. Therefore, it is sensible to fabricate microfluidic devices by three-dimensional (3D)-printing, which is well-recognized for its unique ability to monolithically fabricate complex structures using a near-net-shape additive manufacturing process. As a matter of fact, a great number of 3D-printed microfluidic devices have been reported in the past few years followed by several review papers that provide a fairly comprehensive evaluation of these devices and an optimistic future outlook on 3D-printed microfluidics[16-20]. One of the reviews even touts 3D-printing as the upcoming revolution in microfluidics[21].

While majority studies employ 3D-printing for microfluidic device fabrication, a number of studies go the other way around and incorporate microfluidic components in 3D-printers for added functions and improved printing performance. These microfluidic components offer excellent fluidic control of 3D-printing inks, simplifying multi-material, and high-throughput parallel printing. The laminar flow profile of microfluidics allows concurrent printing of multiple inks through a single nozzle and time-controlled crosslinking of hydrogel inks using hydrodynamic focusing. Furthermore, additional functional components, such as surface acoustic waves, can be incorporated to modulate the distribution of chemical constituents in multiphase inks. These works point out a new direction in which 3D-printing and microfluidics could work synergistically to accomplish previously unattainable tasks.

In this perspective article, we evaluate the up-to-date development of 3D-printed microfluidics and microfluidics-enabled 3D-printing with a strong emphasis on their limitations. We would express our opinions on the future innovations required to overcome these limitations and to develop new high-value applications. We hope to answer whether 3D-printing is more well-suited for microfluidics or it is the other way around, but we will leave the discussion open.

## 2. 3D-printing for Microfluidics

3D-printing is an umbrella term encompassing a number of additive manufacturing technologies, but not all of them are applicable to printing microfluidic devices. Based on their suitability for microfluidics, we loosely categorize 3D-printing into extrusion-based technology (e.g., fused deposition modeling [FDM]), liquid resin-based technology (e.g., stereolithography [SLA], digital light processing, and two-photon polymerization [2PP]) which also includes inkjet-based 3D-printing (e.g., material jetting) due to the similar curing mechanism, powder-based technology (e.g., Multi Jet Fusion [MJF], selective laser sintering [SLS], selective laser melting [SLM], and electron beam melting), and other less common 3D-printing technologies. The technical aspects of these 3D-printing technologies have been discussed extensively in many reviews[16-21]; hence, we will skip it in this article. Majority of microfluidic devices are fabricated with extrusion-based technology or liquid resin-based technology.

The fabrication of microfluidic devices by 3D-printing can be either direct or indirect. Direct 3D-printing constructs the microfluidic chip by enclosing the microchannels and other microfluidic components with the ink materials. Indirect 3D-printing produces a mold using the ink materials, and the chip is fabricated by casting PMDS against the mold. The final microfluidic chip does not consist of any ink materials. In this perspective article, we will mainly focus on the direct printing approach except in a few cases in which a sacrificial mold is required for complex 3D microfluidic networks.

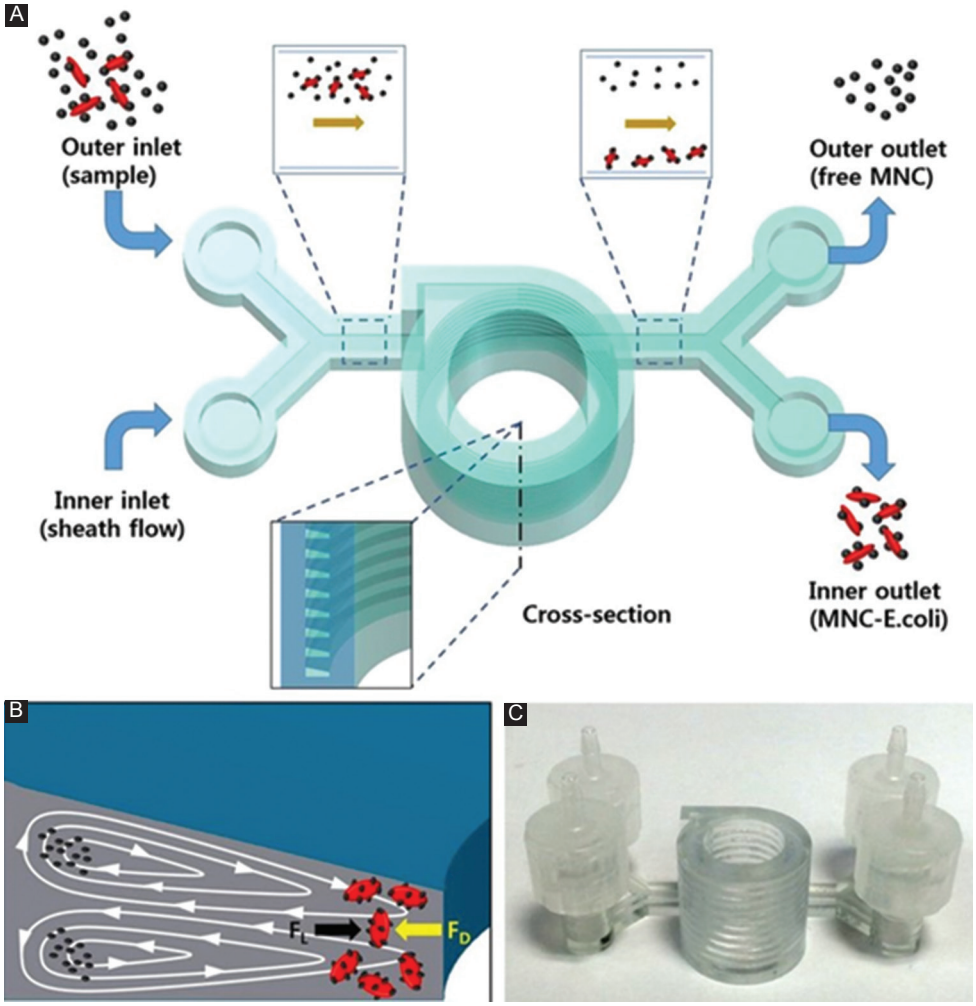


**Figure 1.** A three-dimensional (3D)-printed true 3D microfluidic device with standard fluidic coupling. (**A**) The schematic illustration of the 3D-printed device showing the cross-section of the 3D helical channel. (**B**) The cross-section of the channel is trapezoid in shape. (**C**) The actual 3D helical microfluidic device. Reproduced from Ref. Lee *et al*.[27] with the permission granted under the creative common license.

## 2.1. Current Development in 3D-printed Microfluidics

Research in 3D-printed microfluidics aims to create functional microfluidic components, realize complex microfluidic architecture, and demonstrates biomedical applications.

Earlier work in this field primarily focused on the monolithic fabrication of conventional microfluidic devices to bypass the traditional microfabrication. These microfluidic devices fabricated by 3D-printing were limited to those with only basic passive microfluidic components, such as microchannels and microchambers. Donvito *et al.* printed a monolithic microfluidic device with a T-junction using inkjet-based 3D-printing for microdroplet generation[22]. Chen *et al.* fabricated a microplate reader-compatible microfluidic device using an inkjet-based technique and demonstrated quantitative blood testing on this device[23]. Kitson *et al.* developed several types of 3D-printed chemical reactionware using FDM for both organic and inorganic synthesis[24]. Bishop *et al.* also printed a single-channel microfluidic device with standard interface connectors using FDM for nanoparticle preparation[25]. Takenaga *et al.* developed an SLA-printed biocompatible microfluidic device with integrated biosensor for the study of cell culture conditions[26].

The most notable revolution that 3D-printing brings to microfluidics is the ability to freely design and fabricate in the third dimension. 3D-printing transforms the conventional planar microfluidic features into convoluted 3D microfluidic networks packed into a small footprint. It enables monolithic fabrication of overlapping microfluidic components stacked in the vertical direction, bypassing the multi-layer bonding process required in traditional microfluidic fabrication. The true 3D microfluidic architecture offers an additional degree of freedom for fluidic manipulation. Several groups explore

3D-printing's unique ability to monolithically create 3D structures to realize true 3D microfluidic architectures that were unattainable by the traditional microfabrication techniques. Lee *et al.* fabricated a helical channel using SLA for inertia-based bacteria separation (Figure 1). The helical channel spiraled up in the z-direction and formed a true 3D microchannel with a trapezoid cross-section[27]. The 3D helical design significantly reduced the device footprint compared to the planer spiral design. Shallan *et al.* used a liquid resin-based 3D printer to fabricate 3D microchannels for more efficient passive mixing[28]. Monaghan *et al.* developed a 3D microfluidic device coupled with optical fibers to monitor chemical synthesis[29]. The group used the same approach to fabricate a 3D tree-like chemical gradient generator with reduced footprint and high portability[28]. Cabot *et al.* used a similar 3D-printed microfluidic passive mixer to improve sample mixing in a capillary electrophoresis assay that measured the p$K_a$[30]. A highly complex interconnected 3D microfluidic network was fabricated by casting epoxy or agarose against a 3D-printed sacrificial mold[31]. After casting, the mold made of isomalt was dissolved to clear space for microfluidic channels. 3D-printing also enabled easy integration of chip-user interface that coupled the external fluid into the microfluidic chip. A good example was demonstrated by Anderson *et al*. who fabricated a microfluidic drug screening platform that incorporated standard membrane devices for the cell culture and standard thread fitting for the coupling of tubing[32]. Another example was demonstrated by Au *et al*. who printed a Luer lock fitting on the microfluidic device as a standard fluid connector[33].

One of the reasons for PDMS being so popular in microfluidics is due to its high flexibility that enables the fabrication of multilayer pneumatic valves and pumps. Each multilayer pneumatic valve consists of two overlapping crisscross microchannels separated by a thin PDMS membrane at the intersection. One of the microchannels carries the sample fluid, and the other one carries the control fluid (sometimes just air). When the control channel is pressurized, the thin PDMS membrane deflects, creating a bulge that blocks the fluidic channel. The enabling factor of the multilayer pneumatic valve is the low Young's modulus of PDMS, which allows the thin membrane to deflect easily. In contrast, most 3D-printed plastic materials have Young's modulus hundreds or thousands of times larger than PDMS, which makes it difficult to pneumatically deflect the 3D-printed membrane. Nevertheless, using relatively flexible plastic, active valving has been demonstrated in a 3D-printed monolithic microfluidic device (Figure 2). In this work, Au *et al.* printed a multilayer membrane valve using watershed (a biocompatible resin) with Young's modulus of 2.7 GPa[20]. The diameter and thickness of the circular membrane were 5 mm and 100 μm, respectively. The membrane would deflect by ~200 μm under 2.9 psi pressure. Due to the large Young's modulus, the size of the membrane was considerably larger than the PDMS-based valve to achieve the required deflection for valve closure. A similar circular membrane valve was demonstrated by Gong *et al*.[34] By pushing the thickness of the membrane down to ~20 μm, they were able to reduce the diameter of the membrane to ~1 mm and pack the valves into a dense array. The required diameter of the membrane in the valve at various membrane thickness was studied by Rogers *et al*.[35] The same design was also used as an active Micropump in 3D-printed microfluidics[34]. A 3D-printed Quake valve was demonstrated by Keating *et al*. using an inkjet-based technique that is capable of printing multiple materials[36]. Tangoplus, a rubber-like flexible material was used to print the membrane while other parts of the microfluidic device were printed with rigid plastic material. Nonetheless, Tangoplus was less flexible than PDMS, and the dimension of the control channel was in the millimeter range. In addition to active valves, passive valves were also created in 3D-printed microfluidic devices. These were usually one-way check valves similar to those in silicon-based MEMS device. Sochol *et al.* printed microfluidic circuitry components, such as fluidic diodes and transistors, by incorporating these designs[37]. Chen *et al.* incorporated these passive valves to prevent backflow in a 3D-printed microfluidic multi-chamber cell culture device that modeled the circulatory system[38].

Another enhancement brought to microfluidics by 3D-printing is device modulation. With 3D-printing technology, it is straightforward to fabricate individual modules, each of which contains a single microfluidic component and to incorporate standard connectors on the individual modules for easy assembly. Bhargava *et al.* 3D-printed cubes with a female port and a male connector (Figure 3)[39]. These cubes, which functioned as microfluidic modules, created elastic reversible liquid-tight seals when coupled together. Microfluidic components, such as straight channels, helical channels, and reaction chambers, were embedded in these modules. Non-fluidic components, such as optical components, were also introduced into individual modules. A fully functional 3D microfluidic network was constructed by plug-and-play. Lee *et al.* developed a 3D-printed modular microfluidic system assembled together with horseshoe-shaped pins that functioned somewhat like a stapler bullet[40]. To prevent leakage, O-rings were used at the fluidic interface between the modules. Nie *et al.* designed lego-like microfluidic modules with press-fit connectors along the edge of each modular block. Due to the poor sealing, this system was only designed for capillary-driven flow and could not operate under high

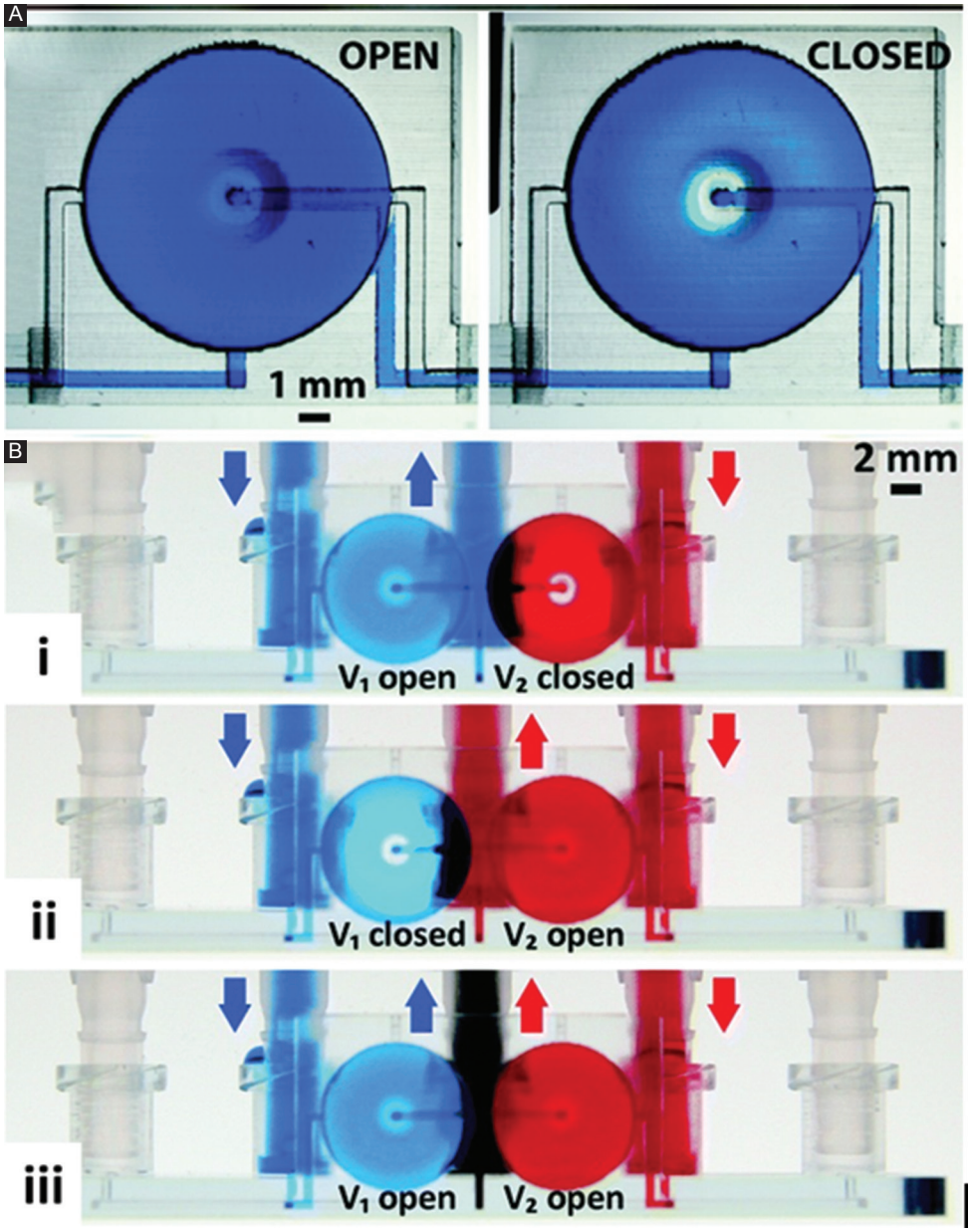


**Figure 2.** Three-dimensional (3D)-printed active microfluidic membrane valve. (**A**) The valve is open and closed configuration. (**B**) Fluidic control with the valve. (i) Valve 1 ($V_1$, left) is open and valve 2 ($V_2$, right) is closed. Only blue liquid flows in the central channel. (ii) V1 is closed and V2 is open. Only red liquid flows in the central channel. (iii) Both valves are open. A mixture of blue and red liquids flow in the central channel. Reproduced from Ref. Au *et al*.[20] with permission from Royal Chemical Society.

pressure. Vittayarukskul and Lee built a truly Lego-like modular microfluidic platform with 3D-printed parts[41]. The microfluidic modules were embedded in the Lego-patented building block[42]. In this design, the motherboard was fabricated by direct 3D-printing, whereas the individual modules were fabricated by casting PDMS against 3D-printed molds. A 3D microfluidic network was constructed by stacking the modules through the press-fit Lego interface. The PDMS acted as a rubber seal to prevent the leakage. Another reconfigurable microfluidic system was reported by Po, which used magnets to couple of individual modules[43]. Two ring magnets were embedded at the two ends of each modular block. The magnetic force pulled two adjacent modules together tightly enough to prevent fluid leakage. The center hole in the ring magnet provided access for fluids at the interface.

## 2.2. 3D-Printed Microfluidics, Are We There Yet?

It seems 3D-printing technology has brought many innovations to microfluidics. Many complex microfluidic architectures and novel fabrication approaches have only been made possible through the use of 3D-printing.

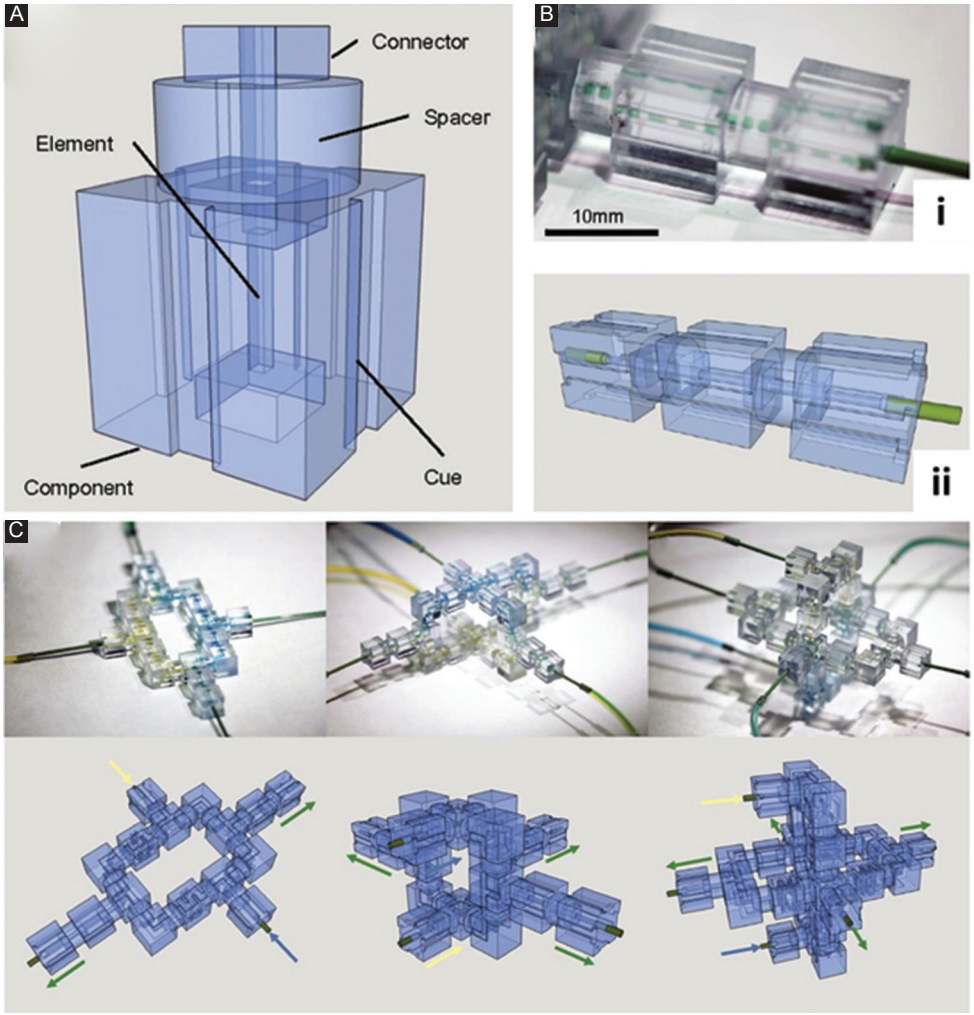


**Figure 3.** Three-dimensional (3D)-printed modular microfluidics. (**A**) Individual microfluidic module. (**B**) A microfluidic droplet generator is constructed by cascading three 3D-printed modules. (**C**) Several complex 3D microfluidic configurations constructed from 3D-printed microfluidic modules. Reproduced from Ref. Bhargava *et al*.[39] with permission from the National Academy of Science (US). Copyright (2015) National Academy of Sciences.

3D-printing also shortens the time required from design to fabrication, providing a valuable rapid prototyping tool for microfluidic devices. But has microfluidics truly benefited from these innovations? Since the first demonstration of the microfluidics-based "lab on a chip" in the 1990s, microfluidics has made a significant process. Nowadays, microfluidics is already a mature technology that enjoys its prosperity in biomedical fields. The research emphasis on microfluidics has gradually shifted from the device fabrication techniques, the fundamental physics of fluidic behaviors, and fluidic actuation and sensing mechanisms, to high-value applications, such as large-scale single-cell/molecule analysis for genomic and proteomic studies as well as sample-to-answer total analysis for point-of-care diagnostics[1]. Therefore, any present and future development in microfluidics ought to be oriented toward specific applications for high scientific and social impact. That is not to say new fabrication technologies, such as 3D-printing, are not in demand, but these new technologies must bring new values and fulfill requirements dictated by the applications.

In spite of its many compelling advantages, 3D-printing faces unique problems that may hinder its applicability in microfluidics for high-value applications.

One of such problems is the limited printer resolution, particularly in the lateral direction. The lateral resolution of a 3D-printer is determined by the minimal line width generated in a single pass, and the vertical resolution is determined by the minimal thickness of each layer. The extrusion-based printers, such as FDM, have a lateral resolution of hundreds of microns and a vertical resolution of tens of microns. The resolution of liquid resin-based printers, such as SLA and inkjet, has a lateral resolution of tens of microns and a vertical resolution of down to single-digital microns[44]. (Although 2PP is also a liquid resin-based 3D-printing technology, it is a

breed of its own, which we will discuss separately in later sections.) Although many 3D-printing systems claim a printing resolution in the true microscale (<100 μm), the actual size of 3D-printed microfluidic features mostly fall in the millimeter to the submillimeter range, because each feature is constructed by several 3D-printed lines. In a rough estimate, the minimal size of a microfluidic feature is one order of magnitude larger than the printer resolution[45]. Many current high-value applications of microfluidics require a high degree of parallelization and the ability to handle micro-objects such as single cells, both of which demand microfluidic features with a size ranging from several microns to tens of microns. For example, the microfluidic feature in the microdroplet generator chip, which is used to create microscale droplets to encapsulate single cells, usually contains features in the range of tens of microns[3,46]. To achieve a microfluidic feature in this size range, the printer resolution has to reach single-digital microns or even lower. Although some of the latest liquid resin-based 3D printers have a submicron vertical resolution, their lateral resolution is still not high enough[47]. So far, the only 3D-printing technology that is capable of true microscale fabrication is 2PP. 2PP pushes the printer resolution to the diffraction limit of the optics, reaching a submicron printer resolution in both lateral and vertical directions. Many amazing 3D microstructures have been fabricated using 2PP. However, the problem of 2PP is its slow printing speed. In addition to the microscale features, the microfluidic devices also consist of other macroscale features. These large features would take too long for 2PP to print, which defeats the whole purpose of rapid prototyping using 3D-printing.

The quality of the 3D-printed microfluidic devices is another big concern. First, the dimension fidelity of 3D-printing is poor at the microscale. In one study, the measured dimension of millimeter and submillimeter features is <6% off nominal[29]. However, when attempting to print true microscale features (<100 μm), the measured dimension is more than 60% off-nominal (Table 1). In addition, the side wall of the 3D-printed microfluidic channel may be leaning, resulting in an undesired trapezoid cross section. Second, the surface of 3D-printed parts is known to be rough with evident welding lines between layers. In bulk parts, the external surface can be easily polished. In 3D-printed microfluidic devices, it is almost impossible to polish the internal surface of the microfluidic components. Besides the welding lines, the surface of 3D-printed microfluidic components is often speckled with particulates and microcavities[48]. The desire to achieve a smooth surface in microfluidics is beyond esthetics but rather a practical concern. The imperfections may substantially alter the flow behavior and the way the surface interacts with biomolecules, leading to unexpected analytical outcomes. To improve the surface quality of 3D-printed microfluidic features, one could either improve the printer resolution or develop micro polishing techniques to smoothen the surface post printing.

**Table 1.** Dimension fidelity of microfluidic channels printed with SLA. Reproduced from Ref. Monaghan *et al.*[29] with permission from the Royal Chemical Society.

| Channel width (μm) | Distance to the next channel in CAD model (μm) | Measured width on test piece (μm) |
|---|---|---|
| 500 | 1000 | 949±2.64 |
| 500 | 500 | 494±2.10 |
| 500 | 250 | 258±1.94 |
| 500 | 125 | 130±4.49 |
| 500 | 62.5 | 104±0.84 |

SLA: Stereolithography; CAD: Computer-aided design

Several other issues of 3D-printed microfluidic devices, such as biocompatibility and optical transparency, have also been noted[16,18,21]. However, these problems have been mitigated with the development of new materials. Nevertheless, a more systematic investigation of these materials would greatly benefit the community.

## 2.3. Future of 3D-printed Microfluidics

To answer the question set in the previous section, I do not believe 3D-printed microfluidics is quite there. The upcoming 3D-printing revolution in microfluidics might be on its way, but definitely not in sight yet. Thus far, 3D-printing has only been used as an alternative fabrication technique for microfluidics, hence does not add much new value to the field. The functions of most reported 3D-printed microfluidic devices can be easily realized by conventional microfluidic devices fabricated using 2D lithography techniques. Compared to the flattened 2D microfluidic network, the 3D microfluidic network does not show significant advantages.

3D-printing adds value by offering monolithic near-net-shape fabrication of complex structures. To truly revolutionize microfluidics, in addition to improving the printer resolution, 3D-printing must also improve its capability of multi-material, multiprocess, and multiscale printing to monolithically create highly integrated and multifunctional microfluidic devices for high-value biomedical applications.

Besides the microfluidic architecture, a fully functional bioanalytical microfluidic platform also includes sensing elements, solid substrate for molecule and cell adsorption, active actuators, and other components. In traditional lithography-based microfabrication, these components are usually fabricated separately and assembled manually at the chip bonding stage. Solid substrate and surface modification are usually introduced post-fabrication by packing additional materials (e.g., particles or gel matrix) in the microfluidic network or through *in situ* chemical reactions. At present, several inkjet-based 3D

printers are able to concurrently print multiple materials. A rigid microfluidic device with flexible membranes as the pneumatic valve has been demonstrated using this approach[36]. Nevertheless, the number of materials that can be printed concurrently is small, and they can only be printed using the same process. The ultimate goal is to be able to print complex microfluidic devices with many types of materials, such as a rigid plastic microfluidic chip with flexible membranes, metal electrodes, hydrogel matrix, nanoparticle-packed beds, and magnetic composite actuators, all in one go.

To accomplish multi-material printing, multiple printing processes must be integrated to cope with different bonding mechanisms. While plastic materials can be printed by extruding molten plastic or crosslinking photopolymer resins with a low-energy light source, metal powders require a high-energy laser or electron beam to bond together. Furthermore, the material feeding mechanisms are also drastically different for different 3D-printing processes. In FDM, material is fed to the extruder in the form of filaments; in SLA, liquid-resin is kept in a reservoir and reflows after each layer is printed; in inkjet printers, liquid resins are feed to the printhead through a tubing; and in SLS and SLM, precursor materials in the form powders are loaded into a powder bed and spread by a roller after each layer is printed. These material bonding and feeding mechanisms are incompatible. To realize multiprocess printing, the partially printed parts need to be transferred between platforms, and the printing processes must have the ability to resume from the breakpoint. A technique known as the print-pause-print (PPP) is able to suspend the printing process for users to add prefabricated components (e.g., electrodes) to the partially printed parts and resume the printing from the breakpoint to embed these added parts within the 3D-printed microfluidic device[49]. This technique points out a possible direction for multiprocess 3D-printing. However, it does not address the challenges associated with the cross-platform transfer of the partially printed parts.

The quality of 3D-printed microfluidic devices can be significantly improved using ultrahigh-resolution 3D-printing technologies such as 2PP. However, it would be impractical to print the entire microfluidic device solely using 2PP due to the extremely slow printing speed. In many microfluidic devices, a large portion of the device body plays a structural rather than functional role, which means a big part of the device body can be printed with a fast and low-resolution process. Only the parts that form the microfluidic architectures need to be printed with a high-resolution process. These parts contain microscale structures that directly interact with the fluids; hence, their surface quality is more critical. Therefore, multiscale 3D-printing that provides both high-speed and high-resolution fabrication of microfluidic devices is highly coveted. The multiscale 3D-printing must be able to adjust the printing resolution and printing speed according to the required specifications.

## 3. Microfluidics for 3D-printing

The relationship between 3D-printing and microfluidics could go the other way around. Microfluidics could also serve as the enabler of 3D-printing technologies. Extrusion-based 3D-printing is one of the most popular technologies, especially in bioprinting. As the scope of bioprinting expands, the type of materials to be printed becomes more and more intricate. New applications often require printing multiphase and multicomponent materials that cannot be handled by the conventional extrusion printhead. Microfluidics, with its exceptional ability to manipulate a small amount of fluids, has been incorporated into the printhead to add a layer of fluidic control for sophisticated bioprinting.

### 3.1. Current Development in Microfluidics-enabled 3D-printing

As a matter of fact, microfluidic components are employed in inkjet 3D printer, such as MJF, to dispense liquid in the form of droplets through microfabricated nozzles. More complex microfluidics-enabled 3D-printing arises from the need to print hydrogel fibers with controlled gelation and composition. Early solutions employ coaxial flow to extrude hydrogel microfibers with cells encapsulated in the fiber core. Ozawa *et al.* created a coaxial flow system by cascading tapered capillary tubing[53]. The coaxial flow focused the cell suspension in the first capillary into the core of the fiber. The gel matrix precursor was injected from the second capillary to encapsulate the core flow. The gelling agent was introduced as the sheath flow from the third capillary, crosslinking the gel matrix and forming a coaxial fiber. Pancreatic β cells encapsulated in these microfibers maintained their viability and functions. Similar approaches were demonstrated by several other groups. Instead of cascaded capillary tubing, a manifold with two orthogonal inlets and a nozzle outlet as the printhead was used to couple the gel matrix precursor and the gelling agent into a coaxial flow. The printing of alginate hydrogel microfibers was demonstrated using this setup in which the cell-laden alginate was focused by the sheath flow containing $Ca^{2+}$[54-56]. The manifold could be replaced by a microfluidic chip with the same configuration and function[57,58]. Capillary tubing or needles were inserted into the microfluidic channel to generate the coaxial flow.

Microfluidics has since moved beyond the simple coaxial flow. In addition to microchannels, various types of microfluidic components have been included in

the printhead to achieve more sophisticated extrusion-based 3D-printing. Microfluidics is skilled at combining multiple flows from separate inlets into a single stream. Due to the low Reynolds number, materials stay in separate laminar layers in a single microfluidic channel; hence, different materials can be printed in close proximity. Colosi *et al.* fabricated a simple two-inlet microfluidic chip as the printhead (Figure 4A and B)[50]. Two separate bioinks were introduced into the microfluidic chip from the two inlets and combined into a single stream. Although extruded as a single hydrogel fiber, the two bioinks stay separate. A similar two-channel design was demonstrated by Hardin *et al*.[59] By adjusting the flow rate at the two inlets, seamless switching between different materials during printing was accomplished. Wei *et al.* demonstrated a multi-inlet microfluidic printhead[60]. Cells, hydrogel precursors, sacrificial material, and water were introduced into the microfluidic chip from separate inlets. These materials were hydrodynamically focused into a single outlet channel and extruded from the nozzle for bioprinting. By adjusting the relative flow rate at the inlets, the same printhead could print cell-laden solid hydrogel fiber, cell-laden hollow hydrogel fiber, and hollow double-layered hydrogel fiber. Leng *et al.* took a step further and developed a programmable multi-inlet microfluidic printhead[61]. The seven inlets for bioinks were individually controlled by solenoid valves. A base biopolymer was introduced into the printhead from a separate channel and extruded continuously from a wide nozzle, forming a polymer ribbon that served as a substrate on which the bioinks were deposited. The opening and closing periods of the solenoid valves determined the extrusion length of the bioink from each of the seven nozzles thus the patterns printed with the bioinks on the base biopolymer substrate. Using this approach, authors were able to print hydrogel sheets with well-controlled pores.

Microfluidics is capable of keeping different bioinks in separate layers; even they are in close proximity. Nonetheless, in certain scenarios, it is desirable to blend multiple materials to create a multicomponent but homogeneous bioink. Fortunately, the mixing in

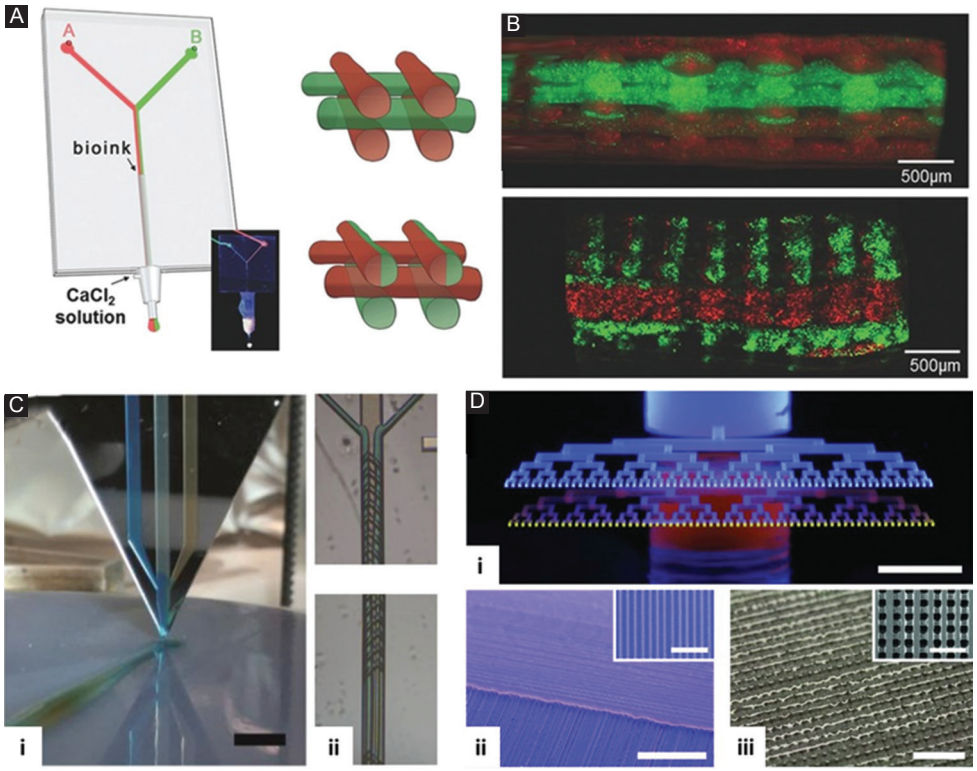


**Figure 4.** Microfluidics-enabled three-dimensional-printing. (**A**) Two-inlet microfluidic devices used as the printhead. Two bioinks are combined into a single micro hydrogel filament for extrusion. (**B**) Hydrogels printed using the microfluidic printhead shown in **A**. Each filament consists of two bioinks combined by the microfluidic printhead. (**C**) A three-inlet microfluidic printhead with passive mixer. (i) Schematic illustration of bioprinting with the microfluidic printhead. (ii) Herringbone passive mixer in the microfluidic printhead. (**D**) High-throughput parallel microfluidic printhead. (i) A high-degree of parallel printing with a bifurcating microfluidic network. (ii) and (iii) Microfilament arrays printed with the microfluidic printhead. **A** and **B** are reproduced from Ref. Colosi *et al*.[50] with permission from Wiley. **C** is reproduced from Ref. Serex *et al*.[51] with the permission granted under the creative common license. **D** is reproduced from Ref. Hansen *et al*.[52] with permission from Wiley.

microfluidics has been studied extensively. Numerous mixing strategies have been developed specifically for microfluidics. Designs of microfluidic mixers, both passive and active, have been incorporated into the extrusion printhead to homogenize multiple bioinks. Serex *et al.* developed a 3-inlet microfluidic printhead[51]. Materials from the inlets merged in the outlet channel. Various microfluidic components could be added to the outlet channel for different purposes. To promote the mixing, a herringbone structure was added to the surface of the outlet channel. As the materials traveled down the outlet channel, the herringbone induced chaotic mixing and homogenized the mixture before extruding it for printing (Figure 4C). Ober *et al.* studied a propeller-based active mixer for the printhead[62]. As materials from different inlets entered the mixing chamber, the propeller efficiently homogenized them in low volumes over a short timescale. Using this approach, the authors printed a structure with a fluorescent concentration gradient obtained by mixing inks at different ratios.

Microfluidics also enables a range of unique fluidic operations, which leads to unique 3D-printing strategies. Microfluidics is well known for its capability of high-degree parallelization which has been explored for high-throughput printing. Hansen *et al.* developed a printhead with a multi nozzle array for parallel printing (Figure 4D)[52]. Bioinks were introduced to the printhead from a single inlet which bifurcated several times, forming up to 64 outlet channels and nozzles. The bifurcating microfluidic network ensured that the extrusion rate at all nozzles was the same. This printhead could significantly improve the printing speed of tissue engineering scaffolds, which usually consisted of a large number of repetitive structures. Composite materials were often printed with multiphase inks composed a liquid-phase resin and solid-phase particles. Microfluidic components were added to the printhead to pre-condition the multiphase ink for printing. One such operation was to concentrate the particles. Serex *et al.* added a passive crossflow filter to the microfluidic printhead, which removed liquid from the ink as it moved toward the nozzle, leading to a high concentration of particles in the extruded ink[51]. The particle concentration could also be realized with an active concentrator. Collino *et al.* incorporated an acoustic wave generator to localize the particles in the microfluidic printhead[63]. When particles were localized to the center of the channel, liquid on both sides was removed by side channels, concentrating the particles to the central channel for printing. The same strategy was used to distribute particles along the print line. Particles with different morphologies would respond differently to the acoustic wave, hence were localized to different positions along the microfluidic channel. Droplet microfluidics was a special type of microfluidic system in which one of the liquids was sheared into the discrete volume by another liquid, resulting in a train of droplets in the microfluidic channel. Li *et al.* used a droplet microfluidic device as the printhead to print hydrogels with embedded liquid droplets[64]. The printhead used the resin to shear the aqueous solution into droplets. Authors demonstrated the printing of self-healing polymer using this approach. When damaged, the embedded droplets at the damaged surface released chemical agents to repair the fracture. Visser *et al.* also used droplet microfluidics for bioprinting[65]. Instead of generating droplets in a microfluidic channel, a piezo-actuated dispenser ejected droplets of hydrogel precursor in the air which later ran into a liquid stream of crosslinker that was also ejected in air. The hydrogel beads generated by the free-space droplet microfluidic system were used as the building block for bioprinting.

### 3.3. What is Next for Microfluidics-enabled 3D-printing?

The incorporation of microfluidic technology in 3D printing could potentially disrupt the current norm. Fluidic operations, such as mixing, sorting, and hydrodynamic focusing, can be further explored to promote the development of new 3D printers or even hybrid 3D-printing process.

Advances in microfluidics, particularly the development of new microfluidic modalities, would also bring new opportunities to 3D-printing. There are many types of microfluidic systems in addition to the conventional closed-channel microfluidics. In a way, 3D-printing is analogous to building construction. The current extrusion-based bioprinting is equivalent to pouring concrete on site. However, buildings could also be constructed with precast modular blocks so is 3D-printing. Instead of curing the ink *in situ*, inks can be pre-shaped into standard modular blocks, and the 3D construction is accomplished by moving these modular blocks to designated locations. Take digital microfluidics, for example, digital microfluidics manipulates discrete droplets on an open surface with a large degree of freedom. It provides an excellent tool to prefabricate discrete building blocks as well as a means to remotely actuate these building blocks. For example, magnetic digital microfluidics manipulates droplets by a magnet through the magnetic particles added to the droplet. It has the ability to move droplets across platforms in 3D with the assistance of surface modifications. Magnetic digital microfluidics could be applied to the manipulation of precast hydrogel blocks for 3D construction.

## 4. Conclusion and Future Perspective

In this work, we take a critical look at both 3D-printed microfluidics and microfluidics-enabled 3D-printing

technology. Certain opinions might be a bit harsh, but our conclusion that neither field is established well enough to make an impact would stand. The capability of 3D-printed microfluidics has not surpassed its conventional counterpart. An alternative fabrication method is unlikely to make a disruptive advancement to a well-established field of microfluidics. Microfluidics-enabled 3D-printing brings more possibility to multimaterial and multiphase printing, but it is currently limited to extrusion-based 3D-printing and faces difficulty in extending to other 3D-printing modalities.

For 3D-printed microfluidics to make a real impact, new multimaterial, multiprocess and multiscale 3D-printing technologies must be developed to address the issues such as surface quality, fabrication speed, and multifunctionality. 3D-printed microfluidics will only be recognized as a field of its own if a multicomponent 3D microfluidic device for high-value biomedical applications can be monolithically fabricated within a reasonably short timeframe. This goal might be achieved by applying microfluidics-enabled 3D-printing to 3D-printed microfluidics, which would provide better control for multimaterial and multiphase printing. In any case, there is still a long way to go.

## Acknowledgment

The author would like to thank the funding support from Nanyang Technological University (Start Up Grant), National Additive Manufacturing Innovation Cluster (NAMIC Singapore, 2017135), Ageing Research Institute for Society and Education (ARISE Singapore, ARISE/2017/22) and Singapore Ministry of Education (Tier 1, RG49/17). This research was conducted in collaboration with HP Inc. and supported/partially supported by the Singapore Government through the Industry Alignment Fund -Industry Collaboration Projects Grant.

## References

1. Whitesides GM, 2006, The Origins and the Future of Microfluidics. *Nature*, 442(7101):368.
2. Mitchell P, 2001, Microfluidics-downsizing Large-scale Biology. *Nat Biotechnol*, 19(8):717.
3. Yin H, Marshall D, 2012, Microfluidics for Single Cell Analysis. *Curr Opin Biotechnol*, 23(1):110-9.
4. Weibel DB, Whitesides GM, 2006, Applications of Microfluidics in Chemical Biology. *Curr Opin Chem Biol*, 10(6):584-91.
5. Grayson ACR, Shawgo RS, Johnson AM, *et al.*, 2004, A bioMEMS Review: MEMS Technology for Physiologically Integrated Devices. *Proc IEEE*, 92(1):6-21. DOI 10.1109/jproc.2003.820534.
6. Ziaie B, Baldi A, Lei M, *et al.*, 2004, Hard and Soft Micromachining for BioMEMS: Review of Techniques and Examples of Applications in Microfluidics and Drug Delivery. *Adv Drug Deliv Rev*, 56(2):145-72. DOI 10.1016/j.addr.2003.09.001.
7. Shawgo RS, Grayson ACR, Li Y, *et al.*, 2002, BioMEMS for Drug Delivery. *Curr Opin Solid State Mater Sci*, 6(4):329-34.
8. Tay FE, 2002, *Microfluidics and BioMEMS Applications*. Berlin, Germany: Springer.
9. Bashir R, 2004, BioMEMS: State-of-the-art in Detection, Opportunities and Prospects. *Adv Drug Deliv Rev*, 56(11):1565-86. DOI 10.1016/j.addr.2004.03.002.
10. Xia Y, Whitesides GM, 1998, Soft Lithography. *Angew Chem Int Ed*, 37(5):550-75.
11. Unger MA, Chou HP, Thorsen T, *et al.*, 2000, Monolithic Microfabricated Valves and Pumps by Multilayer Soft Lithography. *Science*, 288(5463):113-6. DOI 10.1126/science.288.5463.113.
12. Lecault V, White AK, Singhal A, *et al.*, 2012, Microfluidic Single Cell Analysis: From Promise to Practice. *Curr Opin Chem Biol*, 16(3-4):381-90.
13. Kim P, Kwon KW, Park MC, *et al.*, 2008, Soft Lithography for Microfluidics: A Review. *Biochip J,* 2:1-11.
14. Beebe DJ, Mensing GA, Walker GM, 2002, Physics and Applications of Microfluidics in Biology. *Ann Rev Biomed Eng*, 4(1):261-86.
15. Minteer SD, 2006, *Microfluidic Techniques: Reviews and Protocols*. Vol. 321. New York: Springer Science and Business Media.
16. Au AK, Huynh W, Horowitz LF, *et al.*, 2016, 3D-printed Microfluidics. *Angew Chem Int Ed*, 55(12):3862-81. DOI 10.1002/anie.201504382.
17. Yazdi AA, Popma A, Wong W, *et al.*, 2016, 3D Printing: An Emerging Tool for Novel Microfluidics and Lab-on-a-chip Applications. *Microfluid Nanofluidics*, 20(3):50. DOI 10.1007/s10404-016-1715-4.
18. Waheed S, Cabot JM, Macdonald NP, *et al.*, 2016, 3D Printed Microfluidic Devices: Enablers and Barriers. *Lab Chip*, 16(11):1993-2013. DOI 10.1039/c6lc00284f.
19. Ho CMB, Ng SH, Li KHH, *et al.*, 2015, 3D Printed Microfluidics for Biological Applications. *Lab Chip*, 15(18):3627-37. DOI 10.1039/c5lc00685f.
20. Au AK, Bhattacharjee N, Horowitz LF, *et al.*, 2015, 3D-printed Microfluidic Automation. *Lab Chip*, 15(8):1934-41. DOI 10.1039/c5lc00126a.
21. Bhattacharjee N, Urrios A, Kang S, *et al.*, 2016, The Upcoming 3D-printing Revolution in Microfluidics. *Lab*

*Chip*, 16(10):1720-42. DOI 10.1039/c6lc00163g.

22. Donvito L, Galluccio L, Lombardo A*, et al.*, 2015, Experimental Validation of a Simple, Low-cost, T-junction Droplet Generator Fabricated Through 3D Printing. *J Micromech Microeng*, 25(3):035013. DOI 10.1088/0960-1317/25/3/035013.
23. Chen C, Wang Y, Lockwood SY*, et al.*, 2014, 3D-printed Fluidic Devices Enable Quantitative Evaluation of Blood Components in Modified Storage Solutions for Use in Transfusion Medicine. *Analyst*, 139(13):3219-26. DOI 10.1039/c3an02357e.
24. Kitson PJ, Rosnes MH, Sans V*, et al.*, 2012, Configurable 3D-Printed Millifluidic and Microfluidic 'Lab on a Chip'reactionware Devices. *Lab Chip*, 12(18):3267-71. DOI 10.1039/c2lc40761b.
25. Bishop GW, Satterwhite JE, Bhakta S*, et al.*, 2015, 3D-printed Fluidic Devices for Nanoparticle Preparation and Flow-injection Amperometry Using Integrated Prussian Blue Nanoparticle-modified Electrodes. *Anal Chem*, 87(10):5437-43. DOI 10.1021/acs.analchem.5b00903.
26. Takenaga S, Schneider B, Erbay E*, et al.*, 2015, Fabrication of Biocompatible Lab-on-chip Devices for Biomedical Applications by Means of a 3D-printing Process. *Physica Status Solidi A*, 212(6):1347-52. DOI 10.1002/pssa.201532053.
27. Lee W, Kwon D, Choi W*, et al.*, 2015, 3D-printed Microfluidic Device for the Detection of Pathogenic Bacteria using Size-based Separation in Helical Channel with Trapezoid Cross-section. *Sci Rep*, 5:7717. DOI 10.1038/srep09701.
28. Shallan AI, Smejkal P, Corban M*, et al.*, 2014, Cost-effective Three-dimensional Printing of Visibly Transparent Microchips Within Minutes. *Anal Chem*, 86(6):3124-30. DOI 10.1021/ac4041857.
29. Monaghan T, Harding MJ, Harris RA*, et al.*, 2016, Customisable 3D Printed Microfluidics for Integrated Analysis and Optimisation. *Lab Chip*, 16(17):3362-73. DOI 10.1039/c6lc00562d.
30. Cabot JM, Fuguet E, Rosés M*, et al.*, 2015, Novel Instrument for Automated p K a Determination by Internal Standard Capillary Electrophoresis. *Anal Chem*, 87(12):6165-72. DOI 10.1021/acs.analchem.5b00845.
31. Gelber MK, Bhargava R, 2015, Monolithic Multilayer Microfluidics via Sacrificial Molding of 3D-printed Isomalt. *Lab Chip*, 15(7):1736-41. DOI 10.1039/c4lc01392a.
32. Anderson KB, Lockwood SY, Martin RS*, et al.*, 2013, A 3D Printed Fluidic Device that Enables Integrated Features. *Anal Chem*, 85(12):5622-6. DOI 10.1021/ac4009594.
33. Au AK, Lee W, Folch A, 2014, Mail-order Microfluidics: Evaluation of Stereolithography for the Production of Microfluidic Devices. *Lab Chip*, 14(7):1294-301. DOI 10.1039/c3lc51360b.
34. Gong H, Woolley AT, Nordin GP, 2016, High Density 3D Printed Microfluidic Valves, Pumps, and Multiplexers. *Lab Chip*, 16(13):2450-8. DOI 10.1039/c6lc00565a.
35. Rogers CI, Qaderi K, Woolley AT*, et al.*, 2015, 3D Printed Microfluidic Devices with Integrated Valves. *Biomicrofluidics*, 9(1):016501. DOI 10.1063/1.4905840.
36. Keating SJ, Gariboldi MI, Patrick WG*, et al.*, 2016, 3D Printed Multimaterial Microfluidic Valve. *PLoS One*, 11(8):e0160624. DOI 10.1371/journal.pone.0160624.
37. Sochol R, Sweet E, Glick C*, et al.*, 2016, 3D Printed Microfluidic Circuitry via Multijet-based Additive Manufacturing. *Lab Chip*, 16(4):668-78. DOI 10.1039/c5lc01389e.
38. Chen Y, Chan HN, Michael SA*, et al.*, 2017, A Microfluidic Circulatory System Integrated with Capillary-assisted Pressure Sensors. *Lab Chip*, 17(4):653-62. DOI 10.1039/c6lc01427e.
39. Bhargava KC, Thompson B, Malmstadt N, 2014, Discrete Elements for 3D Microfluidics. *Proc Natl Acad Sci*, 111(42):15013-8. DOI 10.1073/pnas.1414764111.
40. Lee KG, Park KJ, Seok S*, et al.*, 2014, 3D Printed Modules for Integrated Microfluidic Devices. *RSC Adv*, 4(62):32876-80. DOI 10.1039/c4ra05072j.
41. Vittayarukskul K, Lee AP, 2017, A Truly Lego®-like Modular Microfluidics Platform. *J Micromech Microeng*, 27(3):035004. DOI 10.1088/1361-6439/aa53ed.
42. Kirk CG, 1961, *Toy Building Brick*. Google Patents.
43. Yuen PK, 2016, A Reconfigurable Stick-n-play Modular Microfluidic System using Magnetic Interconnects. *Lab Chip*, 16(19):3700-7. DOI 10.1039/c6lc00741d.
44. Tumbleston JR, Shirvanyants D, Ermoshkin N*, et al.*, 2015, Continuous Liquid Interface Production of 3D Objects. *Science*, 347(6228):1349-52. DOI 10.1126/science.aaa2397.
45. Beauchamp MJ, Nordin GP, Woolley AT, 2017, Moving from Millifluidic to Truly Microfluidic sub-100-µm Cross-section 3D Printed Devices. *Anal Bioanal Chem*, 409(18):4311-9. DOI 10.1007/s00216-017-0398-3.
46. Mazutis L, Gilbert J, Ung WL*, et al.*, 2013, Single-cell Analysis and Sorting using Droplet-based Microfluidics. *Nat Protoc*, 8(5):870. DOI 10.1038/nprot.2013.046.
47. ASIGA. Available from: https://www.asiga.com/products/printers/pico. [Last retrieved on 2019 Jun 10].
48. Lee JM, Zhang M, Yeong WY, 2016, Characterization

and Evaluation of 3D Printed Microfluidic Chip for Cell Processing. *Microfluid Nanofluidics*, 20(1):5. DOI 10.1007/s10404-015-1688-8.

49. Li F, Macdonald NP, Guijt RM*, et al.*, 2019, Increasing the Functionalities of 3D Printed Microchemical Devices by Single Material, Multimaterial, and Print-pause-print 3D Printing. *Lab Chip*, 19(1):35-49. DOI 10.1039/c8lc00826d.
50. Colosi C, Shin SR, Manoharan V*, et al.*, 2016, Microfluidic Bioprinting of Heterogeneous 3D Tissue Constructs using Low-viscosity Bioink. *Adv Mater*, 28(4):677-84. DOI 10.1002/adma.201503310.
51. Serex L, Bertsch A, Renaud P, 2018, Microfluidics: A New Layer of Control for Extrusion-based 3D Printing. *Micromachines*, 9(2):86. DOI 10.3390/mi9020086.
52. Hansen CJ, Saksena R, Kolesky DB*, et al.*, 2013, High-throughput Printing via Microvascular Multinozzle Arrays. *Adv Mater*, 25(1):96-102. DOI 10.1002/adma.201370002.
53. Ozawa F, Okitsu T, Takeuchi S, 2017, Improvement in the Mechanical Properties of Cell-laden Hydrogel Microfibers using Interpenetrating Polymer Networks. *ACS Biomater Sci Eng*, 3(3):392-8. DOI 10.1021/acsbiomaterials.6b00619.
54. Gao Q, He Y, Fu JZ*, et al.*, 2015, Coaxial Nozzle-assisted 3D Bioprinting with Built-in Microchannels for Nutrients Delivery. *Biomaterials*, 61:203-15. DOI 10.1016/j.biomaterials.2015.05.031.
55. Colosi C, Costantini M, Latini R*, et al.*, 2014, Rapid Prototyping of Chitosan-coated Alginate Scaffolds through the use of a 3D Fiber Deposition Technique. *J Mater Chem B*, 2(39):6779-91. DOI 10.1039/c4tb00732h.
56. Gao Q, Liu Z, Lin Z*, et al.*, 2017, 3D Bioprinting of Vessel-like Structures with Multilevel Fluidic Channels. *ACS Biomater Sci Eng*, 3(3):399-408. DOI 10.1021/acsbiomaterials.6b00643.
57. Attalla R, Ling C, Selvaganapathy P, 2016, Fabrication and Characterization of Gels with Integrated Channels using 3D Printing with Microfluidic Nozzle for Tissue Engineering Applications. *Biomed Microdevices*, 18(1):17. DOI 10.1007/s10544-016-0042-6.
58. Ghorbanian S, Qasaimeh MA, Akbari M*, et al.*, 2014, Microfluidic Direct Writer with Integrated Declogging Mechanism for Fabricating Cell-laden Hydrogel Constructs. *Biomed Microdevices*, 16(3):387-95. DOI 10.1007/s10544-014-9842-8.
59. Hardin JO, Ober TJ, Valentine AD*, et al.*, 2015, Microfluidic Printheads for Multimaterial 3D Printing of Viscoelastic Inks. *Adv Mater*, 27(21):3279-84. DOI 10.1002/adma.201570145.
60. Wei D, Sun J, Bolderson J*, et al.*, 2017, Continuous Fabrication and Assembly of Spatial Cell-laden Fibers for a Tissue-like Construct via a Photolithographic-based Microfluidic Chip. *ACS Appl Mater Interfaces*, 9(17):14606-17. DOI 10.1021/acsami.7b00078.
61. Leng L, McAllister A, Zhang B*, et al.*, 2012, Mosaic Hydrogels: One-step Formation of Multiscale Soft Materials. *Adv Mater*, 24(27):3650-8. DOI 10.1002/adma.201290166.
62. Ober TJ, Foresti D, Lewis JA, 2015, Active Mixing of Complex Fluids at the Microscale. *Proc Natl Acad Sci*, 112(40):12293-8. DOI 10.1073/pnas.1509224112.
63. Collino RR, Ray TR, Fleming RC*, et al.*, 2016, Deposition of Ordered Two-phase Materials using Microfluidic Print Nozzles with Acoustic Focusing. *Extreme Mech Lett*, 8:96-106. DOI 10.1016/j.eml.2016.04.003.
64. Li X, Zhang JM, Yi X*, et al.*, 2018, Multimaterial Microfluidic 3D Printing of Textured Composites with Liquid Inclusions. *Adv Sci*, 6:1800730. DOI 10.1002/advs.201800730.
65. Visser CW, Kamperman T, Karbaat LP*, et al.*, 2018, In-air Microfluidics Enables Rapid Fabrication of Emulsions, Suspensions, and 3D Modular (bio) Materials. *Sci Adv*, 4(1):eaao1175. DOI 10.1126/sciadv.aao1175.

RESEARCH ARTICLE

# Exploring nanofibrous self-assembling peptide hydrogels using mouse myoblast cells for three-dimensional bioprinting and tissue engineering applications

**Wafaa Arab[1†], Kowther Kahin[1,2†], Zainab Khan[1,2†], Charlotte A. E. Hauser[1*]**

[1]Laboratory for Nanomedicine, Division of Biological and Environmental Science and Engineering, King Abdullah University of Science and Technology, Thuwal, Saudi Arabia
[2]Department of Electrical and Computer Engineering, College of Engineering, Effat University, Jeddah, Saudi Arabia
[†]These authors contributed equally to this work.

**Abstract:** Injured skeletal muscles which lose more than 20% of their volume, known as volumetric muscle loss, can no longer regenerate cells through self-healing. The traditional solution for recovery is through regenerative therapy. As the technology of three-dimensional (3D) bioprinting continues to advance, a new approach for tissue transplantation is using biocompatible materials arranged in 3D scaffolds for muscle repair. Ultrashort self-assembling peptide hydrogels compete as a potential biomaterial for muscle tissue formation due to their biocompatibility. In this study, two sequences of ultrashort peptides were analyzed with muscle myoblast cells (C2C12) for cell viability, cell proliferation, and differentiation in 3D cell culture. The peptides were then extruded through a custom-designed robotic 3D bioprinter to create cell-laden 3D structures. These constructs were also analyzed for cell viability through live/dead assay. Results showed that 3D bioprinted structures of peptide hydrogels could be used as tissue platforms for myotube formation – a process necessary for muscle repair.

**Keywords:** Three-dimensional bioprinting; Peptide; Biomaterials; Bioinks; Tissue engineering; Myoblasts

*Correspondence to: Charlotte A. E. Hauser, Laboratory for Nanomedicine, King Abdullah University of Science and Technology, Division of Biological and Environmental Science and Engineering, 4700 Thuwal, 23955-6900, Saudi Arabia; charlotte.hauser@kaust.edu.sa

**Received:** April 12, 2019; **Accepted:** May 07, 2019; **Published Online:** July 20, 2019

**Citation:** Arab W, Kahin K, Khan Z, *et al*., 2019, Exploring nanofibrous self-assembling peptide hydrogels using mouse myoblast cells for three-dimensional bioprinting and tissue engineering applications. Int J Bioprint, 5(2): 198. http://dx.doi.org/10.18063/ijb.v5i2.198

## 1. Introduction

Drastic muscle loss resulting from injury, birth defect, or cancer ablation restrains muscles' ability to reconstruct through self-healing, consequently requiring regenerative treatments through engineered tissues[1]. Around 45 million cases of reconstructive surgeries are reported yearly in the USA[2]. Autologous tissue transfer is the present treatment for massive tissue loss. However, patients undergo complications and functional restrictions resulted from harvesting tissues from a donor[3]. Moreover, the access to sufficient tissues and organs for all patients is nearly impossible, and many patients die waiting for available organs due to long transplant waiting lists. Furthermore, implanting compatible foreign biomaterials can cause dislodgment, fracture, and infection. These challenges have simulated a need to pursue and develop innovative approaches to deliver required tissue[4].

Skeletal muscle is a soft tissue that constitutes approximately half of the human adult body mass[5]. Muscles mass is profoundly affected by many factors such as nutritional level, hormonal status, physical activity,

Exploring nanofibrous self-assembling peptide hydrogels using mouse myoblast cells for three-dimensional bioprinting and tissue engineering applications © 2019 Arab, *et al*. This is an Open Access article distributed under the terms of the Creative Commons Attribution-NonCommercial 4.0 International License (http://creativecommons.org/licenses/by-nc/4.0/), permitting all non-commercial use, distribution, and reproduction in any medium, provided the original work is properly cited.

and illness or injury, which influence the balance of protein synthesis and degradation[6]. Skeletal muscle is a voluntary moveable tissue that has the ability to convert chemical energy into mechanical energy and then transfer it to tendon tissue. It also supports soft tissue and maintains body posture[7]. In addition, this tissue is responsible for different functions of the body such as respiration and protection of abdominal viscera, and also controls the movement of limbs[8]. Skeletal muscle tissue exhibits the native capability to regenerate and repair through the activation of local satellite cells[8,9].

However, this ability declines with age as well as in clinical conditions such as tumor resection and traumatic sport injuries including concussions and strains, and muscular dystrophy that may result in volumetric muscle loss (VML). In these injuries, approximately 20% or more of the muscle mass is lost[10,11] and, as a result, tissues lose the ability to signal each other and become unable to repair themselves through natural physiological processes. Thus, surgical intervention is needed[12-15] to restore normal function and prevent the formation of scar tissue[13], which may lead to muscle atrophy and prevent muscle regeneration[16]. Around the world, millions of people are affected by these clinical conditions which cause significant social and economic problems[17,18]. As such, alternative technologies are urgently needed for the reconstruction of skeletal muscle tissues that have experienced VML and need to regenerate new functional tissue[10,19].

An alternative approach for VML treatment and organ fabrication is tissue engineering through the use of biological scaffolds[20]. The process of muscle tissue engineering is the same as that of skin tissue engineering: The cells are grown in a three-dimensional (3D) environment, similar to how they would grow *in vivo* using biomaterial scaffolds. Particular interest is taken in scaffolds made from self- assembling peptides for 3D culture and bioprinting because of their synthetic, yet natural background. They have been used as biomaterials and matrices to deliver encapsulated bioactive molecules in therapeutic applications and regenerative medicine[21-25]. Many hydrogels have been used and assessed for their mechanical properties, cellular activity, and myogenic potential. However, a need is still present to develop the most appropriate material that is efficient in maintaining mechanical stability and promoting myotube formation[26].

The principle of 3D bioprinting allows the capability of fabricating constructs of a fully customized muscle. This technology depends on forming a complex biological construct by dispensing cells and bionics in a layer-by-layer fashion. Due to these excellent features, 3D bioprinting has become the ultimate solution for tissue engineering, especially when reconstructing skeletal muscles. Inspired by this emerging technology, we aim to study the printability of our custom-designed robotic 3D bioprinting system[27,28] to fabricate 3D scaffolds for the differentiation of myoblast cells. The process of 3D bioprinting is believed to enhance the arrangement of homogeneous cellular scaffolds and improve cell proliferation and adhesion for myotube formation. Two sequences of self-assembling peptides are tested and analyzed for cell viability, proliferation, and differentiation. The promising results indicate that 3D bioprinting of self-assembling ultrashort peptides may valuably improve the process of muscle tissue engineering.

## 2. Materials and Methods

Two tetrameric self-assembling peptides CH-01 and CH-02 were custom-synthesized in our Laboratory for Nanomedicine. Mouse myoblast cells (C2C12) were obtained from ATCC, USA. The following materials were ordered from Gibco, USA: Dulbecco's modified eagle medium (DMEM), fetal bovine serum (FBS), heat-inactivated horse serum, Dulbecco's phosphate-buffered saline (PBS) solution, and penicillin-streptomycin (P/S) antibiotics. An 3-(4,5-Dimethylthiazol-2-yl)-2,5-diphenyltetrazolium bromide (MTT) cell proliferation assay kit and a LIVE/DEAD Viability/Cytotoxicity kit were purchased from Promega, USA. Immunostaining antibody myosin heavy chain (MHC) was purchased from Abcam. Cell culture flasks and 96-well plates were ordered from Corning, USA.

### 2.1. Preparation of Peptide Hydrogel

CH-01 and CH-02 peptide powders were dissolved in Milli-Q water. Then, 10× PBS was mixed into the peptide solution. Gelation of both peptides occurred within a few minutes at a minimum concentration of 4 mg/mL and

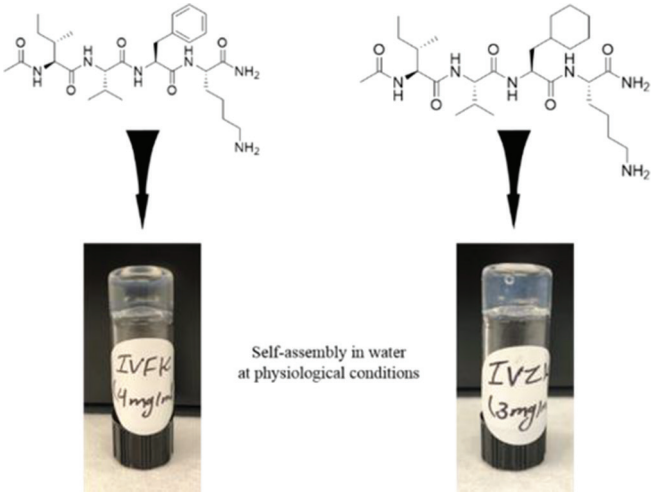


**Figure 1.** The self-assembling peptides CH-01 (4 mg/ml) and CH-02 (3 mg/ml) generate macromolecular nanofibrous hydrogels in an aqueous solution, the gelation was enhanced using phosphate buffer saline.

3 mg/mL for CH-01 and CH-02, respectively, as shown in Figure 1. The final volume ratio of peptide solution and 10× PBS was 9:1.

## 2.2. Characterization of the Topography and Morphology of Peptide Hydrogels

### *2.2.1. Evaluation of Fiber Structures by Field-emission Scanning Electron Microscopy (SEM)*

The peptide nanogels were dehydrated by gradually increasing concentrations of 30%, 50%, 70%, 90%, and 100% (v/v) ethanol solutions for 15 min in each solution. Further dehydration in 100% ethanol solution was continued by changing the absolute ethanol solution with a fresh one twice for 15 min each. The dehydrated samples were subsequently kept in 1:2 ratio of hexamethyldisilazane (HMDS) and ethanol for 20 min, followed by 20 min of incubation in a fresh solution of 2:1 ratio of HMDS and ethanol and then in 100% HMDS, performed twice for 20 min. Finally, the samples were stored overnight in a fume hood to allow HMDS to evaporate. Before imaging, the samples were mounted onto SEM grids using conductive carbon tape, and then sputter-coated with a 5 nm thick coating of iridium and a 3 nm thick coating of gold/palladium. Images were taken of the coated samples with a field emission SEM system (FEI Nova Nano630 SEM, Oregon, USA).

## 2.3. Cell Culture and Growth Conditions

### *2.3.1. Mouse Myoblast Cells (C2C12)*

Mouse myoblast cells (C2C12) were cultured either in a T175 or T75 culture flask in complete DMEM media (10% FBS and 1% P/S). The cells were placed in a humidified incubator with 95% air and 5% $CO_2$ at 37°C. Then they were subcultured using trypsin at approximately 80% confluence. Fresh culture media was added every 48 h.

### *2.3.2. 3D Culture of Myoblast Cells in Peptide Hydrogels*

In a 96-well plate, mouse myoblast cells were encapsulated in peptide hydrogels, as previously described[1]. Briefly, peptide solutions CH-01 (4 mg/ mL) and CH-02 (3 mg/mL) were added at 40 µL/well. Mouse myoblast cells (30,000 cells/well) that were re-suspended in 2xPBS were mixed gently with the peptide solutions. The gelation time was 3-5 min. Subsequently, the culture medium was added to the wells.

### *2.3.3. Differentiation of Myoblast Cells within 3D Culture Construct*

6 days of culturing myoblast cells inside the 3D environment in the growth medium, the culture conditions were then changed to differentiated mode to study differentiation behavior for 8 days. The differentiation medium contained DMEM supplemented with 2% horse serum and 1% P/S.

## 2.4. Biocompatibility Evaluation of Tetrameric Ultrashort Self-assembling Peptides in Two-dimensional (2D) Culture

### *2.4.1. Cell Viability Assay (MTT Assay)*

All biocompatibility studies were performed in a 96-well plate. C2C12 (10,000 cells/well) were seeded in a complete medium. After 2 days, the medium was discarded, and the cells were incubated for 48 h with different concentrations of peptide solution, at 37°C, 95% air, and 5% $CO_2$, Matrigel was used as a control. A colorimetric MTT assay was used to determine cell viability as advised in the manufacturer's protocol. Briefly, the phenol-free fresh medium was mixed with 10% MTT reagent. Each well was incubated for 4 h with 100 µL MTT reagent including the positive control wells. Insoluble crystals of formazan were dissolved by adding 100 µL of dimethyl sulfoxide to each well. Finally, the absorption of individual wells was recorded at 540 nm using a plate reader (PHERAstar FS, Germany).

## 2.5. 3D Bioprinting of Myoblast Cells

### *2.5.1. 3D Bioprinting*

In two vials, 15 mg of CH-01 and CH-02 peptide powder each were weighed out and placed under UV for 30 min sterilization. The peptide powder was dissolved in 1mL of MilliQ water and the peptide solution was then vortexed and sonicated to obtain a homogenous solution. The vials were placed in an incubator at 37°C and 5% $CO_2$. The incubation time for the CH-01 pre-gel bioink solution was 3.5 h, but was 2 h when using the CH-02 pre-gel bioink solution.

A custom-designed robotic 3D bioprinter[27,28] was set up with commercial microfluidic pumps. A homemade two-inlet nozzle was used for extrusion. A heatbed was set to 37°C to create a suitable environment for the cells once extruded within the peptide bioink. Two commercial microfluidic pumps were loaded for extrusion. A simple gcode file was used to create a structure of 8 layers.

Pump 1 was loaded with the peptide pre-gel solution and set to a flow rate of 60 µL/min. Pump 2 was loaded with myoblast cells containing serum-free DMEM culture media. The same procedure was conducted for both peptides. 17-18 samples were printed for each peptide with a height of 7-8 layers for each sample.

### *2.5.2. Live/Dead Assay*

A two-color fluorescence assay was used to assess the cell viability within the printed constructs. Calcein was used

as a marker for living cells and ethidium homodimer for dead cells. The bioprinted tissues were washed in PBS 3 times and treated with calcein AM (green) and ethidium homodimer-1 (red) at 1:2 ratio in PBS. The samples were then placed for 20 min in a dark incubator at 37°C and 5% $CO_2$. After staining, they were washed again 3 times in PBS. A confocal microscope (Leica SP8) was used for image acquisition.

### 2.6. Immunofluorescence Staining of Differentiated Myoblasts

The differentiation of mouse myoblast cells within both hydrogels was studied in a glass confocal dish (12mm) by immunofluorescence analysis. C2C12 (30,000 cells/plate) were embedded in different hydrogels. After 8 days of differentiation, 4% paraformaldehyde solution was used for cells fixation. After 20 min incubation at room temperature, the cells were permeabilized and labeled with primary anti-MHC (1:300 PBS) for 1 h followed by 1 h incubation with secondary anti-mouse IgG-fluorescein isothiocyanate and DAPI. The myotube formation was observed with fluorescence confocal microscopy (Zeiss LSM 710 Inverted Confocal Microscope, Germany).

### 2.7. Statistical Analysis

All results are presented as a mean±standard deviation. Each type of test was repeated in three similar experiments. Statistical differences among the experimental groups were determined with one-way analysis of variance. When $P<0.05$, the results were considered to be statistically significant.

## 3. Results

### 3.1. The Nanofibrous Morphology of Self-assembling Peptides

The nanofibrous morphology of the self-assembling peptides was observed through SEM imaging. It was then compared to the morphology observed in bovine collagen (Figure 2A), which is comprised by a unique triple-helical structure[23]. SEM results confirmed that the fibrous structures of these peptides resemble the fibrous structure of collagen in terms of architecture. The detailed assessment of CH-01 (Figure 2B) and CH-02 (Figure 2 C) showed that the fibrous structures of these peptides resemble the fibrous structure of collagen in terms of architecture. This nanofibrous structure was produced from the antiparallel pairing of two peptide monomers (Figure 1). Subsequently, the assembly of the peptide pairs by stacking facilitated the formation of the fibers. The hydrogel was formed by the condensation of these fibers.

### 3.2. Cell Viability Results (MTT assay)

After 24 h of incubation, cell proliferation was tested with different peptide concentrations to evaluate biocompatibility. The MTT assay was used to quantify the number of viable cells. This was done by plotting a standard curve for a known number of cells (Figure 3B). Test results indicated that the differences between both peptides CH-01 (Figure 3C), CH-02 (Figure 3D), and positive control, Matrigel were non-significant, indicating that both scaffolds were suitable and biocompatible on muscle myoblast cells.

### 3.3. Differentiation of Muscle Myoblasts

To confirm whether these scaffolds induce differentiation of C2C12 myoblasts, the expression of MHC, which is a late-stage differentiation marker of myogenesis, was observed through immunostaining. After inducing differentiation of the cells in differentiation media for 8 days, MHC expression was observed from myoblasts cultured on both scaffolds and was found to be similar to the positive control Matrigel, as shown in Figure 4A. These findings indicate that both scaffolds promote muscle cell differentiation, thus suggesting that these materials may prove to be beneficial in increasing muscle mass. The fusion index was calculated from MHC stained cells, which is defined as the number of nuclei present in myotubes in comparison to the total number of nuclei present in the observed field. Statistical analysis revealed a significant increase in the number of myotubes containing four or more nuclei in cells encapsulated within CH-01, when compared to other tested materials (Figure 4B). In addition, quantitative investigation of cell elongation

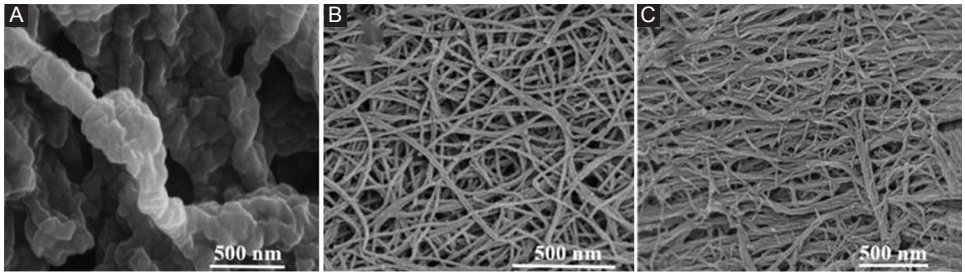


**Figure 2.** Field emission scanning electron microscopy images of nanofibrous structure of 2.5 mg/mL bovine collage type I (**A**), 4 mg/mL CH-01 (**B**), and 3 mg/mL CH-02 (**C**).

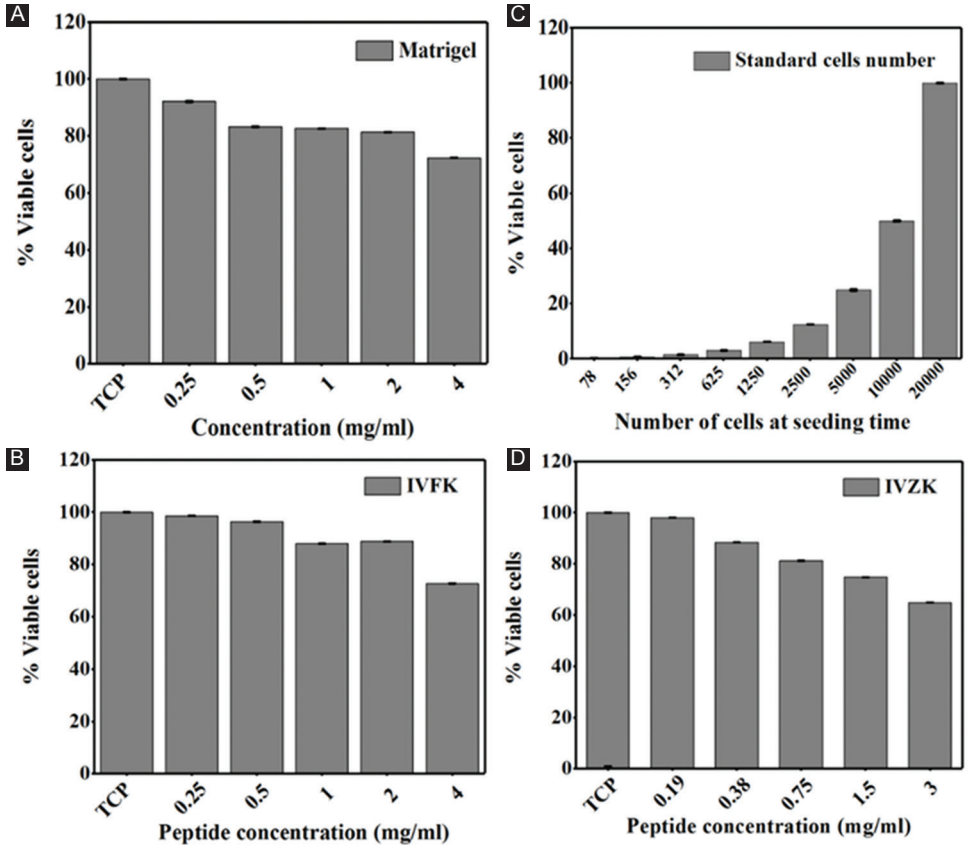


**Figure 3.** Graphical representation of 3-(4,5-Dimethylthiazol-2-yl)-2,5-diphenyltetrazolium bromide assay of mouse myoblast cells incubated with different peptide concentrations for 24 h, CH-01 (**C**), CH-02 (**D**), and positive controls, Matrigel (**A**) was used. A standard curve for a known number of cells (**B**).

within the scaffolds was estimated by the cell aspect ratio, which is defined as the proportion between the length of the longest line and the length of the shortest line across the nuclei. The results demonstrated a slight increase in the cell aspect ratio in the 3D cultures using peptide hydrogels and Matrigel as the 3D control, different to the 2D culture. However, these increases did not reach statistical significance (Figure 4C).

### 3.4. Cell Viability Results of 3D Bioprinted Structures

The intensity of green fluorescence of the 3D printed cell-laden constructs shown in Figure 5 revealed that most of the cells remained viable in both peptide hydrogels throughout 5 days indicating that the diffusion of nutrients and removal of waste products were sufficient to maintain cell viability. There were only very few dead cells visible within the matrix. It is worth mentioning that the reduction in cell viability with 4 mg/ml (Figure 3C) and 3 mg/ml (Figure 3D) is not due to the toxicity of the hydrogels and cell death, but due to a change in the local cellular microenvironment and diffusion barrier.

## 4. Discussion and Conclusion

Myotube formation plays a key role in repairing muscular functions. The enhancement of differentiation of myoblast cells into myotubes using different biomaterials is a valuable area of interest. Conventionally, skeletal muscle tissue is engineered by fabricating muscle tissues *in vitro* using myoblast cells and modified scaffolds. Key factors including biocompatibility, biodegradability, and formation of polar parallel myotubes determine the success of tissue-repaired transplantation. Studies have shown that orderly arranged 3D scaffolds can promote cell adhesion and proliferation[29]. Ideal scaffolds should create environments that are suitable for cell proliferation, differentiation, alignment, orientation, and migration during the reparation of tissue damages[30]. This study used 3D printed structures to promote myogenesis, a process necessary for muscle repair. The structures were 3D bioprinted from biocompatible and biodegradable materials that simulate highly complex structures of extracellular matrix (ECM), and their effects on differentiation in 3D culture myoblast cells were observed.

In this study, we used previously designed tetrameric peptides for the following purposes: The first purpose

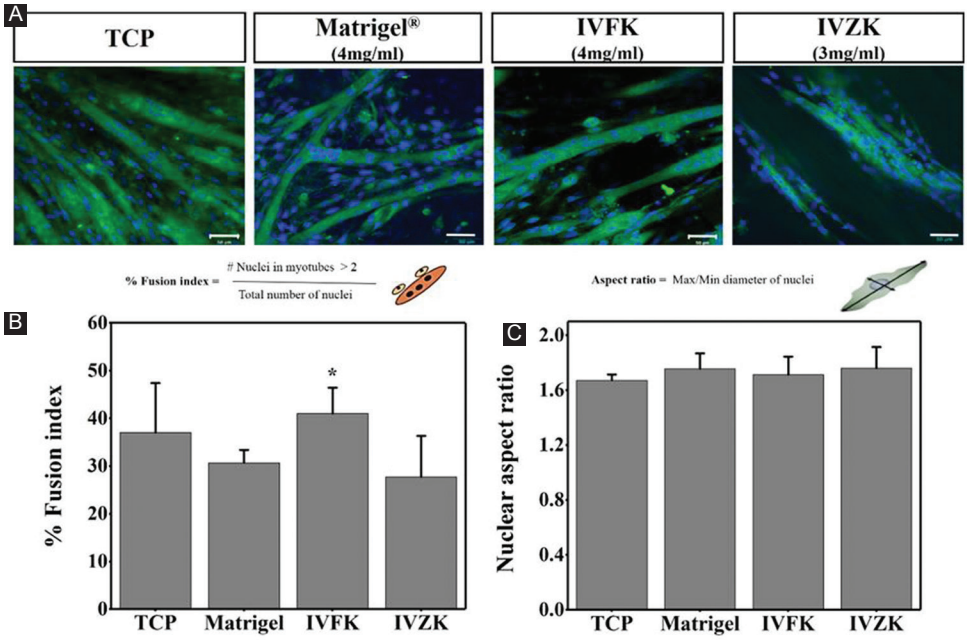


**Figure 4.** Overlaid confocal fluorescent images of differentiated mouse myoblast cells encapsulated in the peptide (4 mg/ml CH-01 and 3 mg/ml CH-02) and 4 mg/ml Matrigel. The encapsulated cells were cultured for 8 days in differentiation medium. Nucleus showed in blue and myosin heavy chain shown in green, (**A**) percentage of fusion index after 8 days, (**B**) and nuclear aspect ratio of differentiated muscle cells, (**C**) scale bar is 50 µm.

aimed to test the ability of these materials to be used as scaffolds to facilitate myotube formation in a 3D culture, which is needed in muscle repair. The second purpose was to test the efficacy of our designed peptide nanogels to maintain the viability of skeletal muscle cells after 3D bioprinting. These purposes focus on the aim to assess the biocompatibility of the tetrameric peptides on skeletal muscle cell proliferation and differentiation as well as to fabricate a 3D muscle model.

The outcome of the nanofiber network formed from the self-assembling of ultrashort peptides CH-01 and CH-02 was confirmed by SEM, with an average diameter of peptide nanofibers of around 10-20 nm, where the fibers structurally resemble collagen fibers with respect to topography[31]. The diameter of these nanoscale fibers ranges within the diametric scope found in the natural ECM (5-300 nm)[32]. In our previous study[33], the mechanical stiffness and stability of both peptide nanogels were determined using oscillatory rheology based on measuring the storage modulus (G') and loss modulus (G"). The G" values of CH-01 and CH-02 were found to be less than their G' values indicating the gel state of both samples[34].

Cellular proliferation, adhesion and the formation of 3D cellular networks play a key role for tissue repair and regeneration. Thus, the cytocompatibility of the peptide nanogels was evaluated using mouse myoblast cells (C2C12). The *in vitro* investigation demonstrated that exposure of C2C12 to different concentrations of peptide nanogels did not affect cell growth when compared to cell growth in tissue culture plates and positive control, Matrigel®. The results demonstrated that the cells were metabolically active in response to different concentrations.

Based on this observation, we could confirm that the peptide nanogels are promising materials for the fabrication of muscle substitutes as well as 3D muscle graft models, particularly in the context of VML. In summary, our studies show that newly developed peptide nanogels provide native cues to mouse myoblast cells as most cells were found to be alive with very few dead cells.

In our previous paper[33], we had shown that both peptides have good printability, which opens the possibility of 3D bioprinting different cell types. In this work, the 3D bioprinted scaffolds, which simulate highly complex structures of ECM, were engineered by our custom-designed robotic 3D bioprinter. The cells were infused into the 3D constructs during printing through a custom extrusion method. The two-inlet nozzle, fabricated in-house, allowed the gelation of the peptide and even distribution of the cells within each layer of the construct. The results showed that the 3D printed scaffolds could enhance adhesion and proliferation for at least 5 days as can be seen in the results of the live-dead assay. Moreover, they could promote myotube formation and hence induce the myogenic differentiation of C2C12 myoblast cells in 3D culture. This confirms the biocompatibility of the 3D bioprinted structures and suggests that they can

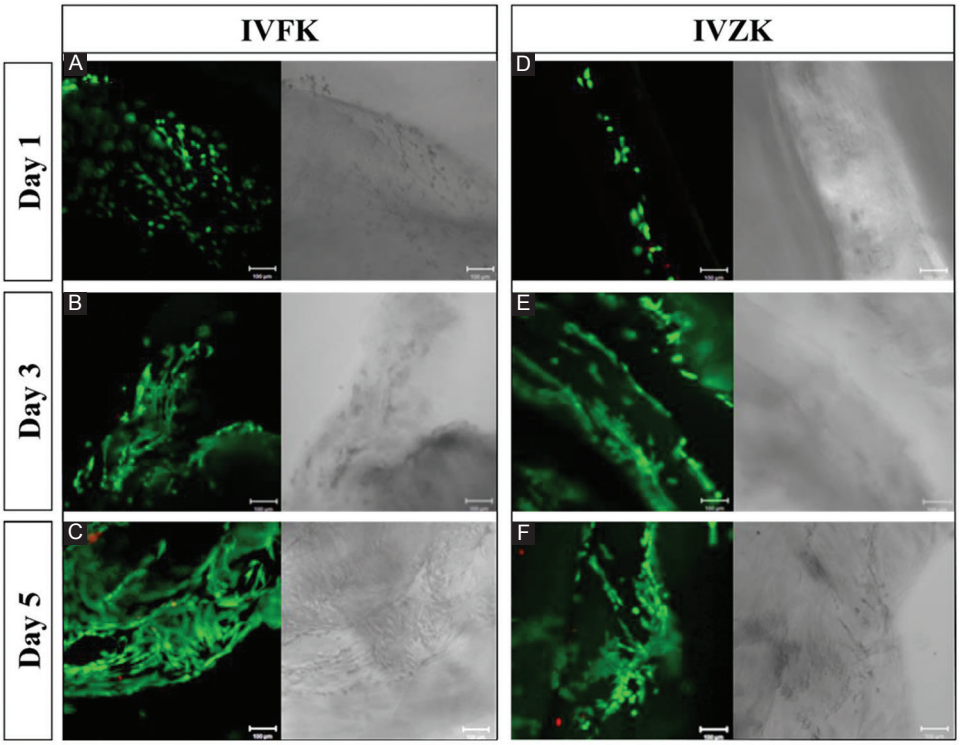


**Figure 5.** Overlaid confocal fluorescent images of three-dimensional bioprinted mouse myoblast cells in peptide hydrogels; CH-01 and CH-02 and cultured for different time points (Live cells shown in green and dead cells in red) CH-01 (**A-C**) and CH-02 (**D-F**) at Days 1, 3, and 5, respectively. Scale bars 100 μm.

potentially be used as cell culture platforms for skeletal tissue engineering and regeneration.

Various studies argue that improved adhesion or proliferation of myoblasts promotes differentiation due to the confluence effect[35]. Our findings show that the 3D culture system not only enhances cell adhesion and proliferation but also helps in myogenic differentiation, as shown by the expression levels of MHC in C2C12 cells cultured within 3D scaffolds. Cell proliferation and migration can be further enhanced by forming a 3D scaffold of cell-laden layers. These scaffolds can strongly influence the polarity of cells through a process called "contact guidance"[35]. The proliferation and differentiation of the cells can only be facilitated if the cells can penetrate into the scaffolds, and hence form skeletal muscle tissues. Although the 3D bioprinted constructs could not completely mimic the structure and functions of a native cell microenvironment, their transplantation into the injured or punctured skeletal muscle in future *in vivo* studies may contribute to improved muscle repair. Overall, our results demonstrate that the 3D bioprinted constructs are biocompatible and may be used as biomimetic platforms to promote cell differentiation, adhesion, and proliferation.

Further, *in vivo* studies should be performed to assess how the 3D peptide scaffolds work when seeded together with autologous myoblast cells. Follow-up studies are critically needed as they will allow for a more precise evaluation of the injuries' fate post-grafting. We believe that the described results represent an advancement in the context of skeletal muscle tissue engineering, opening up opportunities for tissue replacement and repair.

## Acknowledgments

The research reported in this publication was supported by funding from King Abdullah University of Science and Technology (KAUST). The authors would like to acknowledge Dr. Dana Alhattab and Francesca Melle for their contribution to the optimization of the 3D bioprinting process.

## Authors' Contributions

CAEH supervised the project. WA designed and conducted the experiments. KK and ZK handled the 3D bioprinting experiments. All authors wrote the manuscript.

## Conflicts of Interest

The authors declare that they do not have any competing interest.

## References

1. Choi YJ, Jun YJ, Kim DY, *et al*., 2019, A 3D Cell Printed Muscle Construct with Tissue-derived Bioink for the

Treatment of Volumetric Muscle Loss. *Biomaterials*, 206:160-9. DOI 10.1016/j.biomaterials.2019.03.036.

2. Kim JH, Seol YJ, Ko IK, *et al*., 2018, 3D Bioprinted Human Skeletal Muscle Constructs for Muscle Function Restoration. *Scientific Reports*, 8:12307. DOI 10.1038/s41598-018-29968-5.
3. VanDusen KW, Syverud BC, Williams ML, *et al*., 2014, Engineered Skeletal Muscle Units for Repair of Volumetric Muscle Loss in the Tibialis Anterior Muscle of a Rat. *Tissue Engineering Part A*, 20(21-22):2920-30. DOI 10.1089/ten.tea.2014.0060.
4. Chua CK, Yeong WY, 2014, *Bioprinting: Principles and Applications*. Vol. 1. Singapore: World Scientific Publishing Co, Inc.
5. Kwee BJ, Mooney DJ, 2017, Biomaterials for Skeletal Muscle Tissue Engineering. *Current Opinion in Biotechnology*, 47:16-22. DOI 10.1016/j.copbio.2017.05.003.
6. Frontera WR, Ochala J, 2015, Skeletal muscle: A Brief Review of Structure and Function. *Calcified Tissue International*, 96(3):183-95. DOI 10.1007/s00223-014-9915-y.
7. Beldjilali-Labro M, Garcia AG, Farhat F, *et al*., 2018, Biomaterials in Tendon and Skeletal Muscle Tissue Engineering: Current Trends and Challenges. *Materials*, 11(7):1116. DOI 10.3390/ma11071116.
8. Relaix F, Zammit PS, 2012, Satellite Cells are Essential for Skeletal Muscle Regeneration: The Cell on the Edge Returns Centre Stage. *Development*, 139(16):2845-56. DOI 10.1242/dev.069088.
9. Brack AS, Rando TA, 2012, Tissue-specific Stem Cells: Lessons from the Skeletal Muscle Satellite Cell. *Cell Stem Cell*, 10(5):504-14. DOI 10.1016/j.stem.2012.04.001.
10. Grogan BF, Hsu JR, Consortium STR, 2011, Volumetric Muscle Loss. *JAAOS Journal of the American Academy of Orthopaedic Surgeons*, 19:S35-7. DOI 10.5435/00124635-201102001-00007.
11. Turner NJ, Badylak SF, Regeneration of Skeletal Muscle. *Cell and Tissue Research*, 347(3):759-74. DOI 10.1007/s00441-011-1185-7.
12. Lynch GS, Schertzer JD, Ryall JG, 2008, Anabolic Agents for Improving Muscle Regeneration and Function After Injury. *Clinical and Experimental Pharmacology and Physiology*, 35(7):852-58. DOI 10.1111/j.1440-1681.2008.04955.x.
13. Järvinen TA, Järvinen TL, Kääriäinen M, *et al*., 2007, Muscle Injuries: Optimising Recovery. *Best Practice and Research Clinical Rheumatology*, 21(2):317-31. DOI 10.1016/j.berh.2006.12.004.
14. Järvinen TA, Järvinen TL, Kääriäinen M, *et al*., 2005, Muscle Injuries: Biology and Treatment. *The American Journal of Sports Medicine*, 33(5):745-64. DOI 10.1177/0363546505274714.
15. Järvinen TA, Kääriäinen M, Järvinen M, Kalimo H, 2000, Muscle Strain Injuries. *Current Opinion in Rheumatology*, 12(2):155-61. DOI 10.1097/00002281-200003000-00010.
16. Corona BT, Wu X, Ward CL, *et al*., 2013, The Promotion of a Functional Fibrosis in Skeletal Muscle with Volumetric Muscle Loss Injury following the Transplantation of muscle-ECM. *Biomaterials*, 34(13):3324-35. DOI 10.1016/j.biomaterials.2013.01.061.
17. Manring H, Abreu E, Brotto L, *et al*., 2014, Novel Excitation-contraction Coupling Related Genes Reveal Aspects of Muscle Weakness Beyond Atrophy new Hopes for Treatment of Musculoskeletal Diseases. *Frontiers in Physiology*, 5:37. DOI 10.3389/fphys.2014.00037.
18. Grasman JM, Zayas MJ, Page RL, *et al*., 2015, Biomimetic Scaffolds for Regeneration of Volumetric Muscle Loss in Skeletal Muscle Injuries. *Acta Biomaterialia*, 25:2-15. DOI 10.1016/j.actbio.2015.07.038.
19. Mase VJ, Hsu JR, Wolf SE, *et al*., 2010, Clinical Application of an Acellular Biologic Scaffold for Surgical Repair of a Large, Traumatic Quadriceps Femoris Muscle Defect. *Orthopedics*, 33(7):511. DOI 10.3928/01477447-20100526-24.
20. Zorlutuna P, Annabi N, Camci-Unal G, *et al*., 2012, Microfabricated Biomaterials for Engineering 3D Tissues. *Advanced Materials*, 24(14):1782-804. DOI 10.1002/adma.201104631.
21. Hauser CA, Zhang S, 2010, Designer Self-assembling Peptide Nanofiber Biological Materials. *Chemical Society Reviews*, 39(8):2780-90. DOI 10.1039/b921448h.
22. Loo Y, Zhang S, Hauser CA, 2012, From Short Peptides to Nanofibers to Macromolecular Assemblies in Biomedicine. *Biotechnology Advances*, 30(3):593-603. DOI 10.1016/j.biotechadv.2011.10.004.
23. Wu EC, Zhang S, Hauser CA, 2012, Self-assembling Peptides as Cell-interactive Scaffolds. *Advanced Functional Materials*, 22(3):456-68. DOI 10.1002/adfm.201101905.
24. Hauser CA, Deng R, Mishra A, *et al*., 2011, Natural Tri-to Hexapeptides Self-assemble in Water to Amyloid β-type Fiber Aggregates by Unexpected α-helical Intermediate Structures. *Proceedings of the National Academy of Sciences*, 108(4):1361-6. DOI 10.1073/pnas.1014796108.
25. Mishra A, Loo Y, Deng R, *et al*., 2011, Ultrasmall Natural Peptides Self-assemble to Strong Temperature-resistant Helical Fibers in Scaffolds Suitable for Tissue Engineering. *Nano Today*, 6(3):232-9. DOI 10.1016/j.nantod.2011.06.010.
26. Pollot BE, Rathbone CR, Wenke JC, *et al*., 2018, Natural Polymeric Hydrogel Evaluation for Skeletal Muscle Tissue

Engineering. *Journal of Biomedical Materials Research Part B: Applied Biomaterials*, 106(2):672-9. DOI 10.1002/jbm.b.33859.

27. Kahin K, Khan Z, Albagami M, *et al*., 2019, Development of a Robotic 3D Bioprinting and Microfluidic Pumping System for Tissue and Organ Engineering. *Microfluidics, Biomems, and Medical Microsystems*, Doi 10.1117/12.2507237.
28. Khan Z, Kahin K, Rauf S, *et al*., 2018, Optimization of a 3D Bioprinting Process Using Ultrashort Peptide Bioinks. *International Journal of Bioprinting*, 5(1):1-3. DOI 10.18063/ijb.v5i1.173.
29. Brenneisen P, Blaudschun R, Gille J, *et al*., 2003, Essential role of an Activator Protein-2 (AP-2)/Specificity Protein 1 (Sp1) Cluster in the UVB-mediated Induction of the Human Vascular Endothelial Growth Factor in HaCaT Keratinocytes. *Biochemical Journal*, 369(2):341-9. DOI 10.1042/bj20021032.
30. Hendriks J, Riesle J, van Blitterswijk CA, 2007, Co-culture in Cartilage Tissue Engineering. *Journal of Tissue Engineering and Regenerative Medicine*, 1(3):170-8. DOI 10.1002/term.19.
31. Loo Y, Lakshmanan A, Ni M, *et al*., 2015, Peptide Bioink: Self-assembling Nanofibrous Scaffolds for Three-dimensional Organotypic Cultures. *Nano Letters*, 15(10):6919-25. DOI 10.1021/acs.nanolett.5b02859.
32. Jayawarna V, Ali M, Jowitt TA, *et al*., 2006, Nanostructured Hydrogels for Three-dimensional Cell Culture Through Self-assembly of Fluorenylmethoxycarbonyl Dipeptides. *Advanced Materials*, 18(5):611-4. DOI 10.1002/adma.200501522.
33. Arab W, Rauf S, Al-Harbi O, *et al*., 2018, Novel Ultrashort Self-Assembling Peptide Bioinks for 3D Culture of Muscle Myoblast Cells. *International Journal of Bioprinting*, 4(2):129. DOI 10.18063/ijb.v4i1.129.
34. Lakshmanan A, Cheong DW, Accardo A, *et al*., 2013, Aliphatic Peptides Show Similar Self-assembly to Amyloid Core Sequences, Challenging the Importance of Aromatic Interactions in Amyloidosis. *Proceedings of the National Academy of Sciences*, 110(2):519-24. DOI 10.1073/pnas.1217742110.
35. Chen H, Zhong J, Wang J, *et al*., 2019, Enhanced Growth and Differentiation of Myoblast Cells Grown on E-jet 3D Printed Platforms. *International Journal of Nanomedicine*, 14:937-50. DOI 10.2147/ijn.s193624.

RESEARCH ARTICLE

# The mussel-inspired assisted apatite mineralized on PolyJet material for artificial bone scaffold

**Yi-Wen Chen[1,2†], Hsin-Yuan Fang[1,3,4†], Ming-You Shie[1,5], Yu-Fang Shen[6,7*]**

[1]Three-dimensional Printing Medical Research Center, China Medical University Hospital, China Medical University, Taichung, Taiwan
[2]Graduate Institute of Biomedical Sciences, China Medical University, Taichung, Taiwan
[3]Department of Thoracic Surgery, China Medical University Hospital, Taichung, Taiwan
[4]School of Medicine, China Medical University, Taichung, Taiwan
[5]School of Dentistry, China Medical University, Taichung, Taiwan
[6]Three-dimensional Printing Medical Research Institute, Asia University, Taichung, Taiwan
[7]Department of Bioinformatics and Medical Engineering, Asia University, Taichung, Taiwan
[†]These authors contributed equally to this work.

**Abstract:** With the development of three-dimensional (3D) printing, many commercial 3D printing materials have been applied in the fields of biomedicine and medical. MED610 is a clear, biocompatible PolyJet material that is medically certified for bodily contact. In this study, the polydopamine (PDA)/hydroxyapatite (HA) coating was added to the printed MED610 objects to evaluate its physical properties, cell proliferation, cell morphology, and alkaline phosphatase expression level. The results show that the PDA/HA coating helps printed objects to enhance the hardness, biocompatibility, and osteogenic differentiation potential. We expect that PDA/HA coatings contribute to the applicability of MED610 in biomedical and medical applications.

**Keywords:** Three-dimensional printing; Polydopamine; Hydroxyapatite; MED610; Osteogenic differentiation; PolyJet technology

*Correspondence to: Yu-Fang Shen, Three-dimensional Printing Medical Research Institute, Asia University, Taichung 41354, Taiwan; cherryuf@gmail.com

**Received:** April 10, 2019; **Accepted:** May 27, 2019; **Published Online:** July 11, 2019

**Citation:** Chen Y, Fang H, Shie M, *et al*., 2019, The mussel-inspired assisted apatite mineralized on PolyJet material for artificial bone scaffold. *Int J Bioprint*, 5(2): 197. http://dx.doi.org/10.18063/ijb.v5i2.197

## 1. Introduction

With the development of multidetector computed tomography and magnetic resonance imaging (MRI), the three-dimensional (3D) structure of the patient's body can be presented by these medical imaging techniques and computer-aided software engineering. The 3D structures can be converted to the interpreted surface tessellation language files for 3D printing by the computer software processing. Therefore, the 3D printing technology in modern medicine has great development in current years[1]. The events of 3D printing applied in current medical practice were shown below: (1) The manufacturing of *in vitro* mechanical aids: The 3D printing technology can be used to create customized and mechanical aids to restore patient's physical control and action. Cases: Arthrogryposis multiplex congenital and paralyzed patients[2]. Advantages: The small number of customized products can be manufactured. (2) The development of the customized implant molds: The required and customized metal or silicone implants can be fabricated through the molds which are obtained by the 3D printed patient's desired polymer implant models[3,4]. (3) The pre-operative 3D model: By 3D printing of patient's tissue models, the more complicated or high-risk surgery can be planned in advance and the time of surgery can be shortened to decrease the surgical risk[4]. In addition, 3D printing model can also facilitate the improvement of commercial

The mussel-inspired assisted apatite mineralized on PolyJet material for artificial bone scaffold.© 2019 Chen, *et al*. This is an Open Access article distributed under the terms of the Creative Commons Attribution-NonCommercial 4.0 International License (http://creativecommons.org/licenses/by-nc/4.0/), permitting all non-commercial use, distribution, and reproduction in any medium, provided the original work is properly cited.

products, such as artificial pelvis[5]. (4) The manufacturing of customized implants: The implants were fabricated by 3D printing technology and can be used for long-term implantation. Cases: 3D printed bioresorbable airway splint for tracheobronchomalacia[6], 3D printed skull implant[7], hip[8], pelvis[9], jaw[10] and so on.

Although 3D printing in modern medicine had many practical cases and has a lot of advantages, it still has many challenges that need to be solved. First, the biocompatible materials for 3D printing in the market are limited and the materials cannot satisfy the specific needs of desired strength, flexibility, and hardness. In addition, the polymerization of 3D printable materials usually involved with hot and organic solvents. The materials did not have good biocompatibility and cannot be used in biomedical and tissue engineering. Although some natural materials such as collagen or gelatin have been applied in 3D printing technology[11], they cannot provide good mechanical properties and the strength are usually increased by toxic cross-linking agents. Therefore, developing new biocompatible materials or new strategies to enhance the biocompatibility of printed objects is a very important issue.

In the current year, scientists have devoted considerable attention to polydopamine (PDA)-related research[12]. PDA has the excellent adhesive force to bind with various substrates containing plastics, oxides, noble metals, ceramics and so on, and it can also supply secondary reactivity for conjugating molecules[13-15]. It provides a new strategy through simple chemistry to modify various substrates and increase the function and biocompatibility of substrates[16-18]. In 2014, Wu's group showed self-assembled Ca-P/PDA composite nanolayers can modify the surface of materials and provide the bioactivity for bone regeneration[19]. In our previous study, we also demonstrated the angiogenesis and osteogenesis of human mesenchymal stem cells (hMSCs) cultured on the polycaprolactone scaffold with PDA-coated/hydroxyapatite (HA) precipitate can be promoted[20].

In this study, PDA-coated/HA precipitate was modified on the objects printed with the commercial PolyJet photopolymers (MED610), which only support short-term mucosal-membrane contact of up to 24 h. The modified objects had greater biocompatibility and better osteogenesis ability. These results pointed out that this strategy can increase the biocompatibility of printed objects and facilitate the development of 3D printing in biomedicine.

## 2. Materials and Methods

### 2.1 MED610 3D Printed Object Fabrication

The 3D printed objects were through SolidWorks (Dassault Systemes SolidWorks Corp., USA) and fabricated by a Stratasys Objet500 Connex3 PolyJet printer (Objet/Stratasys, USA) with MED610 biocompatible photopolymers (Objet/Stratasys, USA). The objects were printed with a thickness of 3 mm and a diameter of 6 mm for the evaluation of mechanical properties and with a thickness of 3 mm and a diameter of 6 mm for the biological test. The uncured photopolymers were washed away, and the objects were post cured under UV light to obtain fully cured objects. In addition, the objects were washed again for cell culture.

### 2.2 PDA Coating and HA Mineralization

The PDA was deposited onto the MED610 3D printed objects by direct immersion coating. The objects were immersed in a solution of dopamine hydrochloride (Acros Organics) (2 mg/mL in 10 mM Tris, pH 8.5) for PDA coating, shaken at 25 rpm for 12 h at room temperature, and then rinsed several times with deionized water and dried. For HA crystal mineralization, the objects were treated with calcium and phosphate solution. 10× simulated body fluid (SBF) solution was chosen to initiate uniform nucleation and growth. A stable stock solution of $NaH_2PO_4.H_2O$ (1.198 g), NaCl (58.44 g), KCl (0.375 g), $CaCl_2 \cdot 2H_2O$ (1.016 g), and $MgCl_2 \cdot 6H_2O$ (3.675 g) at pH of about 4.1 was prepared and then added $NaHCO_3$ (0.84 g) was added to adjust the pH to about 6.3. The objects were immersed in 10×SBF at room temperature for 1 h.

### 2.3 Characterization

Using X-ray diffractometry (XRD; Bruker D8 SSS, Karlsruhe, Germany) at 30 kV and 30 mA with a scanning speed of 1o/min., the phase composition of the objects with or without coatings was analyzed and the concentration of the measured elements was given in atomic percent. Besides, the scanning electron microscope (SEM) images of the samples were obtained with a SEM (SEM; JSM-6700F, JEOL) operated in the lower secondary electron image mode at 3 kV accelerating voltage. Furthermore, the hardness of the samples was evaluated by the Vickers hardness test.

### 2.4 Cell Proliferation

All samples were immersed in 75% ethanol and exposed to UV light for 30 min for sterilization before cell experiments. The hMSCs were obtained from Sciencell Research Laboratories (Sciencell, Carlsbad, CA) and cultured with mesenchymal stem cell culture medium (Sciencell) at 37°C in a 5% $CO_2$ atmosphere. Cell suspensions at a density of $10^4$ cells/sample were directly seeded on each sample. The cells were cultured on tissue culture plates without materials (control, Ctl) or the objects with or without coatings for different days and the cell viability was evaluated by the PrestoBlue® (Invitrogen, NY, USA) assay. The optical density was

obtained in a multi-well spectrophotometer (Hitachi, Tokyo, Japan) at 570 nm with a reference wavelength of 600 nm.

### 2.5 Cell Morphology

After 12 h of cell culture, the samples with hMSCs were washed with cold PBS and fixed by 1.5% glutaraldehyde (Sigma-Aldrich, MO, USA) for 2 h and then were dehydrated by a graded ethanol series for 20 min at each concentration and dried with liquid $CO_2$ by a critical point dryer device (LADD 28000, LADD, Williston, VT, USA). The dried samples were mounted on stubs, coated with gold particles, and investigated by SEM (JEOL JSM-7401F, Tokyo, Japan).

### 2.6 Osteogenesis Assay

After 3 and 7 days of cell culture, the level of alkaline phosphatase (ALP) activity was evaluated using p-nitrophenyl phosphate (pNPP, Sigma) as the substrate. The samples were mixed with pNPP in 1 M diethanolamine buffer for 15 min, then stopped by the addition of 5N NaOH and quantified by absorbance at 405 nm. The experiments were performed in triplicate.

### 2.7 Statistical Analysis

A one-way variance statistical analysis was used to evaluate the significance of the differences between the groups in each experiment. Scheffe's multiple comparison test was used to determine the significance of the deviations in the data for each specimen. In all cases, the results were considered statistically significant with $P<0.05$.

## 3. Results

### 3.1 The Physical and Chemical Characterization of PDA/HA Scaffolds

Biocompatible materials for 3D printing on the market are limited and the material does not meet the specific needs of the desired hardness, strength, and flexibility. In this study, we used the commercial PolyJet photopolymers (MED610) as the test samples to investigate if PDA/HA coating can enhance the biocompatibility of printed objects and facilitate to improve the applicability of commercial materials.

Figure 1 shows the images of printed objects without and with PDA coating. The printed object coated with PDA exhibited black color and this result indicated that we have successfully modified the PDA to the surface of the object.

The XRD patterns of the MED610 object (M), the MED610 object with HA (MHA), the prepared PDA-coated object (MP), and the PDA/HA-coated object (MPHA) are shown in Figure 2. M and MP have no peaks. The peaks of MHA and MPHA at around 2θ=25.7° and 2θ=31.9° are characteristic of HA precipitates, which occurs during the early mineral phase of bone development and fracture healing[21]. The result shows the PDA/HA-coated MED610 object contains a large amount of HA precipitate.

Figure 3 shows the SEM results of MED610 object with HA, PDA, or PDA/HA coatings. The PDA/HA coated object presents more HA mineral crystallization. Based on these results, it is speculated that the PDA coating can effectively assist the bionics of HA mineralization, thereby producing a hybrid biomaterial having HA. In addition, the addition of a PDA/HA coating can increase the hardness of the printed object (Figure 4).

### 3.2 Cell Proliferation and Morphology

Whether the biomedical materials printed by the 3D printer can be widely used in the medical field, the

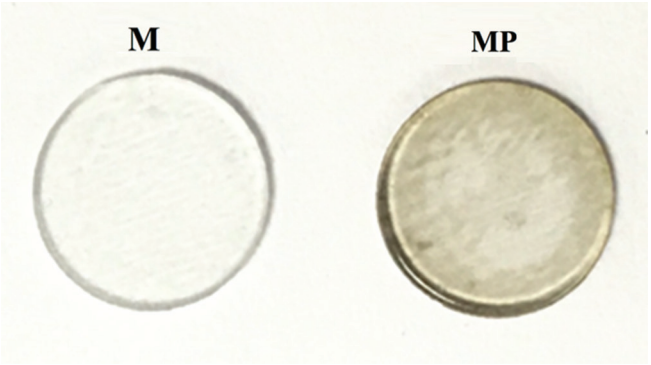


**Figure 1.** The images of the top view of printed objects without (M) and with (MP) PDA coating. The thickness of the objects is 3 mm and a diameter of 6 mm.

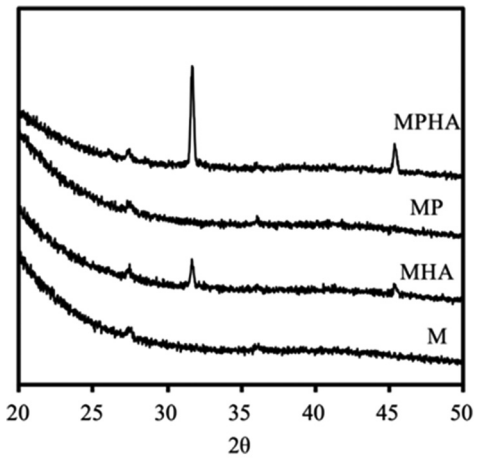


**Figure 2.** The wide-range X-ray diffractometry patterns of MED610 (M), MED610 with HA coating (MHA), MED610 with PDA coating (MP), and MED610 with PDA/HA coating (MPHA).

biocompatibility of materials is extremely important. The cell proliferation of the hMSCs cultured on M, MP, MHA, and MPHA for 1, 3, and 7 days was evaluated by PrestoBlue assay (Figure 5). The result shows that absorbance of MED610 object with PDA coatings (MP and MPHA) is higher than Ctl and without PDA coatings (M and MHA). Besides, the MED610 object without any coatings shows the lowest absorbance. In addition, the hMSCs cultured on MED610 object with both PDA coatings reveals a higher area of cell adhesion and are flat with an intact, well-defined morphology (Figure 6). These results point that MED610 object with PDA coatings can improve its biocompatibility, making it more suitable as a biomedical material.

### 3.3 Osteogenic Differentiation

The hMSCs cultured on M, MP, MHA, and MPHA for 3 and 7 days were analyzed the ALP activity to evaluate the osteogenic differentiation potential which is an important key to determine if the bone formation process is ongoing. Figure 7 shows cells growing on MPHA can express the most ALP levels, and the ALP expression level of MED610 object without coatings was lowest. The results demonstrate that MED610 object with PDA/HA coating helps to improves the osteogenic differentiation potential of stem cells.

## 4. Discussion

MED610 is a biocompatible 3D printing photocurable material commonly used in medical and dental fields requiring precise visualization and patient contact. Although this material is suitable for over 30 days' skin contact and up to 24 h mucosal membrane or bone contact, it can be more widely used if it can be enhanced

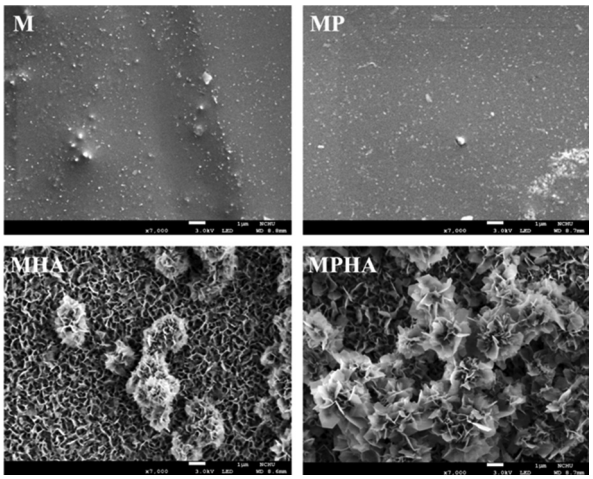


**Figure 3.** Surface scanning electron microscope images of the MED610 substrate with various coatings.

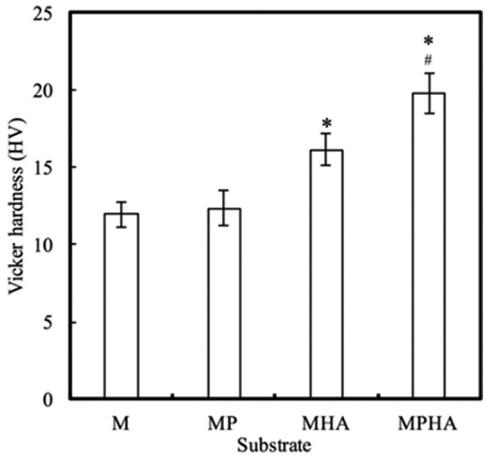


**Figure 4.** Vickers hardness of the MED610 substrate with various coatings.

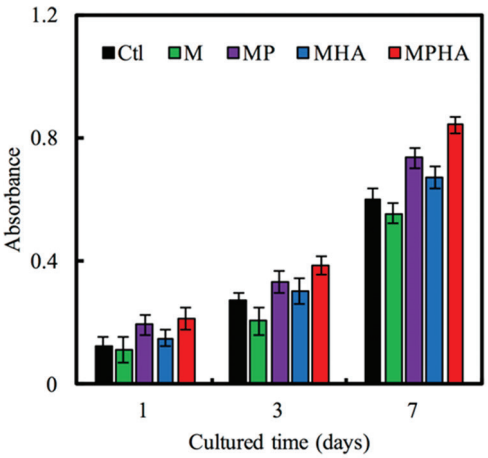


**Figure 5.** The cell proliferation of human mesenchymal stem cells cultured on the MED610 substrate with various coatings for 1, 3, and 7 days.

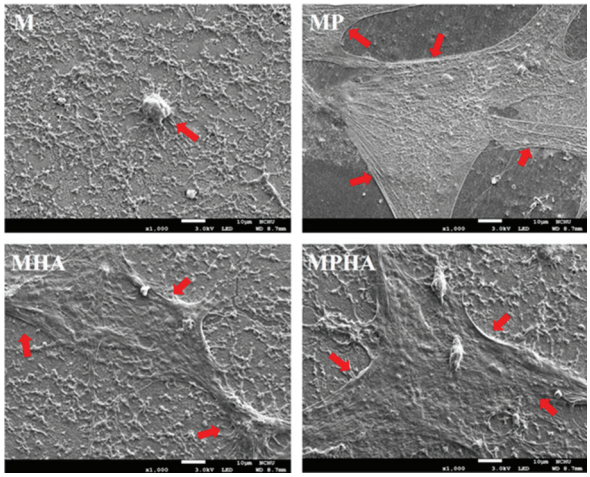


**Figure 6.** Surface scanning electron microscope images of human mesenchymal stem cells cultured on the MED610 substrate with various coatings. Cells are indicated by red arrows.

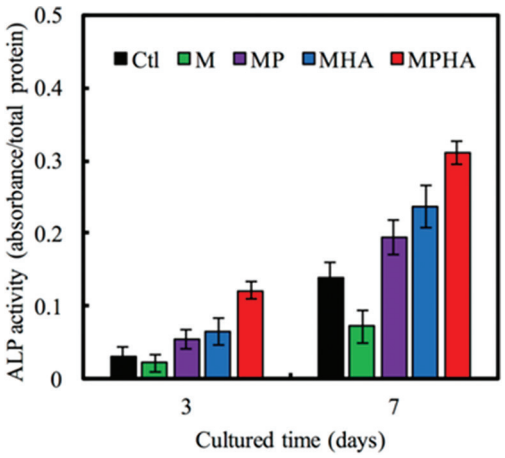


**Figure 7.** Alkaline phosphatase activity of human mesenchymal stem cells cultured on the MED610 substrate with various coatings for 3 and 7 days.

its biocompatibility and be promoted the potential of cell bone differentiation. Previous studies reported that PDA coatings on biological materials could facilitate cell attachment and promote cell proliferation[22,23]. When HA was added in PDA coatings, the phenomenon of cell calcium deposition was significantly promoted[20]. This means that the PDA/HA coatings can help to enhance osteogenic differentiation. In this study, the PDA/HA coatings were applied in MED610 objects. The results show that the biocompatibility, cell morphology, and bone differentiation potential of the cells cultured on the MED610 objects with PDA/HA coating can be improved. This study demonstrates that PDA/HA coating applications also have similar functions[20] on objects printed with MED610 materials to enhance their applicability.

## 5. Conclusion

This study shows that using the PDA/HA coating added to the MED610 biomedical 3D printing material that has been used in the medical field can improve its hardness, HA mineralization, cell proliferation, good cell morphology, and the amount of ALP expression. Therefore, the PDA/HA coating enhances the potential and development of MED610 materials for clinical applications in orthopedics and dentistry.

## Acknowledgments

The authors acknowledge receipt of grants from the National Science Council grants MOST (107-2218-E-468-005 – and 107-2622-E-468-002-CC2) of Taiwan and China Medical University Hospital grants (CRS-106-021).

### Authors' Contributions

Yu-Fang Shen conceived the ideas and organized the main content; Yi-Wen Chen and Hsin-Yuan Fang conducted the experiments and wrote the manuscript; and Ming-You Shie contributed some detailed techniques.

### Conflicts of Interest

The authors declare no competing financial interests.

## References

1. Rengier F, Mehndiratta A, vonTengg-Kobligk H, *et al.*, 2010, 3D Printing Based on Imaging Data: Review of Medical Applications. *Int J Comput Assist Radiol Surg*, 5:335-41. DOI 10.1007/s11548-010-0476-x.
2. Ventola CL, 2014, Medical Applications for 3D Printing: Current and Projected Uses. *P T*, 39:704-11.
3. Ciocca L, Mingucci R, Gassino G, *et al.,* 2007, CAD/CAM Ear Model and Virtual Construction of the Mold. *J Prosthet Dent,* 98:339-43. DOI 10.1016/S0022-3913(07)60116-4.
4. He J, Li D, Lu B, *et al.,* 2006, Custom Fabrication of Composite Tibial Hemi-knee Joint Combining CAD/CAE/CAM Techniques. *Proc Inst Mech Eng H*, 220:823-30. DOI 10.1243/09544119JEIM207.
5. Dai KR, Yan MN, Zhu ZA, *et al.,* 2007, Computer-aided Custom-made Hemipelvic Prosthesis Used in Extensive Pelvic Lesions. *J Arthroplasty,* 22:981-6. DOI 10.1016/j.arth.2007.05.002.
6. Zopf DA, Hollister SJ, Nelson ME, *et al.,* 2013, Bioresorbable Airway Splint Created with a Three-dimensional Printer. *N Engl J Med,* 368:2043-5. DOI 10.1056/NEJMc1206319.
7. Cho HR, Roh TS, Shim KW, et al., 2015, Skull Reconstruction with Custom Made Three-dimensional Titanium Implant. *Arch Craniofac Surg*, 16:11-16. DOI 10.7181/acfs.2015.16.1.11.
8. Jackson B, 2017, 3D Printed Hip Puts Teenager Back on her Feet. Available from: https://www.3dprintingindustry.com/news/materialise-3d-printed-hip-implant-gets-patient-back-feet-126139.
9. Zhao X, Wang X, Sun Y, et al., 2018, Use of Three-dimensional Printing to Fabricate First a Pelvic Model and Then a Semi-pelvic Prosthesis with Sacrum : A Case Report. *Biomed J Sci Tech Res,* 4:1-4. DOI 10.26717/BJSTR.2018.04.001060.
10. Jacek B, Maciej P, Tomasz P, *et al.,* 2018, 3D Printed Models in Mandibular Reconstruction with Bony Free Flaps. *J Mater Sci Mater Med,* 29:23. DOI 10.1007/s10856-018-6029-5.
11. Gopinathan J, Noh I, 2018, Recent Trends in Bioinks for 3D Printing. *Biomater Res,* 22:11. DOI 10.1186/s40824-018-0122-1.
12. Kaushik NK, Kaushik N, Pardeshi S, et al., 2015, Biomedical and Clinical Importance of Mussel-inspired Polymers

and Materials. *Mar Drugs,* 13:6792-817. DOI 10.3390/md13116792.

13. Lee H, Dellatore SM, Miller WM, *et al.,* 2007, Mussel-inspired Surface Chemistry for Multifunctional Coatings. *Science,* 318:426-30. DOI 10.1126/science.1147241.
14. Kang SM, Hwang NS, Yeom J, *et al.,* 2012, One-step Multipurpose Surface Functionalization by Adhesive Catecholamine. *Adv Funct Mater,* 22:2949-55. DOI 10.1002/adfm.201200177.
15. Yang K, Lee JS, Kim J, *et al.,* 2012, Polydopamine-mediated Surface Modification of Scaffold Materials for Human Neural Stem Cell Engineering. *Biomaterials,* 33:6952-64. DOI 10.1016/j.biomaterials.2012.08.001.
16. You I, Kang SM, Byun Y, *et al.,* 2011, Enhancement of Blood Compatibility of Poly(Urethane) Substrates by Mussel-inspired Adhesive Heparin Coating. *Bioconjug Chem,* 22:1264-9. DOI 10.1021/bc2000534.
17. Kim TG, Lee H, Jang Y, *et al.,* 2009, Controlled Release of Paclitaxel from Heparinized Metal Stent Fabricated by Layer-by-layer Assembly of Polylysine and Hyaluronic Acid-g-poly(Lactic-co-glycolic acid) Micelles Encapsulating Paclitaxel. *Biomacromolecules,* 10:1532-9. DOI 10.1021/bm900116r.
18. Ku SH, Park CB, 2010, Human Endothelial Cell Growth on Mussel-inspired Nanofiber Scaffold for Vascular Tissue Engineering. *Biomaterials,* 31:9431-7. DOI 10.1016/j.biomaterials.2010.08.071.
19. Wu C, Han P, Liu X, *et al.,* 2014, Mussel-inspired Bioceramics with Self-assembled Ca-P/Polydopamine Composite Nanolayer: Preparation, Formation Mechanism, Improved Cellular Bioactivity and Osteogenic Differentiation of Bone Marrow Stromal Cells. *Acta Biomater,* 10:428-38. DOI 10.1016/j.actbio.2013.10.013.
20. Cheng YL, Chen YW, Wang K, *et al.,* 2016, Enhanced Adhesion and Differentiation of Human Mesenchymal Stem Cell Inside Apatite-mineralized/Poly(Dopamine)-Coated Poly(ε-Caprolactone) Scaffolds by Stereolithography. *J Mater Chem B,* 4:6307-15. DOI 10.1039/c6tb01377e.
21. Lin CC, Fu SJ, 2016, Osteogenesis of Human Adipose-derived Stem Cells on Poly(Dopamine)-coated Electrospun Poly(Lactic Acid) Fiber Mats. *Mater Sci Eng C Mater Biol Appl,* 58:254-63. DOI 10.1016/j.msec.2015.08.009.
22. Tripathi BP, Dubey NC, Subair R, *et al.,* 2016, Enhanced Hydrophilic and Antifouling Polyacrylonitrile Membrane with Polydopamine Modified Silica Nanoparticles. *RSC Adv,* 6:4448-57. DOI 10.1039/c5ra22160a.
23. Steeves AJ, Atwal A, Schock SC, *et al.*, 2016, Evaluation of the Direct Effects of Poly(Dopamine) on the *in vitro* Response of Human Osteoblastic Cells. *J Mater Chem B*, 4:3145-56. DOI 10.1039/c5tb02510a.

RETRACTION NOTE

# Retraction: Application of 3D printing technology in orthopedic medical implant – Spinal surgery as an example

**Rong Feng Zhang, Peng Yun Wang, Ming Yang, Xuebo Dong, Xue Liu, Yiguang Sang, An Tong**

**Published Online:** July 12, 2019

**Citation:** Zhang RF, Wang PY, Yang M, et al., 2019, Retraction: Application of 3D printing technology in orthopedic medical implant – Spinal surgery as an example. Int J Biprint, 5(2):232. http://dx.doi.org/10.18063/ijb.v5i2.232

Whioce Publishing hereby retracts an article entitled "Application of 3D printing technology in orthopedic medical implant – Spinal surgery as an example" published by the *International Journal of Bioprinting* due to the plagiarism issue.

A careful analysis of this article published in Volume 5, Issue 2 (2019) of *International Journal of Bioprinting* has revealed that this work was highly similar to another paper authored by Dr. Grant *et al.*[1] entitled "Use of 3D Printing in Complex Spinal Surgery: Historical Perspectives, Current Usage, and Future Directions," which has been published in Volume 31, Number 3 (2016) of *Techniques in Orthopaedics*, pp. 172-180.

The investigation panel found that more than 70% of the content in Dr. Grant's original contribution (including most of the figures) was reproduced without any form of authorization and permission in the paper authored by Zhang RF, Wang PY, Yang M, Dong X, Liu X, Sang Y, and Tong A.

This is clearly a case of plagiarism that goes against the publication policy and ethics of the *International Journal of Bioprinting*.

Whioce Publishing apologizes for the fact that the plagiarism issue was not identified during the initial screening process and we offer our sincere apologies to Dr. Caroline A. Grant, Ms. Maree T. Izatt, Dr. Robert D. Labrom, Dr. Geoffrey N. Askin, and Dr. Vaida Glatt for this unacceptable incidence.

Peng Yun Wang and An Tong were contacted but did not respond.

Chee Kai Chua
Editor-in-Chief

## References

1. Grant CA, Izatt MT, Labrom R, *et al*., 2016, Use of 3D Printing in Complex Spinal Surgery: Historical Perspectives, Current Usage, and Future Directions. *Tech Orthop*, 31(3):172-80. DOI 10.1097/BTO.0000000000000186.

Retraction: Application of 3D printing technology in orthopedic medical implant – Spinal surgery as an example © 2019 Zhang , *et al*. This is an Open Access article distributed under the terms of the Creative Commons Attribution-NonCommercial 4.0 International License (http://creativecommons.org/licenses/by-nc/4.0/), permitting all non-commercial use, distribution, and reproduction in any medium, provided the original work is properly cited.

RESEARCH ARTICLE

# *In vitro* model of the glial scar

**Ao Fang[1,2], Zhiyan Hao[1,2], Ling Wang[1,2], Dichen Li[1,2]*, Jiankang He[1,2], Lin Gao[1,2], Xinggang Mao[3], Rubén Paz[4]**

[1]School of Mechanical Engineering, Xi'an Jiaotong University, Xi'an, ShaanXi 710054, China
[2]State Key Laboratory for Manufacturing System Engineering, School of Mechanical Engineering, Xi'an Jiaotong University, Xi'an, ShaanXi 710054, China
[3]Department of Neurosurgery, Xijing Hospital, Fourth Military Medical University, Xi'an, Shaanxi Province 710032, China
[4]Departamento de Ingeniería Mecánica, Universidad de Las Palmas de Gran Canaria, 35017 Las Palmas de Gran Canaria, Spain

**Abstract:** The trauma of central nervous system (CNS) can lead to glial scar, and it can limit the regeneration of neurons at the injured area, which is considered to be a major factor affecting the functional recovery of patients with CNS injury. At present, the study of the glial scar model *in vitro* is still limited to two-dimensional culture, and the state of the scar *in vivo* cannot be well mimicked. Therefore, we use a collagen gel and astrocytes to construct a three-dimensional (3D) model *in vitro* to mimic natural glial scar tissue. The effects of concentration changes of astrocytes on cell morphology, proliferation, and tissue performance were investigated. After 8 days of culture *in vitro*, the results showed that the tissue model contracted, with a measured shrinkage rate of 4.5%, and the compressive elastic modulus increased to nearly 4 times. Moreover, the astrocytes of the 3D tissue model have the ability of proliferation, hyperplasia, and formation of scar clusters. It indicates that the model we constructed has the characteristics of glial scar tissue to some extent and can provide an *in vitro* model for the research of glial scar and brain diseases.

**Keywords:** Glial scar; *In vitro*; Three-dimensional

*Correspondence to: Dichen Li, State Key Laboratory for Manufacturing System Engineering, School of Mechanical Engineering, Xi'an Jiaotong University, Xi'an, ShaanXi 710054, China; xjtudcli@sina.com

**Received:** July 10, 2019; **Accepted:** July 18, 2019; **Published Online:** July 30, 2019

**Citation:** Fang A, Hao Z, Wang L, *et al.*, 2019, *In vitro* model of the glial scar. *Int J Bioprint*, 5(2): 235. http://dx.doi.org/10.18063/ijb.v5i2.235

## 1. Introduction

The central nervous system (CNS) is very complex, and trauma, disease, and infection of it is urgent problems to be solved, all of them are basically inseparable from resulting scars. Two types of scarring tissue are formed in the injured CNS. One is a fibrotic scar that is formed by fibroblasts, and the other is a glial scar, which consists of astrocytes, microglia, and other glial precursor cells[1]. Once CNS is injured, fibroblasts invade the region of the lesion and interact to form glia limitans with astrocytes[2-4]. However, fibrotic scars do not always exist in CNS tissue repair, such as no fibrotic scar formation during the astrocytic reconstruction of the blood-brain barrier[5,6]. Therefore, fibrotic scar does not play a key role in CNS tissue repair[1]. On the contrary, a glial scar plays an important role. A glial scar is mainly caused by CNS trauma. The formation of a glial scar is mainly caused by the action of astrocytes, such as barrier forming, mitosis, and migration to the injured area to fill space[7,8]. Astrocytes play a significant role in CNS injury response[9,10]. The response of them varies with the location of the injury. The ones near the damaged tissues become hypertrophic, hyperplastic, and deformed. Moreover, the glial fibrillary acidic protein (GFAP) goes up[11,12], the cells migrate[13-15], and the dense scar tissue begin to isolate the damaged area from the surrounding healthy tissue[16-18]. In general, the morphology, proliferation, and migration of astrocytes are the main causes of glial scar formation.

*In vitro* model of the glial scar © 2019 Fang A, *et al*. This is an Open Access article distributed under the terms of the Creative Commons Attribution-NonCommercial 4.0 International License (http://creativecommons.org/licenses/by-nc/4.0/), permitting all non-commercial use, distribution, and reproduction in any medium, provided the original work is properly cited.

However, the research on the glial scar is mainly based on two-dimensional (2D) culture. Yu *et al.*[19] used a sterile plastic pipette to scratch the astrocytes in the 2D culture to simulate the damage and compared the protein content to estimate the degree of injury. In addition, they found that the surrounding part of the damaged area had also suffered a certain degree of trauma. The response to the scratching can be mimicked and this kind of 2D scratch-would model is widely used. Kimura-Kuroda *et al.*[20] constructed a glial scar-like structure by 2D coculturing of meningeal fibroblasts and brain astrocytes with transforming growth factor-β1 (TGF-β1). The model can inhibit the neurite outgrowth of neurons remarkably. In general, the traditional method of 2D cell culture cannot mimic the cell growth conditions *in vivo* and the physiological activities of normal cells. Hence, it cannot reflect the nature glial scar tissue properly. However, the three-dimensional (3D) model is expected to be able to express the glial scar effect from a more comprehensive level. Spencer *et al.*[21] constructed a kind of glial scar model that combines linear actuators to simulate axial Micro Motion around neural implants in a collagen gel. They found that local strain fields could stimulate the formation of the glial scar. Rocha *et al.*[22] built a 3D culture system mimicking the glial scar by the alginate gels embedded with astrocytes cultured in meningeal fibroblast conditioned medium. The model behaved similarly to that of the glial scar, for initiating changes in gene expression and inhibiting neuronal outgrowth. In this study, a 3D astrocytes model with collagen gel is constructed to mimic the glial scar tissue (hypertrophy and hyperplasia). The rate of gel contraction is dependent on the density of the cells within the block as well as the migration and proliferation of astrocytes.

## 2. Materials and Methods

In the paper, a 3D tissue was constructed using collagen gel with astrocytes, and the contraction of the tissue was examined by microscope. The immunofluorescence results of the cells were observed by laser scanning confocal microscope (LSCM). Scanning electron microscope (SEM) was used to analyze the morphology and pore size of the surface and section of the tissue. The specific process is shown in Figure 1.

### 2.1 Cell Isolation and Culture

Primary astrocytes were extracted from the cortices of 1-day-old mouse pups (Kunming strain, FMMU, Xi'an). The cortical tissue was removed and immersed in HBSS (Hank's balanced salt solution) (14175-095, Gibco, USA) at 4°C. The tissue was cut into pieces and digested with 0.25% trypsin (0458, Amresco, USA) for 20 min at 37°C and was transferred to complete

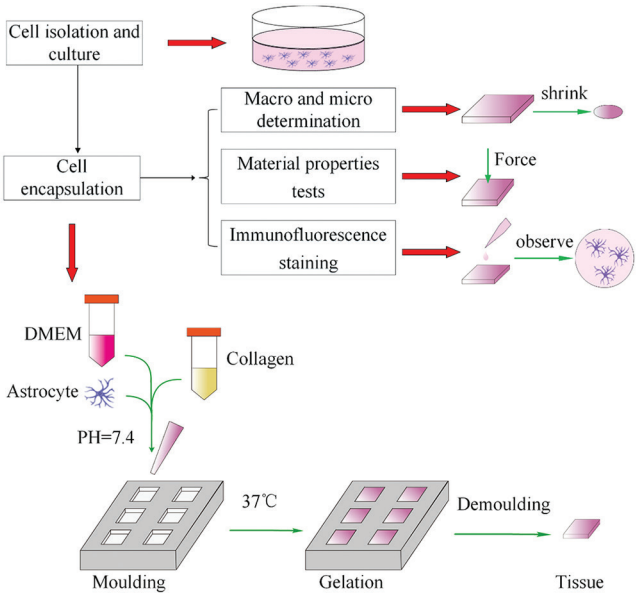


**Figure 1.** The flow chart of the experiment.

Dulbecco's modified eagle medium (DMEM) media containing DMEM (SH30022.01, HyClone, USA), 20% fetal bovine serum (FBS), 10270-106, Gibco), and 1% penicillin/streptomycin (P1400-100, Solarbio, USA). Finally, the medium was filtered through a 40-μm cell strainer (352340, Falcon) to dissociate the astrocytes. The isolated astrocytes were re-suspended in complete DMEM media containing 20% FBS (10270-106, Gibco) and 1% penicillin/streptomycin (P1400-100, Solarbio) at 37°C with 5% $CO_2$. The medium was changed every 2 days, and the cells at passage three were used for the experiment.

### 2.2 Cell Encapsulation

A rat tail-derived type I collagen solution (4 mg/mL in 0.1 M glacial acetic acid) was mixed with complete DMEM media at a ratio of 1:3. The pH value of the collagen and medium solution was adjusted to 7.4 before it was used to resuspend the cells at the specified concentration at 4°C. The mixture of collagen solution and astrocytes ($5 \times 10^5$ cells/mL, $1 \times 10^6$ cells/mL, and $2 \times 10^6$ cells/mL) was molded into $10 \times 10 \times 2$ $mm^3$ block for SEM study, macroscopic determination and immunofluorescence staining. The mixture was also molded into $6 \times 6 \times 6$ $mm^3$ block for material properties tests. The samples were kept at 37°C for 40 min to cure. The embedding process is shown in Figure 1. Then, the tissue blocks with cells were cultured in complete DMEM media at 37°C with 5% $CO_2$. The collagen gels embedded in $5 \times 10^5$ cells/mL, $1 \times 10^6$ cells/mL, and $2 \times 10^6$ cells/mL were marked Group 0.5, Group 1, and Group 2, respectively.

### 2.3 Macroscopic and Microcosmic Determination Collagen Gels

The collagen gel blocks of 10 × 10 × 2 $mm^3$ were observed under the inverted fluorescence microscope (Ti-S, CHANSN, China) for macroscopic determination. The inverted fluorescence microscope software NIS was used for measuring the side lengths of the block. The side of 10 × 10 $mm^2$ was the measured object. The area of this face was calculated.

SEM was used for microcosmic determination. The 10 × 10 × 2 $mm^3$ and 6 × 6 × 6 $mm^3$ collagen gel blocks were both fixed with 4% paraformaldehyde for an hour. The 10 × 10 × 2 $mm^3$ blocks were freeze-dried by freeze dryer (VFD2000, BIOCOOL, China) overnight directly. The 6 × 6 × 6 $mm^3$ blocks were sliced with a freezing microtome (CM1860, Leica, German) for section views before freeze-drying. Each slice was 40 μm. After metal spraying, the freeze-dried tissues were examined using SEM (su-8010, Hitachi, Japan).

### 2.4 Material Mechanical Properties Tests

The 6 × 6 × 6 $mm^3$ collagen gel blocks were used for the determination of the compression elastic modulus in a microcomputer-controlled universal testing machine (ETM103A, Shenzhen Wance Testing Equipment Company limited, China). Before measuring, the gel blocks were fixed with 4% paraformaldehyde for an hour. And then, each of them was placed on the platform of the microcomputer-controlled universal testing machine, and the liquid on the surface of the block was removed by a plastic pipette. The loading speed was set to 2 mm/min and the compression stroke was set to 1 mm. Three samples were tested for each group.

### 2.5 Immunofluorescence Staining

The embedded astrocytes were fixed with 4% paraformaldehyde for an hour and washed with 1× PBS (phosphate-buffered saline, HyClone, SH30256.01) 6 times at 10 min intervals. Then, the method of freezing slice was used to obtain 40 μm thickness slices for the immunofluorescence staining of the embedded cells. Afterward, the slices were incubated in 1× PBS with 5% goat serum (AR0009, Boster, USA), 1:200 diluted primary antibody GFAP (3670S, CST, USA) and 0.3% Triton X-100 (T8200, Solarbio) overnight at 4°C. The tissues were then washed with 1× PBS 6 times at 10 min intervals. Next, the tissue was incubated in 1× PBS with 5% goat serum, 1:200 diluted secondary antibody goat anti-mouse IgG, FITC-conjugated (CW0113S, CWBIO, China), and 0.3% Triton X-100 for 4 h. Subsequently, 4,6-diamino-2-phenyl indole (DAPI) (AR1176, Boster) was added for an additional 10 min. Finally, the tissues were washed 6 times in 1× PBS at 10 min intervals and observed under a LSCM.

## 3. Results

### 3.1 Morphology and Proliferation of Astrocytes Embedded in Collagen Gel

After 8 days of cultivation, the astrocytes were distributed throughout the collagen gels and demonstrated typical stellate morphologies, and widespread process extension was observed. The process extension of the astrocytes became longer (Figure 2). To measure the proliferation, the cells were observed by laser confocal microscopy in 3D space style. DAPI was used to stain the nuclei and the concentration was obtained by dividing the number of DAPI (cells) by the volume of the 3D space. According to the results, the number of cells in the three groups increased with the increase of culture time (Figure 3). In the first 4 days, the number of cells in Group 0.5 was always lower than in Groups 1 and 2, and the concentration was below 1.5 × $10^6$ cells/mL. The astrocyte process extension was also poorer compared to the other groups (Figure 2). On day 8, the cell concentration increased to 1.9 × $10^6$ cells/mL, and then the cells were able to communicate and extend more easily. Compared with it,

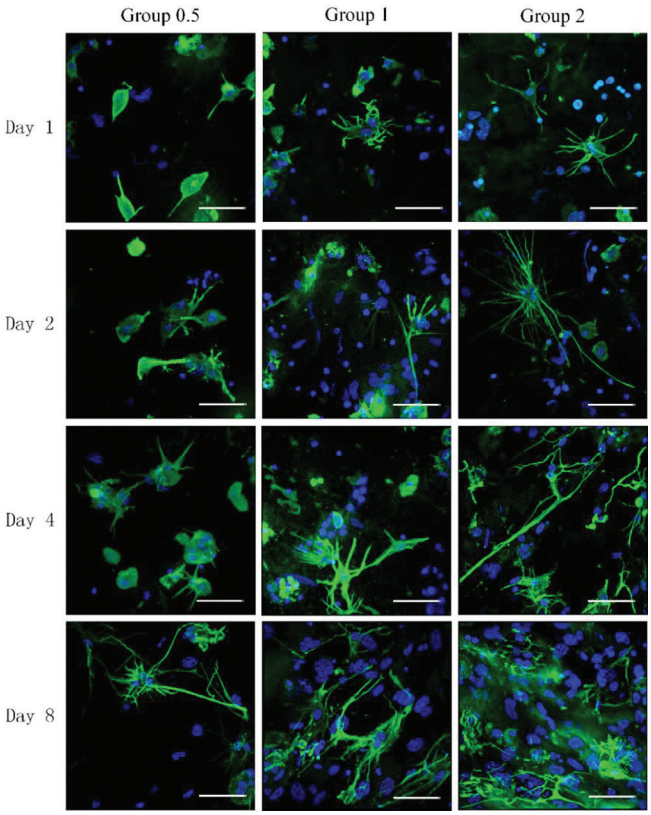


**Figure 2.** Immunofluorescence staining of different gradient concentration astrocytes embedded in collagen gel on day 1, day 2, day 4, and day 8. The astrocytes stained with glial fibrillary acidic protein (green) and nuclei stained with DAPI (blue). Scale bar: 50 μm.

the cell densities of Group 1 and Group 2 were larger, so did the number of the cells. In particular, the length of the protrusion extension was higher, and the cell proliferation was faster in Group 2. In addition, the further longer protrusions of the cells occurred in Group 1 and Group 2 on day 4. At the same time, the proliferation did not stop, and the cell concentration was $4.5 \times 10^6$ cells/mL for Group 2 and $3 \times 10^6$ cells/mL for Group 1. On day 8, the cell density increased further, and the cell concentration was $7.4 \times 10^6$ cells/mL for Group 2 and $4.7 \times 10^6$ cells/mL for Group 1. Especially in Group 2, the cells were still in a discrete state in some regions, with a high degree of process extension. However, the cells aggregated in many areas of Group 2. The number of cell nuclei stained with DAPI increased obviously, and a large number of cells clustered together and became denser.

## 3.2 The Deformation (shrinkage) of Tissue Blocks

The size of the collagen gel block was $10 \times 10 \times 2$ mm$^3$ and the side of $10 \times 10$ mm$^2$ was selected as the observation object. The vertical direction along the gel tissue was the observation direction. The area of the collagen gel blocks without cells did not change, but the embedded astrocytes ones shrank. The degree of shrinking depends on cell concentration and the days of culture (Figure 4). The area of collagen gel of Group 0.5, Group 1, and Group 2 continued to shrink with the increase of culture time, and the degree of contraction was positively correlated with the concentration of embedded cells and culture time.

The transparency of the gels also changed during the process of shrinking. As the astrocytes proliferated and migrated, the water was squeezed out, and the area was reduced continuously. When the collagen gel had just been constructed, the gel was almost transparent, but it gradually became opaque (Figure 4A). When the area of gel block shrank by 60% or more, the four corners of the block began to disappear and changed to an ellipsoid or sphere gradually. From the front view of the collagen gel block, the block was thickened in the vertical direction and the middle part of it became more and more abrupt. As the concentration of the embedded cells and the culture day increased, the lateral direction of the model was gradually shortened, the vertical direction was gradually increased, and the central portion was arched. With the process of culture, the original rectangular section became ellipsoid and gradually approximated to spherical shape at the end of the culture. On day 8, the shape of the collagen gel blocks of Group 0.5, Group 1, and Group 2 had been changed into ellipsoids or spheres and the areas of them were about 8.9%, 6.3%, and 4.5% of their initial areas, respectively (Figure 4B).

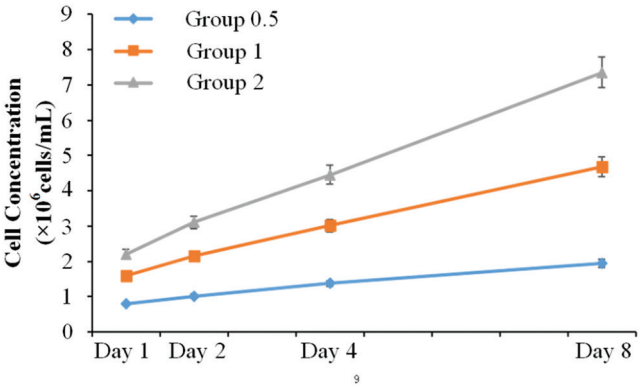


**Figure 3.** Proliferation of astrocytes of different concentration astrocytes embedded in collagen gel, $n$=4.

## 3.3 Effects of Astrocytes on Collagen Gel Blocks Surface

SEM tests of the surface of the samples on day 4 were carried out to analyze the reason of collagen shrinkage. The SEM images of collagen gel blocks surface showed that the embedded astrocytes and no cells blocks were

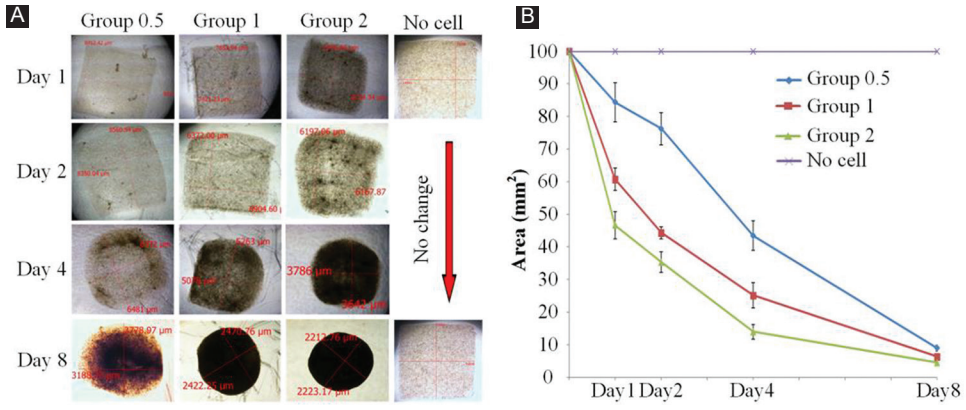


**Figure 4.** (**A**) The collagen gel blocks with different concentration astrocytes under the microscope. (**B**) The area of collagen gels changes with different concentration astrocytes, $n$=5.

quite different. The surface morphology of collagen gel blocks without cells was fibrous, porous, and flat (Figure 5C). On the contrary, the one with embedded cells had obvious folds (Figure 5D). The macroscopic gel blocks corresponding to the two kinds of surfaces are shown in Figure 5A and B. From the enlarged images, it could be found that the surface morphology of the collagen gel blocks without cells was porous (Figure 5E), and the surface morphology of the astrocytes embedded ones was almost non-porous, smooth and solid, and relatively (Figure 5F).

### 3.4 Effects of Astrocytes on Collagen Gel Blocks Cross Section

The cross-sectional morphology of collagen gel blocks of Group 0.5, Group 1, and Group 2 was examined by SEM (Figure 6). After the embedded astrocytes were cultured for 1 day, the collagen fiber pores of the cross sections were observed. The pores of Group 0.5 (around 10 μm) were relatively larger than the ones of the other groups. On day 2, the collagen fiber pores shrank. Similar results were obtained after 4 days in culture; the collagen fibers were aggregated, causing the pores between the fibers to shrink further; Group 0.5 shrank to about 2 μm, Group 1 shrank to about 1 μm; and Group 2 shrank to about 0.5 μm. On day 8, the pores between collagen fibers of Group 2 were almost invisible, and the pores of the Group 0.5 and Group 1 samples could be seen, but they were small, both of them around 0.5 μm (Figure 6).

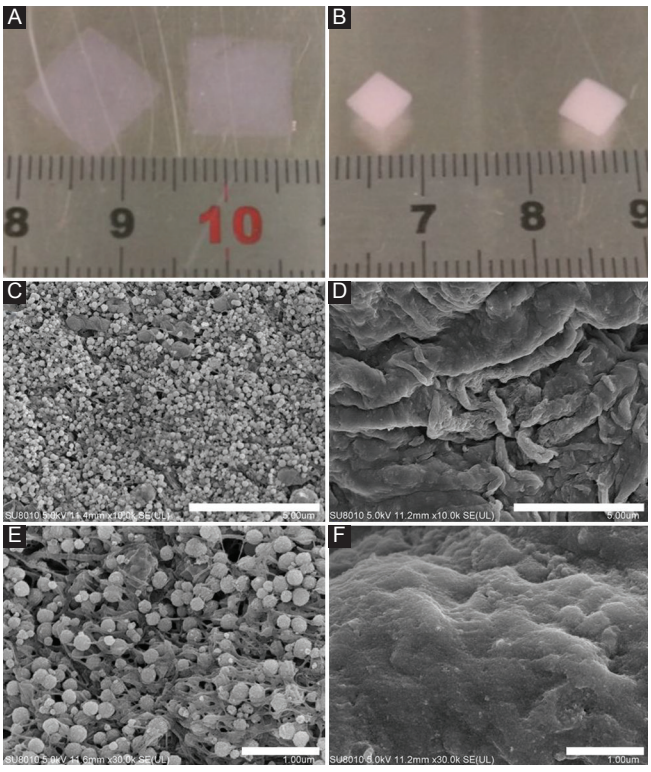


**Figure 5.** The surface of the collagen gel blocks on day 4. (**A**) Collagen gel block without cells. (**B**) Collagen gel blocks with astrocytes. (**C**) Scanning electron microscope (SEM) of the surface of collagen gel blocks without cells. Scale bar: 5 μm (**D**) SEM of the surface of collagen gel blocks with astrocytes. Scale bar: 5 μm. (**E**) Enlargement SEM of the surface of collagen gel blocks without cells. Scale bar: 1 μm. (**F**) Enlargement SEM of the surface of collagen gel blocks with astrocytes. Scale bar: 1 μm.

### 3.5 Compressive Elastic Modulus of Gel Blocks

The modulus of the glial tissue increased with the increment of culture time. Moerover, the modulus of Group 2 tissue was larger than the other two groups. In the first 2 days, Group 0.5 and Group 1 collagen tissue modulus was close. On day 4, the modulus gap widened between the two groups. On day 8, the modulus of Group 0.5 and Group 1 returned to a relatively closed state (Figure 7A). On the other hand, the modulus increased, with the increase of shrinkage rate. Overall, the Group2 modulus varied most greatly with the shrinkage. Therefore, it can be observed that for the same shrinkage change, the greater the concentration of the cells, the higher the increase of the modulus (Figure 7B).

## 4. Discussion

At present, the *in vitro* scar research model is limited to 2D models, and 2D culture does not characterize the culture environment *in vivo* well. In this paper, a 3D glial scar model of CNS *in vitro* was constructed using three different concentration astrocytes, and the changes of the cells and gel structure have been studied. The model can reflect the formation of glial scars from two aspects, cell and the macroscopic and microscopic perspectives of the model. From the cellular point of view, the cells proliferated and migrated. The study of proliferation and migration characteristics was carried out by adjusting the initial concentration of the cells embedded in collagen gel. We found that the higher the initial concentration and the more proliferation ability and interaction of the cells, the better for glial scar-like cluster formation. Figure 8A shows this cluster formation, which is similar to the results of literature[20]. In this reference, the authors carried out the coculture of meningeal fibroblasts and cerebral astrocytes with TGF-β1 to form a scar-like structure. The model constructed in this paper reproduces the characteristics of glial scar clusters in 3D space (Figure 8B), which has advantages compared with 2D cell growth[23,24]. In addition, the morphology of the cells embedded in collagen gel block at the concentration of $2 \times 10^6$ cells/mL is hypertrophic, hyperplastic, and deformed (Figure 9), and the similar phenomenon occurs during the glial scar formation. That is to say, the model constructed by us has similar characteristics to the glial scar in terms of

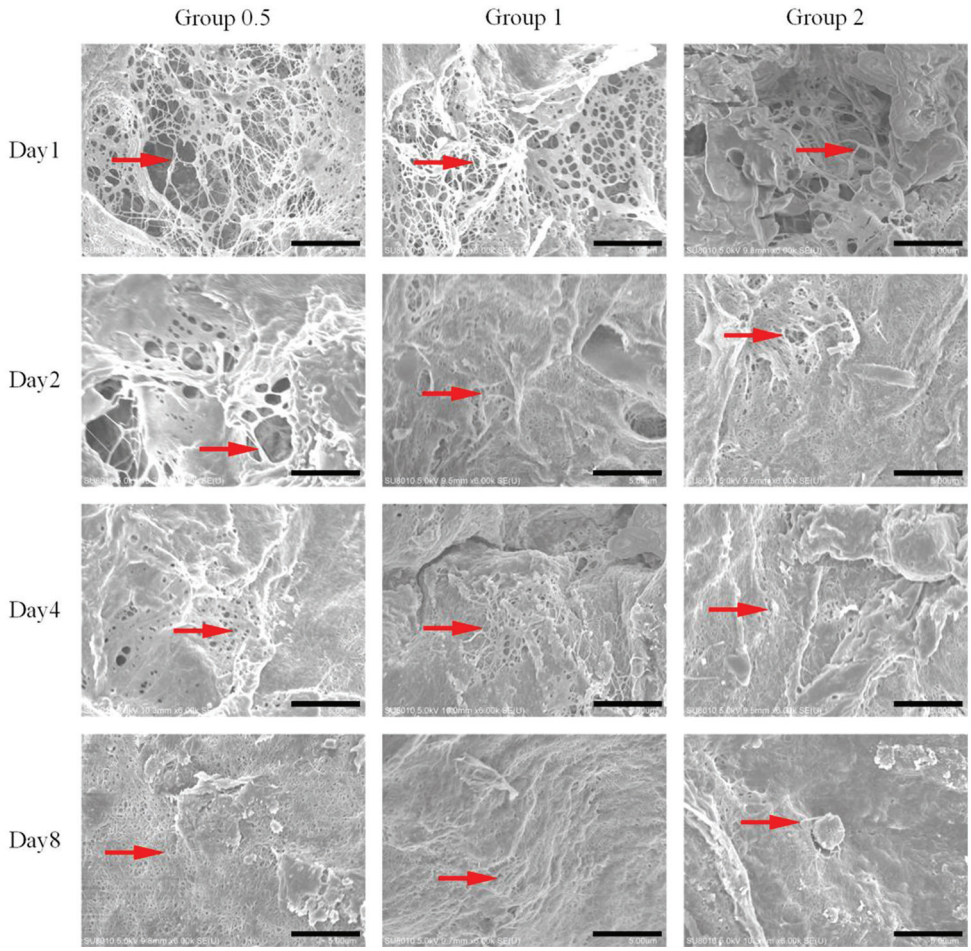


**Figure 6.** Scanning electron microscope images of cross sections of collagen gel blocks embedded in different concentration gradient cells. Arrows indicate the collagen fiber. Scale bar: 5 μm.

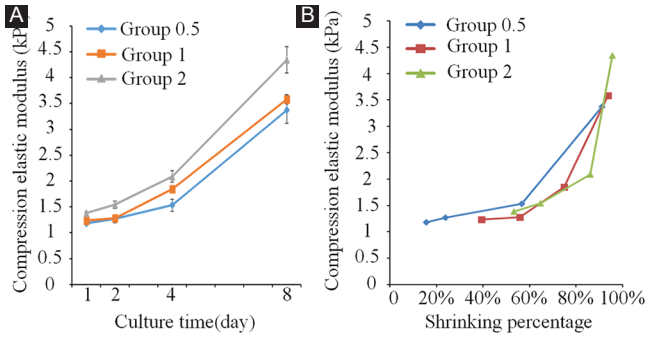


**Figure 7.** (**A**) Compression elastic modulus of the collagen gel blocks changes with the increase of culture time. (**B**) Compression elastic modulus of the collagen gel blocks changes with the shrink of the blocks.

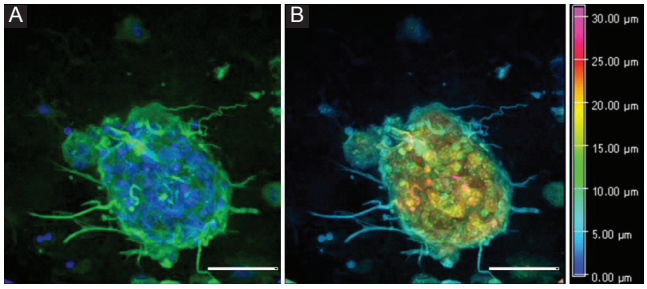


**Figure 8.** (**A**) Glial scar-like cluster formed by astrocytes aggregation in three-dimensional collagen gel tissue, cells stained with glial fibrillary acidic protein (green) for astrocytes, DAPI (blue) for nuclei. (**B**) Images (depth decoding) of glial scar-like cluster. Different colors represent the different planes along the Z-axis, Scale bars: 50 μm.

cell morphology[19], which further proves that the tissue model has the potential to form glial scars.

From the macroscopic and microscopic point of view, the collagen gel block with astrocytes shrinks with the increase of culture time. However, the size of the collagen gel block without cells does not change significantly, the reason why the shrinkage of collagen gel is mainly related to the proliferation and migration of astrocytes, which are similar to the glial scar formation in the CNS *in vivo*[12,18]. In addition, the gel shrinking in culture is similar to the phenomenon of fibroblast collagen gel tissue[25], which is related to the formation of scars, wound repair,

and filling. Thus, the proposed 3D collagen gel tissue constructed with astrocytes has scar formation properties, and the glial scars are mainly produced by astrocytes. It is quite coincidental that the similar phenomenon of tissue shrinking also occurs in the brain of a Sorex araneus. Scientists have discovered that the skull of the Sorex araneus pup shrinks in the late summer, as well as the brain, whose weight is also reduced. During the winter, the part of brain lost can grow back partly. This phenomenon is called Dehnel's phenomenon[26-28]. It is similar to the results of this article, occurring in the brain. To a certain extent, it may provide some reference for the study of brain plasticity and evolution. It may have a certain value for reference to the study of brain plasticity and evolution.

On the basis of this shrinkage, the folds can be found on the surface of the block, and the pores are reduced with the increase of culture time. Tallinen *et al*.[29] used a similar principle to construct a fold model of the human brain from a macro perspective. At this stage, the cells traction caused the deformation of the extracellular matrix[30-32], resulting in a stronger collagen fiber aggregation. With different initial cell concentrations, the degree of reduction is also different. The higher the concentration, the more cells proliferate and migrate, and the more seriously the gel tissue shrinks. The collagen gel with astrocytes shrinks due to cell proliferation and migration. Consequently, the collagen fibers gradually extrude each other, the surface pores disappear, and the fiber pores decrease. Meanwhile, the surface of the collagen gel is deformed to form a relatively solid and wrinkled surface because of the movement of the cells. The process of gel contraction is similar to the course of wound healing[33]. The force produced by cell proliferation and migration does not affect the collagen gel without cells. Hence, the surface remains flat and porous. In addition, the shrinkage rates of blocks with different concentration astrocytes were relatively similar on day 8, but the moduli of them were quite different. This indicates that the concentration of cells also has a certain effect on the modulus when the collagen gel shrinks. The higher the cell concentration, the larger the collagen tissue modulus. From this, the reason for collagen gel macroscopic and microscopic size-changing can be inferred (Figure 10). The results of the experiment can demonstrate that the model we constructed can form glial scars.

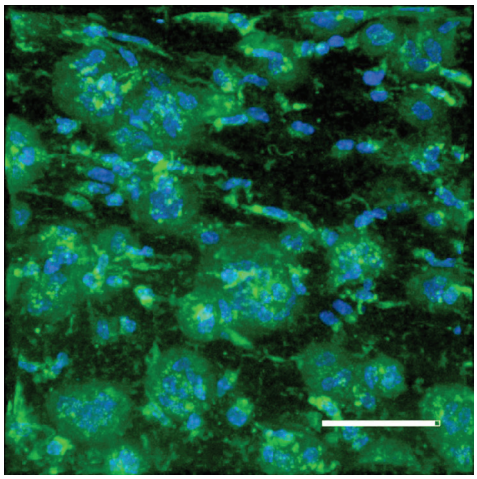

**Figure 9.** The hypertrophic cytoplasm of astrocytes embedded in collagen gel on day 8, astrocytes were stained by glial fibrillary acidic protein in green, nuclei were stained by DAPI in blue, Scale bars: 50 μm.

## 5. Conclusion

In this study, a 3D astrocytes model with collagen gel *in vitro* has been constructed. This model shows the characteristics of the glial scar (hypertrophy and hyperplasia). The constructed 3D model reveals overall shrinkage with the prolongation of culture time. On the other hand, the shrinkage rate and compression elastic

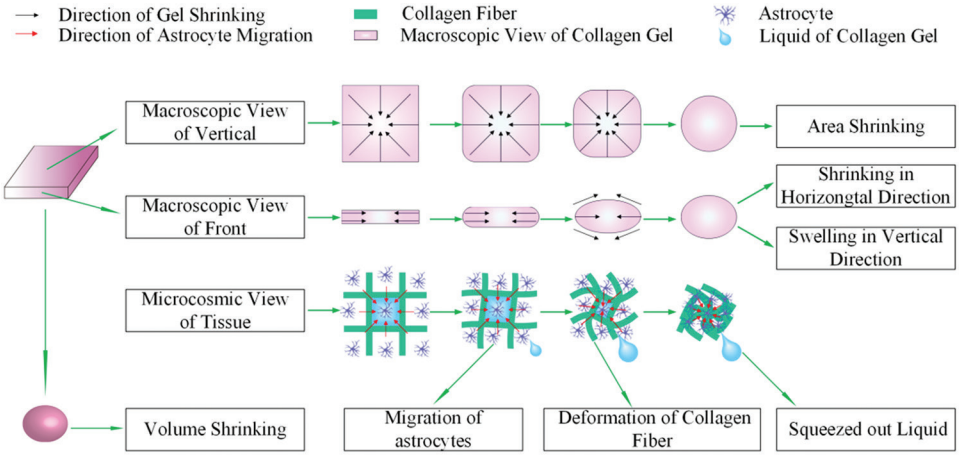


**Figure 10.** The reason for collagen gel block size changing from macroscopic and microscopic.

modulus are positively correlated with the culture time and cell concentration, because of the migration and proliferation of astrocytes. The construction method of the 3D tissue studied in this paper can be used to create *in vitro* glial tissue models, which can be useful for the study of glial scar and related brain diseases.

## Acknowledgments

The work was supported by the Program of the National Natural Science Foundation of China [51675411] and the Youth Innovation Team of Shaanxi Universities.

## Authors' Contributions

AF and LW designed the study; AF and ZY experimented. AF, LW, and RP drafted the manuscript. DC, LW, LG, XG, and JK coordinated the project and discussed the results. All authors read and approved the final manuscript.

## Conflicts of Interest

The authors declare that they do not have any competing interests.

## References

1. Kawano H, Kimura-Kuroda J, Komuta Y, *et al*., 2012, Role of the Lesion Scar in the Response to Damage and Repair of the Central Nervous System. *Cell Tissue Res*, 349:169-80. DOI 10.1007/s00441-012-1336-5.
2. Aand JM, Berry M, 1985, Observation on Astrocyte Response to a Cerebral Stab Wound in Adult Rats. *Brain Res*, 327:61-9.
3. Maxwell W, Follows R, Ashhurst D, *et al*., 1990, The Response of the Cerebral Hemisphere of the Rat to Injury. I. The Mature Rat. *Philos Trans R Soc Lond B Biol Sci*, 328:479-500. DOI 10.1098/rstb.1990.0121.
4. Mand CS, Fawcett J, 2001, The Astrocyte/Meningeal Cell Interface a Barrier to Successful Nerve Regeneration? *Cell Tissue Res*, 305:267-73. DOI 10.1007/s004410100384.
5. Yoshioka N, Kimura-Kuroda J, Saito T, *et al*., 2011, Small Molecule Inhibitor of Type I Transforming Growth Factor-beta Receptor Kinase Ameliorates the Inhibitory Milieu in Injured Brain and Promotes Regeneration of Nigrostriatal Dopaminergic Axons. *J Neurosci Res*, 89(3):381-93. DOI 10.1002/jnr.22552.
6. Yoshioka N, Hisanaga S, Kawano H, 2010, Suppression of Fibrotic Scar Formation Promotes Axonal Regeneration Without Disturbing Blood-Brain Barrier Repair and Withdrawal of Leukocytes After Traumatic Brain Injury. *J Comp Neurol*, 518:3867-81. DOI 10.1002/cne.22431.
7. Mand P, Nilsson M, 2005, Astrocyte Activation and Reactive Gliosis. *Glia*, 50:427-34.
8. Anderson MF, Blomstrand F, Blomstrand C, *et al*., 2003, Astrocytes and Stroke: Networking for Survival? *Neurochem Res*, 28(2):293-305. DOI 10.1023/a:1022385402197.
9. Tatsumi K, Haga S, Matsuyoshi H, *et al*., 2005, Characterization of Cells with Proliferative Activity after a Brain Injury. *Neurochem Int*, 46(5):381-9. DOI 10.1016/j.neuint.2004.12.007.
10. Norenberg MD, 1994, Astrocyte Responses to CNS Injury. *J Neuropathol Exp Neurol*, 53(3):213-20.
11. Gao K, Wang CR, Jiang F, *et al*., 2013, Traumatic Scratch Injury in Astrocytes Triggers Calcium Influx to Activate the JNK/c-Jun/AP-1 Pathway and Switch on GFAP Expression. *Glia*, 61(12):2063-77. DOI 10.1002/glia.22577.
12. Sofroniew MV, 2015, Astrogliosis. *Cold Spring Harb Perspect Biol*, 7(2):a20420.
13. Kozai TDY, Jaquins-Gerstl AS, Vazquez AL, *et al*., 2015, Brain Tissue Responses to Neural Implants Impact Signal Sensitivity and Intervention Strategies. *ACS Chem Neurosci*, 6(1):48-67. DOI 10.1021/cn500256e.
14. Woeppel K, Qand Y, Cui XT, 2017, Recent Advances in Neural Electrode-Tissue Interfaces. *Curr Opin Biomed Eng*, 4:21-31.
15. Chen N, Luo B, Yang IH, *et al*., 2018, Biofunctionalized Platforms Towards Long-term Neural Interface. *Curr Opin Biomed Eng*, 6:81-91.
16. Jand S, Miller JH, 2014, Regeneration Beyond the Glial Scar. *Exp Neurol*, 253(1):197-207.
17. Rand FA, Silver J, 2016, Targeting Astrocytes in CNS Injury and Disease: A Translational Research Approach. *Prog Neurobiol*, 144:173-87.
18. Zhan JS, Gao K, Chai RC, *et al*., 2017, Astrocytes in Migration. *Neurochem Res*, 42(1):272-82.
19. Yu AC, Lee YL, Eng LF, 1993, Astrogliosis in Culture: I. The Model and the Effect of Antisense Oligonucleotides on Glial Fibrillary Acidic Protein Synthesis. *J Neurosci Res*, 34(3):295-303. DOI 10.1002/jnr.490340306.
20. Kimura-Kuroda J, Teng X, Komuta Y, *et al*., 2010, An *in vitro* Model of the Inhibition of Axon Growth in the Lesion Scar Formed after Central Nervous System Injury. *Mol Cell Neurosci*, 43(2):177-87. DOI 10.1016/j.mcn.2009.10.008.
21. Spencer KC, Sy JC, Falcón-Banchs R, *et al*., 2017, A Three Dimensional *in vitro* Glial Scar Model to Investigate the Local Strain Effects from Micromotion Around Neural Implants. *Lab A Chip*, 17(5):795-804. DOI 10.1039/c6lc01411a.
22. Rocha DN, Ferraz-Nogueira JP, Barrias CC, *et al*., 2015, Extracellular Environment Contribution to Astrogliosis Lessons Learned from a Tissue Engineered 3D Model of

the Glial Scar. *Front Cell Neurosci*, 9(1):377. DOI 10.3389/fncel.2015.00377.

23. García-Fernández L, Halstenberg S, Unger RE, *et al*., 2010, Anti-Angiogenic Activity of Heparin-like Polysulfonated Polymeric Drugs in 3D Human Cell Culture. *Biomaterials*, 31(31):7863-72. DOI 10.1016/j.biomaterials.2010.07.022.
24. Jand S, Pompe T, 2018, Biomimetic Tumor Microenvironments Based on Collagen Matrices. *Biomater Sci*, 6:2009-24. DOI 10.1039/c8bm00303c.
25. Bell E, Ivarsson B, Merrill C, 1979, Production of a Tissue-like Structure by Contraction of Collagen Lattices by Human Fibroblasts of Different Proliferative Potential *in vitro*. *Proc Natl Acad Sci U S A*, 76(3):1274-8. DOI 10.1073/pnas.76.3.1274.
26. Lázaro J, Dechmann DKN, Lapoint S, *et al*., 2017, Profound Reversible Seasonal Changes of Individual Skull Size in a Mammal. *Curr Biol*, 27(20):3576. DOI 10.1016/j.cub.2017.10.064.
27. Lapoint S, Keicher L, Wikelski M, *et al*., 2017, Growth Overshoot and Seasonal Size Changes in the Skulls of Two Weasel Species. *R Soc Open Sci*, 4(1):160947. DOI 10.1098/rsos.160947.
28. Lázaro J, Hertel M, Sherwood CC, *et al*., 2018, Profound Seasonal Changes in Brain Size and Architecture in the Common Shrew. *Brain Struct Funct*, 223:2823-40. DOI 10.1007/s00429-018-1666-5.
29. Tallinen T, Chung JY, Rousseau F, *et al*., 2016, On the Growth and form of Cortical Convolutions. *Nat Phys*, 12(6):588-93.
30. Checa S, Rausch MK, Petersen A, *et al*., 2014, The Emergence of Extracellular Matrix Mechanics and Cell Traction Forces as Important Regulators of Cellular Self-organization. *Biomech Model Mechanobiol*, 14(1):1-13. DOI 10.1007/s10237-014-0581-9.
31. Galbraith CG, Mand YK, Sheetz MP, 2002, The Relationship between Force and Focal Complex Development. *J Cell Biol*, 159(4):695-705. DOI 10.1083/jcb.200204153.
32. Riveline D, Zamir E, Balaban NQ, *et al*., 2001, Focal Contacts as Mechanosensors. Externally Applied Local Mechanical Force Induces Growth of Focal Contacts by an Mdia1-Dependent and Rock-Independent Mechanism. *J Cell Biol*, 153(6):1175-86. DOI 10.1083/jcb.153.6.1175.
33. Corin KA, Gibson LJ, 2010, Cell Contraction Forces in Scaffolds with Varying Pore Size and Cell Density. *Biomaterials*, 31(18):4835-45. DOI 10.1016/j.biomaterials.2010.01.149.

METHODS

# A methodology to develop a vascular geometry for *in vitro* cell culture using additive manufacturing

**Laurène Lenoir[1], Frédéric Segonds[1]*, Kim-Anh Nguyen[2,3], Pablo Bartolucci[2,4]**

[1]Product Design and Innovation Laboratory (LCPI), Arts et Métiers ParisTech, Paris, 151 Boulevard de l'Hôpital, 75013, France
[2]EFS UITC, Center Felix Reyes, Research team 2, Créteil, 5 rue Gustave Eiffel, 94017, France
[3]Imagine Institute, Paris, 24 Boulevard du Montparnasse, 75015, France
[4]Sickle Cell Referent, Créteil, Center Mondor Hospital, 94017, France

**Abstract:** Today, additive manufacturing (AM) is implemented in medical industry and profoundly revolutionizes this area. This approach consists of producing parts by additions of layers of successive materials and offers advantages in terms of rapidity, complexity of parts, competitive costs that can be exploited and can lead to a significant advancement in biological research. Everything becomes technically feasible and gives way to a "techno-centered" approach. Many parameters must be controlled in this field, so it is necessary to be guided for the development of such a product. This article aims to present a state of the art of existing design methodologies focused on AM to create medical devices. Finally, a development method is proposed that consists of producing vascular geometry using AM, based on patient data, designed for cell culture *in vitro* studies.

**Keywords:** Innovation; Design; Additive manufacturing; Biology; Medical device

*Correspondence to: Frédéric Segonds, Product Design and Innovation Laboratory (LCPI), Arts et Métiers ParisTech, Paris, 151 Boulevard de l'Hôpital, 75013, France; frederic.segonds@ensam.eu

**Received:** June 27, 2019; **Accepted:** July 12, 2019; **Published Online:** July 29, 2019

**Citation:** Lenoir L, Segonds F, Nguyen KA, *et al*., 2019, A methodology to develop a vascular geometry for *in vitro* cell culture using additive manufacturing. *Int J Bioprint*, 5(2): 238. http://dx.doi.org/10.18063/ijb.v5i2.238

## 1. Introduction

In recent years, additive manufacturing (AM) offers significant benefits for a wide range of applications, especially in the medical sector. Among these applications, bioprinting has emerged, covering printing of biological cells as well as printing of materials (e.g. polymer, ceramic or even metal) that are used for cellular culture. Thus, AM can be used to create vascular geometries, designed for *in vitro* studies. This approach allows to better understand the physiopathology of many diseases such as sickle cell disease (SCD), the most common severe monogenic disorders in the world with 275,000 cases detected each year in newborns[1,2].

It is due to a mutation in the hemoglobin (Hb) beta-globin gene leading to the production of abnormal HbS. The change in molecular structure allows HbS in the deoxygenated state to form polymers that promote Hb polymerization, red blood cell (RBC) membrane damage, decreased RBC deformability, intravascular, and extravascular hemolysis. These RBC abnormalities lead to vessel inflammation, vaso-occlusion, and ultimately organ injury[3].

About 114,000 SCD patients die every year from complications[4]. Among them, cerebral vasculopathy is responsible for stroke all lifelong. However, the physiopathology of cerebral vasculopathy in SCD remains misunderstood. Today, blood exchange transfusions are prescribed for SCD patients with high risk, but this conventional treatment has suspensive effects. Bone marrow transplants offer the only potential cure for SCD but are limited by the number of compatible donors (potential human leukocyte antigen-matched hematopoietic stem cells)[5]. In the future, gene therapy

A methodology to develop a vascular geometry for in vitro cell culture using additive manufacturing © 2019 Frederic S, *et al*. This is an Open Access article distributed under the terms of the Creative Commons Attribution-NonCommercial 4.0 International License (http://creativecommons.org/licenses/by-nc/4.0/), permitting all non-commercial use, distribution, and reproduction in any medium, provided the original work is properly cited.

will offer a new approach to cure SCD. The long-term goal of this research is to better understand the pathophysiology of cerebral arterial disease in SCD and possibly to discover or predict the chances of success, of new therapeutic approaches. Unfortunately, animal models do not allow the analysis of the pathophysiology of cerebral vasculopathy because of the huge difference between animal and human according to the vessel geometry and the hemorheological parameters.

Moreover, *in vitro* 3D models can allow the analysis of extreme conditions that can occur in pathophysiological conditions but are difficult to reproduce except *in vitro* conditions. A first step is to develop cell culture on a AM vascular geometry for *in vitro* studies. Actually, there are very few methodologies intended to help the designer to manufacture a vascular geometry in AM and to perform *in vitro* cell culture on it. As the product is innovative and highly multidisciplinary, it is mandatory to answer the following research question: Which methodology should be used to develop an AM vascular geometry designed for cell culture in these *in vitro* models? This paper presents the design approach used to develop this experimental product. More generally, this method could be applied to all human-based products designed for biological purposes using AM. Finally, a use-case is proposed to validate the method.

## 2. Research Objectives and Specifications

In the first part of the project, the aim is to decipher the biological pathways involved in the vessel damage due to hemorheological pathological conditions found in SCD children. Previous work provided shear stress abnormalities in the *in silico* study that should be reproduced and analyzed in a 3D model. Thanks to AM, the prototype of a vascular geometry can be rapidly realized. Then, the effect of sheer stress in a child with SCD will be understood. The constraints established by the various stakeholders involved in this project are as follows: The material must allow to study *in vitro* the interactions between the blood and the endothelium but also the impact of pathological speeds of the blood flow on the endothelial cells.

## 3. State-of-The-Art

### 3.1. Methodologies to Develop Innovative Medical Devices

Design of innovative complex products in the medical field often involves both engineers and medical experts. As innovative medical devices require collaboration between multidisciplinary teams, it is important to set up a framework to transfer knowledge an efficient between those two domains[6]. Arntzen-Bechina and Leguy proposed several tools or activities to exchange knowledge, such as literature reviews, informal meetings and discussions with managers, engineers, researchers, and physicians, punctual observations of work practices, and knowledge transfer processes[7]. Wong *et al*. proposed to follow a process to manage the engineering and production of biomedical devices. The product development strategy includes a product conceptualization, a market survey and the establishment of strategic alliances, the design, prototyping, and product development, the testing and commissioning, and technology protection, through patents[8].

Bradbury *et al*. provided an innovative method for rapid design, manufacture, and selection of biomedical devices such as implants or oral dosage pills using electronic data and modeling transmissions through computer networks such as the internet, intranets or extranets[9].

A multi-dimensional digital model may be created based on radiological data and patient information. A collaboration between clinical professionals and engineers allows modification of the digital model. Once the digital model is approved, it may be converted into machine instructions to build the biomedical device. This method for rapid construction of biomedical devices may be applied to AM. Thus, it is necessary first of all to analyze the medical need. Then, the knowledge between the medical profession and the engineers is shared throughout the project.

### 3.2. Methodologies to Design Innovative Products based on AM

According to Chu *et al*., the main role of AM technologies is to produce "parts and devices that are geometrically complex, have graded material compositions, and can be customized." Besides, it is possible to build almost any shape with a large range of materials, which could be difficult to produce using conventional manufacturing methods such as milling, turning, or casting. AM also offers fabrication of parts with reduced costs and with rapid availability[10].

Bourell *et al*. advocated to develop new design methodologies dedicated to AM: Design for AM (DFAM)[11]. The most widespread definition of DFAM is a methodology which "maximize product performance through the synthesis of shapes, sizes, hierarchical structures, and material compositions, subject to the capabilities of AM technologies" and "to best utilize manufacturing process capabilities to achieve desired performance and other life-cycle objectives"[12,13].

Wong and Hernandez presented the general process of AM[14]. It is also presented by Noorani in Figure 1. It summarizes the stages of product development using rapid prototyping and shows that there can be several iterations before the final product.

Chu *et al*. (2008) proposed a method for DFAM, specialized in cellular materials, presented in Figure 2. Usually, the microstructure of the part is analyzed and examined after processing it, to determine its mechanical properties. Here, as the material is more complex, the approach consists of reversing the process by "specifying desired behavior.

After planning a manufacturing process, the idea is that the process will be simulated on the current design to determine the as-manufactured shapes, sizes, mesostructures, and microstructures. Then manufactured model will be analyzed to determine whether or not it actually meets design objectives."

In a multidisciplinary environment, combining engineers and health professionals for instance, not only the process to produce pieces using AM is important but also the way that information, data, and documents are shared and managed.

As Ponche *et al*. resumed in a study, the "partial approach" in DFAM consists in starting from an initial geometry in a computer-aided design (CAD) model[16].

In general, this geometry is not really designed for an AM process: It will be necessary to modify and improve it for rapid prototyping. The partial approach thus can be used in the case someone has an initial CAD model and wants to manufacture it by AM.

The methodology proposed in this study is presented in Figure 3. It is divided into three main steps. The first step is a global analysis which allows the delimitation of the design problem in terms of geometrical dimensions in relation to the dimensional characteristics of the AM process. The second step allows the fulfillment of the dimensional and geometrical specifications in relation to the AM process capability and the finishing process characteristics. Finally, the third step allows the fulfillment of the physical and assembly requirements in relation to the capability of the AM process.

In general, a rapid prototyping methodology is composed of four phases: Initialization, Design, Development/Manufacturing, and Validation. In addition, the specifications are defined at the flow rate, as are the

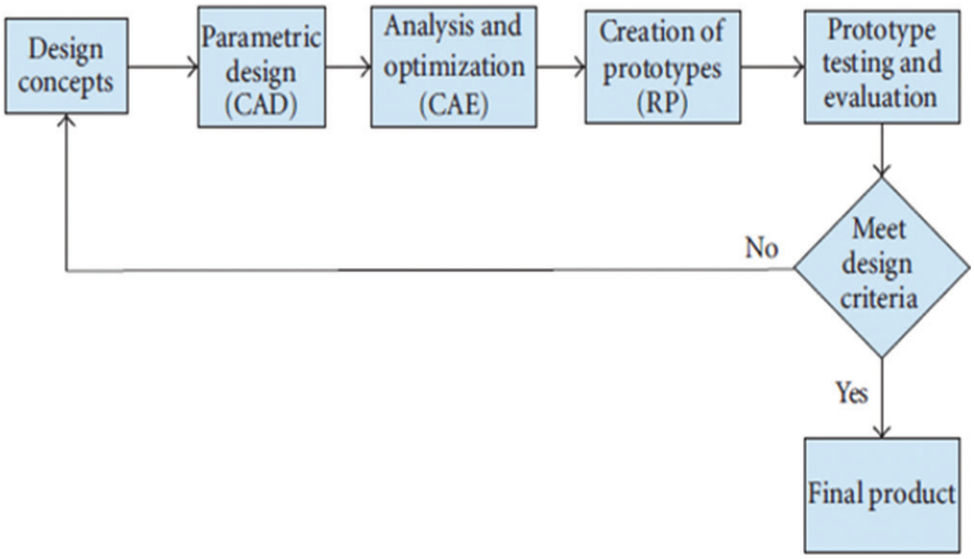


**Figure 1.** Product development cycle adapted from Noorani[15].

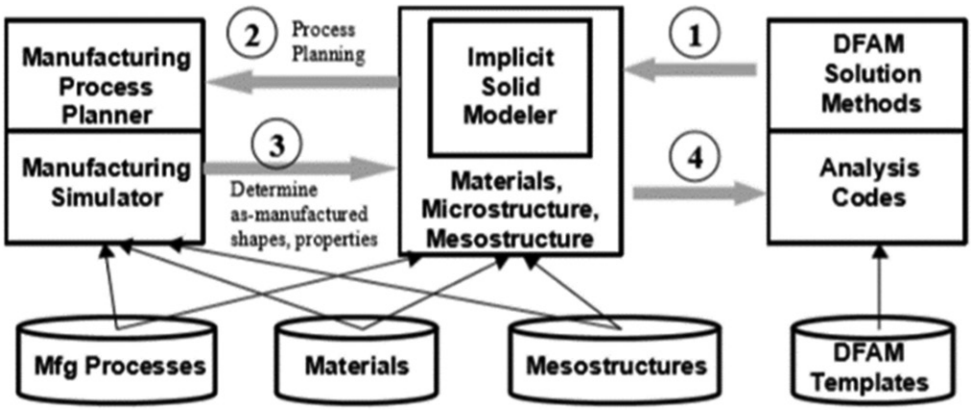


**Figure 2.** Design for additive manufacturing system and overall method from Chu *et al*.[10]

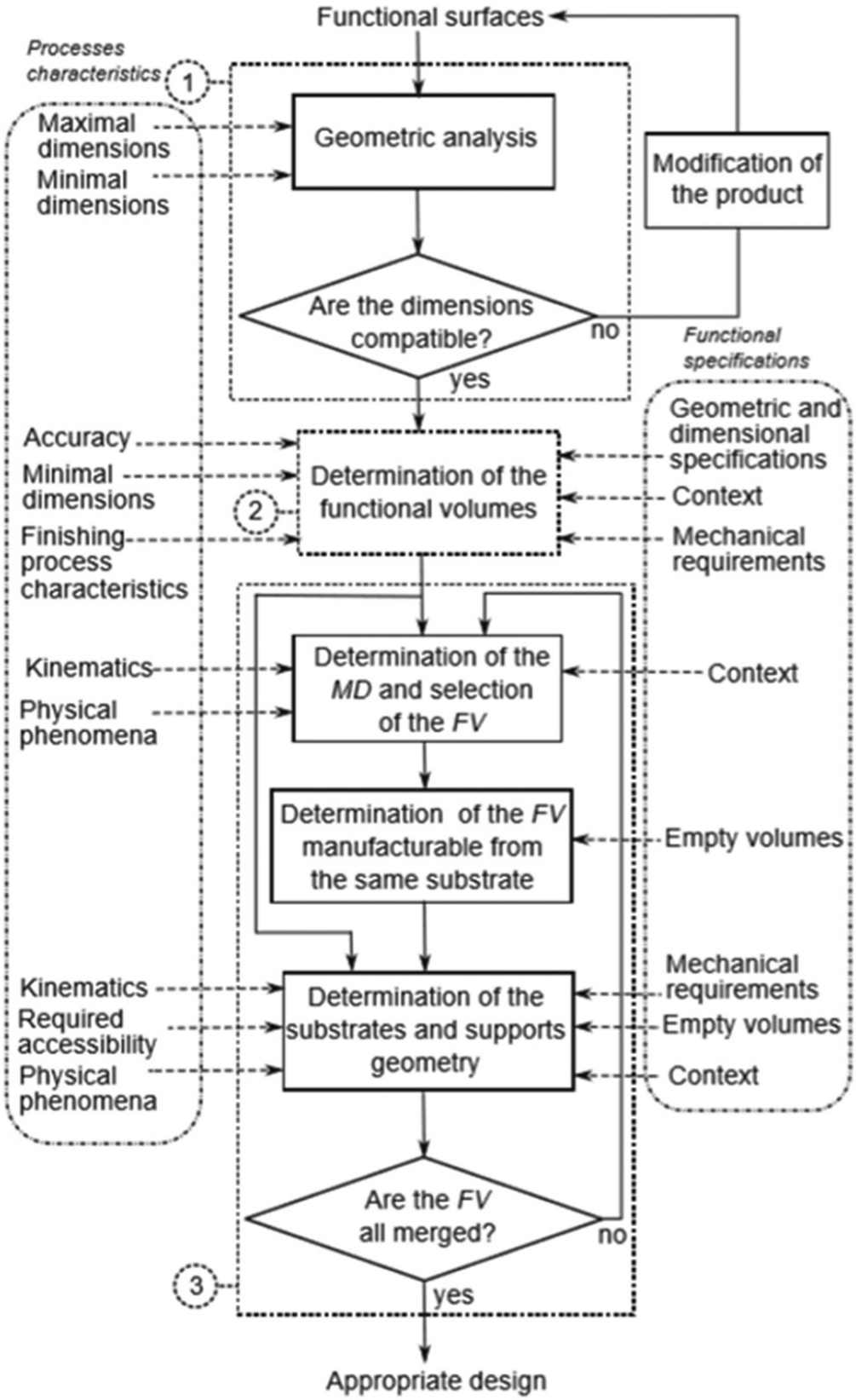


**Figure 3.** A proposed design for additive manufacturing methodology (Ponche *et al*. 2012).

manufacturing plan and the strategic choices. Finally, the different methodologies propose a product improvement phase.

### 3.3. Manufacturing Process of Devices for Biological Application

Only methodologies to design and manufacture a product for biological application based on an initial patient medical imaging exist. Wong *et al*. suggested a framework in five steps (Figure 4): Measurement, verification, design evaluation, design modification, and finally, design optimization[8]. The first phase is based on both *in vivo* and *in vitro* measurement to define the geometry. Verification is needed by modeling the geometry and experimental conditions. Then, the design will be evaluated and analyzed: Surfaces of the previous medical imaging are rebuilt thanks to a CAD model, and flow visualization is generated using different software tools. The model can be modified after a clinical testing phase that requires medical knowledge. Finally, an optimization may start once the product is approved.

Today, polydimethylsiloxane (PDMS) and Flexdym are privileged material for cell-culture devices[17,18]. Concerning microfluidic devices, Shin *et al*., reported the development of a methodology to create an endothelialized network with a vascular geometry in a biocompatible polymer, PDMS[19].

Using photolithography, master molds were fabricated by etching the network pattern into silicon wafers. Closed channels were created from silicon master molds by replica molding of PDMS and subsequent plasma-bonding of a patterned PDMS template to a flat PDMS sheet.

Usually, laboratories' chips made of PDMS are relatively simple shapes, which can be manufactured by stereolithography or equivalents.

However, these techniques are not adapted to produce complex geometries. With the recent advances in AM, use of PDMS for the fabrication of such complex shapes has gained considerable interest.

The results of Ozbolat *et al*. demonstrated that 3D printing of PDMS elastomers is possible and improves the mechanical properties of fabricated samples up to three-fold compared to that of cast ones. It also facilitates the adhesion and the growing[20].

The PDMS is very appreciated for its qualities of translucent and rigidity. However, it has many flaws that

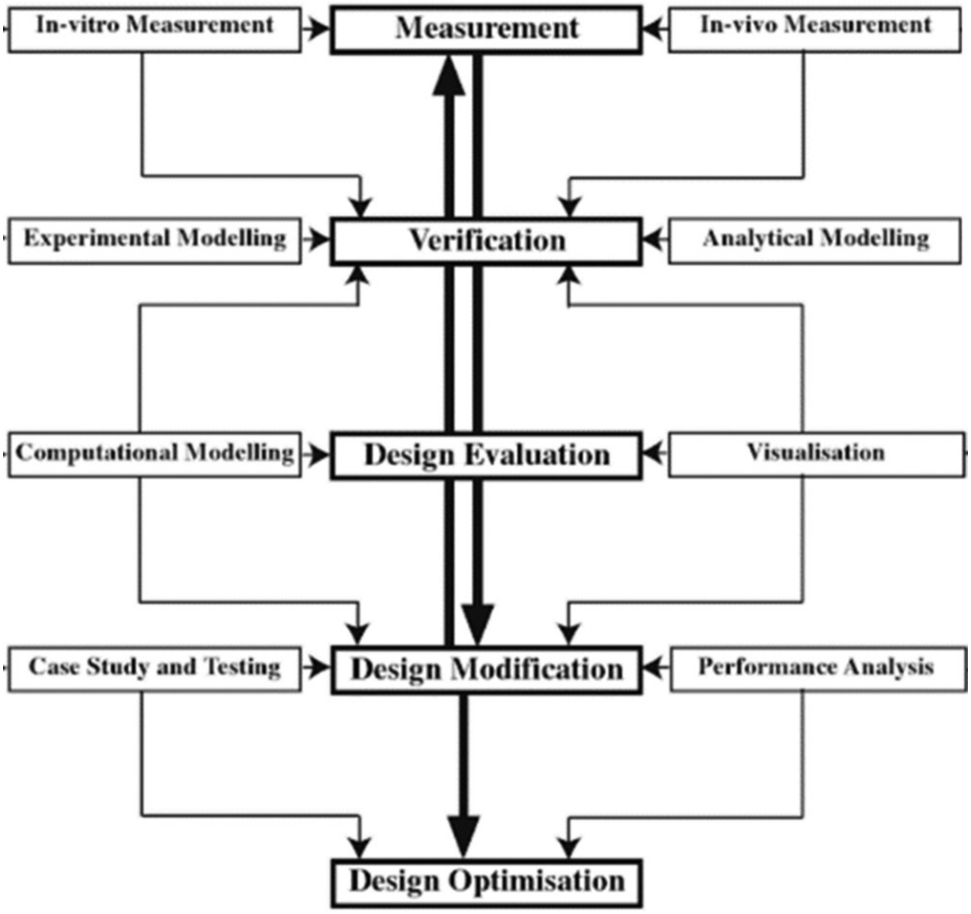


**Figure 4.** The proposed method by Wong *et al*. (2013) to produce a health device based on medical imaging.

prevent it from being marketable on a large scale. However, the disadvantages of PDMS are the absorption of small molecules, the manufacturing method incompatible with mass production and also its reversible hydrophilicity.

Lachaux *et al*. found a new polymer (Flexdym) offering flexibility and translucent comparable to PDMS. Flexdym is a copolymer block solution, composed of Di or Triblock according to the different grade. It is similarities with the PDMS but without the drawbacks. Easy and inexpensive microstructuration method, microfluidic devices are fabricated in less than a minute[21].

Furthermore, microfabrication can be performed using a hot-embossing machine or a very simple press equipment; downstream Flexdym is amenable for rapid manufacturing technology such as injection molding. Flexdym can be bonded easily without surface treatments and pressure loads, thanks to is mechanical properties.

Sealing can be achieved either on a simple hot plate or even at room temperature. It is flexible and thus allows cutting into small pieces. It is translucent and biocompatible which will allow the study of cell culture. Due to its bonding qualities, two-part molding is envisaged.

Recently, cell culture studies have been released on VeroClear, AM material. Lu *et al*. used Veroclear because of its good formation properties and high precision. However, the interactions between cells and materials are affected by topography and surface chemistry of the implant materials, such as roughness and hydrophilic properties[22].

In this study, authors have developed a method of coating waterborne polyurethane (WPU) onto the Veroclear resin to improve the biocompatibility. WPU (Safe polymeric material) is a coating material for creating barriers between corrosive environments and material surfaces. WPU has been used in medical implants because of its low toxicity, good biocompatibility, and coating characteristics.

### 3.4. Synthesis

Only a few papers rely on AM to produce biomedical parts. This paper highlights existing methodologies for designing innovative products based on AM, others that can help develop innovative medical devices. However, it is difficult to find a methodology that combines these two aspects; there are only a few at the intersection of these two technologies.

The interesting points of these different methodologies are:

- Well understand the goals and needs of the user
- Engineers and health professionals pool their knowledge throughout the project
- Strategic choice and plan of manufacturing before prototyping
- Design by performing user tests
- Optimization of the product with iterations
- Final validation
- Make sure the product is correctly used
- Tests prototype and medical return to improve the model.

Thus, in this article, an innovative methodology to achieve a complex vascular geometry using AM is proposed. As mentioned before, there are few methodologies that combine the realization of medical devices and AM processes. Existing methodologies do not propose to simplify the complex geometry to allow faster validation of all subsequent steps such as the choice of material or the cellular study. Here, we can proceed with iteration loops and improve our design each time to finally fulfill the complex form. Thus, the proposed method can be adapted to any case study.

## 4. A Methodology to Develop Vascular Geometry for *In Vitro* Cell Culture using AM: AM-Biopart

The proposed method (Figure 5) is based on important points told in the synthesis that chosen from the existing methods seen previously.

The method proposed by Lenoir *et al*. (2019) is divided into four steps. The first "Initialization" consists of understanding and summarizing the objectives, needs, and constraints desired by the medical profession. Knowledge is capitalized and well transferred between engineers and health professionals.

Then, Step II, "concept and feasibility" allow to search and define the different manufacturing methods and then to know their costs.

For Step III, "design and development" is more complex. Geometry simplification strategy is included (Step III, 1) to allow engineers to focus first on the material to be used that meets the different constraints.

Once these parameters have been approved (Step III, 8), the geometry can be made more complex (Step III, 9). Then, the whole process can start again (Steps III, 2) to (Steps III, 7), through an improvement of the design, until the final validation of the realistic 3D model.

Finally, during the last step, the design is optimized by performing user tests. At the end, once everything is validated and optimized, only training for clinical use remains.

## 5. Use Case AM-Biopart Adapted to the Manufacturing of a Carotid

In this section, the method is tested on the manufacturing of a carotid (Figure 6) *in vitro* to understand the physiopathology.

This carotid was modeled by ARM (Figure 7), on a sickle cell child. ARM is an exam that specifically

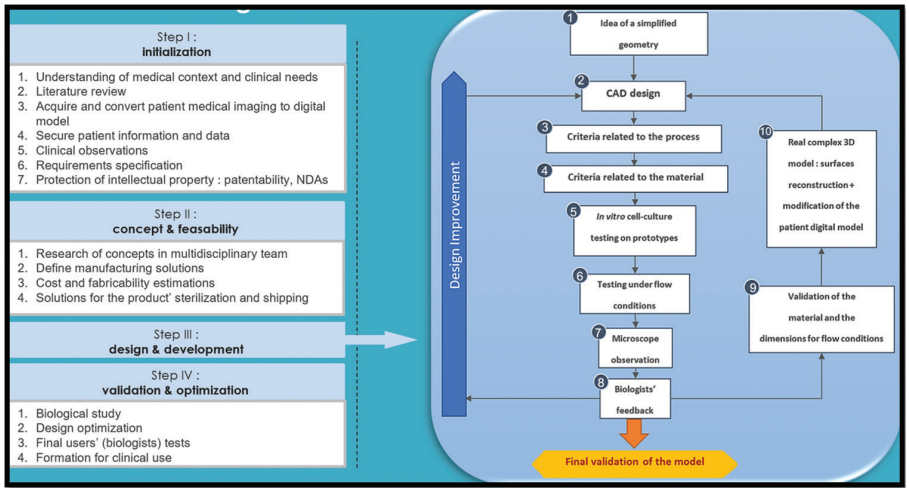


**Figure 5.** Proposed method additive manufacturing-Biopart by Lenoir *et al*.[23]

addresses the body's vessels, arteries, and veins, often better visualized after injection, of a product[25].

The focus is made on Step III "design and development":

1. Idea of simplified geometry
   The carotid geometry have a very complex form that is why it bring back to a simplified form. The complex geometry is changed in a tube of 50 mm length and 4 mm internal diameter. With each side connectors for the pump (Figure 7).
   The simplification of the model has been established by engineers and biological researchers. It consists of bringing the complex model back to a simple shape, here a tube. Thus, this simplified geometry will make it possible to validate as quickly as possible all the elements on the cellular culture part as well as the manufacturing method of the tube. Finally, once everything is approved, a new iteration is performed with more complex geometry.
2. CAD design
   Achievements of several CAD with CATIA software (Figure 8) show a half-mold for casting.
3. Criteria related to process and the material
   After the CAD, it is necessary to choose the process and the material to use. Here, the molds are made in AM with a material called acrylonitrile butadiene styrene, which is a thermoplastic polymer having good impact strength, relatively rigid, lightweight, and moldable. Then, the PDMS was cast; the result is shown in Figure 9.
4. *In vitro* cell-culture testing on prototypes and testing under flow conditions
   PDMS has been tested in cell culture and inflow conditions, using a pump that can send large flows.
   During flow cell culture development, the prototype and manufacturing of PDMS tube were ameliorated to optimize la perfusion at high flow and observation on microscopy.

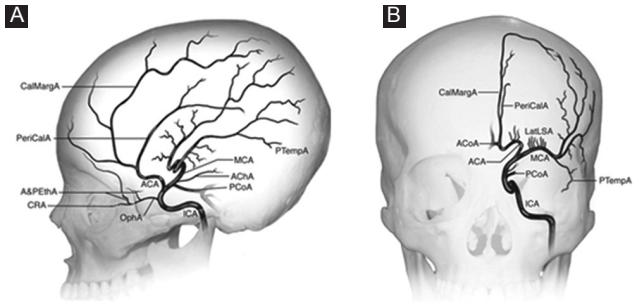


**Figure 6.** Branches of the internal carotid artery (**A**) lateral view (**B**) anteroposterior view (PEACE 2017)[24].

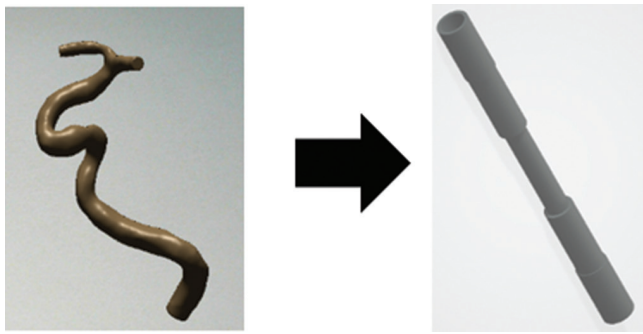

**Figure 7.** Simplification of the carotid geometry.

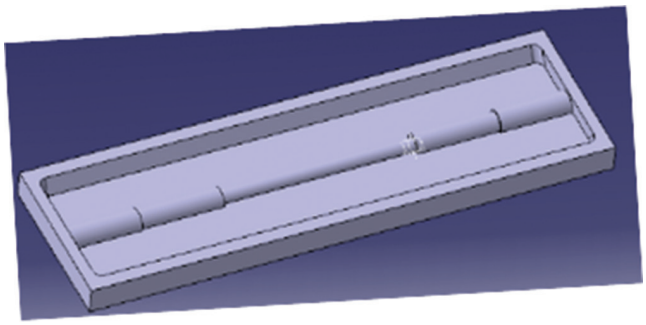

**Figure 8.** Half-mold for casting.

5. Observation and biologist Feedback
   Human umbilical vein endothelial cells (HUVECs) were seeded in a tube fabricated by two-half mold technique. After 2 h of static culture, a homogenous monolayer with confluence was observed (Figure 10). A weak flow rate perfusion (Figure 11, shear stress 1 dyn/cm²) was then applicated on cells for 3H following by immunostaining to visualize specific markers of endothelial cells (PECAM-1, Platelet endothelial cell adhesion molecule 1) and their nuclear (DAPI). The results demonstrated that HUVECs monolayer was still confluence (Figure 12).

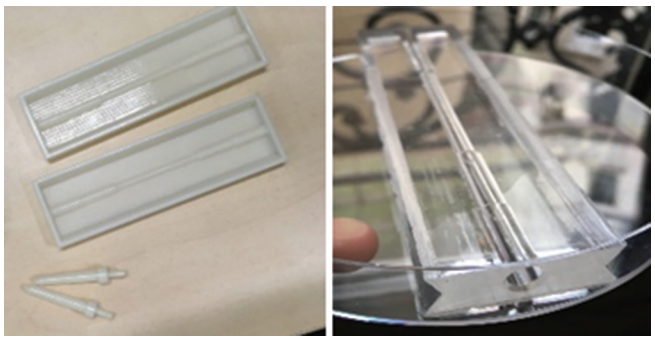

**Figure 9.** Polydimethylsiloxane cast in two parts in mold printed in 3D.

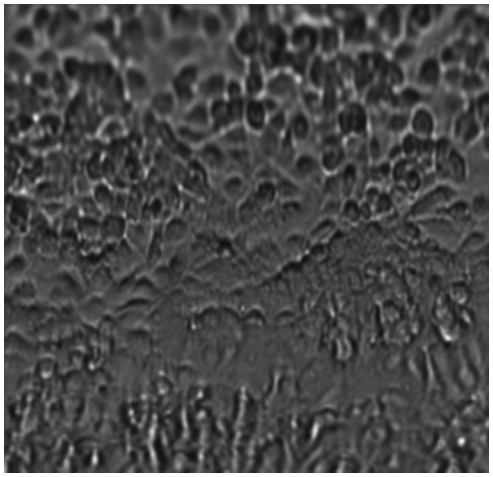

**Figure 10.** Human umbilical vein endothelial cells after 2 h of static culture.

As flow experiments in artificial carotid will be performed at high shear stress, HUVECs monolayer was challenged with flow culture at high flow rate perfusion (shear stress 6.5 dyn/cm²). However, the assay was stopped after 12 min because of medium leaking at bonding site on the two-half tube. Moreover, on phase-contrast microscopy, cells detachments were found in many areas (Figure 13).

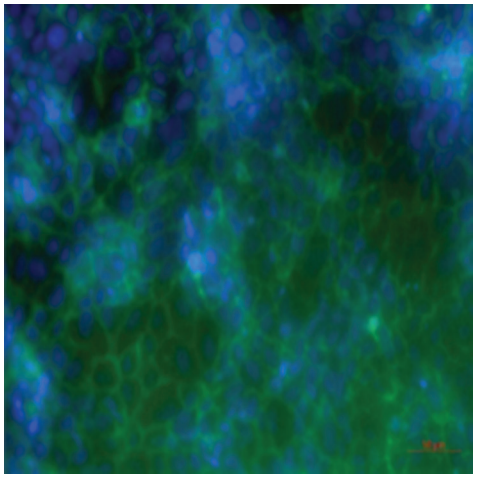

**Figure 12.** Human umbilical vein endothelial cells (HUVECs) culture with weak flow rate perfusion. Immunostaining of platelet endothelial cell adhesion molecule-(green, a membrane specific marker of HUVECs) and nuclei (DAPI, blue).

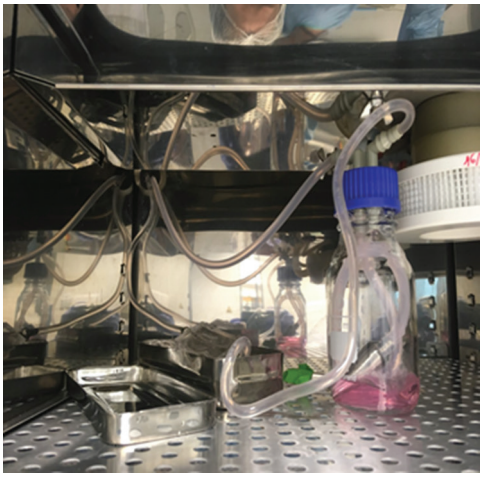

**Figure 11.** Experimental of blood flow in a polydimethylsiloxane molded carotid (100 mL/min).

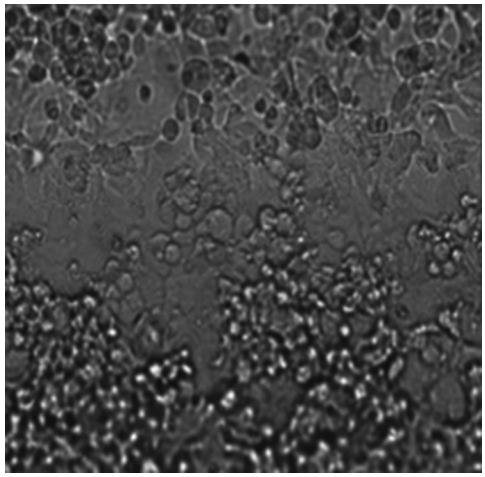

**Figure 13.** Human umbilical vein endothelial cells culture with high flow rate perfusion.

Therefore, to reach the objective of flow experiment in carotid, molding technique, and cells resistance under high shear stress must be improved.

## 6. Conclusion and Future Work

In this paper, a global framework of design approach focused on AM to develop vascular geometry is proposed. It can be applied to all human-based products designed for biological purposes using AM. The main research question of this article is: Which methodology should be used to develop an AM vascular geometry designed for cell culture in these *in vitro* models?

The proposed AM-Biopart methodology takes place in four stages with initialization, concept and feasibility, design and development, and finally validation and optimization. This allows us to have a common thread for people wishing to achieve vascular geometry in AM, with the collaboration of different trades. The proposed method has been successfully applied to the design of a carotid artery. However, for later if we want to guarantee a fully optimized part, some process parameters, such as the choice of laser power, scanning speed, and hatch spacing, must be taken into account in the process. Future work will involve testing the proposed methodology on a more complex case study.

## Conflicts of Interest

No potential conflicts of interest were reported by the authors.

## Authors' Contributions

*Laurène Lenoir* is an engineering student at Arts et Metiers Paristech School of Engineering in Paris, France and in a double degree of master research Innovation and Design at Product Design and Innovation Laboratory (LCPI).

*Frédéric Segonds* is Associate Professor of Mechanical Engineering at Arts et Metiers ParisTech School of Engineering in Paris, France, and member of the Product Design and Innovation Laboratory (LCPI). His research interests focus on product lifecycle management, early stages of design collaboration optimization and Creativity and Design With/For Additive Manufacturing (DWAM/DFAM).

*Pablo Bartolucci*, MD, PhD is full Professor in medicine at French Sickle Cell Referent Center – Henri Mondor hospital, and leader of research group (Mondor Institute Biomedical research, INSERM U955 IMRB-team 2)

*Kim-Anh Nguyen* MD, PhD is a researcher at Imagine Institute and French Blood Establishment, Mondor Institute Biomedical research, INSERM U955-team 2.

## References


1. Lorec A, 2017, Un Vecteur Made in CEA Contre la Drépanocytose. *Les Défis Du Cea*, 24(213):8-9.
2. Rees DC, Williams TN, Gladwin MT, 2010, Sickle-cell Disease. *Lancet*, 376(9757):2018-31. DOI 10.1016/S0140-6736(10)61029-X.
3. Roseff SD, 2009, Sickle Cell Disease: A Review. *Immunohematol J Blood Group Serol Educ*, 25(2):67-74.
4. GBD, 2015, Mortality and Causes of Death Collaborators 2016, Global, Regional, and National Life Expectancy, All-cause Mortality, and Cause-specific Mortality for 249 Causes of Death, 1980-2015: A Systematic Analysis for the Global Burden of Disease Study 2015. *Lancet*, 388(10053):1459-544. DOI 10.1016/S0140-6736(16)31012-1.
5. National Heart, Lung and Blood Institute, 2016, How is Sickle Cell Disease Treated? Amended; 2017. Available from: https://www.nhlbi.nih.gov/health-topics/sickle-cell-disease. [Last accessed on 2019 May 24].
6. Hagedorn TJ, Grosse IR, Krishnamurty S, 2015, A Concept Ideation Framework for Medical Device Design. *J Biomed Inform*, 55:218-30. DOI 10.1016/j.jbi.2015.04.010.
7. Arntzen-Bechina A, Leguy C, 2007, A Model of Knowledge Sharing in Biomedical Engineering: Challenges and Requirements. *J Bus Chem*, 4(1):27-43.
8. Wong KK, Tu JY, Sun Z, *et al*., 2013, *Methods in Research and Development of Biomedical Devices*. Singapore: World Scientific Publishing Co.
9. Bradbury TJ, Gaylo CM, Fairweather JA, *et al*., 2004, *System and Method for Rapidly Customizing Design, Manufacture and/or Selection of Biomedical Devices*. U.S. Patent Number 6772026.
10. Chu C, Graf G, Rosen DW, 2008, Design for Additive Manufacturing of Cellular Structures. *Comput Aided Des Appl*, 5(5):686-96.
11. Bourell DL, Beaman JB, Leu MC, *et al*., 2009, A Brief History of Additive Manufacturing and the 2009 Roadmap for Additive Manufacturing: Looking Back and Looking Ahead. In: *Proceedings of the US-Turkey Workshop on Rapid Technologies*, pp. 24-25.
12. Gibson I, Rosen D, Stucker B, 2015, *Additive Manufacturing Technologies: 3D Printing, Rapid Prototyping, and Direct Digital Manufacturing.* New York: Springer. DOI 10.1007/978-1-4939-2113-3.
13. Rosen DW, 2007, Computer-Aided Design for Additive Manufacturing of Cellular Structures. *Comput Aided Des Appl*, 4(5):585-94.

14. Wong KV, Hernandez A, 2012, A Review of Additive Manufacturing. *ISRN Mech Eng*, 2012:1-10.
15. Noorani RI, 2006, *Rapid Prototyping: Principles and Applications*. Los Angeles: John Wiley and Sons.
16. Ponche R, Hascoet JY, Kerbrat O, *et al*., 2012, A New Global Approach to Design for Additive Manufacturing. *Virtual Phys Prototyp*, 7(2):93-105.
17. Mcdonald JC, Duffy DC, Anderson JR, *et al*., 2000, Fabrication of Microfluidic Systems in Poly (Dimethylsiloxane). *Electrophoresis*, 21(1):27-40. DOI 10.1002/(sici)1522-2683(20000101)21:1<27:aid-elps27>3.0.co;2-c.
18. Kaihara S, Borenstein J, Koka R, *et al*., 2000, Silicon Micromachining to Tissue Engineer Branched Vascular Channels for Liver Fabrication. *Tissue Eng*, 6:105-17. DOI 10.1089/107632700320739.
19. Shin M, Matsuda K, Ishii O, *et al*., 2004, Endothelialized Networks with a Vascular Geometry in Microfabricated Poly(Dimethyl Siloxane). *Biomed Microdevices*, 6:269-78. DOI 10.1023/b: bmmd.0000048559.29932.27.
20. Ozbolat V, Dey M, Ayan B, *et al*., 2018, 3D Printing of PDMS Improves Its Mechanical and Cell Adhesion Properties. *ACS Biomater Sci Eng*, 4(2):682-93. DOI 10.1021/acsbiomaterials.7b00646.
21. Lachaux J, Alcaine C, Gómez-Escoda B, *et al*., 2017, Thermoplastic Elastomer with Advanced Hydrophilization and Bonding Performances for Rapid (30 s) and Easy Molding of Microfluidic Devices. *Lap Chip*, 17:2581-94. DOI 10.1039/c7lc00488e.
22. Lu Z, Jiang X, Zuo X, *et al*., 2016, Improvement of Cytocompatibility of 3D-printing Resins for Endothelial Cell Adhesion. *RSC Adv*, 6(104):102381-8. DOI 10.1039/c6ra20700f.
23. Lenoir L, Segonds F, Bartolucci P, *et al*., 2019, *A Methodology to Product a Complex Vascular Geometry Using Mainly Additive Manufacturing*. Paris: CONFERE.
24. Peace D, 2017, Chapter 1: Neuro-ophthalmic anatomy. *Fastest Otolaryngol Ophthalmol Insight Eng*, 1: 1-8.
25. Vignon I, 2018, *Carotid Angiography-MRI Model*. Inria: Internal Report.

RESEARCH ARTICLE

# Preparation and printability of ultrashort self-assembling peptide nanoparticles

**Sarah Ghalayini, Hepi Hari Susapto, Sophie Hall, Kowther Kahin, Charlotte A. E. Hauser***

Laboratory for Nanomedicine, Division of Biological and Environmental Science and Engineering, King Abdullah University of Science and Technology, Thuwal, Kingdom of Saudi Arabia

**Abstract:** Nanoparticles (NPs) have left their mark on the field of bioengineering. Fabricated from metallic, magnetic, and metal oxide materials, their applications include drug delivery, bioimaging, and cell labeling. However, as they enter the body, the question remains – where do they go after fulfilling their designated function? As most materials used to produce NPs are not naturally found in the body, they are not biodegradable and may accumulate overtime. There is a lack of comprehensive, long-term studies assessing the biodistribution of non-biodegradable NPs for even the most widely studied NPs. There is a clear need for NPs produced from natural materials capable of degradation *in vivo*. As peptides exist naturally within the human body, their non-toxic and biocompatible nature comes as no surprise. Ultrashort peptides are aliphatic peptides designed with three to seven amino acids capable of self-assembling into helical fibers within macromolecular structures. Using a microfluidics flow-focusing approach, we produced different peptide-based NPs that were then three-dimensional (3D) printed with our novel printer setup. Herein, we describe the preparation method of NPs from ultrashort self-assembling peptides and their morphology in both manual and 3D-printed hydrogels, thus suggesting that peptide NPs are capable of withstanding the stresses involved in the printing process.

**Keywords:** Nanoparticles; Ultrashort peptides; Self-assembly; Microfluidics; Biomaterials

*Correspondence to: Charlotte A.E. Hauser, Laboratory for Nanomedicine, King Abdullah University of Science and Technology, Division of Biological and Environmental Science and Engineering, 4700 Thuwal, 23955-6900, KSA; charlotte.hauser@kaust.edu.sa

**Received:** July 18, 2019; **Accepted:** July 24, 2019; **Published Online:** July 31, 2019

**Citation:** Ghalayini S, Susapto HH, Hall S, *et al*., 2019, Preparation and printability of ultrashort self-assembling peptide nanoparticles. *Int J Bioprint*, 5(2): 239. http://dx.doi.org/10.18063/ijb.v5i2.239

## 1. Introduction

Given the interest surrounding nanomaterials, it is of little surprise that recent advancements have only led to an increase in the number of applications for nanoparticles (NPs) in biomedicine, optics, and electronics. Their unique size- and material-dependent properties have made them an excellent option in the search for new materials to address global challenges[1]. NPs made from semiconductors yield quantum confinement[2], whereas NPs produced from metals such as gold and silver, and magnetic materials exhibit surface plasmon resonance and superparamagnetism, respectively[3,4]. For biomedical applications, it is crucial to ensure that the material used is biocompatible and non-immunogenic to avoid inducing adverse effects within the host. Gold NPs are perhaps the most widely studied type in the realm of nanomedicine, and, however, they lack the inherent biodegradability of peptide[5-8]. As they are derived from naturally occurring amino acids, peptides are biocompatible, biodegradable, and generally non-toxic, thus an excellent material choice for the production of NPs. Self-assembling peptide has been used to form NPs of different types such as tubes, vesicles, and hydrogels[9,10]. Various preparation methods for peptide NPs exist, including pH variation, spray drying, rapid laminar jet, milling, polymer chain collapse, coacervation, and phase separation[11-18].

The intrinsic properties of a material are often dependent on its composition, and peptides are no different. One class of peptides, ultrashort peptides,

Preparation and printability of ultrashort self-assembling peptide nanoparticles © 2019 Ghalayini S, *et al*. This is an Open Access article distributed under the terms of the Creative Commons Attribution-NonCommercial 4.0 International License (http://creativecommons.org/licenses/by-nc/4.0/), permitting all non-commercial use, distribution, and reproduction in any medium, provided the original work is properly cited.

is comprised peptides with no more than 7 amino acid residues, capable of self-assembly into supramolecular fibrous network structures due to their peptide motifs. Through a microfluidics flow-focusing method[19], we can prepare NPs from ultrashort peptides of different sequences for applications ranging from drug delivery to bioimaging[20,21]. This fabrication method is particularly advantageous due to its ability to continually produce peptide NPs at a scale that allows for use in experiments.

In the past, our laboratory has reported on the use of peptide hydrogels as scaffolds for tissue engineering and regenerative medicine, as well as on the preparation of hydrogels with slow-releasing silver NPs (AgNPs) for antimicrobial applications[22-25]. The addition of peptide NPs to peptide hydrogels allows for the localized delivery of any drugs or growth factors conjugated to the surface of the NPs. This is facilitated by way of a composite of sorts made entirely from a single material. In addition, we have published on our novel three-dimensional (3D) printer setup where we have explored the printability of bioinks produced in the laboratory in conjunction with various cell types[26-30]. Inspired by the potential of peptide NPs and 3D bioprinting, we decided to combine the two technologies to study the printability of our NPs. Two sequences of self-assembling peptides are tested and assessed for shape fidelity. The promising results indicate that different to the manual approach the 3D printing of ultrashort self-assembling peptide NPs may result in hydrogels embedded with a more homogenous distribution of NPs.

## 2. Materials and Methods

The NPs are fabricated through a microfluidic-driven flow-focusing method. The system is comprised a Dolomite 6 Junction microfluidic chip (dimensions: 45 mm × 15 mm, channel depth and width at cross-section: 50 µm × 55 µm), Nikon Eclipse TS 100 inverted microscope, Harvard Apparatus PhD Ultra syringe pump, Chemyx Fusion 200 syringe pump, and plastic syringes (BD, Luer Lok in 10 mL and 1 mL). About 50% (v/v) of ethanol solution was prepared by diluting absolute ethanol (Sigma-Aldrich) and then filtering through a Millex-GP syringe filter with a pore size of 0.22 µm. Tetrameric self-assembling peptides CH-01 and CH-02 were custom synthesized in our laboratory for nanomedicine through solid-phase peptide synthesize and purified to higher than 95% using preparative high-performance liquid chromatography.

### 2.1 Manual Hydrogel Sample Preparation

The CH-01 and CH-02 peptide powders were dissolved in Milli-Q water, then mixed with ×10 phosphate-buffered saline (PBS) at a final volume ratio of 9:1 (peptide solution to PBS). Gelation of both peptides occurred within a few minutes at a minimum concentration of 4 mg/mL and 3 mg/mL for CH-01 and CH-02, respectively, as shown in Figure 1. As described in section 2.3, the 3D printing system prints using a higher concentration of peptide solution as the increased viscosity enables printing at a higher resolution. Due to this, to prepare the manual hydrogel samples for these experiments, a concentration of 10 mg/mL of peptide was used to ensure a final concentration comparable to those of the printed samples. For manual sample conditions made with NPs, approximately 0.9 mg of NPs were added to the peptide solution before the addition of the PBS either by volume from the product of the microfluidic chip or in the form of lyophilized NPs.

### 2.2 NP Fabrication and Characterization

#### *2.2.1 NP Fabrication Process*

NPs were fabricated through a microfluidic flow-focusing method by way of a Dolomite 6 Junction Droplet Chip. This chip has six separate junctions that combine into one output channel for increased product. At the junction, the main channel is intersected perpendicularly by the two side channels (Figure 2A). The peptide solution in water flowing through the main channel is funneled by two side channels containing 50% (v/v) ethanol solution into a jet-like stream. The pressure from the side channels, through which 50% of ethanol in water solution (v/v) is running focuses the mainstream and leads to NP formation. Through the flow-focusing mechanism, the peptide aggregates in the water. The ultrashort peptide of a given sequence was dissolved in Milli-Q water and loaded into a 1 mL syringe to be pushed through the central channel in the junctions of the chip, and an

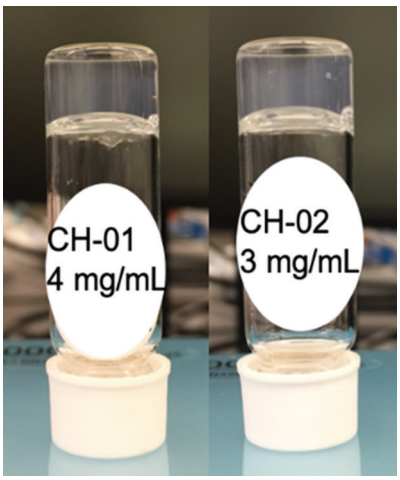


**Figure 1.** The self-assembling peptides CH-01 (4 mg/ml) and CH-02 (3 mg/ml) produce hydrogels in aqueous solution; the gelation was enhanced using phosphate-buffered saline.

aqueous solution of 50% filtered ethanol was loaded into a 10 mL syringe to be pushed through the side channels of the junctions, as shown in Figure 2.

The ratios of the flow rates of the ethanol solution to the peptide solution were found to be crucial for NP production and thus an optimization process, described in the following section, was employed to determine the ideal ratio. Before starting the actual NP production process, the microfluidic chip was stabilized by running the syringe pumps at the desired starting flow rates with the ethanol solution and with water replacing the peptide solution. This stabilization step ensures that the flow is constant and consistent across all the channels and junctions to avoid variations in morphology or decreases in NP yield due to potential blockages. Once the system started running with the peptide solution loaded, the junctions were closely watched using the optical microscope to ensure that no blockages or disruptions to the flow occur. Produced NPs were suspended in ethanol solution which was collected in a 15 mL polystyrene conical falcon tube. The NPs in solution were then frozen with liquid nitrogen and lyophilized in preparation for the printing process.

### *2.2.2 NP Characterization with Dynamic Light Scattering (DLS)*

The NP samples were also characterized using DLS on a Zetasizer (Model X) to determine the average size. This was done during the optimization process to decide which flow rates were best for each peptide as several options were tested to obtain the largest quantity of NPs with the most uniform size distribution.

## 2.3 Printed Hydrogel Sample Preparation

Two vials of CH-01 and CH-02 peptide powders, 18 mg each, were weighed out and then dissolved in 1 mL of Milli-Q water by vortexing and sonicating into a homogenous solution. For the samples containing NPs, around 0.9 mg of lyophilized NPs were weighed out and dissolved in the peptide solution.

A custom-designed 3D bioprinter was set up with commercial microfluidic pumps as described in our previous publications, and a homemade two-inlet nozzle was used for extrusion[29,30]. Structures were printed directly onto 18 mm × 18 mm glass coverslips from Thermo Fischer to facilitate imaging later. Two syringe pumps were loaded for extrusion and the samples were printed into a grid construct made up of two layers using gcode.

The first syringe pump was loaded with the peptide solution and set to a flow rate of 55 µL/min. The second pump was loaded with ×5 PBS and set to a flow rate of 20 µL/min. Three samples were printed for each condition (whether CH-01 or CH-02 and printed with or without NPs) with a height of two to three layers for each sample for easier imaging. The same procedure was conducted for both peptides.

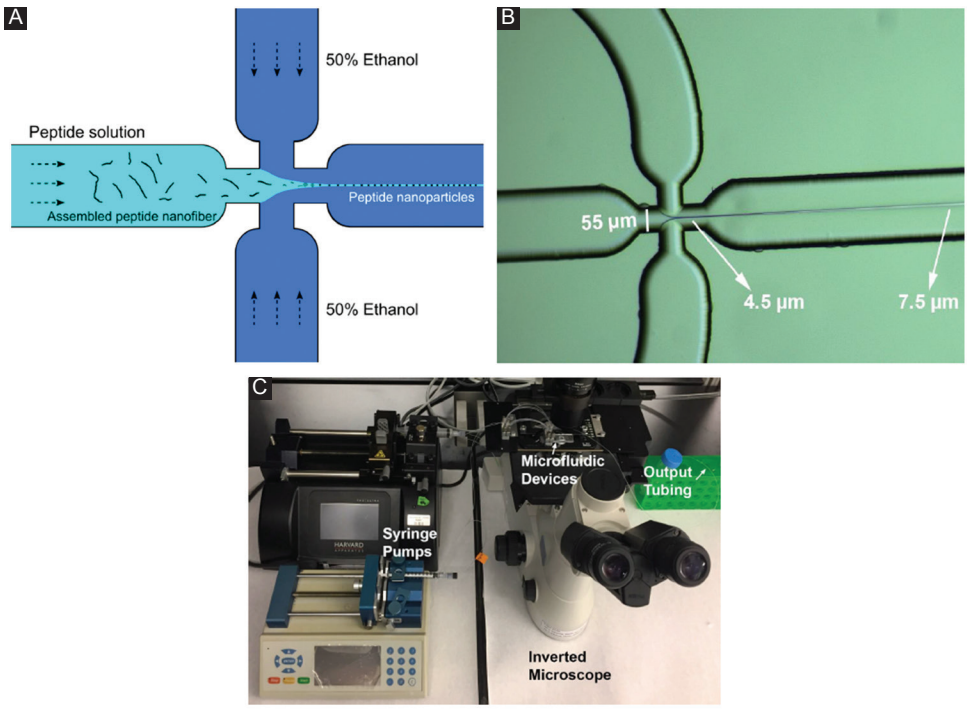


**Figure 2.** Peptide nanoparticles (NPs) preparation. Schematic representation of flow-focusing chip junctions **(A)**, the diameter of the stream is started from 4.5 µm to higher than 7.5 µm **(B)**, and image of the setup of the microfluidic platform for peptide NP fabrication **(C)**.

### 2.4 Scanning Electron Microscopy (SEM) Characterization of the Peptide NPs

During the optimization process, the peptide NPs were characterized using SEM to visualize the morphology and size distribution of the particles. Samples were prepared on SEM silicon wafers polished with acetone and isopropanol before drying with KimWipes and nitrogen gas. The silicon wafers were placed on double-stick conductive carbon tape attached to the SEM aluminum pin stub. The collected NP solutions were vortexed briefly before pipetting 15 µL of solution onto the silicon wafer. Prepared samples were left overnight to dry in a vacuum desiccator, then sputter coated with a 5 nm thickness of iridium before imaging. Images were taken with FEI Magellan XHR and FEI Quanta 600 FEG.

### 2.5 SEM Characterization of the Peptide Hydrogels

The peptide NPs were characterized using SEM to visualize the morphology of the NPs. This was done for samples with NPs that were printed and made manually, as well as for samples with NPs straight from the ethanol solution and those that were lyophilized to compare the integrity of the NPs. As the samples were printed on 18 × 18 mm glass coverslips, the samples were left to solidify for 10-20 min post-formation. At this point, the hydrogel samples were dehydrated by gradually immersing in increasing concentrations of 20%, 40%, 60%, 80%, and 100% (v/v) ethanol solutions for 5 min in each solution. Further, dehydration in 100% ethanol solution was continued by changing the absolute ethanol solution with a fresh one twice for 5 min each followed by the 3$^{rd}$ time for 2 h. The dehydrated samples were subsequently placed into the critical point dryer for evaporation before being mounted onto SEM aluminum pin stubs with double-stick conductive carbon tape and a final sputter coating of 10 nm of iridium. Images were taken with FEI Teneo SEM.

## 3. Results

### 3.1 NPs Fabrication

We first optimized the concentration of ethanol for use in the flow-focusing microfluidic platform. This was done by running the system as described above while modifying the ethanol concentration. We did this by running 1 mg/mL CH-01 through the microfluidic platform with 25%, 50%, and 75% filtered aqueous ethanol solutions at the same flow rates. The products were imaged at ×20,000, and the results can be shown in Figure 3. We then continued to optimize the flow rate ratio of the peptide and ethanol solutions for the production of peptide NPs. These experiments were done in the same way as the ethanol optimization process only changing the ratio of the flow rates used (Figure 3A and B). The parameters were selected based on fabrication throughput and a qualitative analysis of the size distribution.

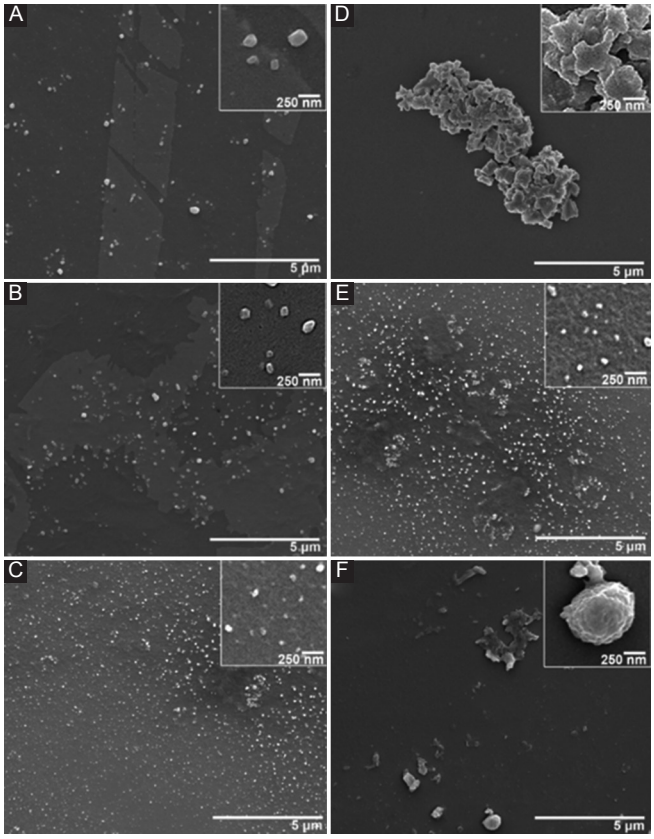


**Figure 3.** Scanning electron microscopy images of CH-01 during optimization of nanoparticles fabrication process. Left: Flow rate optimization, 1 mg/mL CH-01 run with 50% ethanol, at peptide-to-ethanol flow rate ratios of **(A)** 1:1 µL/min, **(B)** 1:5 µL/min, and **(C)** 1:10 µL/min. Right: Ethanol concentration optimization, 1 mg/mL CH-01 run at a peptide-to-ethanol flow rate ratio of 1:10 µL/min, with differing ethanol concentrations of **(D)** 25% ethanol, **(E)** 50% ethanol, and **(f)** 75% ethanol.

### 3.2 NPs Characterization

The prepared NPs were characterized with DLS using a Zetasizer to compare samples prepared at different flow rates. The plots of the distribution of NPs size are shown in Figure 4 and a table of the distribution analysis for the CH-01 and CH-02 NPs is presented in Table 1. The average diameter for the CH-01 NPs was measured to be around 73.05 ± 0.14 nm and that of the CH-02 NPs was found to be 73.02 ± 0.20 nm. The average size for the NPs of both peptides was observed to be very similar, around 73 nm. An explanation for this is provided in the discussion section.

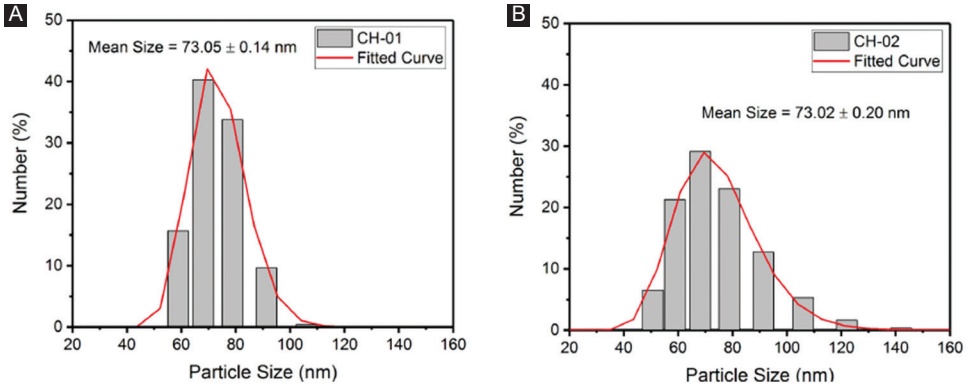


**Figure 4.** Plots of the number percent of **(A)** CH-01 and **(B)** CH-02 nanoparticles at a range of sizes obtained through dynamic light scattering.

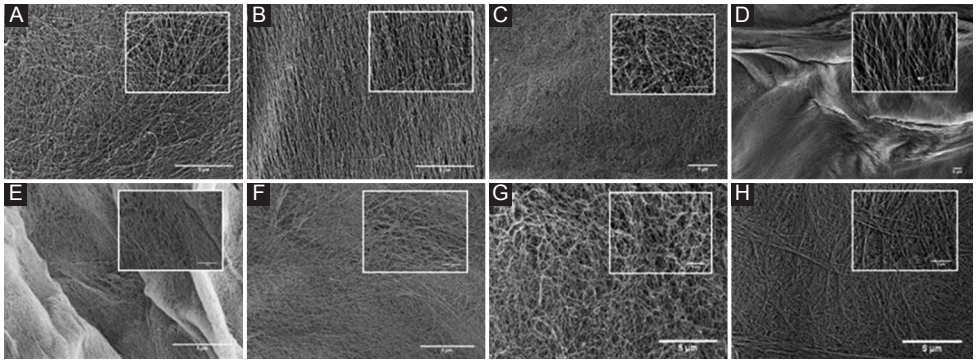


**Figure 5.** Scanning electron microscopy images taken at ×20,000 and ×80,000 (inset) of the following samples: **(A)** CH-01 manually prepared hydrogel, **(B)** CH-02 manually prepared hydrogel, **(C)** CH-01 manually prepared hydrogel with lyophilized nanoparticles (NPs), **(D)** CH-02 manually prepared hydrogel with lyophilized NPs, **(E)** CH-01 three-dimensional (3D) printed hydrogel, **(F)** CH-02 3D-printed hydrogel, **(G)** CH-01 3D-printed hydrogel with lyophilized NPs, and **(H)** CH-02 3D-printed hydrogel with lyophilized NPs.

**Table 1.** Distribution analysis of NPs for CH-01 and CH-02.

| CH-01 | | CH-02 | |
|---|---|---|---|
| **Size (nm)** | **NPs (%)** | **Size (nm)** | **NPs (%)** |
| 45-55 | 0 | 45-55 | 6.48 |
| 55-65 | 15.7 | 55-65 | 21.3 |
| 65-75 | 40.3 | 65-75 | 29.1 |
| 75-85 | 33.8 | 75-85 | 23.0 |
| 85-95 | 9.67 | 85-95 | 12.7 |
| 95-105 | 0 | 95-105 | 0 |
| 105-115 | 0.414 | 105-115 | 5.33 |
| Mean: 73.05 ± 0.14 nm | | Mean: 73.02 ± 0.20 nm | |

NPs: Nanoparticles

### 3.3 SEM Imaging of Hydrogel Samples

The SEM imaging of the samples can be shown in Figure 5 at ×20,000 and ×80,000. The conditions imaged are as follows: CH-01 manually prepared hydrogel, CH-02 manually prepared hydrogel, CH-01 3D-printed hydrogel, CH-02 3D-printed hydrogel, CH-01 manually prepared hydrogel with lyophilized NPs, CH-02 manually prepared hydrogel with lyophilized NPs, CH-01 3D-printed hydrogel with lyophilized NPs, and CH-02 3D-printed hydrogel with lyophilized NPs. The images were taken and analyzed for NPs embedded within the hydrogel structure. This was done to confirm that the NPs did not collapse under the stress of the printing process. NPs are labeled within each sample image for easier viewing.

## 4. Discussion

The peptide self-assembles through a combination of non-covalent interactions that are the driving force behind the observed secondary structure, and thus size and shape, of the assembled peptide molecules[31-36]. These interactions are affected by a number of parameters including the solvent choice, solvent concentration, peptide concentration, ethanol-to-peptide flow rate ratio, and the actual flow rates themselves. To assess the efficacy of each ethanol concentration tested for use in the flow-focusing microfluidic platform, the output solution for each condition was imaged using SEM. This experiment was run several times and the resulting images were compared to determine which concentration produced the largest number of homogenous NPs. From Figure 4, it is

clear that the run with 50% ethanol performed the best. As such, the subsequent experiments were all performed using an optimized ethanol concentration of 50% for the side streams at each junction. Following the optimization of the ethanol concentration, the flow rate ratio of the peptide to ethanol solutions for the production of peptide NPs was also optimized using the same criteria described for the ethanol optimizations. In the experiments with lower peptide to ethanol flow rate ratios – such as 1:1 or 1:5, we observed that significantly more of the peptide formed a fiber network in the background (Figure 3A and B). Our results from several trials of these experiments suggest that as the flow rate of the ethanol increases relative to that of the peptide, more peptide NPs form. As such, the flow rate ratio of peptide to ethanol of 1:10 was used in all of the following experiments.

Characterization of the NPs using DLS revealed that the average size of both the CH-01 and CH-02 NPs was around 73.0 nm. The size distribution plot shown in Figure 4 suggests a homogenous batch of NPs, and the average size of the NPs from the DLS results is consistent with the measured sizes of the NPs seen in the SEM images in Figure 5. The similar average size for NPs produced from both peptides is due to the fact that similar parameters were used during their production with the microfluidic flow-focusing chip. As such, the original peptide solutions were subject to very similar forces and pressure from the ethanol side stream, thus resulting in similar behavior. On close examination of the SEM images of the hydrogels in Figure 5, we can draw comparisons between the size, morphology, and relative distribution of the NPs within each printed versus manually prepared hydrogel sample. As the images are quite similar, the results suggest that the NPs are capable of withstanding the stress associated with the printing process. A comparison of the manually prepared and 3D-printed samples without the addition of NPs to those made with NPs provides confirmation that the NPs observed in SEM are only present in the samples with the NPs added. The samples prepared with the addition of the NPs in ethanol solution serve as a reference to ensure that the general morphology of the NPs is not affected by the lyophilizing process.

## 5. Conclusion

The discovery and characterization of biomaterials suitable for use in medicine are an area of keen interest in the world of research. For tissue engineering, peptide-based hydrogels have emerged as an excellent material to serve as a scaffold that is biocompatible, biodegradable, and promotes cell proliferation and migration as it mimics the natural extracellular matrix. One of the biggest challenges with using these peptide hydrogels in conjunction with specific therapeutic molecules or growth/differentiation factors is the diffusion gradient that emerges as a result of the nanofibrous network that hinders the ability of the species to migrate to the center of the hydrogel[37]. This means that the therapeutic molecules or specific factors needed for cell growth are not evenly distributed within the sample. By producing peptide NPs modified to have these specific molecules attached to their surface[38] and by distributing these NPs throughout the hydrogel, we can overcome the diffusion gradient and allow for a slow, controlled release of these therapeutics/specific factors to the surrounding cells. The previous reports on the controlled release of NPs within a peptide hydrogel have focused on AgNPs[25] used for antimicrobial applications. The use of peptide NPs allows for the introduction of a scaffold and carriers comprised only a single foreign material to the body of the host, thus minimizing the likelihood of any adverse effects. This series of experiments serves as a proof of principle study of the ability to produce and print NPs from ultrashort self-assembling peptides into peptide-based hydrogels. Perhaps, the best way to ensure a uniform distribution of NPs within each sample is to automate the process through the use of 3D printing technology. Although future experiments are needed to further confirm and optimize the homogenous distribution of NPs within the hydrogel samples, this paves the way for an exciting future where we can possibly make use of this system for applications in medicine. One interesting area to work toward is the ability to reprogram stem cells through careful control of the ratio of each of the Yamanaka factors attached to 3D-printed peptide NPs embedded within a hydrogel scaffold[39].

## Acknowledgments

The authors acknowledge Ms. Zainab Khan for her valuable contributions to the design of the 3D printing system used for these studies. We also thank Ms. Kholoud Seferji for her help in obtaining the DLS measurements. The research reported in this publication was supported by funding from King Abdullah University of Science and Technology.

## Authors' Contributions

C.A.E.H. developed the concept of ultrashort self-assembling peptides and supervised the project, S.G. wrote the manuscript, H.H.S. and S.H. optimized the NP preparation method, S.G. fabricated the NPs, H.H.S. and S.G. did the SEM imaging, K.K. printed the samples together with S.G., and H.H.S. helped with the SEM sample preparation.

## Conflicts of Interest

The authors declare that they have no conflicts of interest.

## References


1. Bobo D, Robinson KJ, Islam J, *et al*., 2016, Nanoparticle-Based Medicines: A Review of Materials and Clinical Trials to Date. *Pharm Res*, 33:2373-87. DOI 10.1007/s11095-016-1958-5.
2. Smith AW, Nie S, 2010, Semiconductor Nanocrystals. *Acc Chem Res*, 43:190-200. DOI 10.1021/ar9001069.
3. Jain PK, Huang X, El-Sayed IH, *et al*., 2007, Review of Some Interesting Surface Plasmon Resonance-enhanced Properties of Noble Metal Nanoparticles and Their Applications to Biosystems. *Plasmonics*, 2:107-18. DOI 10.1007/s11468-007-9031-1.
4. Mikhaylova M, Kim DK, Bobrysheva N, *et al*., 2004, Superparamagnetism of Magnetite Nanoparticles: Dependence on Surface Modification. *Langmuir*, 20:2472-7. DOI 10.1021/la035648e.
5. Semmler-Behnke M, Kreyling WG, Lipka J, *et al*., 2008, Biodistribution of 1.4 and 18-nm Gold Particles in Rats. *Small*, 4:2108-11. DOI 10.1002/smll.200800922.
6. De Jong WH, Hagens WI, Krystek P, *et al*., 2008, Particle Size-dependent Organ Distribution of Gold Nanoparticles after Intravenous Administration. *Biomaterials*, 29:1912-9. DOI 10.1016/j.biomaterials.2007.12.037.
7. Goel R, Shah N, Visaria R, *et al*., 2009, Biodistribution of TNF-alpha-coated Gold Nanoparticles in an *in vivo* Model System. *Nanomedicine*, 4:401-10. DOI 10.2217/nnm.09.21.
8. Zhang G, Yang Z, Lu W, *et al*., 2009, Influence of Anchoring Ligands and Particle Size on the Colloidal Stability and *in vivo* Biodistribution of Polyethylene Glycol-coated Gold Nanoparticles in Tumor-xenografted Mice. *Biomaterials*, 30:1928-36. DOI 10.1016/j.biomaterials.2008.12.038.
9. Sun L, Fan Z, Wang Y, *et al*., 2015, Tunable Synthesis of Self-assembled Cyclic Peptide Nanotubes and Nanoparticles. *Soft Matter*, 11:3822. DOI 10.1039/c5sm00533g.
10. Habibi N, Kamaly N, Memic A, *et al*., 2016, Self-assembled Peptide-based Nanostructures: Smart Nanomaterials Toward Targeted Drug Delivery. *Nano Today*, 11:41-60. DOI 10.1016/j.nanotod.2016.02.004.
11. DeFrates K, Markiewicz T, Gallo P, *et al*., 2018, Protein Polymer-Based Nanoparticles: Fabrication and Medical Applications. *Int J Mol Sci*, 19:1717-36. DOI 10.3390/ijms19061717.
12. Lammel AS, Xiao H, Park SH, *et al*., 2010, Controlling Silk Fibroin Particle Features for Drug Delivery. *Biomaterials*, 31:4583-91. DOI 10.1016/j.biomaterials.2010.02.024.
13. Oliveira A, Guimarães K, Cerize N, *et al*., 2013, Nano Spray Drying as an Innovative Technology for Encapsulating Hydrophilic Active Pharmaceutical Ingredients (API). *J Nanomed Nanotechnol*, 4:6. DOI 10.4172/2157-7439.1000186.
14. Haas PA, 1992, Formation of Uniform Liquid Drops by Application of Vibration to Laminar Jets. *Ind Eng Chem Res*, 31:959-67. DOI 10.1021/ie00003a043.
15. Yadav TP, Yadav RM, Singh D, 2012, Mechanical Milling: A Top down Approach for the Synthesis of Nanomaterials and Nanocomposites. *Nanosci Nanotechnol*, 2:22-48. DOI 10.5923/j.nn.20120203.01.
16. Aiertza MK, Odriozola I, Cabañero G, *et al*., 2011, Single-chain Polymer Nanoparticles. *Cell Mol Life Sci*, 69:337-46. DOI 10.1007/s00018-011-0852.
17. Yoon J, Kwag J, Shin TJ, *et al*., 2014, Nanoparticles of Conjugated Polymers Prepared from Phase-Separated Films of Phospholipids and Polymers for Biomedical Applications. *Adv Mater*, 26:4559-64. DOI 10.1002/adma.201400906.
18. Yang Y, Khoe U, Wang X, *et al*., 2009, Designer Self-assembling Peptide Nanomaterials. *Nano Today*, 4:193-210. DOI 10.1016/j.nanotod.2009.02.009.
19. Karnik R, Gu F, Basto P, *et al*., 2008, Microfluidic Platform for Controlled Synthesis of Polymeric Nanoparticles. *Nano Lett*, 8:2906-12. DOI 10.1021/nl801736q.
20. Ni M, Zhuo S, Iliescu C, *et al*., 2019, Self-assembling Amyloid-like Peptides as Exogenous Second Harmonic Probes for Bioimaging Applications. *J Biophotonics*, 4:e201900065. DOI 10.1002/jbio.201900065.
21. Ni M, Tresset G, Iliescu C, *et al*., 2019, Microfluidics-assisted Self-assembly of Ultrashort Peptides and their Application as Theranostic Nanoparticles.
22. Arab W, Rauf S, Al-Harbi O, *et al*., 2018, Novel Ultrashort Self-assembling Peptide Bioinks for 3D Culture of Muscle Myoblast Cells. *Int J Bioprinting*, 4(2):129. DOI 10.18063/ijb.v4i2.129.
23. Arab WT, Niyas AM, Seferji K, *et al*., 2018, Evaluation of Peptide Nanogels for Accelerated Wound Healing in Normal Micropigs. *Front Nanosci Nanotech*, 4(4):1-9. DOI 10.15761/fnn.1000173.
24. Arab WT, Kahin K, Khan Z, *et al*., 2019, Exploring Nanofibrous Self-assembling Peptide Hydrogels using Mouse Myoblast Cells for 3D Bioprinting and Tissue Engineering Applications. *Int J Bioprinting*, 5(2):198. DOI 10.18063/ijb.v5i2.198.
25. Reithofer MR, Lakshmanan A, Ping ATK, *et al*., 2014, *In situ* Synthesis of Size-controlled, Stable Silver Nanoparticles within Ultrashort Peptide Hydrogels and their Anti-bacterial Properties. *Biomaterials*, 35:7535-42. DOI 10.1016/j.

biomaterials.2014.04.102.

26. Loo Y, Lakshmanan A, Ni M, *et al*., 2010, Peptide Bioink: Self-assembling Nanofibrous Scaffolds for 3d Organotypic Cultures. *Nano Lett*, 15:6919-25. DOI 10.1021/acs.nanolett.5b02859.
27. Sundaramurthi D, Rauf S, Hauser CAE, 2016, 3D Bioprinting Technology for Regenerative Medicine Applications. *Int J Bioprinting*, 2:9-16. DOI 10.18063/ijb.2016.02.010.
28. Loo Y, Hauser CAE, 2016, Bioprinting Synthetic Self-assembling Peptide Hydrogels for Biomedical Applications. *Biomed Mater*, 11:114103. DOI 10.1088/1748-6041/11/1/014103.
29. Khan Z, Kahin K, Rauf S, *et al*., 2019, Optimization of a 3D Bioprinting Process using Ultrashort Peptide Bioinks. *Int J Bioprinting*, 5(1):173. DOI 10.18063/ijb.v5i1.173.
30. Kahin K, Khan Z, Albagami M, *et al*., 2019, Development of a Robotic 3D Bioprinting and Microfluidic Pumping System for Tissue and Organ Engineering. *Proc SPIE*, 17:108750Q. Doi 10.1117/12.2507237.
31. Zhao X, Pan F, Xu H, *et al*., 2010, Molecular Self-assembly and Applications of Designer Peptide Amphiphiles. *Chem Soc Rev*, 39:3480-98.
32. Versluis F, Marsden HR, Kros A, 2010, Power Struggles in Peptide-amphiphile Nanostructures. *Chem Soc Rev*, 39:3434-44. DOI 10.1039/b919446k.
33. Lakshmanan A, Hauser CAE, 2011, Ultrasmall Peptides Self-assemble into Diverse Nanostructures: Morphological Evaluation and Potential Implications. *Int J Mol Sci*, 12:5736-46. DOI 10.3390/ijms12095736.
34. Loo Y, Zhang S, Hauser CAE, 2012, From Short Peptides to Nanofibers to Macromolecular Assemblies in Biomedicine. *Biotech Adv*, 30:593-603. DOI 10.1016/j.biotechadv.2011.10.004.
35. Cui H, Webber M, Stupp S, 2010, Self-Assembly of Peptide Amphiphiles: From Molecules to Nanostrucutres to Biomaterials. *Biopolymers*, 94:1-18. DOI 10.1002/bip.21328.
36. Lakshmanan A, Zhang S, Hauser CAE, 2012, Short Self-assembling Peptides as Building Blocks for Modern Nanodevices. *Trends Biotech*, 30:155-65. DOI 10.1016/j.tibtech.2011.11.001.
37. Hauser CAE, Zhang S, 2010, Designer Self-assembling Peptide Nanofiber Biological Materials. *Chem Soc Rev*, 39:2780-90. DOI 10.1039/b921448h.
38. Reithofer MR, Chan KH, Lakshmanan A, *et al*., 2014, Ligation of Anti-cancer Drugs to Self-assembling Ultrashort Peptides by Click Chemistry for Localized Therapy. *Chem Sci*, 5:625-30. DOI 10.1039/c3sc51930a.
39. Liu X, Huang J, Chen T, *et al*., 2008, Yamanaka Factors Critically Regulate the Developmental Signaling Network in Mouse Embryonic Stem Cells. *Cell Res*, 18(12):1177-89. DOI 10.1038/cr.2008.309.

# INTERNATIONAL JOURNAL OF BIOPRINTING

ISSN (print): 2424-7723

## ABOUT THE JOURNAL

**International Journal of Bioprinting** is a biannual, double-blind peer-reviewed, open access journal. This journal focuses on the use of 3D printing technology with materials that incorporate viable living cells or biological elements to produce tissue or biotechnological products. Further discourses and technological advancements in bioprinting are the goals behind acceptance of high-quality basic and applied research: from concept creation to fabrication of the bioprinting process, associated clinical applications as well as social implications.


**Whioce Publishing**, official publisher for the journal welcomes researchers to submit their papers relevant to bioprinting for consideration via **http://ijb.whioce.com/** For general enquiries and order for prints and reprints, please write in to **IJB@whioce.com** for a fast response.

SUBMIT YOUR PAPERS HERE

WHIOCE
PUBLISHING PTE. LTD.

## ABOUT THE PUBLISHER

**Whioce Publishing** in Singapore is a registered publisher of excellent quality academic journals for an international readership. We deliver exceptional editorial support for the advancement and dissemination of scientific research by linking readers and researchers with networks and industries. We have ambitions to get our journals indexed in prominent databases such as EI, SCI, SSCI and AHCI, thereby aiming to be a first-class knowledge platform for researchers worldwide.

Whioce Publishing also engages in publishing e-books, organizing academic conferences and educational trainings, and providing translational services.

International Journal of Bioprinting is an
independent open access journal published
by Whioce Publishing Pte.Ltd.

WHIOCE PUBLISHING PTE. LTD.
PROVIDING
FIRST-CLASS SCIENTIFIC INFORMATION
FOR TOP SCHOLARS

Whioce Publishing Pte.Ltd.
7030 Ang Mo Kio Avenue 5
#04-15 Northstar@AMK
Singapore 569880
**Tel:** +65 65702707/65702718
**Fax:** +65 65702803

See www.whioce.com/contact for a full list of offices and contact information.

Whioce Publishing Pte.Ltd. is a company registered in Singapore (No. 201427293E), whose registered office is at 7030 Ang Mo Kio Avenue 5 #04-15 Northstar@AMK Singapore 569880